

*METAL- AND COVALENT ORGANIC FRAMEWORKS
FOR ADVANCED APPLICATIONS:
HETEROGENEOUS CATALYSIS AND SENSING*

Parviz Gohari Derakhshandeh
Ghent University

Center for Ordered Materials,
Organometallics and Catalysis

**Dissertation submitted in fulfilment of the requirements for the degree of
Doctor of Science: Chemistry**

June 2021



Promoters

Prof. dr. Pascal Van Der Voort

Prof. dr. Kristof Van Hecke

Department

Chemistry

Chemistry

Members of the Jury

Prof. dr. Damien Debecker

Prof. dr. Louis Vanduyfhuys

Prof. dr. Anna Kaczmarek

Prof. dr. Henk Vrielinck

Prof. dr. Jeriffa De Clercq

Dr. Amrita Chatterjee

Affiliation

Université Catholique de Louvain

Ghent University

Ghent University

Ghent University

Ghent University

Ghent University

Ghent University

Faculty of Sciences

Department of Chemistry

Krijgslaan 281 S3, 9000 Ghent, Belgium

Tel.: +32-9-264.44.49

Fax.: +32-9-264.49.83

This research was funded by FWO G000117N.



© 2021 Ghent University, Department of Chemistry, COMOC-Center for Ordered Materials, Organometallics & Catalysis, Krijgslaan 281-S3, 9000 Gent, Belgium

Alle rechten voorbehouden. Niets uit deze uitgave mag worden gereproduceerd, opgeslagen in een geautomatiseerd gegevensbestand, of openbaar gemaakt, in enige vorm of op enige wijze, hetzij elektronisch, mechanisch, door printouts, kopieën, of op welke manier dan ook, zonder voorafgaande schriftelijke toestemming van de uitgever.

All rights reserved. No part of this publication may be reproduced, stored in a retrieval system or transmitted in any form or by any means, electronic, mechanical, photocopying, recording or otherwise, without prior permission from the publisher.

ACKNOWLEDGEMENTS

This thesis would not have been possible without the inspiration and support of a number of wonderful individuals. My thanks and appreciation to all of them for being part of this journey and making this thesis possible.

I owe my deepest appreciation to my promoter, Prof. Pascal Van Der Voort for considerable influence on my development as a scientist. I thank him greatly for providing me with ample resources and freedom to explore my ideas. I am very much grateful to him for profound insight into the value and motivation of my scientific research. All his support and encouragement made me unafraid of risk-taking for approaching science and weighing the novelty and creativity of my research project. His kindness and assistance go beyond the research. Thanks for thinking and helping me in all directions of my life.

I would like to highly appreciate Prof. Kristof Van Hecke for my first opportunity to engage in scientific research at Ghent University and for great mentorship.

I deeply acknowledge Prof. Anna Kaczmarek for providing me with greater perspective on luminescence thermometry. I am very grateful for all your guidance and collaboration on the research I performed.

Thanks to Dr. Karen Leus to be always there to help me with everything. You have been a mentor to me in the lab and a very good friend in personal life.

I also want to thank Prof. Christian Stevens, Prof. Veronique Van Speybroeck and Prof. Ying-Ya Liu for their support through the GOA and FWO-China meetings. I am so much grateful to my collaborators who had a great impact on enriching the research – Prof. Markus Antonietti, Prof. Jan Janczak, Prof. Rik Van Deun, Prof. Andre G. Skirtach, Prof. Sasanka Dalapati, Prof. Isabel Van Driessche, Prof. Freddy Callens, Prof. Henk Vrielinck, Prof. Rino Morent, Prof. Nathalie De Geyter, Dr. Aleksandr Savateev, Dr. Maria Meledina, Dr. Johannes Schmidt, Anatolii Abalymov, Parinaz Saadat Esbah Tabaei and Savita K P Veerapandian.

I would like to sincerely thank my PhD examination committee for spending their valuable time to read and correct my thesis. I want to thank Ghent University and FWO for the funding for my PhD and Wiley grant for the funding for my travel abroad.

Thanks again to Prof. Pascal Van Der Voort who has created a wonderful group to work in, who I will further acknowledge below.

I wish to express my special thanks to the colleagues at COMOC – Sara, Karen, Andreas, Geert, Jiamin, Roy, Laurens, Chidharth, Hui, Chunhui, Amrita, Himanshu, Bram, Mahdiah, Elmira, Xander, Gills, Vincent and Yoran . I always remember all the fun, group activities and the time we spent together during these years. Thanks to the former colleagues at COMOC, XStruct and L3 – Els, Hannes, Kevin (alpha and beta), Judith, Norini, Xiao, Mei, Shuna, Guangbo, Jeroen, Flore Tim, Sander, Mina and Dimitrije. Thanks to all my friends from other research groups of S3.

I had the great fortune to develop my skills beyond academia. Tom and Steve, I am so much thankful to you to enrich my expertise and to make me a critical thinker to further developing my industrial career. You were always there to give me motivation and helping me to deal with challenges. I never forget this journey and all the fun we had during the group activities during the Expedition DO.

Of course, I am not forgetting the ATP members of the department – Tom, Katrien, Els, Bart, Pat and Funda. I specifically would like to appreciate Pierre and Kathleen for their continuous support and assistance.

My wonderful Iranian friends from outside of the university, you made my life full of energy, motivation, fun and happiness. Ehsan & Sami, Behnam & Pani, Amin & Leila, Amir & Niloofar, Sepehr & Naghmeh, Kaveh & Mahtab, Behrooz & Farzanhe, Kavoos & Sahel, Setareh & Rasool; I cannot imagine my life without you guys. You were and will be my extended family. I never forget the fun games we had and on top of them the Mafia and Pantomime! All my Iranian friends who I could not name one by one, I am very thankful to you for the great time we had together.

My lovely family, you are on top of my list for appreciation. I am always honored to have you mom and dad who always believed in me and have been my number one supporter.

It was very hard moving 2,779 miles from you but being able to pause and think about you who I love, and who love me was always a source of comfort and perspective. Special thanks to my younger sister, Neda and brothers, Arman and Milad who have been not only the best siblings but also my best friends. Without your unlimited help and support besides mom and dad, the success of my startup company was impossible. Thanks a lot for all years, months, days, hours and minutes you put into our project to run the company with full speed even in my absence.

I would like to highly appreciate my father-, mother- and sisters-in-law (Maryam and Mona) for everything. Your countless assistance and support is not forgettable. My father-in-law you are in my hearth and I always remember all the fun talks we had. Missing you forever was my biggest lost during my PhD.

At the end, I would like to put my warmest appreciation to Sara who has been not only my wonderful wife but also my dearest friend, encourager and colleague. Without you paving my way was not possible. With your company and sympathy, I successfully passed all the challenges I had not only in PhD but also with my startup company. You make impossible possible with all your effort, intelligence and accuracy.

Parviz Gohari Derakhshandeh

Ghent, June 2021

To :

My Love, Sara

SCIENTIFIC A1 PUBLICATIONS

As first author/shared first author

1. A lanthanide-functionalized covalent triazine framework as a physiological molecular thermometer

P Gohari Derakhshandeh, S Abednatanzi, L Bourda, S Dalapati, A Abalymov, M Meledina, Y-Ya Liu, A G. Skirtach, K Van Hecke, A M. Kaczmarek, P Van Der Voort, **J. Mater. Chem. C**, **2021**, 9, 6436

2. A Ru-Complex Tethered to A N-Rich Covalent Triazine Framework for Tandem Aerobic Oxidation–Knoevenagel Condensation Reactions

G Watson,¹ **P Gohari Derakhshandeh**,¹ S Abednatanzi, J Schmidt, K Leus, P Van Der Voort, **Molecules** 26, **2021**, 838.

3. Covalent Triazine Frameworks as Metal-Free Heterogeneous Photocatalysts for Pollutant Degradation

P Gohari Derakhshandeh, M Ovisi, S Abednatanzi, M Alinia Asli, N M Mahmoodi, P Saadat Esbah Tabaei, R Morent, N De Geyter, P Van Der Voort, **2021**, submitted.

4. Metal-free activation of molecular oxygen by covalent triazine frameworks for selective aerobic oxidation

S Abednatanzi,¹ **P Gohari Derakhshandeh**,¹ K Leus, H Vrielinck, F Callens, J Schmidt, A Savateev, P Van Der Voort, **Science Advances** 6, **2020**, eaaz2310.

5. Mixed-metal metal-organic frameworks

S Abednatanzi,¹ **P Gohari Derakhshandeh**,¹ H Depauw, FX Coudert, H Vrielinck, P Van Der Voort, K Leus, **Chemical Society Reviews** 48, **2019**, 2535.

6. Ce(III)-Based Frameworks: From 1D Chain to 3D Porous Metal–Organic Framework

P Gohari Derakhshandeh, S Abednatanzi, K Leus, J Janczak, R Van Deun, P Van Der Voort, K Van Hecke, **Crystal Growth & Design** 19 (12), **2019**, 7096.

7. Mechanochemically synthesized crystalline luminescent 2D coordination polymers of La³⁺ and Ce³⁺, doped with Sm³⁺, Eu³⁺, Tb³⁺, and Dy³⁺: synthesis, crystal structures and luminescence properties

P Gohari Derakhshandeh, J Soleimannejad, J Janczak, AM Kaczmarek, K Van Hecke, R Van Deun, *CrystEngComm* 18, 2016, 6738.

8. Sonochemical synthesis of a new nano-sized cerium(III) supramolecular compound; Precursor for nanocerium

P Gohari Derakhshandeh, J Soleimannejad, *Ultrasonics Sonochemistry* 31, 2016, 122.

9. Sonochemical synthesis of a new nano-sized cerium(III) coordination polymer and its conversion to nanocerium

P Gohari Derakhshandeh, J Soleimannejad, J Janczak, *Ultrasonics Sonochemistry* 26, 2015, 273.

As co-author

10. Combinatorial effects of coral addition and plasma treatment on the properties of chitosan/polyethylene oxide nanofibers intended for bone tissue engineering

P Saadat Esbah Tabaei, M Asadian, R Ghobeira, P Cools, M Thukkaram, **P Gohari Derakhshandeh**, S Abednatanzi, P Van Der Voort, K Verbeken, C Verduyck, H Declercq, R Morent, N De Geyter, *Carbohydrate Polymers* 253, 2021, 117211.

11. Red Edge Effect and Chromoselective Photocatalysis with Amorphous Covalent Triazine-based Frameworks

Y Zou, **P Gohari Derakhshandeh**, S Abednatanzi, NV Tarakina, P Van Der Voort, JW Shi, M Antonietti, A Savateev, 2021, submitted.

12. Elucidating the Promotional Effect of a Covalent Triazine Framework in Aerobic Oxidation

S Abednatanzi, **P Gohari Derakhshandeh**, P Tack, F Muniz-Miranda, YY Liu, J Everaert, F Vanden Bussche, L Vincze, CV Stevens, V Van Speybroeck, H Vrielinck, F Callens, K Leus, P Van Der Voort, *Applied Catalysis B: Environmental* 269, 2020, 118769.

13. Covalent Triazine Framework Hybrids: a Novel Class of Metal-free Electrocatalysts for the Reduction of CO₂

A Laemont, S Abednatanzi, **P Gohari Derakhshandeh**, F Verbruggen, E Fiset, K Van Daele, K Rabaey, T Breugelmanns, P Van Der Voort, K Leus, *Green Chemistry* 22, 2020, 3095.

14. Synthesis, X-ray characterization, and in vitro biological approach of dimeric and polymeric mercury(II) complexes with α -keto stabilized sulfur ylide

- SJ Sabounchei, MS Hashemi, R Karamian, SH Moazzami Farida, P Gohari Derakhshandeh, RW Gable, K Van Hecke, Journal of Coordination Chemistry* 71, 2019, 3277.
15. Spectral, crystallographic, theoretical and antibacterial studies of palladium(II)/platinum(II) complexes with unsymmetric diphosphine ylides
SJ Sabounchei, K Badpa, M Bayat, R Karamian, F Ghasemlou, RW Gable, P Gohari Derakhshandeh, K Van Hecke, Applied Organometallic Chemistry 33, 2019, e4658.
 16. New pallada- and platinacycle complexes of phosphorus ylide: Synthesis, structural characterization, antioxidant capacity and catalytic behavior towards Mizoroki-Heck reactions
SJ Sabounchei, A Hashemi, A Yousefi, P Gohari Derakhshandeh, R Karamian, M Asadbegy, K Van Hecke, Polyhedron 135, 2017, 1.
 17. Synthesis, characterization and catalytic properties of a copper-containing polyoxovanadate nanocluster in azide-alkyne cycloaddition
M Amini, S Bahadori Tekantappeh, B Eftekhari-Sis, P Gohari Derakhshandeh, K Van Hecke, Journal of Coordination Chemistry 70, 2017, 1564.
 18. POM@IL-MOFs – inclusion of POMs in ionic liquid modified MOFs to produce recyclable oxidation catalysts
S Abednatanzi, K Leus, P Gohari Derakhshandeh, F Nahra, K De Keukeleere, K Van Hecke, I Van Driessche, A Abbasi, SP Nolan, P Van Der Voort, Catalysis Science & Technology 7, 2017, 1478.
 19. Direct Synthesis of an Iridium(III) Bipyridine Metal–Organic Framework as a Heterogeneous Catalyst for Aerobic Alcohol Oxidation
S Abednatanzi, P Gohari Derakhshandeh, A Abbasi, P Van Der Voort, K Leus, ChemCatChem 8, 2016, 3672.
 20. Molybdenum(VI)-oxodiperoxo complex containing an oxazine ligand: synthesis, X-ray studies, and catalytic activity
M Aminia, M Bagherzadeh, B Atabaki, P Gohari Derakhshandeh, A Ellern, LK Woo, Journal of Coordination Chemistry 67, 2014, 1429.
 21. A novel iron complex containing an N,O-type bidentate oxazoline ligand: Synthesis, X-ray studies, DFT calculations and catalytic activity
M Amini, A Arab, P Gohari Derakhshandeh, M Bagherzadeh, A Ellern, LK Woo, Spectrochimica Acta Part A: Molecular and Biomolecular Spectroscopy 133, 2014, 432.

22. An efficient glucose-based ligand for Heck and Suzuki coupling reactions in aqueous media

M Bagherzadeh, M Amini, P Gohari Derakhshandeh, MM Haghdoost, Journal of Iranian Chemical Society, 11, 2014, 441.

23. Molybdenum oxo-peroxo complex: A very fast catalyst for oxidation and reduction of sulfur-based compounds

M Bagherzadeh, MM Haghdoost, M Amini, P Gohari Derakhshandeh, Catalysis Communications, 23, 2012, 14.

Book Chapter

24. Alcohol Oxidation: Reaction, Effects and Applications, Chapter 3: Selective Alcohol Oxidation by Metal-Organic Frameworks and Covalent Organic Frameworks

S Abednatanzi, P Gohari Derakhshandeh, K Leus, P Van Der Voort, Nova Science Publishers, 2018, ISBN: 978-1-53614-604-2.

ENGLISH SUMMARY

As two newly emerging classes of advanced porous materials, metal-organic frameworks (MOFs) and covalent triazine frameworks (CTFs), introduced in 1999 and 2008 respectively, have exhibited promising potential for numerous applications. These materials are now being extensively studied and explored by both academic and industrial scientists due to their unique features. Still, the structural design and advanced applications of these materials are relatively unexplored and deserve further investigation. In the first part of this thesis, new MOFs were synthesized and advancements were made in typical applications of MOFs in the fields of heterogeneous catalysis. The second part of the thesis highlights the importance of the synthesis strategies for designing CTFs. An in-depth understanding of the structural properties of CTFs based on the synthesis method is provided. Furthermore, several new CTFs were synthesized in this thesis, applying various synthesis procedures. The heterogeneous thermal catalysis, photocatalysis, and temperature sensing of the obtained materials were investigated.

In Chapter 1, a class of porous materials, named MOFs, is introduced. The predominant investigated structures are listed, and general synthesis procedures of these materials are described. Emphasis is placed on the catalytic application of MOFs, this dissertation's main application.

Chapter 2 provides a general overview of COFs, focusing more specifically on a subclass of COFs, namely covalent triazine frameworks (CTFs), which exhibit remarkably high thermal and chemical stability, high permanent porosity, easy tunability, and functionalities. An overview of the evolution of CTFs and different synthetic approaches for building these materials are discussed, followed by a discussion of the application of these unique materials, particularly as supports for catalytically active metals. The recent advancements in the field of photocatalysis and sensing are also presented.

Chapter 3 describes the immobilization of an Ir(III) complex onto a MOF support to obtain a new heterogenized iridium catalyst for the oxidation of benzyl alcohol. The $[\text{IrCp}^*\text{Cl}_2]_2$ complex was utilized as an iridium precursor to tether onto the bipyridine moiety of the COMOC-4 MOF via pre-functionalization and post-synthetic modification routes. The

covalent attachment of the complex onto a stable MOF support is an efficient strategy to prevent leaching of the metal ions and therefore to create a truly heterogenized catalyst. The importance of the synthesis strategy on the structural properties of the final materials has been investigated in details which is rarely studied in the previous reports.

In **chapter 4**, the design and synthesis of three new Ce(III)-based frameworks using 2,4-pyridinedicarboxylic acid as the linker were established. Small changes to the reaction conditions led to three different structures, ranging from a one-dimensional coordination polymer to a three-dimensional porous MOF. As a proof-of-concept, the catalytic properties of the 3D MOF in acetalization reactions of different aldehydes with methanol were investigated.

In **chapter 5**, an efficient catalytic system for tandem aerobic oxidation–Knoevenagel condensation reaction was introduced. A highly N-rich CTF containing bipyridine (bipy) building blocks (bipy-CTF) is used as the catalyst support. The bipy building units provide excellent docking sites for immobilization of a Ru^{III} complex, examined initially in the selective aerobic oxidation of alcohols to aldehydes. The bipy-CTF material not only acts as anchoring points but also promotes the sequential reaction of aldehydes and nitriles due to the presence of N-rich basic functionalities. The results indicate that the synergistic effects between the N-rich bipy-CTF and the Ru^{III} complex are beneficial for obtaining a highly active and selective catalyst for tandem catalysis in the absence of any co-oxidant.

Chapter 6 presents the design of two new CTFs containing S and N heteroatom functionalities via the condensation reaction of aldehydes and amidines in mild conditions. The CTFs were applied as metal-free photocatalysts, examined in dye degradation in order to investigate the effect of heteroatoms on the physicochemical properties and photocatalytic efficiency.

In **chapter 7**, a novel application of CTFs as photoluminescent materials was investigated. The highly crystalline bipyridine-based CTF was synthesized via the polycondensation reaction. The nitrogen-rich material provides excellent docking sites for the immobilization of various guests, examined for two different lanthanide guests (Eu³⁺ and Tb³⁺). The bipy sites not only act as anchoring points for lanthanides but also enable the excitation of Ln³⁺ ions through an intramolecular energy transfer known as the

“antenna effect”. The obtained materials exhibit excellent temperature sensing properties in the physiological range.

Chapter 8 provides a summary and general conclusions of this thesis and provides future perspectives.

DUTCH SUMMARY

Metal Organic frameworks (MOFs) en covalent triazine frameworks (COFs) , respectievelijk geïntroduceerd in 1999 en 2008, zijn als opkomende klasse van geavanceerde poreuze materialen veelbelovend voor tal van toepassingen. Door hun unieke eigenschappen worden deze materialen uitvoerig onderzocht door zowel de academische als de industriële wereld. Toch zijn het structureel ontwerp en de geavanceerde toepassingen van deze materialen weinig onderzocht, terwijl verder onderzoek nuttig kan zijn voor tal van nieuwe of bestaande toepassingen. In het eerste deel van deze thesis, werden nieuwe MOFs gesynthetiseerd en typische toepassingen van MOFs in heterogene katalyse werden geoptimaliseerd. Het tweede deel van deze thesis gaat dieper in op de rol van synthese strategieën in het ontwerpen van CTFs. Er wordt een gedetailleerde uitleg over de structuur van CTFs gebaseerd op de syntheseroute gegeven. Verder werden er verschillende nieuwe CTFs gesynthetiseerd op basis van verschillende syntheseroutes. De eigenschappen van deze CTFs werden onderzocht met het oog op toepassing in heterogene thermische katalyse, licht geïnduceerde katalyse en temperatuurmeting.

In Hoofdstuk 1 wordt een klasse van poreuze materialen, genaamd MOFs, geïntroduceerd. De belangrijkste onderzochte structuren zijn getabelleerd, samen met algemene synthese procedures voor deze materialen. De belangrijkste toepassing in deze thesis, is het gebruik van MOFs als katalysator en daar ligt dus ook de nadruk op.

Hoofdstuk 2 geeft een algemeen overzicht van COFs. Vooral over een specifieke subgroep van COFs, nl. covalent triazine frameworks CTFs. Deze CTFs hebben een opmerkelijk hoge thermische en chemische stabiliteit, hoge permanente porositeit en zijn gemakkelijk te modificeren en functionaliseren. Er wordt een overzicht gegeven over de ontwikkeling van CTFs doorheen de jaren. Eveneens worden er synthese-strategieën besproken, gevolgd door een discussie over de toepassing van deze materialen, voornamelijk als houder-materiaal voor katalytisch actieve metalen. De recente vorderingen op gebied van licht-geïnduceerde katalyse en gebruik als meetinstrument worden ook gegeven.

Hoofdstuk 3 beschrijft het immobiliseren van een Ir(III) complex op het oppervlak van een MOF. Zo wordt een nieuwe heterogene iridium katalysator, voor de oxidatie van benzylalcohol, verkregen. $[\text{IrCp}^*\text{Cl}_2]_2$ werd gebruikt als precursor om het iridium-complex te binden aan de bipyridine-functionaliteit van de COMOC-4 MOF. Dit gebeurde zowel via pre-functionaliteit als via post-modificatie syntheses. Het covalent binden van het metaal-complex voorkomt dat de omgeving wordt blootgesteld aan metaal-ionen. Men spreekt dus van een typische heterogene katalysator. De rol van de synthese-strategie in de uiteindelijke structurele eigenschappen werd in deze thesis uitvoerig onderzocht en gerapporteerd. Dit soort onderzoek is nauwelijks eerder gerapporteerd.

In Hoofdstuk 4 wordt dieper ingegaan op het ontwerpen en synthetiseren van drie nieuwe Ce(III)-gebaseerde MOFs met 2,4-pyridinedicarbonzuur als linker. Kleine aanpassingen in de reactiecondities leiden tot drie verschillende structuren, gaande van een één-dimensionaal polymeer tot een driedimensionaal, poreuze MOF. Om het concept te bewijzen, werden de katalytische eigenschappen van de 3D MOF in acetylering reacties van verschillende aldehydes met methanol onderzocht.

In Hoofdstuk 5 wordt een efficiënt katalytisch systeem voor de tandem aerobe oxidatie-Knoevenagel condensatie gegeven. Een CTF met hoog N-gehalte en dat bipyridine (bipy) bevat, nl. bipy-CTF, wordt gebruikt als dragermateriaal voor de katalysator. De bipy bouwstenen introduceren een ideale bindingsplaats voor een Ru(III)-complex. Dit werd eerst onderzocht via de selectieve aerobe oxidatie van alcoholen tot aldehydes. De bipy-CTF heeft niet alleen een uitstekend ankerpunt voor katalyse, maar het promoot ook de opeenvolgende reacties van aldehydes en nitrillen. Dit is vooral te danken aan basische N-bevattende functionele groepen. De resultaten tonen aan dat de synergetische effecten tussen de N-rijke bipy-CTF en het Ru(III)-complex gunstig zijn voor het verkrijgen van een zeer actieve en selectieve katalysator, voor de tandem katalyse in afwezigheid van enige co-oxidator.

Hoofdstuk 6 stelt het ontwerp van twee nieuwe CTFs, die S en N heteroatoom-functionaliteiten bevatten, voor. Dit via de condensatie reactie van aldehydes en amidines in milde condities. De CTFs werden gebruikt als metaal-vrije licht-geïnduceerde katalysatoren in een degradatie reactie van kleurstoffen, dit om het effect van de

heteroatomen op de fysicochemische eigenschappen en licht-geïnduceerde katalyse-efficiëntie te onderzoeken.

In Hoofdstuk 7 wordt een nieuwe toepassing als licht-geïnduceerde luminescentie onderzocht. De volledig kristallijne op bipyridine gebaseerde CTF was gesynthetiseerd via een polycondensatie. Het N-rijke materiaal zorgt voor uitstekende ankerpunten voor allerlei complexen. Dit werd onderzocht voor twee verschillende lanthaniden (Eu^{3+} and Tb^{3+}). De bipy functionaliteiten dienen niet enkel als ankerpunt voor lanthaniden maar ze zorgen ook voor de excitatie van Ln^{3+} ionen, via een intramoleculaire energie transfer, ook wel het “antenna-effect” genoemd. De verkregen materialen hebben uitstekende eigenschappen als thermometers in fysiologische condities.

Hoofdstuk 8 geeft een samenvatting en algemene besluiten over deze thesis en geeft verdere perspectieven.

CONTENTS

POROUS INORGANIC MATERIALS: METAL-ORGANIC FRAMEWORKS	1
1.1. Introduction.....	2
1.2. Metal-Organic Frameworks (MOFs)	4
1.2.1. MOF design principle	8
1.2.1.1. Direct synthesis approach or one-pot reaction.....	9
1.2.1.2. Pre-functionalization approach using metallo-linkers	12
1.2.1.3. Post-synthetic modification (PSM).....	13
1.2.1.4. Post-synthetic exchange.....	16
1.3. MOFs in heterogeneous catalysis	17
1.3.1. MOFs in oxidation reactions.....	18
1.3.2. Epoxidation Reactions	21
1.3.3. Condensation Reactions.....	23
1.3.4. Tandem Reactions.....	24
1.3.5. CO ₂ Reduction Reaction (CRR)	26
1.3.6. Photocatalysis	27
1.4. Objectives: Synthetic Opportunities	30
1.5. References.....	31
POROUS ORGANIC MATERIALS: COVALENT ORGANIC/TRIAZINE FRAMEWORKS	36
2.1. Introduction.....	37
2.2. Synthesis of CTFs.....	39
2.2.1. Ionothermal synthesis	40
2.2.2. Bronsted Acid	40
2.2.3. Sulfur-mediated.....	41
2.2.4. Phosphorus pentoxide (P ₂ O ₅).....	42
2.2.5. Amidine synthesis based on a polycondensation method.....	42
2.3. Application of CTFs	45
2.3.1. Catalysis.....	45
2.3.2. Photocatalysis	49
2.3.3. Luminescence and sensing applications	55
2.4. Objectives	57

2.5. References:.....	59
DIRECT SYNTHESIS OF AN Iridium(III)-BIPYRIDINE-METAL-ORGANIC FRAMEWORK AS HETEROGENEOUS CATALYST FOR AEROBIC ALCOHOL OXIDATION	63
3.1. Introduction.....	65
3.2. Results and Discussion	67
3.2.1. Synthesis and structural information	67
3.2.2. Characterization of Ir(III)Cp*Cl@COMOC-4	68
3.2.2.1. X-ray diffraction, nitrogen adsorption and thermogravimetric analysis.....	68
3.2.2.2. Spectroscopic analysis	72
3.3. Catalytic tests	73
3.4. Stability and regenerability tests	76
3.5. Conclusions.....	79
3.6. Experimental Section	79
3.6.1. Materials and instrumentation.....	79
3.6.2. Synthesis of the Ir(III)Cp*Cl@COMOC-4 materials	79
3.6.2.1. Post-synthetic modification approach.....	79
3.6.2.2. Pre-functionalization approach	80
3.6.3. Catalytic setup.....	80
3.7. References.....	81
3.8. Supporting Information.....	84
CE(III)-BASED FRAMEWORKS: FROM 1D CHAIN TO 3D POROUS METAL-ORGANIC FRAMEWORK	89
4.1. Introduction.....	91
4.2. Results and Discussion	92
4.2.1. Synthesis and Preliminary Characterization	92
4.2.2. Structural Analysis.....	93
4.2.3. Catalytic acetalization reaction	103
4.3. Conclusion	105
4.4. Experimental Section	105
4.4.1. Materials and instrumentation.....	105
4.4.2. Synthesis	105
4.4.3. General procedure for the acetalization reaction of benzaldehyde	106
4.5. References.....	107

4.6. Supporting Information.....	112
A RU-COMPLEX TETHERED TO A N-RICH COVALENT TRIAZINE FRAMEWORK FOR TANDEM AEROBIC OXIDATION–KNOEVENAGEL CONDENSATION REACTIONS	134
5.1. Introduction.....	135
5.2. Results and Discussion	137
5.2.1. Synthesis and characterization of the modified bipy-CTF with the Ru Complex (Ru ^{III} @bipy-CTF).....	137
5.3. Catalytic activity of the Ru ^{III} @bipy-CTF catalyst in the tandem aerobic oxidation–Knoevenagel condensation reaction	141
5.4. Conclusions.....	146
5.5. Experimental Section.....	146
5.5.1. Materials and instrumentation.....	146
5.5.2. Synthesis of bipy-CTFs and Ru ^{III} @bipy-CTF materials	146
5.5.3. Catalytic reactions.....	147
5.6. References.....	148
5.7. Supporting Information.....	151
COVALENT TRIAZINE FRAMEWORKS AS METAL-FREE HETEROGENEOUS PHOTOCATALYSTS FOR POLLUTANT DEGRADATION	159
6.1. Introduction.....	161
6.2. Results and Discussion	163
6.2.1. Synthesis and Characterization of heteroatom-embedded CTFs	163
6.2.2. Catalytic performance of heteroatom-embedded CTFs for the photocatalytic degradation of Rhodamine B (RB)	167
6.2.3. Mechanistic studies for the photocatalytic degradation of Rhodamine B over the TT-CTF catalyst	169
6.3. Conclusions.....	171
6.4. Experimental Section.....	172
6.4.1. Materials and instrumentation.....	172
6.4.2. Synthesis of heteroatom-embedded CTFs	172
6.4.3. Photocatalytic dye removal.....	173
6.5. References.....	173
6.6. Supporting Information.....	177
LANTHANIDE FUNCTIONALIZED COVALENT TRIAZINE FRAMEWORK AS PHYSIOLOGICAL MOLECULAR THERMOMETER	182

Metal- and Covalent Organic Frameworks for Advanced Applications: Heterogeneous Catalysis and Sensing

7.1. Introduction.....	184
7.2. Results and Discussion	186
7.2.1. Synthesis and Characterization of Ln@Bipy-CTF	186
7.2.2. Luminescence Thermometry of Ln@Bipy-CTF.....	190
7.3. Conclusions.....	196
7.4. Experimental Section.....	196
7.4.1. Materials and instrumentation.....	196
7.4.2. Synthesis of 2,2'-bipyridine-5,5'-diamidine dihydrochloride	197
7.4.3. Synthesis of Bipy-CTF	197
7.4.4. Synthesis of Ln@Bipy-CTF	197
7.5. References.....	198
7.6. Supporting Information.....	201
CONCLUSIONS AND OUTLOOK	215
8.1. Heterogeneous catalysis with MOFs	216
8.2. Heterogeneous catalysis with CTFs.....	218
8.3. Heterogeneous photocatalysis with CTFs.....	219
8.4. Physiological luminescent thermometry with CTFs.....	220
8.5. General outlook.....	221
8.6. References.....	223
Appendix.....	224

LIST OF TABLES

Table 1. 1. Application of MOFs in heterogeneous catalysis.	28
Table 3. 1. Properties of the Ir(III)Cp*Cl@COMOC-4 materials.	72
Table 3. 2. Catalytic performance of Ir(III)Cp*Cl@COMOC-4 in the oxidation of benzyl alcohol.	75
Table 3. 3. Comparison of the results obtained for the aerobic oxidation of benzyl alcohol catalyzed by different iridium catalysts.	76
Table 4. 1. Crystal data and refinement details for 1 , 2 and 3	94
Table 4. 2. Catalytic performance of the MOF 3 catalyst towards the acetalization reaction of various benzaldehyde derivatives with alcohols.	104
Table 5. 1. Elemental analysis of the pristine and modified CTF materials.	139
Table 5. 2. Catalytic performance of different catalysts in the oxidation of benzyl alcohol.	142
Table 5. 3. Catalytic performance of Ru ^{III} @bipy-CTF catalyst in tandem aerobic oxidation–Knoevenagel condensation reaction.	143
Table 5. 4. Comparison of the Ru ^{III} @bipy-CTF catalyst with other heterogeneous catalysts for selective tandem oxidation–Knoevenagel condensation reaction.	145

LIST OF FIGURES

Figure 1. 1. Examples of naturally occurring porous materials placed alongside the length scale according to their critical dimensions. The scanning electron microscopy (SEM) images of original biological hierarchically porous structures are shown from bottom to top: diatom, butterfly, wood, leaf, macaw feather, grass stem, kelp, coral, cotton, human bone, cuttlefish bone, and sponge. ...	3
Figure 1. 2. Series of isorecticular MOFs based on MOF-5. In IRMOF-1 to IRMOF-7 the organic linker had a different functionality whereas in IRMOF-8 to IRMOF-16, the length of the organic linker was changed.....	5
Figure 1. 3. Lattice structures (middle) and corresponding SBUs (metal nodes (left), and organic linkers (right)) of some of the MOFs discussed in this chapter. (Atom definition: blue–metal, red–oxygen, purple–nitrogen, grey–carbon, green–chlorine).....	6
Figure 1. 4. Employed linkers and their assembly into a Zr-based UiO-67(BPy) MOF. The structure is obtainable by one-pot synthesis (left) or by post-functionalization (right).....	7
Figure 1. 5. The distinction between an ionic interaction and a covalent interaction in carboxylate MOFs.	8
Figure 1. 6. The % covalency of the metal-carboxylate bonding as a result of the analysis of 6163 different structures..	9
Figure 1. 7. Schematic illustration of the direct synthesis of MOFs with (a) one and (b) two metal precursors.....	10
Figure 1. 8. Multivariate MOF-74 materials having up to 10 various metals within their structure..	11
Figure 1. 9. Schematic representation of the synthesis of MOFs using metallo-linkers	12
Figure 1. 10. (a) Augmented tetracarboxylic porphyrinic linkers, TCBPP-X (X = H ₂ , Zn, Co, Fe). (b) 12-connected Zr ₆ (μ ₃ -O) ₄ (μ ₃ -OH) ₄ (O ₂ C) ₁₂ cluster. (c) Cubic cage with 2.5 nm edge length. (d) The 3D network with Zr ₆ clusters shown as polyhedra and 3D cubic-cavity packing in CPM-99Fe. Color scheme: Zr (teal); Fe (lime); O (red); N (blue); C (gray). (e) Photograph of CPM-99Fe. .	13
Figure 1. 11. Formation of MM-MOF through post-synthetic metal complexation/insertion.	14
Figure 1. 12. Representation of different PSM routs of MOFs.	14
Figure 1. 13. Schematic of MIL-101 structure	15

Figure 1. 14. Schematic illustration of the preparation of PW/DAIL/MIL-101(Cr)..	16
Figure 1. 15. Post-synthetic exchange to introduce reduced metal cations in MOF-5.	17
Figure 1. 16. Aerobic oxidation of cyclohexene using Co/Ni-MOF-74.	20
Figure 1. 17. Schematic illustration of modified MOFs with copper complexes: (a) Cu(II)/MOF-NH ₂ , (b) PCN-700-BPYDC(Cu)-TPDC-R ₂ .	21
Figure 1. 18. Post-synthetic metal exchange in porph@MOM-10 for styrene epoxidation.	22
Figure 1. 19. Condensation of glycerol with acetone over a series of MIL catalysts.	23
Figure 1. 20. Cu-doped ZIF-8 for Friedländer and Combes condensations.	24
Figure 1. 21. One-pot Strecker reaction using benzaldehyde, aniline, and TMSCN.	25
Figure 1. 22. Tandem Friedel–Crafts addition and oxidation reaction catalyzed by MIL-100 (Sc/Fe).	26
Figure 1. 23. Synthesis procedure of UiO-67(Ru/Ti) for photodegradation under visible light.	28
Figure 2. 1. Example of porous 2D COFs with different topologies.	37
Figure 2. 2. Reaction scheme for the synthesis of the first reported CTF denoted as CTF-1.	38
Figure 2. 3. Series of nitrile building blocks for the synthesis of CTF materials.	39
Figure 2. 4. (a) Schematic illustration of the preparation of the porous CTF materials under ionothermal conditions. (b) Ionothermal trimerization of 1,4-dicyanobenzene monomer in molten ZnCl ₂ to trimers and oligomers and subsequently to a covalent triazine-based framework (CTF-1).	41
Figure 2. 5. (a) Reaction mechanism of the amidine-based polycondensation method for triazine formation in the synthesis of amorphous CTFs. (b-e) Representative structures of CTF-HUST-1, CTF-HUST-2, CTF-HUST-3 and CTF-HUST-4, respectively, were synthesized by different aldehyde monomers. The green and purple circles represent the presence of two types of pores in the structure.	43
Figure 2. 6. (a) The general strategy of <i>in-situ</i> aldehyde formation by slow oxidation of alcohol to control the nucleation rate for the formation of CTF. (b) Range of monomers applied within this method.	44

Figure 2. 7. (a) Trimerization of 2,6-dicyanopyridine in molten $ZnCl_2$, conversion to a CTF and subsequent platinum coordination (Pt-CTF), (b) Periana's platinum bipyrimidine complex. 46

Figure 2. 8. Schematic representation of the Ir@CTF and Pt@CTF catalysts. 47

Figure 2. 9. (a) Schematic representation of the CTF-DCE-Ag catalyst, (b) Direct carboxylation of terminal alkynes with CO_2 49

Figure 2. 10. (a) Two-step synthesis of CTF-1-X materials, (b) Powder XRD patterns and photographs of pre-CTF and CTF-1-X materials with $X = 2.5-30$ min, (c) Photocatalytic H_2 evolution of pre-CTF and CTF-1-X materials under visible light irradiation. 51

Figure 2. 11. (a) Schematic representation of thiophene-based CTF formation pathway on SBA-15, (b) Proposed reaction mechanism for the selective oxidation of benzyl alcohol using CTF-Th@SBA-15 photocatalyst. 54

Figure 2. 12. (a) Schematic representation of heteroatom-containing CTFs, (b) Hydrogen evolution performance of CTFs with the time course (inset). 55

Figure 2. 13. (a) Synthesis procedure to make PCTF-8, (b) the fluorescence quenching performance of PCTF-8. 56

Figure 2. 14. (a) Synthesis route to make F-CTF-3, (b) The emission spectra of F-CTF-3 dispersed in water upon the addition of PA, and (c) Representation of the mechanism for the selective fluorescence response of F-CTF-3 to PA. 57

Figure 3. 1. XRPD patterns of the COMOC-4 and Ir(III)Cp*Cl@COMOC-4 materials. 70

Figure 3. 2. Nitrogen adsorption isotherms of the COMOC-4, and Ir(III)Cp*Cl@COMOC-4 materials. 71

Figure 3. 3. Far-IR spectra of the COMOC-4, Ir- H_2bpydc metallo-linker, and Ir(III)Cp*Cl@COMOC-4 materials. 73

Figure 3. 4. Hot filtration test for the Ir(III)Cp*Cl@COMOC-4 catalyst. 77

Figure 3. 5. Recyclability of the Ir(III)Cp*Cl@COMOC-4 catalyst in the presence of KCl. Reaction conditions: Benzyl alcohol (0.33 mmol), base (0.4 mmol), iodobenzene (0.4 mmol), KCl (0.4 mmol), toluene (330 μ l). 77

Figure 3. 6. XRPD patterns of the Ir(III)Cp*Cl@COMOC-4 catalyst after each catalytic run. .. 78

Figure 4. 1. (a) Coordination environment of the Ce(III) cation in 1. (b, c) Fragment of the 1D coordination polymer chain of 1. (d, e) Fragment of the 3D supramolecular framework of 1..... 96

Figure 4. 2. (a) Coordination environment of the Ce(III) cation in 2. (b, c and d) Fragment of the 2D coordination polymer grid of 2. (e, f) Fragment of the 3D supramolecular framework of 2.. 98

Figure 4. 3. (a) Asymmetric unit of 3. (b) Coordination environment of Ce1 and Ce2. (c) Fragment of the 3D network of 3. (d) View of helical channel in 3. 99

Figure 4. 4. View of (a) the 3-c net topological structure of 1, (b) the 3,5-c net with stoichiometry (3-c)(5-c) of 2 (color codes: blue codes represent the center ring of the 3-connected Hpydc⁻ and pydc²⁻ ligands and pink codes represent Ce³⁺ ions) and (c) the 8-c net topological structure of 3. 101

Figure 4. 5. Nitrogen sorption isotherm of MOF 3..... 102

Figure 5. 1. Schematic representation of the ideal ordered structure of Ru^{III}@bipy-CTF material. 137

Figure 5. 2. Structural characterization of bipy-CTF and Ru^{III}@bipy-CTF materials. (a) DRIFT spectra. (b) Nitrogen adsorption/desorption isotherms. (c) Powder XRD patterns. (d) TGA curves. 139

Figure 5. 3. Structural characterization of bipy-CTF and Ru^{III}@bipy-CTF materials. (a) N 1S XPS spectrum of the bipy-CTF. (b) N 1s XPS spectrum of the Ru^{III}@bipy-CTF. (c) Ru 3p XPS spectrum of the Ru^{III}@bipy-CTF. (d) Ru 3d XPS spectrum of the Ru^{III}@bipy-CTF. 140

Figure 5. 4. Recyclability of the Ru^{III}@bipy-CTF catalyst (1 mol% catalyst, 0.33 mmol benzyl alcohol, 0.4 mmol Cs₂CO₃, 500 μl toluene, 0.33 mmol malononitrile, O₂, 100 °C, 12 h (1st step) and 70 °C, 1 h (2nd step)). 145

Figure 6. 1. Synthesis of covalent triazine frameworks via condensation of different aldehyde monomers with amidine..... 163

Figure 6. 2. (a) DRIFT spectra, (b) Nitrogen adsorption/desorption isotherms, (c) Powder XRD patterns, (d) TGA curves..... 165

Figure 6. 3. (a-c) TEM images of TT-CTF, BT-CTF and CTF-1, respectively. 166

Figure 6. 4. (a-c) N 1s spectra of TT-CTF, BT-CTF and CTF-1, respectively, (d-e) S 2p spectra of TT-CTF and BT-CTF, respectively. 166

Figure 6. 5. Photocatalytic degradation of RB (50 mg L^{-1}) over (a) TT-CTF, (b) BT-CTF and (c) CTF-1 using various amounts of photocatalysts (2, 3, 4 and 5 mg) under visible light irradiation. (d) The degradation efficiency of RB under visible light processes at various pollutant concentrations. 168

Figure 6. 6. (a) Solid state UV-Vis spectra, (b) Tauc plot analyses for bandgap calculations of the CTFs..... 169

Figure 6. 7. (a) Photodegradation of RB over TT-CTF with different scavengers. (b) Schematic illustration of RB photodegradation over TT-CTF under visible light irradiation and in the presence of air. 170

Figure 6. 8. Regeneration of the TT-CTF photocatalyst..... 171

Figure 7. 1. A) Scheme showing the triazine framework synthesis through in situ formation of aldehyde monomers by controlled oxidation of alcohol monomers and condensation with amidine, and B) LnCTF ($\text{Ln} = \text{Eu, Tb}$) synthesis. C) DRIFTS of Bipy-CTF, diamidine linker, terephthalaldehyde and 1,4-benzendimethanol. D) Background corrected experimental (black) and Pawley refined (red) PXRD patterns of Bipy-CTF AA stacking, accompanied with the difference plot (blue) and Bragg peak positions (green) of the model. E) Top and side views of the Bipy-CTF structure, carbon is shown in grey, nitrogen in blue, hydrogens were omitted for clarity. F) Nitrogen (N_2) adsorption/desorption isotherms of Bipy-CTF (black) and EuTb@Bipy-CTF (red). G) Solid-state ^{13}C CP/MAS NMR spectra of Bipy-CTF. H) TGA data of Bipy-CTF (black) and EuTb@Bipy-CTF (red) measured under air atmosphere..... 188

Figure 7. 2. ADF-STEM image of A) pristine Bipy-CTF B) Bipy-CTF after loading together with corresponding FFT in the inset revealing the crystallinity of the materials. 189

Figure 7. 3. A) Photo taken when placing 1, 2, 3 and 4 (from left to right) samples under a UV lamp (302 nm excitation). Combined excitation-emission spectra of B) 1, C) 2, D) 3 and E) 4 compounds. The labeled peaks have been assigned in the SI (Table S7.2-S7.5). 191

Figure 7. 4. A) Emission map of 3 recorded between 200-340 K with a step size of 20K. B) Plot presenting the calibration curve of 3 when the equation for Δ is employed. The points show the experimental delta parameters and the solid like presents the best fit of the experimental points. C) Plot presenting the relative sensitivity S_r values at varied temperatures (200-340 K) for compound 3. D) Emission map of 4 recorded between 253-333 K with a step size of 10K. E) Plot presenting the calibration curve of 4 when the equation for Δ is employed. The points show the experimental delta parameters and the solid like presents the best fit of the experimental points; F) Plot presenting the relative temperature sensitivity S_r values at varied temperatures (253-333 K) for compound 4. The solid line is a guide to increase visibility. G) Graph presenting the temperature

uncertainty for compound 3 and H) compound 4. I) Cycle test showing reusability of the compound 3 thermometer material (98.5% repeatability). 193

Figure 7. 5. A) Emission map of sample 3 recorded between 283.15-323.15 K with a step size of 5 K in a water suspension. B) Plot presenting the calibration curve of compound 3 when the equation for Δ is employed. The points show the experimental delta parameters and the solid line presents the best fit of the experimental points. C) Plot presenting the relative sensitivity S_r values at varied temperatures (283.15-323.15 K) for compound 3 in water suspension. D) Graph presenting the temperature uncertainty for 3 measured in water suspension. 194

Figure 7. 6. A) Graph presenting the cell viability (%) after exposure to different concentrations of the BipyCTF and compound 2 particles. An asterisk (*) indicates significant differences from the control cell group. The statistical analysis was performed by ANOVA followed by the Tukey test ($p < 0.05$). B) Fluorescence microscopy images of the cells at different compound concentrations (cells are green). Scale bar is 250 μm 195

LIST OF ABBREVIATIONS AND ACRONYMS

A

AC	Activated carbon
Acac	Acetylacetonate

B

BET	Brunauer--Emmett--Teller
Bpy	Bipyridine

C

COF	Covalent organic framework
COMOC	Center for Ordered Materials, Organometallics, and Catalysis
CPM	Crystalline porous material
CTF	Covalent triazine framework
CUM	Coordinatively unsaturated metal

D

DFT	Density functional theory
DRIFT	Diffuse reflectance infrared Fourier transform spectroscopy
DRS	Diffuse reflectance spectroscopy
DTA	Differential Thermal Analysis

F

FID	Flame ionization detector
FT-IR	Fourier Transform Infrared Spectroscopy

G

GC	Gas chromatography
----	--------------------

H

HKUST	Hong Kong University of Science & Technology
-------	--

I

ICP-OES	Inductively coupled plasma-optical emission spectrometry
IRMOF	Isoreticular MOF
M	
MB	Methylene blue
MIL	Materials Institute Lavoisier
MM-MOF	Mixed-metal MOF
MOF	Metal-organic framework
MS	Mass spectrometry
N	
NMR	Nuclear Magnetic Resonance
P	
PL	Photoluminescent
POP	Porous organic polymer
PSM	Post-synthetic modification
R	
RB	Rhodamine B
S	
SBU	Secondary building units
SEM	Scanning electron microscopy
(S)TEM	(Scanning) transmission electron microscopy
T	
TBHP	<i>tert</i> -butyl hydroperoxide
TFMS	Trifluoromethanesulfonic acid
TGA	Thermal gravimetric analyses
TOF	Turnover frequency
TON	Turnover number
X	
XPS	X-ray photoelectron spectroscopy
XR(P)D	X-ray (powder) diffraction
Z	
ZIF	Zeolitic Imidazole Framework

AIM OF THE THESIS

Although the field of Metal Organic framework and Covalent Triazine Frameworks has seen a rapid development in recent years, it is still in its infancy. The full potential of MOFs and COFs are not yet exploited at all. These advanced materials show huge promise in many fields of application. In this thesis, the focus is on the development of novel MOFs and CTFs for application in heterogeneous catalysis and sensing. Detailed attention is given towards the synthesis and characterization of these materials as these are essential in understanding the role of chemical functionalities and structure of these porous materials for the corresponding application. Compared to traditional catalysts such as activated carbons, zeolites, and PMOs, both MOFs and CTFs have the benefit of a molecular control over the incorporated functionalities.

For the application of MOFs in catalysis, a typical strategy is to attach a (metal-containing) catalytic function to the already metal-containing MOF, often creating bimetallic systems. For this, bipyridine building blocks are ideal as they provide bidentate coordination site and have been utilized in other porous materials for grafting of metal complexes improving the stability of catalytic centers. The second strategy is to design and synthesize MOFs with active catalytic sites in their metallic nodes.

However, it has become clear that many MOFs still suffer from a suboptimal physical and chemical stability. In this regard, the second part of the thesis is about using CTFs in heterogeneous catalysis because of their high physical and chemical stability, which is essential in catalytic applications. These materials can be used either as catalyst supports or as catalysts themselves. To act as catalyst supports, the materials must have strong chelating ligands to stabilize homogeneous catalytic complexes. Moreover, the materials must also be sufficiently porous (large surface areas, pore volumes) to allow substrate diffusion. Apart from being catalytic supports, CTFs can also be used as organocatalysts due to the presence of catalytic active sites. This is desirable for a next generation of catalysts, as transition metal containing catalysts can show unwanted leaching during the

catalysis and the spent catalysts need to be processed with care to avoid the spilling of the transition metal ions into the environment. CTFs made using ionothermal synthesis contain several defective nitrogen sites which have been previously found in N-doped activated carbons and N-doped graphene. Such sites have shown promising catalytic activity for oxidation and Knoevenagel condensation reaction.

Recently, it became apparent that COFs and CTFs can be made in such a way that they are photoactive in the visible light region. Most of the ionothermally synthesized CTFs are not photoactive. Hence, milder reaction conditions are applied to obtain CTFs suitable for photocatalysis. Upon light irradiation, certain CTFs can generate charge carriers (electron-hole pairs). Especially, the formation of conjugated CTFs can be useful for charge transfer and separation. The separated photoelectrons can be used for reduction reactions and the separated photoholes can be used for oxidation reactions. In this thesis, we developed new heteroatom doped CTFs by incorporating novel functionalities into the CTF structure to perform photocatalytic organic pollutant removal under environmental friendly conditions.

On top of the (photo)catalytic applications, also the crystallinity of the mild synthesized CTFs has been improved and a new application of CTFs as luminescent sensors has been explored and reported.

CHAPTER 1

POROUS INORGANIC MATERIALS: METAL-ORGANIC FRAMEWORKS



This chapter is based on the published review article and book chapter:

S. Abednatanzi,[‡] **P. Gohari Derakhshandeh**,[‡] H. Depauw, F.-X. Coudert, H. Vrielinck, P. Van Der Voort, K. Leus, Mixed-metal metal–organic frameworks. **Chemical Society Reviews**, 48, 2019, 2535-2565. [‡] Both authors contributed equally to this work.

S. Abednatanzi, **P. Gohari Derakhshandeh**, K. Leus, P. Van Der Voort, Alcohol oxidation: reaction, effects and applications, 2018, **Nova Science Publishers**, Chapter 3: Selective alcohol oxidation by metal-organic frameworks and covalent organic frameworks, ISBN: 978-1-53614-604-2.

1.1. Introduction

Porous materials contain voids, channels, holes, or basically pores. These materials have shown promising potential as the presence of pores means that the material possesses an internal surface area of interest for all type of applications. Many porous materials are naturally occurring and were first produced in “Nature’s laboratory” without any human influence.¹ Such naturally occurring porous materials are commonly found in living organisms and are of great importance to obtain optimal properties and performance which allows adaptation to permanent environmental changes through long term evolution.² Many biological materials with remarkable efficiencies (diatom, butterfly, leaf, etc.) are complex composites with hierarchically porous structures (Figure 1.1). Recently, great progress has been made in the design, synthesis and use of naturally occurring porous materials in diverse applications.² These materials are composed of a multimodal hierarchically porous structure made of interconnected pores with different sizes ranging from micro (< 2 nm), meso (2–50 nm) to macro pores (> 50 nm).

Nowadays, many porous materials are made in the laboratory and can even be produced on a large industrial scale. Inorganic porous materials either crystalline or amorphous have developed rapidly over the past half-century.³ These materials have broad applications in adsorption, catalysis, nanotechnology and energy applications. The open structure and high-surface-area (interior surface and outer surface) of porous materials promote their catalytic and adsorption abilities. The inorganic porous materials include zeolites, silica, metal oxides and even organic-inorganic hybrid materials including metal-organic frameworks (MOFs).³

In this chapter, we will describe the synthesis of MOF materials and typical applications of MOFs in the field of heterogeneous catalysis.

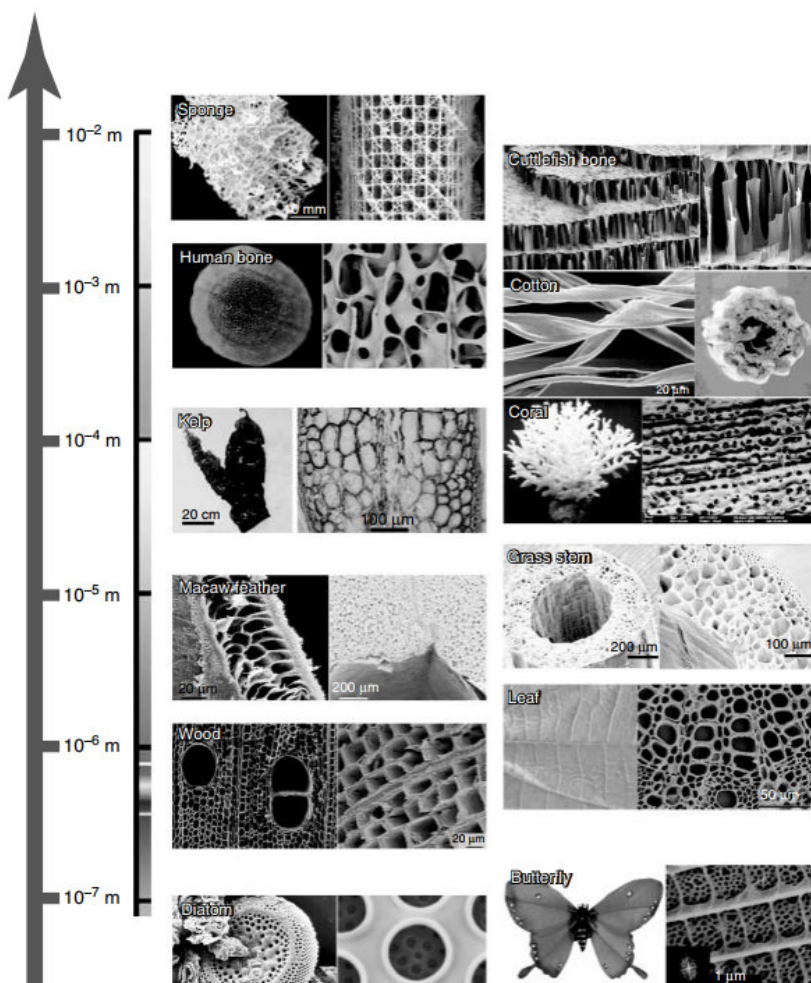


Figure 1.1. Examples of naturally occurring porous materials placed alongside the length scale according to their critical dimensions. The scanning electron microscopy (SEM) images of original biological hierarchically porous structures are shown from bottom to top: diatom, butterfly, wood, leaf, macaw feather, grass stem, kelp, coral, cotton, human bone, cuttlefish bone, and sponge.²

1.2. Metal-Organic Frameworks (MOFs)

Metal-Organic Frameworks (MOFs) were introduced in the scientific field more than 20 years ago, with the pioneering publications of Yaghi,⁴ Kitagawa⁵ and Férey.⁶ Twenty years later the field is still in full expansion. And even up to date one reads in the introduction of many papers that “MOFs are a relatively new class of materials, consisting of inorganic nodes, linked by multifunctional ligands to form highly porous crystalline hybrid materials, finding many applications in catalysis, adsorption, gas storage and sensing”. It is indeed surprising that MOFs are still experienced and proclaimed as relatively new, while for instance, SBA-15, published by Stucky and Zhao⁷ one year earlier (1998) is experienced much more as an “old” material.

MOFs consist of two main components: the organic linkers and the metal inorganic clusters. The linkers connect the metal ions to create the MOF architecture. For this reason, the synthesis of MOFs is often based on trial-and-error techniques. However, the need for “designable MOFs” is high. Within this context, O’Keeffe and Yaghi⁸ introduced in 2002 the concept of *isorecticular synthesis* (*iso*: the same, *reticular*: forming a net) which is based on the association of designed rigid secondary building units (SBU) into predetermined ordered structures (networks) which are held together by strong bonds. They illustrated this by reproducing the octahedral inorganic SBU of MOF-5 by using similar but other organic linkers.⁸ Several functionalities could be easily built into the framework as $-\text{Br}$, $-\text{NH}_2$, $-\text{OC}_3\text{H}_7$ and $-\text{OC}_2\text{H}_{11}$. In addition, the pores size could be readily expanded by using elongated organic linkers such as biphenyl, terphenyl and pyrene (Figure 1.2). This allowed the synthesis of large series of isorecticular MOFs (IRMOFs) in which the functionality could be tuned, and the pore size could be varied from the microporous to the mesoporous range. They were able to increase the pore size from 0.38 nm to 2.88 nm without changing the original topology. The isorecticular principle of Eddaoudi and Yaghi has been cited over 7000 times (in February 2021) and the designability of MOFs has become a major topic. In the fields of catalysis and gas separation, the MOFs are “designed” to have the optimal pore apertures, surface energies, elemental composition for that specific application. Next to isorecticular design, mixing linkers and/or metals are common strategies to tune the properties of the MOFs.

The advantages and disadvantages of MOFs are well established by now.⁹⁻¹⁰ It is clear that the advantages of MOFs are primarily the high tunability of the materials, in topology, in pore size and in functionalities. The isoreticular chemistry, introduced by Yaghi, offers almost infinite possibilities. In some cases, also the ease of synthesis is a bonus. The most important disadvantages are the use of some unpopular metal ions, such as Cr^{3+} . While Cr^{3+} is not toxic, it is unlikely that companies will want to use it on a large scale due to the strict regulations on storage and disposal of Cr. Although, the most stable MOF (MIL-101(Cr)) is a Cr-MOF.¹⁰ Because of this, MOFs have found so far most of their applications in the fields of gas storage and gas separation. Many spin-offs and companies are emerging in this field. Research on creating MOFs with multiple functionalities is also a very important field of research with 385 papers in Web of Science in 2020 alone, using the tags Metal, Framework and Multifunctional. Figure 1.3 shows some examples of the most studied MOFs.

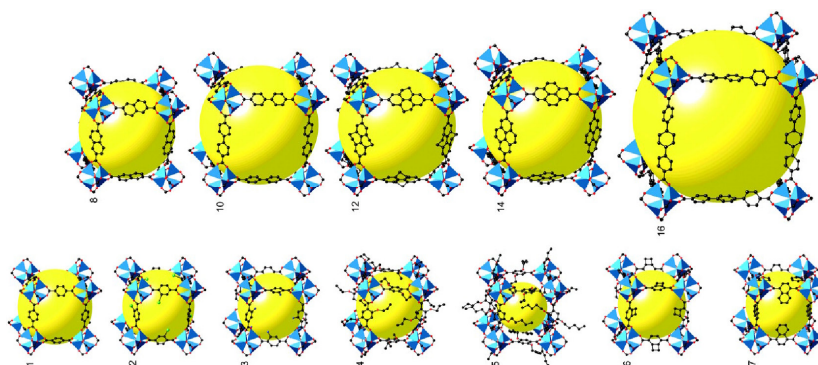


Figure 1.2. Series of isoreticular MOFs based on MOF-5. In IRMOF-1 to IRMOF-7 the organic linker had a different functionality whereas in IRMOF-8 to IRMOF-16, the length of the organic linker was changed. Reprinted from ref.⁸ with permission. Copyright 2002, American Association for the Advancement of Science.

Metal- and Covalent Organic Frameworks for Advanced Applications: Heterogeneous Catalysis and Sensing

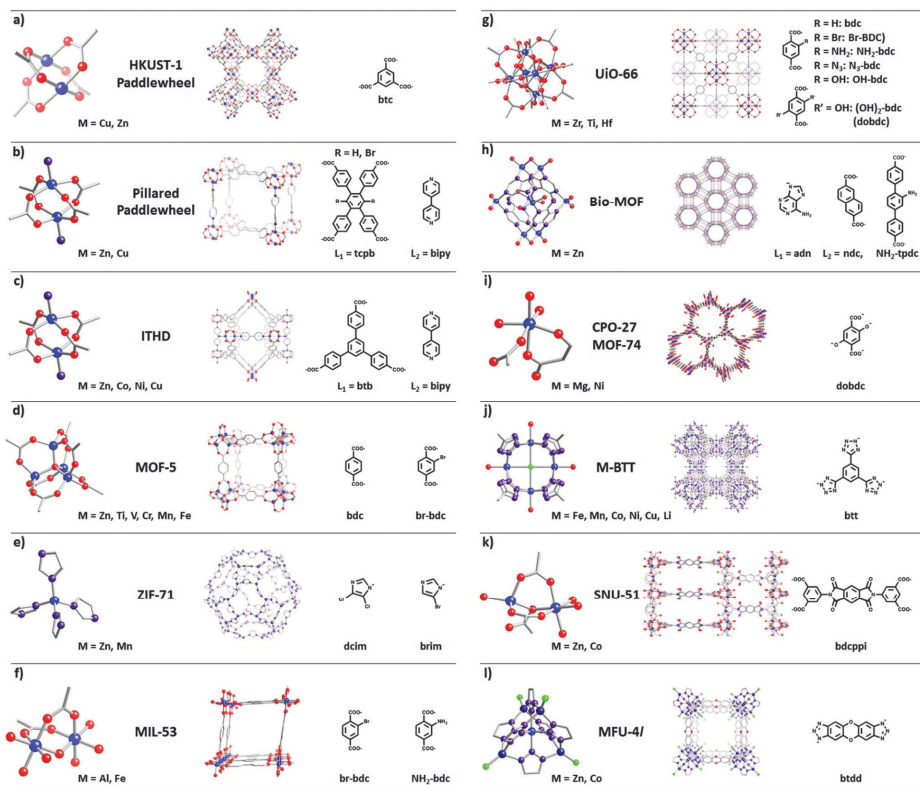


Figure 1.3. Lattice structures (middle) and corresponding SBUs (metal nodes (left), and organic linkers (right)) of some of the MOFs discussed in this chapter. (Atom definition: blue–metal, red–oxygen, purple–nitrogen, grey–carbon, green–chlorine).

As one route, materials can be made by a mixed-linker approach in an attempt to introduce multiple functionalities into the same material.¹¹⁻¹² Isostructural ligands with different functionalities are required here. Although the principle itself looks straightforward, in practice it is often very hard to obtain a nice mixed-linker MOF. Often, in our own experience, the functional groups on the linker will interfere with the coordination to the metal nodes, resulting in an ill-defined, often amorphous material.

One particular example of a mixed-linker MOF that has been frequently used is the well-known UiO-67¹³, an isorecticular variant of the UiO-66. UiO-67 is composed of biphenyl-4,4'-dicarboxylic acid (H₂BPDC) linkers that are connected to the Zr₆(μ₃-O)₄(μ₃-OH)₄(COO)₁₂ cluster, giving a three-dimensional face-centered cubic (fcu) network. This framework is interesting due to the possibility to replace the BPDC linker with 2,2'-bipyridine-5,5'-dicarboxylic acid (H₂BPy). The structure of the mixed-linker UiO-67 MOF containing bipyridyl functional groups is shown in Figure 1.4. This replacement provides an opportunity to the design of the UiO-67(BPy) framework with controlled BPy functional groups for each unit cell.

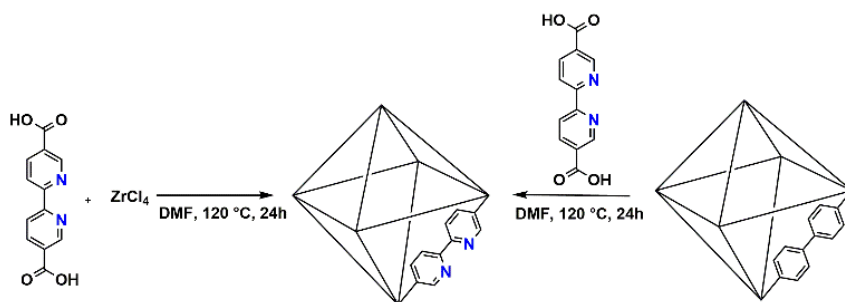


Figure 1.4. Employed linkers and their assembly into a Zr-based UiO-67(BPy) MOF. The structure is obtainable by one-pot synthesis (left) or by post-functionalization (right). Reproduced from ref.¹⁴ with permission from the Royal Society of Chemistry.

Moreover, the ability to introduce a large variety of active components, including metal complexes, nanoparticles and organic functional groups into the framework by utilizing the modified ligands directly in the solvothermal synthesis (pre-functionalization) or chemical modification of the framework after synthesis (post-synthetic modification) is an extra advantage to obtain advanced MOF materials suitable for more specialized applications.

1.2.1. MOF design principle

The stability of monometallic MOFs is hugely determined by the metal-ligand bond. Bu *et al.*¹⁵ described in a ChemComm review how this interaction can be viewed upon as a simple Lewis acid (metal ion node)–Lewis base (ligand) interaction. The ligands are usually O- or N-donors. A strong bond will protect the resulting MOFs against hydrolysis. As a simple rule of thumb, for carboxylic interactions, metals with high charges (typically M^{3+} or M^{4+}) will form strong Lewis acids that will interact with the strong COO^- Lewis base. On the linker side, a higher stability is obtained if the pK_a of the ligand is increased. This strategy was introduced by Jeffrey Long, and his group that synthesized a pyrazolate MOF ($pK_a = 19.8$).¹⁶ The famous ZIFs (Zeolitic Imidazole Frameworks) rely on the same principle, the imidazolate having a pK_a of 18.6. Moreover, the dihedral angle closely resembles the siloxane angle, that's why they are referred to as zeolitic frameworks. In an interesting study, Hambley *et al.*¹⁷ analyzed 40000 crystal structures in the Cambridge Structural Database to study the metal-ligand covalency from the bonding in carboxylate ligands. The distinction between an ionic interaction and a covalent interaction is shown in Figure 1.5.

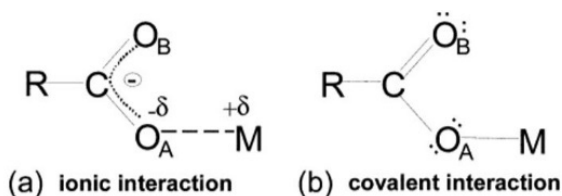


Figure 1.5. The distinction between an ionic interaction and a covalent interaction in carboxylate MOFs.

The distinction between the two interactions can be made by analyzing the two C-O bond lengths. The larger the covalent interaction, the less resonance in the “arms” of the carboxylate group, and the larger the difference in bond lengths between C-O_A and C-O_B. In Figure 1.6, the % covalency of the metal-carboxylate bonding is shown, as a result of the analysis of 6163 different structures. It is indeed confirmed by this summary that the

fraction of covalency increases as the oxidation state of the metal cation increases. For instance, Mn^{2+} -carboxylates have a low fraction of covalency (10%), while Mn^{4+} -carboxylates have a covalency of around 50%. A well-known example is the MIL-101 series, of which the Cr-MIL-101 is one of the most stable MOFs. The same applies to the Zr-based MOFs, built from $\text{Zr}_6\text{O}_4(\text{OH})_4$ nodes with carboxylate linkers. M^{2+} metals will form unstable structures with carboxylates, *i.e.*, they will degenerate in the presence of water. We refer to the paper of Van Der Voort and co-workers that explicitly discusses the stability of some of the most common MOFs.¹⁰

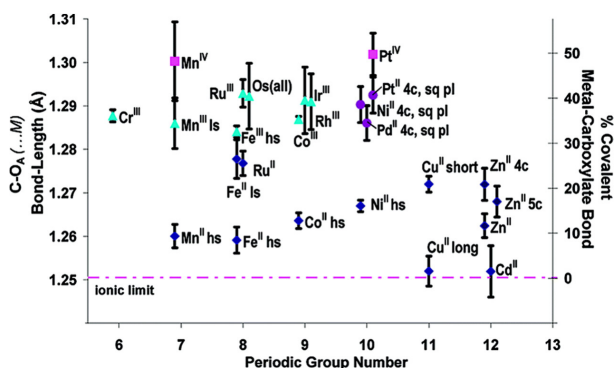


Figure 1.6. The % covalency of the metal-carboxylate bonding as a result of the analysis of 6163 different structures. Reproduced from ref.¹⁷ with permission. Copyright 2003, the American Chemical Society.

1.2.1.1. Direct synthesis approach or one-pot reaction

MOFs can be prepared by using one or multiple metal precursors as reactants during the conventional solvothermal synthesis, in a one-pot approach (see Figure 1.7). The main attractiveness of this approach is the simplicity and the reduced number of steps. However, in the case of mixed-metal MOFs (MM-MOFs), the main disadvantage of this strategy is the lack of control over the final metal distribution.

To be able to produce MM-MOFs in a controlled way, it is important to note that the introduced metal cations should react concomitantly to allow a controlled incorporation

and to avoid the formation of frameworks based on a single cation. This was for example demonstrated by the group of Serre¹⁸ in which a bimetallic MIL-53 (Cr/Fe) framework was obtained by a direct synthesis. As Cr³⁺ is rather inert while Fe³⁺ is highly reactive, the authors used the less reactive Fe⁰ to slow down the reaction of iron-components and to allow a controlled introduction of both metals by controlling the reactivity of the metal ions.

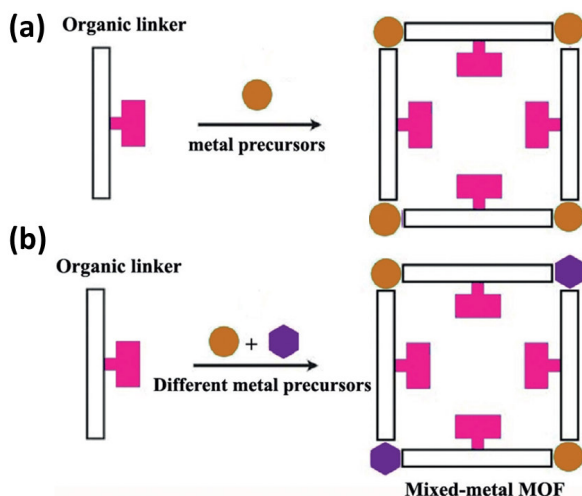


Figure 1.7. Schematic illustration of the direct synthesis of MOFs with (a) one and (b) two metal precursors. Reproduced from ref.¹⁹

Most often the one-pot synthesis strategy results in a more or less homogeneous dispersion of the introduced cations. Also the group of Walton²⁰ observed that a difference in crystal growth rate resulted in MM-MOFs having an inhomogeneous distribution of the divalent metal cations. They performed a detailed study to examine the influence of the synthesis temperature and solvent on the final metal composition in Mg/Ni and Mg/Co-MOF-74 materials. All the mixed MOF-74 materials were prepared by a one-pot solvothermal synthesis. The scanning electron microscopy (SEM)/EDX mapping revealed an inhomogeneous metal distribution because of the difference in the crystal growth rate of the mixed MOF-74 materials. In addition, inductively coupled plasma-optical emission

spectrometry (ICP-OES) measurements indicated that Ni and Co were preferentially introduced. The authors observed that the solvent only had a minor influence on the introduced cations whereas the effect of the temperature was more pronounced as the temperature influences the nucleation and the crystal growth. In most cases, 2 metal ions are mixed in one SBU to create bimetallic MOFs however Yaghi and co-workers demonstrated that up to 10 divalent metals could be included in one structure.²¹ They reported on the synthesis and characterization of five isorecticular microcrystalline MOF-74 structures having 2 (Mg and Co), 4 (Mg, Co, Ni and Zn), 6 (Mg, Sr, Mn, Co, Ni and Zn), 8 (Mg, Ca, Sr, Mn, Fe, Co, Ni and Zn) and 10 (Mg, Ca, Sr, Ba, Mn, Fe, Co, Ni, Zn and Cd) divalent metals within one structure (Figure 1.8). The multivariate MOFs were obtained through a solvothermal reaction of 2,5-dihydroxyterephthalic acid in the presence of varying amounts of metal salts. The authors observed that there is a preferential incorporation of Mg, Mn, Fe, Co, Ni, Zn and Cd whereas Ca, Sr and Ba are less present because of their tendency to have a higher coordination number (8 instead of 6). However, the authors stated that not only the coordination number but also many other parameters play a crucial role as the final molar ratio of the incorporated metal ions is highly influenced by the pH of the reaction mixture, solubility, reactivity and coordination sphere. In addition, the authors demonstrated that the employed highly reproducible synthesis approach could also be used to introduce metal ions (Ca, Sr, Ba and Cd) from which the parent MOF-74 could not be made directly.

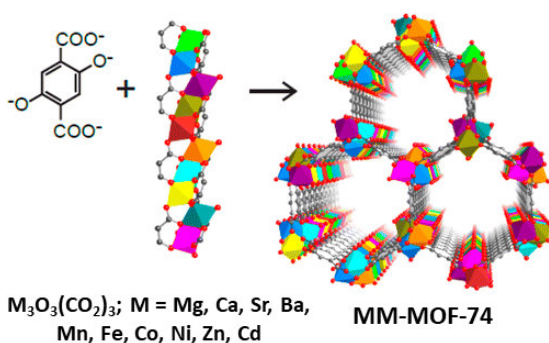


Figure 1.8. Multivariate MOF-74 materials having up to 10 various metals within their structure. Reproduced from ref. ²¹ with permission. Copyright 2014, the American Chemical Society.

1.2.1.2. Pre-functionalization approach using metallo-linkers

Another strategy to design MOFs is the use of pre-functionalized linkers that already contain a second metal complex (metallo-linkers) compatible with the MOF synthesis conditions (Figure 1.9). This method is one of the promising methodologies to anchor metal complexes onto/into porous MOFs. However, the direct synthesis of MOFs using pre-functionalized ligands is still challenging as the decomposition of the transition metal complexes under the applied reaction conditions can occur. Furthermore, it is essential to find the appropriate reaction conditions to form a particular MOF structure. As a result, very few papers report on the modification of MOFs using the pre-functionalized method, whereas many studies considering the classical post-synthetic modification route to incorporate functional groups. This approach gives MOFs with accessible metal complexes immobilized in large and extra-large channels that can exhibit high stability against complex agglomeration that is a common deactivation process occurring for these soluble metal complexes.

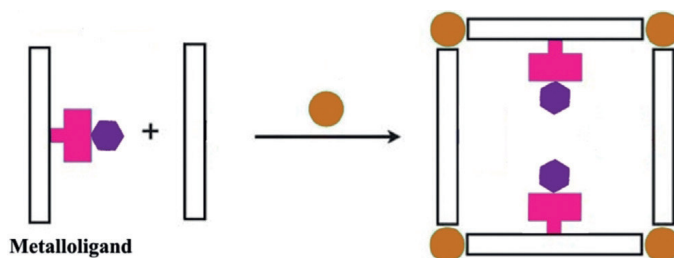


Figure 1.9. Schematic representation of the synthesis of MOFs using metallo-linkers (Reproduced from ref. ¹⁹)

In this regard, porphyrin metallo-linkers have been applied to make porphyrin-functionalized zirconium-carboxylate frameworks (Figure 1.10). These ultra-stable, crystalline frameworks can be made with or without secondary metal ions and are denoted as CPM-99X (CPM = crystalline porous material, X = H₂, Zn, Co, Fe). They feature a binodal cubic net composed of 12-connected Zr₆O₄(OH)₄ cuboctahedra linked by longer tetrakis(4-carboxybiphenyl)porphyrin (TCBPP).

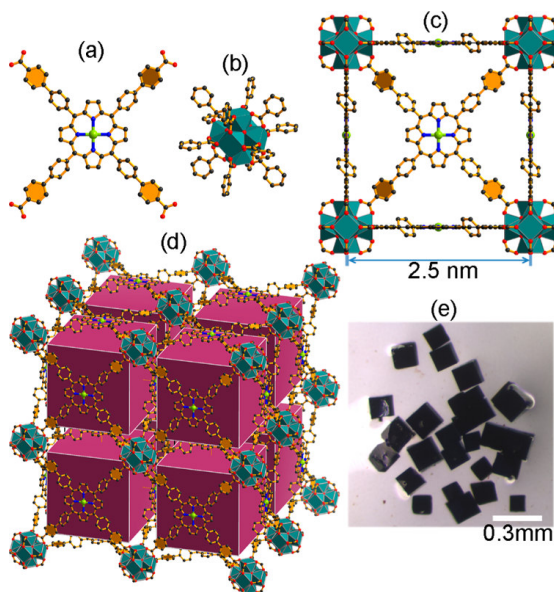


Figure 1.10. (a) Augmented tetracarboxylic porphyrinic linkers, TCBPP-X (X = H₂, Zn, Co, Fe). (b) 12-connected Zr₆(μ₃-O)₄(μ₃-OH)₄(O₂C)₁₂ cluster. (c) Cubic cage with 2.5 nm edge length. (d) The 3D network with Zr₆ clusters shown as polyhedra and 3D cubic-cavity packing in CPM-99Fe. Color scheme: Zr (teal); Fe (lime); O (red); N (blue); C (gray). (e) Photograph of CPM-99Fe.

1.2.1.3. Post-synthetic modification (PSM)

Another route for obtaining MOFs suitable for advanced applications is by post-synthetic modification (PSM). Rather than the direct synthesis of MOFs using functionalized ligands, the chemical modification of frameworks can be done after their synthesis. Figure 1.11 shows the general scheme to design MM- MOFs through post-synthetic modification. Since the time that Wang and Cohen²² performed the first detailed study of PSM in 2007, considerable efforts have been devoted to the development of efficient heterogeneous catalysts.

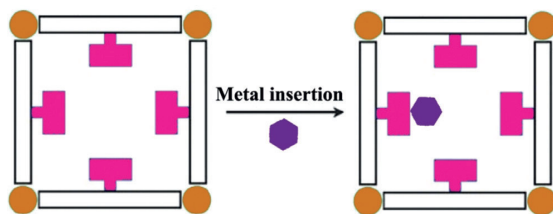


Figure 1.11. Formation of MM-MOF through post-synthetic metal complexation/insertion (Reproduced from ref. ¹⁹).

The main advantage of the PSM route compared to the direct synthesis is the excellent control over the kinds and number of functional groups that can be incorporated into the framework. A large variety of metals can be incorporated into the MOF pores via three main strategies including (a) covalent modification (chemical modification of the organic linker of the MOF), (b) coordinate covalent modification (ligands coordination to coordinatively unsaturated metal (CUMs) sites or metals coordination to the organic linker of MOFs), (c) covalent and coordinate covalent modification (the organic linker within the MOF can be appended with a ligand and consequently metallated)²³ (Figure 1.12).

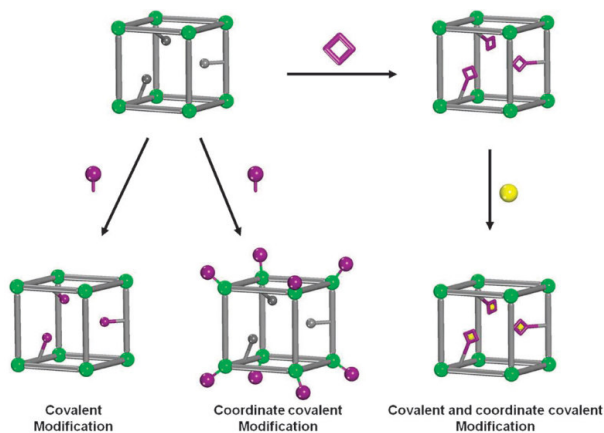


Figure 1.12. Representation of different PSM routs of MOFs. Reprinted from ref.²³ with permission.

MOFs with high surface areas and large pores are good candidates to introduce various functionalities through PSM. MIL-101(Cr), a three-dimensional chromium(III) terephthalate MOF, possesses regular mesoporous cages of 29 and 34 Å, which are accessible through windows of ca. 12 and 16 Å (Figure 1.13).²⁴

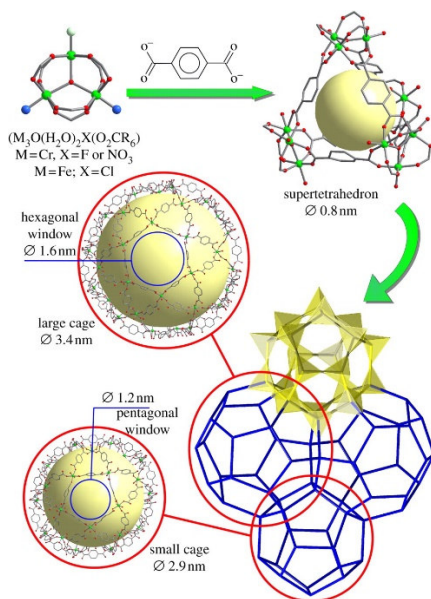


Figure 1.13. Schematic of MIL-101 structure, Reprinted from ref.²⁴ with permission.

Interestingly, the existence of coordinatively unsaturated chromium sites (CUSs) in the framework provides opportunities for the incorporation of active species. Recently, phosphotungstic acid ($H_3PW_{12}O_{40}$, HPW) was immobilized into the nanocages of a dual amino-functionalized ionic liquid (DAIL)-modified MIL-101(Cr) framework under mild conditions.²⁵ The PW cluster, with dimensions of about 12 Å, has the appropriate size to diffuse through the larger windows of the framework (Figure 1.14).

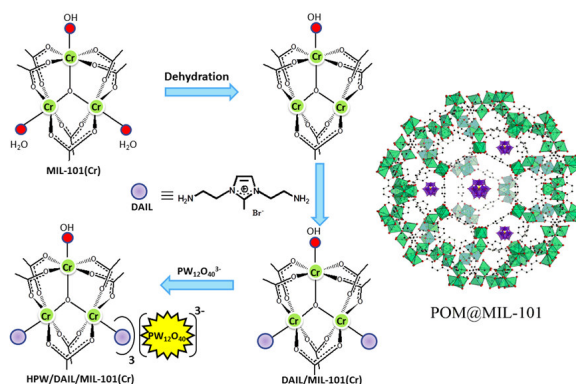


Figure 1.14. Schematic illustration of the preparation of PW/DAIL/MIL-101(Cr). Reprinted from ref.²⁵ with permission.

1.2.1.4. Post-synthetic exchange

The post-synthetic exchange method allows the formation of frameworks that are difficult or unattainable through a direct synthesis approach. Up until now, the majority of the reports on post-synthetic modifications dealt with mixed-linkers and only a small number of examples have involved the metal ion exchange to create MM-MOFs. The transmetalation or exchange of the metal nodes typically proceeds by immersing the MOF in a metal ion solution, typically nitrates or chlorides, for several days at room or elevated temperatures to have an (incomplete) transmetalation. The post-synthetic exchange strategy is also useful to introduce redox active di- and trivalent first row transition metals into MOFs. Among the thousands of reported MOFs none are known to contain for example V²⁺, as these reduced metal cations (Ti³⁺, V²⁺, Cr²⁺) are incompatible with the typical synthesis conditions of MOFs. Dinca and co-workers²⁶ demonstrated that the post-synthetic ion metathesis method can be used to introduce V²⁺, Ti³⁺, Cr²⁺, Cr³⁺, Mn²⁺ and Fe²⁺ ions into the MOF-5 host to enable redox reactivity (Figure 1.15). This was achieved by soaking the MOF-5 crystals in concentrated DMF solutions of VCl₂(pyridine)₄, CrCl₂, MnCl₂ or Fe(BF₄)₂·6H₂O for one week to obtain M-MOF-5 (M = V²⁺, Cr²⁺, Mn²⁺ or Fe²⁺) while TiCl₃·3THF, VCl₃·3THF or CrCl₃·3THF was used to introduce Ti³⁺, V³⁺ or Cr³⁺.

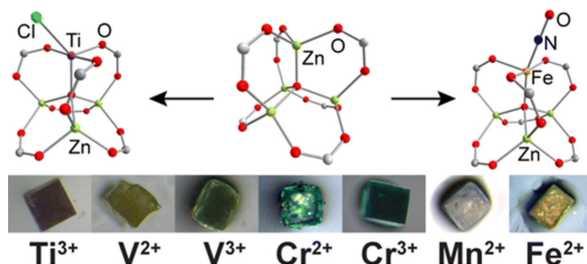


Figure 1.15. Post-synthetic exchange to introduce reduced metal cations in MOF-5. Reprinted from ref. ²⁶ with permission. Copyright 2013, the American Chemical Society.

1.3. MOFs in heterogeneous catalysis

As described, MOFs are crystalline atomically ordered materials, with an almost unlimited choice of building bricks, allowing a very precise control over morphology, pore size and functionalities in the walls.²⁷⁻²⁸ The crystalline nature of MOFs allows a full characterization and therefore a thorough understanding of their behavior is possible. MOFs have typically large surface areas (up to 7000 m²/g), pore volumes and pore openings up to 9.8 nm. Moreover, MOFs are highly designable due to the chemical versatility and the secondary building blocks that help to build up the framework.^{8, 29} Due to their attractive properties, many research groups started to explore these materials for several applications. Especially gas storage, gas separation, sensing, drug delivery and heterogeneous catalysis are research themes that are quickly emerging.³⁰

In heterogeneous catalysis, MOFs have been successfully used as catalysts in hydrogenation and oxidation reactions, enantioselective reactions, photocatalysis, hydrodesulfurization and many more.³¹⁻³² The highly tunable structure allows the MOF to act both as a heterogeneous catalyst and as a solid support. MOFs with unsaturated metal centers can be directly used as the heterogeneous catalyst. For example, MIL-101³³ (Fe, Cr, Al) (MIL stands for Materials Institute Lavoisier) and HKUST-1(Cu)³⁴ (HKUST stands for the Hong Kong University of Science & Technology), which both contain unsaturated metal centers at the nodes of the framework and have shown good catalytic activity in a wide range of reactions.³⁵⁻³⁸

For non-catalytic active MOFs, catalytic sites can be introduced by pre-/post-synthetic modification.³⁹⁻⁴⁰ By using the “ship-in-bottle” approach, catalytically active polyoxometalate clusters, metal complexes, or nanoparticles can be encapsulated inside the MOF cavities.^{25, 41-42} Furthermore, by pre-/post-synthetic modification on the organic linker, complementary catalytic activity can be introduced.⁴³⁻⁴⁴ With all these efforts, MOF materials can, in principle, combine different catalytic functions in which the unsaturated metal centers can provide Brønsted or Lewis acidity and basicity, or redox active centers. The fine-tunable cavity size (from microporous to mesoporous) permits shape selectivity by avoiding the formation of undesired intermediates or product.

MOFs with tunable structures undoubtedly represent important potential and advantages in synergistic catalysis. One of the main objectives of the development of MOFs and their modification is to expand the scope of catalytic reactions with enhanced catalytic performances. Hence, it is necessary to gain a fundamental understanding of the roles of active components and their cooperation to achieve enhanced properties. In this section, selected examples of heterogeneous reactions catalyzed by MOFs and their synergistic effect are described. An overview of the applied MOFs for a variety of catalytic reactions can be found in Table 1.1.

1.3.1. MOFs in oxidation reactions

Selective catalytic oxidation is of industrial importance for fine chemical syntheses.^{25, 45-46} Many homogeneous catalysts, often (transition) metal complexes or oxides are still used in some industrial processes.⁴⁷⁻⁴⁸ By varying the metal center and the surrounding ligands of these homogeneous catalysts, the chemo-, regio- and stereo-selectivity can be tuned. The metallic sites within MOFs can be employed as active centers for a wide range of heterogeneous catalytic reactions, particularly for oxidations. Within the concept of green chemistry, more efforts should go to performing the oxidation reactions using heterogeneous catalysts with clean oxidants such as air or oxygen. The combination of a heterogeneous metal catalyst with molecular oxygen or air represents one of the best alternatives in the field.⁴⁹ M-MOF-74 with the general formula of $M_2(\text{DOBDC})$ (M^{2+} :

divalent metal ions; DOBDC⁴⁻: 2,5-dioxido-1,4-benzenedicarboxylate) is a three-dimensional honeycomb-like network. MOF-74 is a good candidate in oxidation reactions due to its high chemical stability. Additionally, its catalytic activity can be tuned through the replacement of Ni²⁺ in Ni-MOF-74 framework by active Co²⁺ via a post-synthetic metal exchange method.⁵⁰ It is interesting to note that Ni-MOF-74 shows almost no activity for cyclohexene oxidation, while its isostructural Co-MOF-74 is active under the same reaction conditions using oxygen as oxidant. With the aim of enhancing the catalytic performance of this framework, the Ni²⁺ ions were substituted partially with the active Co²⁺ ions. The catalytic performance of the partially Co-substituted Ni-MOF-74 (MOF-74 (Co/Ni)) increased with the amount of incorporated Co²⁺, demonstrating that the incorporated Co²⁺ is serving as the active sites in catalysis (Figure 1.16). The products observed under the reaction conditions are cyclohexene oxide, 2-cyclohexen-1-ol, 2-cyclohexen-1-one, and cyclohexene hydroperoxide. MOF-74 (Co/Ni) displayed superior catalytic performance even better than pure Co-MOF-74 as Co was placed at positions that were more accessible to the substrate. Additionally, the recycling tests showed no significant loss of the catalytic activity over MOF-74 (Co/Ni) after three reaction runs, exhibiting the overall stability of the material under the reaction conditions. On the other hand, MOF-74 (Cu/Co) with different Cu/Co ratios were obtained via a facile one-pot synthesis method.⁵¹ The bimetallic Cu and Co MOF-74(Cu/Co) catalysts were applied in the oxidation of styrene using O₂ under solvent-free and mild reaction conditions. The results indicate that not only the styrene conversion over MOF-74 (Cu/Co) but also the selectivity towards benzaldehyde, styrene oxide and phenylacetaldehyde can be tuned by varying the Cu/Co ratio in MOF-74. While MOF-74(Cu) has a very low catalytic activity (0.6% conversion) with 100% selectivity to benzaldehyde, MOF-74(Co) shows higher catalytic activity (47.3% conversion) with a reduced selectivity, resulting in the formation of benzaldehyde, styrene epoxide, phenylacetaldehyde and polystyrene. Interestingly, the incorporation of Cu²⁺ in MOF-74(Co) effectively hinders the polymerization of styrene, however, the incorporation of Co²⁺ in MOF-74(Cu) can improve the conversion of styrene to benzaldehyde, styrene epoxide, and phenylacetaldehyde. The higher activities of MOF-74(Cu/Co) catalysts compared to the physical mixtures of MOF-74(Cu) and MOF-74(Co) with almost the same amounts of Cu and Co proves the synergistic effect of Cu²⁺

and Co^{2+} in the same framework. These studies clearly indicate the superior catalytic activity of mixed-metal MOF-74 over the corresponding single metal MOF, however, the catalysts suffer from serious limitations, like deficient selectivity and conversion with narrow substrate scope.

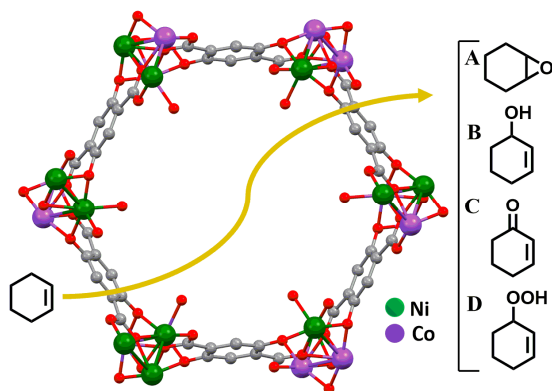


Figure 1.16. Aerobic oxidation of cyclohexene using Co/Ni-MOF-74. Reproduced from ref.⁵⁰ with permission. Copyright 2015, the American Chemical Society.

Besides the synthesis of MOFs with high catalytic activity, it is highly desired to apply the unique properties of MOFs and more specifically their PSM to design materials for more specialized applications. This can be achieved by decorating the pore environment of MOFs with multiple functional groups. An elegant example is PCN-700 and its catalytic activity in alcohol oxidation. Using PCN-700 with coordinatively unsaturated Zr_6 clusters, 12 linkers with different lengths and functionalities were installed in the parent framework (Figure 1.17).⁵² The length of the linkers has a direct impact on the MOF porosity and channel sizes. This leads to a highly tunable multifunctional MOF system that is capable of size selective catalysis. By installation of TPDC with different functional groups (methyl, phenyl, and hexyl) within the PCN-700-BPYDC-TPDC- R_2 catalyst (BPYDC = 2,2'-bipyridine-5,5'-dicarboxylate, TPDC = terphenyl-4,4''-dicarboxylate), the size selectivity can be fine-tuned. The TPDC partially blocks the channel limiting the diffusion of substrates as well as the accessibility of the Cu^+ as the active center. A reduction in yields

of alcohols was observed by increasing the size of substituents on the TPDC linker. Using the catalyst with TPDC-Hex₂, the 9-anthracene alcohol is almost excluded by the small MOF cavity, which explains the lowest yield (< 1%). This comprehensive study proves the importance of the linker installation method to decorate the pore environment of MOFs resulting in catalysts with different activity and selectivity.

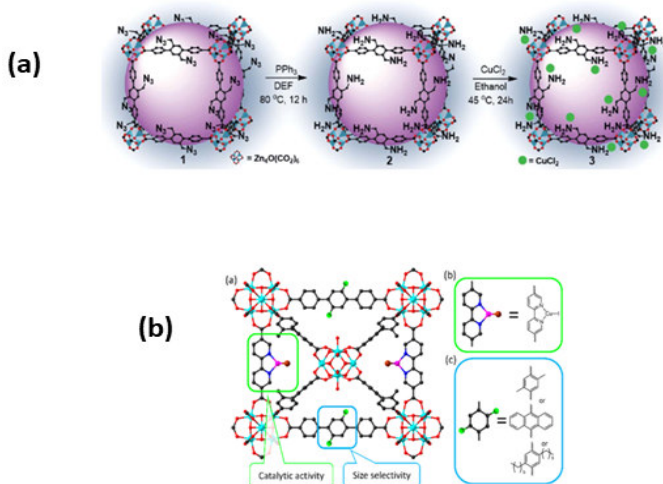


Figure 1.17. Schematic illustration of modified MOFs with copper complexes: (a) Cu(II)/MOF-NH₂, (b) PCN-700-BPYDC(Cu)-TPDC-R₂. Reprinted from Ref.⁵²⁻⁵³ with permission.

1.3.2. Epoxidation Reactions

The selective epoxidation of olefins to the corresponding epoxides is a fundamental transformation both in laboratory synthesis and industrial production.⁵⁴ As shown in Figure 1.18, a Cd²⁺-based microporous MOF was synthesized by employing *meso*-tetra(N-methyl-4-pyridyl)porphine tetratosylate (TMPyP) as a template for the generation of porph@MOM-10 material.⁵⁵ Porph@MOM-10 showed promising applicability to undergo metal exchange affording efficient heterogeneous epoxidation catalysts. More specifically, the substitution of Cd²⁺ ions with Mn²⁺ and Cu²⁺ enhances the catalytic activity compared to the pristine porph@MOM-10. The porphyrin-based frameworks were

used in the selective epoxidation of *trans*-stilbene as a typical reaction catalyzed by metalloporphyrins. Similar to the blank reaction, porph@MOM-10 has a low activity in the epoxidation reaction showing a conversion < 10%. The improved activity is observed in the case of Mnporph@MOM-10-Mn and Cuporph@MOM-11-CdCu with 75% (turnover number (TON) = 178) and 79% (TON = 182) conversion of *trans*-stilbene, respectively. The epoxidation reactions were performed in the presence of *tert*-butyl hydroperoxide (TBHP) as oxidant and stilbene oxide and benzaldehyde were the major products.

Another type of porphyrin-based MOF denoted as MMPF-5, is synthesized consisting of Cd²⁺-metallated tetrakis(3,5-dicarboxyphenyl)porphine (tdcpp(Cd)) moieties that are connected to triangular Cd(CO₂)₃ moieties.⁵⁶ MMPF-5(Co) was obtained by placing crystals of MMPF-5 into a DMSO solution of Co(NO₃)₂. The catalytic activity of the bimetallic porphyrin-based framework was evaluated in the epoxidation of *trans*-stilbene using TBHP as oxidant in acetonitrile at 60 °C. The control experiments revealed the higher efficiency of MMPF-5(Co) exhibiting a great yield of 87% with 81.5% selectivity towards the epoxide product. The inactivity of MMPF-5 and low activity of the homogeneous tdcmp(Co) catalyst (28.1% yield) highlights the importance of synthesized MM- porphyrin-based framework in the mentioned reaction. Furthermore, no significant leaching of the Co species was observed. So far, the activity of MM-MOFs has been examined only for styrene epoxidation and no studies were done to expand the substrate scope to other more challenging substrates such as linear olefins.

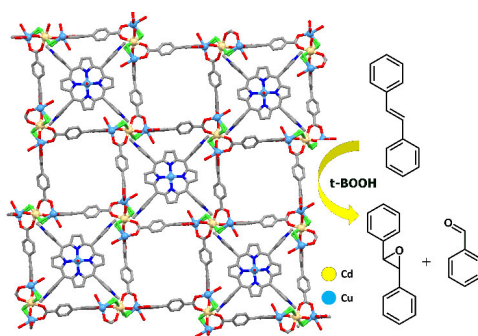


Figure 1.18. Post-synthetic metal exchange in porph@MOM-10 for styrene epoxidation. Reproduced from ref.⁵⁵ with permission. Copyright 2012, the American Chemical Society.

1.3.3. Condensation Reactions

MOFs show promising applications in a variety of condensation reactions to generate useful cyclic organic compounds such as solketal and quinoline derivatives. Recently, Jung *et al.* has compared the influence of the metallic centers in a series of isostructural MOFs of the MIL family based on M^{3+} ions.⁵⁷ This study provides an insight into the correlation between the nature of the metal ions and catalytic performance for the synthesis of solketal from acetone and glycerol over catalytic MOF materials, namely, MIL-100(M) and MIL-53(M) ($M = V, Al, Fe$ and Cr), as well as mixed MIL-53 (Al/V). The main products of the condensation reaction were a five-membered solketal (2,2-dimethyl-1,3-dioxane-4-methanol, (II)) and a six-membered acetal (2,2-dimethyl-dioxane-5-ol, (III)) as depicted in Figure 1.19. It was found that the glycerol conversion and isomer selectivity rely on different parameters including the nature of the metal ion, the length of the M-O bond, exchange of the coordinated water molecules and the presence of Brønsted acidity. Therefore, the highest conversion of glycerol is observed in the presence of MIL-100(V) (85.4%) and MIL-47(V) (75.9%) due to the higher acidity and easier replacement of water molecules by the reactants. A similar catalytic behavior of MIL-53(Al/V) samples with mixed metal-oxide clusters in the SBU was observed. The conversion of glycerol increases from 12.5 to 57.7%, as the vanadium content increases from 0 in MIL-53 (Al) to 75% in MIL-53 (Al/V) (25/75) with high selectivity (> 90%) towards the five-membered solketal (II).

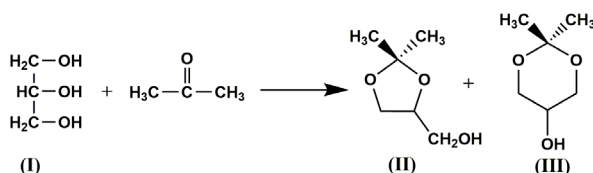


Figure 1.19. Condensation of glycerol with acetone over a series of MIL catalysts. Reproduced from ref. ⁵⁷ with permission. Copyright 2017, Elsevier.

Doping of ZIF-8 with Cu^{2+} ions through the direct reaction of $Cu(NO_3)_2$, $Zn(NO_3)_2$, and 2-methylimidazole under solvothermal conditions results in the formation of Cu/ZIF-8

material (Figure 1.20) with preserving the thermal stability (up to 350 °C in air) and crystallinity of ZIF-8.⁵⁸ Molar percentages of 1, 5, 10 and 25% of $\text{Cu}(\text{NO}_3)_2$ to $\text{Zn}(\text{NO}_3)_2$ were applied to prepare bimetallic ZIF materials. Even at high dopant percentage of Cu^{2+} ions within the backbone (25% Cu relative to Zn) only a slight decrease of the specific area and pore size was observed ($\text{Cu}_{25\%}/\text{ZIF-8}$: $1205 \text{ m}^2\text{g}^{-1}$ and $0.44 \text{ cm}^3\text{g}^{-1}$, ZIF-8: $1700 \text{ m}^2\text{g}^{-1}$, $0.662 \text{ cm}^3\text{g}^{-1}$). However, at a higher doping percentage (50%) the framework decomposes. For catalysis, the Cu^{2+} doping significantly enhances the Lewis acidity of the ZIF-8 which is desirable for achieving high catalytic activity for Friedländer reaction of 2-aminobenzophenone with an active methylene compound catalyzed by the Cu/ZIF-8 material. Furthermore, the Combes condensation of aniline with acetylacetone under solvent-free conditions was studied. Using the Cu5%/ZIF-8 catalyst, the corresponding quinoline was isolated in 96% yield after 5 h at 100 °C. The catalyst was reused for five consecutive runs without a decrease in the yield.

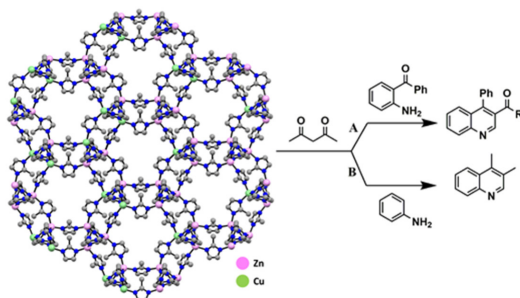


Figure 1.20. Cu-doped ZIF-8 for Friedländer and Combes condensations. Reproduced from ref.⁵⁸ with permission from the Royal Society of Chemistry.

1.3.4. Tandem Reactions

Tandem or cascade reactions consist of two or more individual reactions combined in a single system without isolating and purifying the intermediates.⁵⁹ Therefore, this reaction is one of the ambitions in heterogeneous catalysis. Initially, the reactants are reacted by the first type of active site to generate an intermediate that is further catalyzed by the

second type of active site to provide the desired product. As a critical note, truly interesting catalysts would be of the kind that outperform the simple mixture of two MOFs, in other words that form a transition state between the two metals and the substrate. Such reports, however, are very rare. One of the main features of MOFs is the possibility to develop this kind of multifunctional solid catalysts.

An elegant example is the synthesis of a MOF with the general formula $[\text{In}_x\text{Ga}_{1-x}(\text{O}_2\text{C}_2\text{H}_4)_{0.5}(\text{hfipbb})]$ (H_2hfipbb = 4,4' (hexafluoroisopropylidene) bis(benzoic acid)).⁶⁰ The obtained isostructural MOFs were applied in the three-component one-pot Strecker reaction between benzaldehyde, aniline, and trimethylsilyl cyanide (TMSCN) under solvent-free conditions (Figure 1.21). Both the monometallic (Al, Ga, In) and bimetallic (In, Ga) compounds were found to exhibit high activity in the mentioned reaction. The monometallic MOFs displayed distinctive behavior in this catalytic reaction producing three different products that are shown in Figure 1.21. More specifically, AIPF-1 ($[\text{Al}(\text{OH})(\text{hfipbb})]$) resulted in 99% yield of the expected aminonitrile product (A) with a TON value of 99. In contrast, GaPF-1 ($[\text{Ga}(\text{OH})(\text{hfipbb})]$) gave the aldehyde cyanosilylation product (B) with 99% yield. It is mentioned that the quick activation of both the silyl and carbonyl groups followed by reaction with TMSCN inhibited the imine formation. On the other hand, the imine product (C) was formed over InPF-1. Interestingly, the combination of both metal ions, $\text{In}_{0.28}\text{Ga}_{0.72}\text{PF-3}$ MOF, could give the desired α -aminonitrile product within 0.33 h. The results confirm that the presence of a small amount of indium is sufficient to promote the imine formation over the aldehyde cyanosilylation. The presence of Lewis acid sites results in the benzaldehyde activation followed by the imine formation. Hereafter, the Lewis base-activated TMSCN attacked the imine group, giving α -aminonitrile. This study shows the possibility to tune the catalytic activity of MOFs through modulating the ratio of active metal sites.

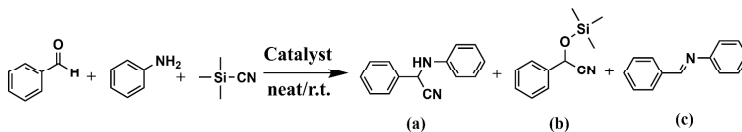


Figure 1.21. One-pot Strecker reaction using benzaldehyde, aniline, and TMSCN. Reproduced from ref.⁶⁰ with permission. Copyright 2015, the American Chemical Society.

In another example, a three-dimensional M^{3+} trimesate catalyst MIL-100 (Sc/Fe) was synthesized, with Fe^{3+} as well as Sc^{3+} as framework sites.⁶¹ The coordinately unsaturated metal sites can effectively be used in oxidation catalysis. The MIL-100 framework is a great potential host for the active sites due to its large surface area with accessible cages. The catalytic activity of this catalyst was tested for the Lewis acid-catalyzed tandem Friedel–Crafts addition reaction between 2-methylindole and trifluoroacetaldehyde ethyl hemiacetal followed by oxidation of the product in the presence of TBHP (Figure 1.22). The first two steps of the reaction (deacetalization and alkylation) proceed through Sc^{3+} Lewis acid sites, while the Fe^{3+} sites promote alcohol oxidation. More interestingly, this study showed that tandem reactions may overcome the usual diffusion limitations of reactants since *in situ* generated intermediates are located near the active sites. Therefore, enhanced catalytic performance can be observed compared to an individual process.

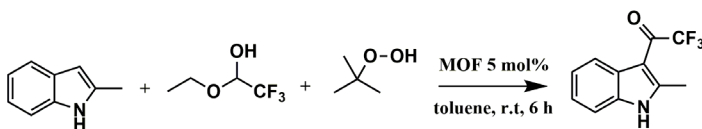


Figure 1.22. Tandem Friedel–Crafts addition and oxidation reaction catalyzed by MIL-100 (Sc/Fe). Reproduced from ref.⁶¹ with permission. Copyright 2014, John Wiley & Sons, Inc.

1.3.5. CO₂ Reduction Reaction (CRR)

Besides the capture and storage of CO₂, another appealing strategy is the conversion of CO₂ into fuels or chemical stocks, which is an ideal way to alleviate the environmental problems as this will not only reduce the atmospheric CO₂ levels but also decrease the fossil fuel consumption. Nevertheless, due to the chemical inertness of the CO₂ molecule, appropriate catalysts are required to convert large quantities of CO₂ into the production of valuable chemicals such as carbon monoxide (CO), formic acid (HCOOH) and formaldehyde (HCHO). MOFs, which have already shown their capability in a variety of applications, have the potential to selectively reduce CO₂. Recently, a single-atom catalyst having Ni sites was synthesized with the aid of a MOF for efficient

electroreduction of CO₂.⁶² The synthesis was based on the ionic exchange between Zn nodes of pristine ZIF-8 with Ni²⁺ ions followed by pyrolysis at 1000 °C. This synthesis process gave a nitrogen doped porous carbon material with well dispersed single Ni sites providing improved electronic conductivity. The resultant material demonstrated a great turnover frequency (5273 h⁻¹) for CRR with a high Faradaic efficiency (FE) of 71.9% for CO evolution at an overpotential of 0.89 V.

1.3.6. Photocatalysis

An interesting class of materials for photocatalysis is the class of Ti-based MOFs because of their photocatalytic features, redox activity and the low toxicity of Ti. MIL-125 was the first Ti-based MOF that exhibited photocatalytic activity under UV radiation.⁶³ Nevertheless, the synthesis of Ti-based MOFs is still challenging, and few relevant Ti-based MOFs have been reported.

The post-synthetic exchange process is another alternative to obtain heterometallic MOFs with Ti as the desired active sites for photocatalysis. A multifunctional UiO-67-based MOF has been synthesized using the pre-functionalized Ru(bpy)₂(5,5'-dcbpy) linker followed by post-synthetic metal exchange process to include Ti sites (Figure 1.23).⁶⁴ The prepared MOF was applied for photocatalytic degradation of methylene blue (MB) in aqueous solution under visible irradiation (419 nm). These results confirm that the photocatalytic reaction is promoted through the synergistic effect between the Ru complex to work as a light antenna and Ti as photocatalyst. Still, the photocatalytic activities of most (all) MOFs are not yet competitive to the robust and cheap titania materials. After the first synthesis of a Ti-doped Zr-UiO-66 by Cohen *et al.*³⁹, we have shown recently the enormous impact on the bandgap of doping the Zr-UiO-66 with Ti⁴⁺, Ce⁴⁺, and different lanthanides on the photochemical behavior of these MOFs. We were able to synthesize following doped and pristine MOFs, using a microwave synthesis procedure.⁶⁵ The UiO-66(Ce) also exists as a pure monometallic MOF. Combination of modelling and experimental results showed how doping could enhance the photocatalytic activities of these MOFs, by drastically changing the band gap of these materials.

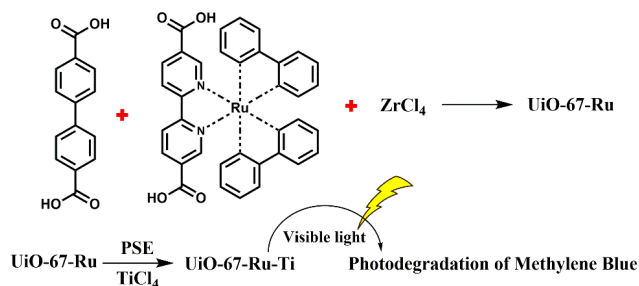


Figure 1.23. Synthesis procedure of UiO-67(Ru/Ti) for photodegradation under visible light. Reproduced from ref.⁶⁴ with permission from the Royal Society of Chemistry.

Table 1.1. Application of MOFs in heterogeneous catalysis.

Entry	Catalyst	Synthesis approach	Reaction	Take home message	Ref.
1	MIL-53 (Al ³⁺ /V ³⁺)	Direct synthesis	Condensation of glycerol with acetone	Enhanced conversion compared to MIL-53(Al) (from 12.5% to 75.9% as the V ³⁺ content increases)	57
2	MOF-74 (Cu ²⁺ /Co ²⁺)	Direct synthesis	Styrene oxidation	Synergistic effect of Cu ²⁺ and Co ²⁺ in one framework (conv. 30.4%)	51
3	MIL-100 (Sc ³⁺ /Fe ³⁺)	Direct synthesis	Alcohol oxidation, Tandem C-C Bond Formation	Higher catalytic activity of mixed-metal MIL-100 compared to MIL-100 (Sc) (yield > 48% vs. < 10%)	61
4	MOF-74 (Ni ²⁺ /Co ²⁺)	Post-synthetic exchange in DMF	Oxidation of cyclohexene	Superior catalytic performance compared with pure Co-MOF-74 (conv. 61% vs. 4.7%)	50
5	{[CuM(pdc) ₂ (H ₂ O) _x · YH ₂ O] _n (x = 0, 3, 4, 5, Y = 0-2) Cu ²⁺ /Mg ²⁺ Cu ²⁺ /Ca ²⁺ Cu ²⁺ /Sr ²⁺ Cu ²⁺ /Ba ²⁺	Direct synthesis	Epoxidation of olefins followed by epoxide ring opening	Enhanced activity with an increase in the size of the alkaline-earth metals (TOF _{Cu/Mg} = 533 vs. TOF _{Cu/Ba} = 103 for cyclohexene)	66
6	UiO-66 (Zr ⁴⁺ /Ce ^{3+/4+})	Direct synthesis	Catalytic decomposition of methanol into CO ₂	Enhanced binding of methanol in the substituted material	67
7	MIL-101 (Cr ³⁺ /Ce ^{3+/4+} (modified with Pd NPs)	Direct synthesis	H ₂ production from ammonia borane	Synergistic effect between Pd NPs and Ce doped MOFs (TON _{Pd/Ce-MIL} = 2357 vs. TON _{Pd/MIL} = 977)	68

Chapter 1: Porous Inorganic Materials: Metal-Organic Frameworks

8	ZIF-8 (Zn^{2+}/Cu^{2+})	Direct synthesis	Cycloaddition of organic azides with alkynes, Friedländer and Combes condensations	High stability and the ease of regeneration	58
9	$[CoNi(\mu_3\text{-tp})(\mu_2\text{-pyz})_2] (Co^{2+}/Ni^{2+})$	Direct synthesis	Dye removal	Good activity and stability	69
10	MFM-300(Ga_2) (Ga^{3+}/Fe^{3+})	Direct synthesis	Epoxide ring-opening, acetylation of benzaldehyde	Higher conversion rates than MFM-300(Ga_2) for the ring-opening reaction (98% vs. 46% for styrene oxid)	70
11	$\{[Zn_2(L)(H_2O)_2] \cdot (5D MF) \cdot (4H_2O)\} (Zn^{2+}/Cu^{2+})$	Post-synthetic exchange in DMF	Knoevenagel condensation	Size-selective catalyst	71
12	porph@MOM-10 (Cd^{2+}/Mn^{2+} Cd^{2+}/Cu^{2+})	Post-synthetic exchange in CH_3OH	Epoxidation of <i>trans</i> -stilbene	Metalloporphyrins as a template for the generation of MOFs	55
13	$[In_xGa_{1-x}(O_2C_2H_4)_{0.5}(hfpbb)] (Ga^{3+}/In^{3+})$	Direct synthesis	A^3 Strecker Reaction	Control of activity by modulating the ratio of metals	60
14	ZIF-8 (Zn^{2+}/Ni^{2+})	Post-synthetic exchange in <i>n</i> -hexane	Electroreduction of CO_2	Excellent TOF (5273 h^{-1}) with a Faradaic efficiency for CO production of 71.9%	62
15	$NH_2\text{-UiO-66} (Zr^{4+}/Ti^{4+})$	Post-synthetic exchange in DMF	CO_2 reduction and hydrogen evolution	Facilitated electron transfer through Ti substituent	72
16	UiO-66 (Zr^{4+}/Ti^{4+})	Post-synthetic exchange in DMF	CO_2 reduction to HCOOH	More efficient photocatalyst compared to $NH_2\text{-MIL-125(Ti)}$ (TON ~ 6.27 vs. 1.52)	73
17	UiO-67 (Zr^{4+}/Ti^{4+})	Post-synthetic exchange in DMF	Degradation of methylene blue	Improved photocatalytic reaction by the communication of the Ru with the Ti	64
18	UiO-66 (Zr^{4+}/Ti^{4+})	Post-synthetic exchange through microwave-assisted reaction	PCVG to reduce Se^{6+}	Higher activity than either UiO-66 or a simple mixture of UiO-66 and $TiCp_2Cl_2$	74
19	NDC-MOFs (Zr^{4+}/Ti^{4+})	Post-synthetic exchange in DMF	Cascade MPV reduction and Etherification	Beneficial effect on the final activity (conv. $_{Zr/Ti-NDC}$ = 90% vs. conv. $_{Zr-NDC}$ = 19%, MPV of methoxybenzaldehyde)	75
20	MIL-101 (Cr^{3+}/Fe^{3+})	Direct synthesis	Dye degradation	High photo-Fenton activity and stability	76
21	MMPF-5 (Cd^{2+}/Co^{2+})	Post-synthetic exchange in DMSO	Epoxidation of <i>trans</i> -stilbene	Higher activity than the homogeneous (tdcmpp(Co)) catalyst (conv. 87% vs. 28.1%)	56
22	UiO-66-sal-CuCl ₂	Post-synthetic modification	Alcohol oxidation	Higher activity compared to UiO-66-sal-Cu(NO_3) ₂ and UiO-66-sal-Cu(OAc) ₂	77
23	PCN-700	Post-synthetic modification	Alcohol oxidation	Pore environment engineering resulted in a size selective catalyst	52

24	Cu(II)/MOF-NH ₂	Post-synthetic modification	Alcohol oxidation	Broad substrate scope: big pore size and surface functionality, base-free catalysis	53
25	CoAl(OH) ₂ @NU-1000	Post-synthetic modification	Alcohol oxidation	Higher efficiency compared to their homometallic counterparts	78
<p>H₂Pdc = pyridine-2,5-dicarboxylic acid, tp = terephthalic acid, pyz = pyrazine, MFM-300(Ga)₂; ((Ga₂(OH)₂(L)), H₄L = biphenyl-3,3',5,5'-tetracarboxylic acid), L = 2'-amino-[1,1':3',1''-terphenyl]-3,3'',5,5''-tetracarboxylic acid ligand, porph@MOM-10 = Cd₆(BPT)₄Cl₄(H₂O)₄]·[C₄₄H₃₆N₈CdCl]·[H₃O]·[solvent], H₂hfipbb = 4,4'-(hexafluoroisopropylidene) bis(benzoic acid), PCVG = photochemical vapor generation, NDC = 2,6-naphthalendicarboxylate, MPV = Meerwein-Ponndorf-Verley, MMPF = metalmetalloporphyrin framework, tdcmp = tetrakis(3,5-dicarboxymethylphenyl)porphine.</p>					

1.4. Objectives: Synthetic Opportunities

From the above discussion, we can conclude that MOFs have shown tremendous potential as smart materials. Considering the great diversity of MOF structures, it can be predicted that this area will grow in the near future to bring the performance of these materials in different applications much beyond that achieved with state-of-the-art porous materials. However, their potential has not yet been recognized fully and there are countless opportunities just based on the design criteria. For example, there are numerous possibilities that these materials offer to introduce additional functionalities into their frameworks. Modification of functional groups in the linkers can modify the chemical properties and promote the performance of materials in many areas and specifically in catalysis. Moreover, the synthesis strategy can be modified to tune the pore volume and surface area of the materials which is crucial in many applications. Even the topological structure of the materials can be important for applications such as catalysis and adsorption.

One of the main objectives targeted in this thesis is to apply different synthesis strategies to design novel MOFs for applications in heterogeneous catalysis. The importance of synthesis methods and their effect on the properties of the final material are discussed in detail in the following chapters. From a design perspective, there are a lot of opportunities yet to be explored to design stable MOF-based catalysts with required functionalities. Moreover, based on the synthesis route, a better control over the porosity and accessible active sites can be achieved to enhance the catalytic performance.

1.5. References

1. Van Der Voort, P., Leus, K., De Canck, E., *Introduction to porous materials*. Wiley: 2019; p 448.
2. Yang, X. Y.; Chen, L. H.; Li, Y.; Rooke, J. C.; Sanchez, C.; Su, B. L., Hierarchically porous materials: synthesis strategies and structure design. *Chem Soc Rev* **2017**, *46* (2), 481-558.
3. Qiao, Z. A.; Huo, Q. S., Chapter 15 - Synthetic Chemistry of the Inorganic Ordered Porous Materials. In *Modern Inorganic Synthetic Chemistry (Second Edition)*, Xu, R.; Xu, Y., Eds. Elsevier: Amsterdam, 2017; pp 389-428.
4. Li, H.; Eddaoudi, M.; O'Keeffe, M.; Yaghi, O. M., Design and synthesis of an exceptionally stable and highly porous metal-organic framework. *Nature* **1999**, *402* (6759), 276-279.
5. Kitagawa, S.; Kondo, M., Functional micropore chemistry of crystalline metal complex-assembled compounds. *B Chem Soc Jpn* **1998**, *71* (8), 1739-1753.
6. Cheetham, A. K.; Ferey, G.; Loiseau, T., Open-framework inorganic materials. *Angew Chem Int Edit* **1999**, *38* (22), 3268-3292.
7. Zhao, D. Y.; Huo, Q. S.; Feng, J. L.; Chmelka, B. F.; Stucky, G. D., Nonionic triblock and star diblock copolymer and oligomeric surfactant syntheses of highly ordered, hydrothermally stable, mesoporous silica structures. *J Am Chem Soc* **1998**, *120* (24), 6024-6036.
8. Eddaoudi, M.; Kim, J.; Rosi, N.; Vodak, D.; Wachter, J.; O'Keeffe, M.; Yaghi, O. M., Systematic design of pore size and functionality in isorecticular MOFs and their application in methane storage. *Science* **2002**, *295* (5554), 469-472.
9. Hendon, C. H.; Rieth, A. J.; Korzynski, M. D.; Dinca, M., Grand Challenges and Future Opportunities for Metal-Organic Frameworks. *Acs Central Sci* **2017**, *3* (6), 554-563.
10. Leus, K.; Bogaerts, T.; De Decker, J.; Depauw, H.; Hendrickx, K.; Vrielinck, H.; Van Speybroeck, V.; Van Der Voort, P., Systematic study of the chemical and hydrothermal stability of selected "stable" Metal Organic Frameworks. *Micropor Mesopor Mat* **2016**, *226*, 110-116.
11. Dhakshinamoorthy, A.; Asiri, A. M.; Garcia, H., Mixed-metal or mixed-linker metal organic frameworks as heterogeneous catalysts. *Catal Sci Technol* **2016**, *6* (14), 5238-5261.
12. Bitzer, J.; Kleist, W., Synthesis strategies and structural arrangements of isorecticular mixed-component metal-organic frameworks. *Chemistry A European Journal* **2018**.
13. Bernales, V.; Ortuno, M. A.; Truhlar, D. G.; Cramer, C. J.; Gagliardi, L., Computational Design of Functionalized Metal-Organic Framework Nodes for Catalysis. *Acs Central Sci* **2018**, *4* (1), 5-19.
14. Fei, H. H.; Cohen, S. M., A robust, catalytic metal-organic framework with open 2,2'-bipyridine sites. *Chem Commun* **2014**, *50* (37), 4810-4812.
15. Li, N.; Xu, J.; Feng, R.; Hu, T. L.; Bu, X. H., Governing metal-organic frameworks towards high stability. *Chem Commun* **2016**, *52* (55), 8501-8513.
16. Colombo, V.; Galli, S.; Choi, H. J.; Han, G. D.; Maspero, A.; Palmisano, G.; Masciocchi, N.; Long, J. R., High thermal and chemical stability in pyrazolate-bridged metal-organic frameworks with exposed metal sites. *Chem Sci* **2011**, *2* (7), 1311-1319.
17. Hocking, R. K.; Hambley, T. W., Structural measure of metal-ligand covalency from the bonding in carboxylate ligands. *Inorg Chem* **2003**, *42* (9), 2833-2835.
18. Nouar, F.; Devic, T.; Chevreau, H.; Guillou, N.; Gibson, E.; Clet, G.; Daturi, M.; Vimont, A.; Greneche, J. M.; Breeze, M. I.; Walton, R. I.; Llewellyne, P. L.; Serre, C., Tuning the breathing behaviour of MIL-53 by cation mixing. *Chem Commun* **2012**, *48* (82), 10237-10239.
19. Masoomi, M. Y.; Morsali, A.; Dhakshinamoorthy, A.; Garcia, H., Mixed-Metal MOFs: Unique Opportunities in Metal-Organic Framework (MOF) Functionality and Design. *Angew Chem Int Edit* **2019**, *58* (43), 15188-15205.
20. Jiao, Y.; Morelock, C. R.; Burtch, N. C.; Mounfield, W. P.; Hungerford, J. T.; Walton, K. S., Tuning the Kinetic Water Stability and Adsorption Interactions of Mg-MOF-74 by Partial Substitution with Co or Ni. *Ind Eng Chem Res* **2015**, *54* (49), 12408-12414.

21. Wang, L. J.; Deng, H. X.; Furukawa, H.; Gandara, F.; Cordova, K. E.; Peri, D.; Yaghi, O. M., Synthesis and Characterization of Metal-Organic Framework-74 Containing 2, 4, 6, 8, and 10 Different Metals. *Inorg Chem* **2014**, *53* (12), 5881-5883.
22. Wang, Z. Q.; Cohen, S. M., Postsynthetic covalent modification of a neutral metal-organic framework. *J Am Chem Soc* **2007**, *129* (41), 12368-+.
23. Tanabe, K. K.; Cohen, S. M., Postsynthetic modification of metal-organic frameworks—a progress report. *Chem Soc Rev* **2011**, *40* (2), 498-519.
24. Maksimchuk, N. V.; Zalomaeva, O. V.; Skobelev, I. Y.; Kovalenko, K. A.; Fedin, V. P.; Kholdeeva, O. A., Metal-organic frameworks of the MIL-101 family as heterogeneous single-site catalysts. *P Roy Soc a-Math Phys* **2012**, *468* (2143), 2017-2034.
25. Abednatanzi, S.; Leus, K.; Derakhshandeh, P. G.; Nahra, F.; De Keukeleere, K.; Van Hecke, K.; Van Driessche, I.; Abbasi, A.; Nolan, S. P.; Van Der Voort, P., POM@IL-MOFs - inclusion of POMs in ionic liquid modified MOFs to produce recyclable oxidation catalysts. *Catal Sci Technol* **2017**, *7* (7), 1478-1487.
26. Brozek, C. K.; Dinca, M., Ti³⁺-, V^{2+/3+}-, Cr^{2+/3+}-, Mn²⁺-, and Fe²⁺-Substituted MOF-5 and Redox Reactivity in Cr- and Fe-MOF-5. *J Am Chem Soc* **2013**, *135* (34), 12886-12891.
27. Long, J. R.; Yaghi, O. M., The pervasive chemistry of metal-organic frameworks. *Chem Soc Rev* **2009**, *38* (5), 1213-1214.
28. Rowsell, J. L. C.; Yaghi, O. M., Metal-organic frameworks: a new class of porous materials. *Micropor Mesopor Mat* **2004**, *73* (1-2), 3-14.
29. Doonan, C. J.; Morris, W.; Furukawa, H.; Yaghi, O. M., Isoreticular Metalation of Metal-Organic Frameworks. *J Am Chem Soc* **2009**, *131* (27), 9492-+.
30. Czaja, A. U.; Trukhan, N.; Muller, U., Industrial applications of metal-organic frameworks. *Chem Soc Rev* **2009**, *38* (5), 1284-1293.
31. Gandara, F.; Puebla, E. G.; Iglesias, M.; Proserpio, D. M.; Snejko, N.; Monge, M. A., Controlling the Structure of Arenedisulfonates toward Catalytically Active Materials. *Chem Mater* **2009**, *21* (4), 655-661.
32. Abednatanzi, S.; Derakhshandeh, P. G.; Depauw, H.; Coudert, F. X.; Vrielinck, H.; Van Der Voort, P.; Leus, K., Mixed-metal metal-organic frameworks. *Chem Soc Rev* **2019**, *48* (9), 2535-2565.
33. Ferey, G.; Mellot-Draznieks, C.; Serre, C.; Millange, F.; Dutour, J.; Surble, S.; Margiolaki, I., A chromium terephthalate-based solid with unusually large pore volumes and surface area. *Science* **2005**, *309* (5743), 2040-2042.
34. Chui, S. S. Y.; Lo, S. M. F.; Charmant, J. P. H.; Orpen, A. G.; Williams, I. D., A chemically functionalizable nanoporous material [Cu-3(TMA)(2)(H2O)(3)](n). *Science* **1999**, *283* (5405), 1148-1150.
35. Banerjee, M.; Das, S.; Yoon, M.; Choi, H. J.; Hyun, M. H.; Park, S. M.; Seo, G.; Kim, K., Postsynthetic Modification Switches an Achiral Framework to Catalytically Active Homochiral Metal-Organic Porous Materials. *J Am Chem Soc* **2009**, *131* (22), 7524-+.
36. Hong, D. Y.; Hwang, Y. K.; Serre, C.; Ferey, G.; Chang, J. S., Porous Chromium Terephthalate MIL-101 with Coordinatively Unsaturated Sites: Surface Functionalization, Encapsulation, Sorption and Catalysis. *Adv Funct Mater* **2009**, *19* (10), 1537-1552.
37. Marx, S.; Kleist, W.; Baiker, A., Synthesis, structural properties, and catalytic behavior of Cu-BTC and mixed-linker Cu-BTC-PyDC in the oxidation of benzene derivatives. *J Catal* **2011**, *281* (1), 76-87.
38. Noei, H.; Amirjalayer, S.; Muller, M.; Zhang, X. N.; Schmid, R.; Muhler, M.; Fischer, R. A.; Wang, Y. M., Low-Temperature CO Oxidation over Cu-Based Metal-Organic Frameworks Monitored by using FTIR Spectroscopy. *Chemcatchem* **2012**, *4* (6), 755-759.

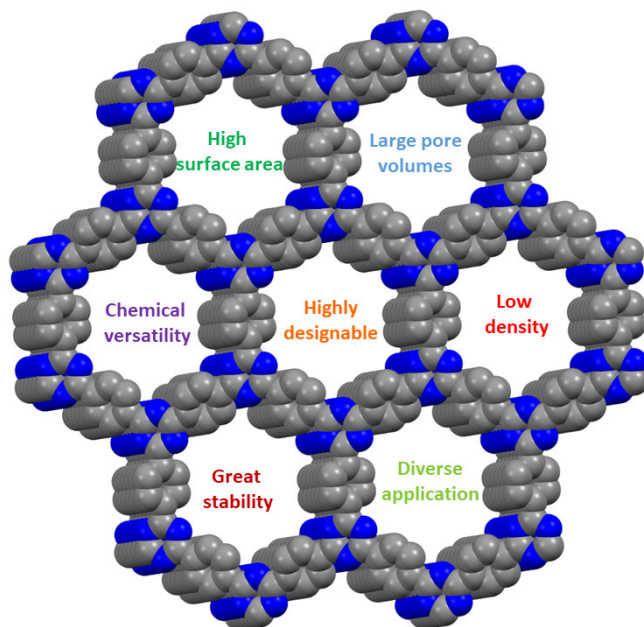
39. Kim, M.; Cahill, J. F.; Fei, H. H.; Prather, K. A.; Cohen, S. M., Postsynthetic Ligand and Cation Exchange in Robust Metal-Organic Frameworks. *J Am Chem Soc* **2012**, *134* (43), 18082-18088.
40. Gandara, F.; de Andres, A.; Gomez-Lor, B.; Gutierrez-Puebla, E.; Iglesias, M.; Monge, M. A.; Proserpio, D. M.; Snejko, N., A rare-earth MOF series: Fascinating structure, efficient light emitters, and promising catalysts. *Cryst Growth Des* **2008**, *8* (2), 378-380.
41. Zhu, Q. L.; Li, J.; Xu, Q., Immobilizing Metal Nanoparticles to Metal-Organic Frameworks with Size and Location Control for Optimizing Catalytic Performance. *J Am Chem Soc* **2013**, *135* (28), 10210-10213.
42. Juan-Alcaniz, J.; Gascon, J.; Kapteijn, F., Metal-organic frameworks as scaffolds for the encapsulation of active species: state of the art and future perspectives. *J Mater Chem* **2012**, *22* (20), 10102-10118.
43. Zhao, H. Y.; Gabbai, F. P., A bidentate Lewis acid with a telluronium ion as an anion-binding site. *Nat Chem* **2010**, *2* (11), 984-990.
44. Leus, K.; Liu, Y. Y.; Meledina, M.; Turner, S.; Van Tendeloo, G.; Van der Voort, P., A Mo-VI grafted Metal Organic Framework: Synthesis, characterization and catalytic investigations. *J Catal* **2014**, *316*, 201-209.
45. Abednatanzi, S.; Derakhshandeh, P. G.; Abbasi, A.; Van der Voort, P.; Leus, K., Direct Synthesis of an Iridium(III) Bipyridine Metal-Organic Framework as a Heterogeneous Catalyst for Aerobic Alcohol Oxidation. *Chemcatchem* **2016**, *8* (23), 3672-3679.
46. Kung, H. H., *Transition Metal Oxides: Surface Chemistry and Catalysis*. Elsevier: Amsterdam, The Netherlands 1989; Vol. 45.
47. Hagen, J., *Industrial catalysis : a practical approach*. Wiley-VCH: Weinheim, 2006.
48. Weissrermel, K.; Arpe, H.-J. r., *Industrial organic chemistry*. Wiley-VCH: Weinheim; New York; Basel; Cambridge, 1993.
49. Parmeggiani, C.; Matassini, C.; Cardona, F., A step forward towards sustainable aerobic alcohol oxidation: new and revised catalysts based on transition metals on solid supports. *Green Chem* **2017**, *19* (9), 2030-2050.
50. Sun, D. R.; Sun, F. X.; Deng, X. Y.; Li, Z. H., Mixed-Metal Strategy on Metal-Organic Frameworks (MOFs) for Functionalities Expansion: Co Substitution Induces Aerobic Oxidation of Cyclohexene over Inactive Ni-MOF-74. *Inorg Chem* **2015**, *54* (17), 8639-8643.
51. Fu, Y. H.; Xu, L.; Shen, H. M.; Yang, H.; Zhang, F. M.; Zhu, W. D.; Fan, M. H., Tunable catalytic properties of multi-metal-organic frameworks for aerobic styrene oxidation. *Chem Eng J* **2016**, *299*, 135-141.
52. Yuan, S.; Chen, Y. P.; Qin, J. S.; Lu, W. G.; Zou, L. F.; Zhang, Q.; Wang, X.; Sun, X.; Zhou, H. C., Linker Installation: Engineering Pore Environment with Precisely Placed Functionalities in Zirconium MOFs. *J Am Chem Soc* **2016**, *138* (28), 8912-8919.
53. Taher, A.; Kim, D. W.; Lee, I. M., Highly efficient metal organic framework (MOF)-based copper catalysts for the base-free aerobic oxidation of various alcohols. *Rsc Adv* **2017**, *7* (29), 17806-17812.
54. Amini, M.; Haghdoost, M. M.; Bagherzadeh, M., Oxido-peroxido molybdenum(VI) complexes in catalytic and stoichiometric oxidations. *Coordin Chem Rev* **2013**, *257* (7-8), 1093-1121.
55. Zhang, Z. J.; Zhang, L. P.; Wojtas, L.; Nugent, P.; Eddaoudi, M.; Zaworotko, M. J., Templated Synthesis, Postsynthetic Metal Exchange, and Properties of a Porphyrin-Encapsulating Metal-Organic Material. *J Am Chem Soc* **2012**, *134* (2), 924-927.
56. Wang, X. S.; Chranowski, M.; Wojtas, L.; Chen, Y. S.; Ma, S., Formation of a Metalloporphyrin-Based Nanoreactor by Postsynthetic Metal-Ion Exchange of a Polyhedral-Cage Containing a Metal-Metalloporphyrin Framework (vol 19, pg 3297, 2013). *Chem-Eur J* **2013**, *19* (37), 12187-12187.

57. Timofeeva, M. N.; Panchenko, V. N.; Khan, N. A.; Hasan, Z.; Prosvirin, I. P.; Tsybulya, S. V.; Jung, S. H., Isostructural metal-carboxylates MIL-100(M) and MIL-53(M) (M: V, Al, Fe and Cr) as catalysts for condensation of glycerol with acetone. *Appl Catal a-Gen* **2017**, *529*, 167-174.
58. Schejn, A.; Aboulaich, A.; Balan, L.; Falk, V.; Lalevee, J.; Medjahdi, G.; Aranda, L.; Mozet, K.; Schneider, R., Cu²⁺-doped zeolitic imidazolate frameworks (ZIF-8): efficient and stable catalysts for cycloadditions and condensation reactions. *Catal Sci Technol* **2015**, *5* (3), 1829-1839.
59. Huang, Y. B.; Liang, J.; Wang, X. S.; Cao, R., Multifunctional metal-organic framework catalysts: synergistic catalysis and tandem reactions. *Chem Soc Rev* **2017**, *46* (1), 126-157.
60. Aguirre-Diaz, L. M.; Gandara, F.; Iglesias, M.; Snejko, N.; Gutierrez-Puebla, E.; Monge, M. A., Tunable Catalytic Activity of Solid Solution Metal-Organic Frameworks in One-Pot Multicomponent Reactions. *J Am Chem Soc* **2015**, *137* (19), 6132-6135.
61. Mitchell, L.; Williamson, P.; Ehrlichova, B.; Anderson, A. E.; Seymour, V. R.; Ashbrook, S. E.; Acerbi, N.; Daniels, L. M.; Walton, R. I.; Clarke, M. L.; Wright, P. A., Mixed-Metal MIL-100(Sc,M) (M=Al, Cr, Fe) for Lewis Acid Catalysis and Tandem C-C Bond Formation and Alcohol Oxidation. *Chem-Eur J* **2014**, *20* (51), 17185-17197.
62. Zhao, C. M.; Dai, X. Y.; Yao, T.; Chen, W. X.; Wang, X. Q.; Wang, J.; Yang, J.; Wei, S. Q.; Wu, Y. E.; Li, Y. D., Ionic Exchange of Metal Organic Frameworks to Access Single Nickel Sites for Efficient Electroreduction of CO₂. *J Am Chem Soc* **2017**, *139* (24), 8078-8081.
63. Dan-Hardi, M.; Serre, C.; Frot, T.; Rozes, L.; Maurin, G.; Sanchez, C.; Ferey, G., A New Photoactive Crystalline Highly Porous Titanium(IV) Dicarboxylate. *J Am Chem Soc* **2009**, *131* (31), 10857-+.
64. Amador, R. N.; Carboni, M.; Meyer, D., Sorption and photodegradation under visible light irradiation of an organic pollutant by a heterogeneous UiO-67-Ru-Ti MOF obtained by post-synthetic exchange. *Rsc Adv* **2017**, *7* (1), 195-200.
65. Hendrickx, K.; Joos, J. J.; De Vos, A.; Poelman, D.; Smet, P. F.; Van Speybroeck, V.; Van Der Voort, P.; Lejaeghere, K., Exploring Lanthanide Doping in UiO-66: A Combined Experimental and Computational Study of the Electronic Structure. *Inorg Chem* **2018**, *57* (9), 5463-5474.
66. Sahap, D.; Hazra, D. K.; Maity, T.; Koner, S., Heterometallic Metal-Organic Frameworks That Catalyze Two Different Reactions Sequentially. *Inorg Chem* **2016**, *55* (12), 5729-5731.
67. Nouar, F.; Breeze, M. I.; Campo, B. C.; Vimont, A.; Clet, G.; Daturi, M.; Devic, T.; Walton, R. I.; Serre, C., Tuning the properties of the UiO-66 metal organic framework by Ce substitution. *Chem Commun* **2015**, *51* (77), 14458-14461.
68. Wen, M. C.; Kuwahara, Y.; Mori, K.; Zhang, D. Q.; Li, H. X.; Yamashita, H., Synthesis of Ce ions doped metal-organic framework for promoting catalytic H₂ production from ammonia borane under visible light irradiation. *J Mater Chem A* **2015**, *3* (27), 14134-14141.
69. Abbasi, A.; Soleimani, M.; Najafi, M.; Geranmayeh, S., New interpenetrated mixed (Co/Ni) metal-organic framework for dye removal under mild conditions. *Inorg Chim Acta* **2016**, *439*, 18-23.
70. Krap, C. P.; Newby, R.; Dhakshinamoorthy, A.; Garcia, H.; Cebula, I.; Easun, T. L.; Savage, M.; Eyley, J. E.; Gao, S.; Blake, A. J.; Lewis, W.; Beton, P. H.; Warren, M. R.; Allan, D. R.; Frogley, M. D.; Tang, C. C.; Cinque, G.; Yang, S. H.; Schroder, M., Enhancement of CO₂ Adsorption and Catalytic Properties by Fe-Doping of [Ga-2(OH)(2)(L)] (H₄L = Biphenyl-3,3',5,5'-tetracarboxylic Acid), MFM-300(Ga-2). *Inorg Chem* **2016**, *55* (3), 1076-1088.
71. Pal, T. K.; De, D.; Neogi, S.; Pachfule, P.; Senthilkumar, S.; Xu, Q.; Bharadwaj, P. K., Significant Gas Adsorption and Catalytic Performance by a Robust Cu-II-MOF Derived through Single-Crystal to Single-Crystal Transmetalation of a Thermally Less-Stable Zn-II-MOF. *Chem-Eur J* **2015**, *21* (52), 19064-19070.

72. Sun, D. R.; Liu, W. J.; Qiu, M.; Zhang, Y. F.; Li, Z. H., Introduction of a mediator for enhancing photocatalytic performance via post-synthetic metal exchange in metal-organic frameworks (MOFs). *Chem Commun* **2015**, 51 (11), 2056-2059.
73. Lee, Y.; Kim, S.; Kang, J. K.; Cohen, S. M., Photocatalytic CO₂ reduction by a mixed metal (Zr/Ti), mixed ligand metal-organic framework under visible light irradiation. *Chem Commun* **2015**, 51 (26), 5735-5738.
74. Tu, J. P.; Zeng, X. L.; Xu, F. J.; Wu, X.; Tian, Y. F.; Hou, X. D.; Long, Z., Microwave-induced fast incorporation of titanium into UiO-66 metal-organic frameworks for enhanced photocatalytic properties. *Chem Commun* **2017**, 53 (23), 3361-3364.
75. Rasero-Almansa, A. M.; Iglesias, M.; Sanchez, F., Synthesis of bimetallic Zr(Ti)-naphthalendicarboxylate MOFs and their properties as Lewis acid catalysis. *Rsc Adv* **2016**, 6 (108), 106790-106797.
76. Vu, T. A.; Le, G. H.; Dao, C. D.; Dang, L. Q.; Nguyen, K. T.; Dang, P. T.; Tran, H. T. K.; Duong, Q. T.; Nguyen, T. V.; Lee, G. D., Isomorphous substitution of Cr by Fe in MIL-101 framework and its application as a novel heterogeneous photo-Fenton catalyst for reactive dye degradation. *Rsc Adv* **2014**, 4 (78), 41185-41194.
77. Hou, J. Y.; Luan, Y.; Tang, J.; Wensley, A. M.; Yang, M.; Lu, Y. F., Synthesis of UiO-66-NH₂ derived heterogeneous copper (II) catalyst and study of its application in the selective aerobic oxidation of alcohols. *J Mol Catal a-Chem* **2015**, 407, 53-59.
78. Thompson, A. B.; Pahis, D. R.; Bernales, V.; Gallington, L. C.; Malonzo, C. D.; Webber, T.; Tereniak, S. J.; Wang, T. C.; Desai, S. P.; Li, Z. Y.; Kim, I. S.; Gagliardi, L.; Penn, R. L.; Chapman, K. W.; Stein, A.; Farha, O. K.; Hupp, J. T.; Martinson, A. B. F.; Lu, C. C., Installing Heterobimetallic Cobalt-Aluminum Single Sites on a Metal Organic Framework Support. *Chem Mater* **2016**, 28 (18), 6753-6762.

CHAPTER 2

*POROUS ORGANIC MATERIALS:
COVALENT ORGANIC/TRIAZINE
FRAMEWORKS*



2.1. Introduction

Covalent organic frameworks (COFs) are an emerging type of organic crystalline polymers with highly organized structures and inherent porosity.¹⁻² COFs are crystalline nanoporous polymeric frameworks consisting entirely of light elements (C,N,B,O,S,H) linked via covalent bonds. They have similar characteristics in comparison to the well-known metal-organic frameworks (MOFs). In general, COFs possess very low densities (0.17 g cm^{-3}), high surface areas (up to $4210 \text{ m}^2\text{g}^{-1}$) and tunable pore sizes which can be tuned by using bigger/smaller building units. In short, COFs are structurally pre-designable, synthetically controllable, and functionally adaptable. COFs represent a higher thermal and chemical stability compared to MOFs allowing pre- or post-synthetic modifications for specific applications. They are formed via covalent condensation of lightweight molecular building blocks. Since their invention (2005), the development of new COFs has increased rapidly. COFs can be classified depending on the structural building units including boronate, imide, hydrazone, nitrile, imine and triazine-based functionalities.¹ Figure 2.1 shows some examples of 2D COFs composed of extended organic layers stacked in periodic columnar π -arrays.

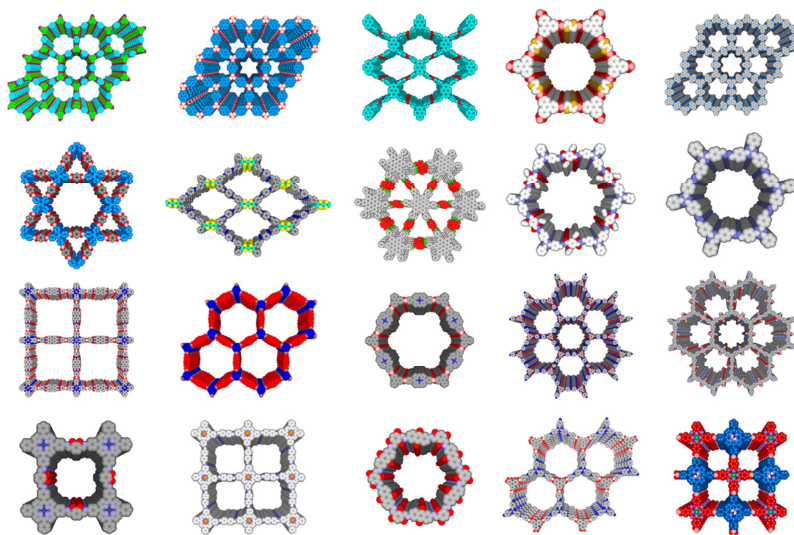


Figure 2.1. Example of porous 2D COFs with different topologies.

The first covalent triazine framework (CTF) was reported in 2008 by Thomas and Antonietti.³ CTFs are microporous conjugated polymers that are linked together by 1,3,5-triazine units. The individual sheets then stack by π - π interactions into a hexagonal 2D layered structure. The synthesis approach to design a typical CTF-1 is shown in Figure 2.2.

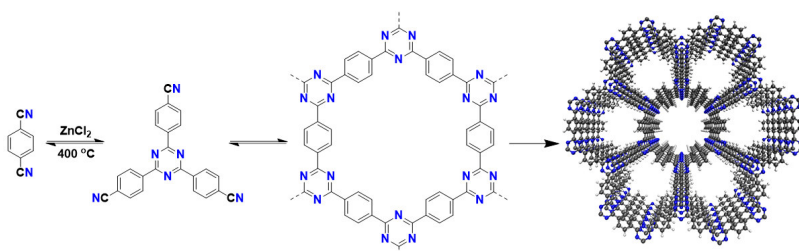


Figure 2.2. Reaction scheme for the synthesis of the first reported CTF denoted as CTF-1.

In general, CTFs can be regarded as smart multi-functional materials and have the following advantages for heterogeneous (photo) catalysis and sensing applications:

- CTFs have a high chemical, thermal and mechanical stability allowing pre- or post-synthetic modifications for specific applications.
- They are composed of molecular building blocks having abundant nitrogen atoms which can be used for grafting both d- and f-metal ions and complexes.
- They have permanent tunable nanometer-sized pores with very large surface areas (> 1500 m²/g).
- The possibility to apply a wide range of molecular building blocks provides opportunities to optimize light harvesting, charge separation and charge transport.
- The photoactive building blocks can be locked in a rigid structure, enhancing the lifetime of the excited states by preventing deactivation through collision.
- The extended π -electron conjugation enhancement boosts luminescence properties.
- The crystalline or semi-crystalline nature of these materials facilitates charge transport and minimizes charge trapping at defect sites.

- They have a very low density, much lower than MOFs as they are solely composed of light elements such as C, N, O, S, H.

Consequently, enormous efforts have been done to rationally design and synthesize various CTFs. Aside from the 1,4-dicyanobenzene linker (monomer for CTF-1), several other building blocks have been used for the preparation of CTFs which are presented in Figure 2.3.

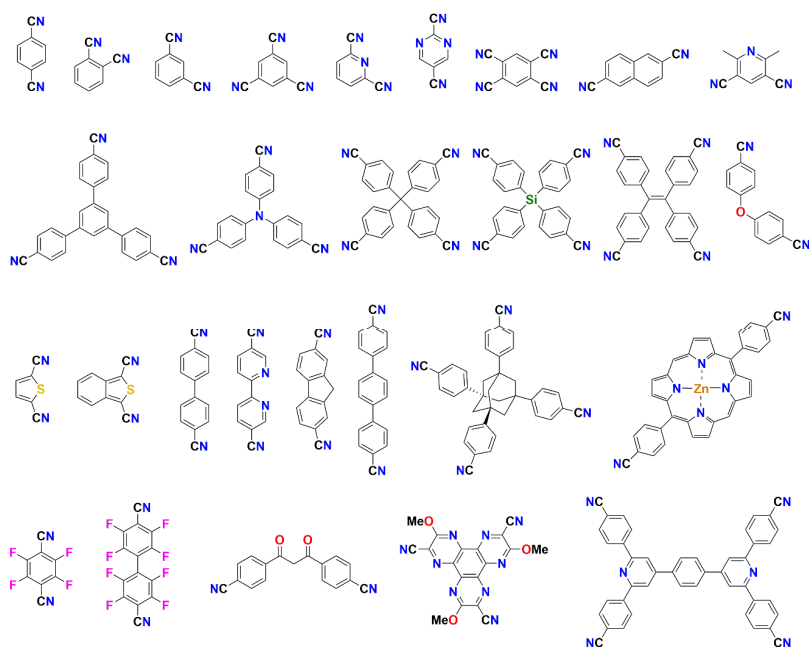


Figure 2.3. Series of nitrile building blocks for the synthesis of CTF materials.

2.2. Synthesis of CTFs

Various synthesis strategies have been discussed and developed in the literature to design CTFs. CTFs with desired topology, functionality and pore size can be constructed from different monomers with specific functional groups under a proper reaction condition. The properties and performance of CTFs rely heavily on the synthetic approaches and the diversity of their functionalities. These approaches are discussed below.

2.2.1. Ionothermal synthesis

In the first report of a CTF, by Thomas *et al.*, the dynamic trimerization of nitriles in molten ZnCl_2 at high temperatures is reported. ZnCl_2 acts both as the solvent and catalyst for the trimerization reaction.³ In this method, the nitrile monomer and ZnCl_2 were placed into a glass or quartz ampule, which was fully evacuated and sealed. The black porous material was obtained after heating at 400 °C for around 40–48 h (Figure 2.4). So far, most of the reported CTFs have been prepared under ionothermal conditions and are amorphous. The high stability of the triazine linkage causes low reversibility of the polymerization process and subsequently low crystallinity of CTFs. The influence of various reaction parameters on the chemical structure and properties of materials is investigated by the same group. This includes reaction temperature, ZnCl_2 /monomer ratio and the geometry and functionalities of the monomers.⁴ An excess amount of ZnCl_2 and/or an increase in the synthesis temperature results in a higher specific surface area (up to 3300 m^2/g) and pore volume (up to 2.4 cm^3/g). However, irreversible carbonization occurs at elevated temperatures causing loss of nitrogen, creation of structural defects, rather undefined surface functionalities and consequently resulting in mainly amorphous materials. On the other hand, synthesis at a temperature below 350 °C and even with extended reaction time up to 168 h leads to the formation of non-porous oligomeric products. Later on, a relatively milder reaction condition using microwave-assisted polymerization was applied by Zhang *et al.* to reduce the reaction time (from the typical 40 h to less than 1 h).⁵

2.2.2. Bronsted Acid

Although the ionothermal method is efficient for triazine ring formation, the harsh reaction conditions might limit practical applications. In this regard, Cooper and co-workers proposed another method for the synthesis of CTFs using trifluoromethanesulfonic acid (TFMS) as the catalyst at room temperature and microwave-assisted conditions.⁶ Compared to the ionothermal method, this approach showed significant advantages such as milder reaction conditions, no carbonization, easier work up and no metal (Zn) residual in the final material. More importantly, unlike the black CTFs obtained via ionothermal synthesis, the materials produced through TFMS catalyzed condensation are photoactive and fluorescent.

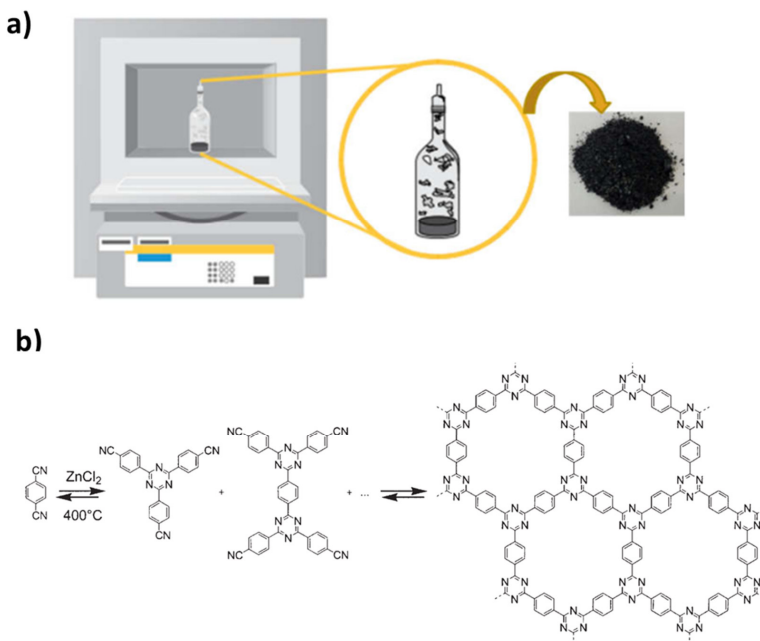


Figure 2.4. (a) Schematic illustration of the preparation of the porous CTF materials under ionothermal conditions. (b) Ionothermal trimerization of 1,4-dicyanobenzene monomer in molten ZnCl_2 to trimers and oligomers and subsequently to a covalent triazine-based framework (CTF-1).³

These features make them attractive for photocatalytic or sensing applications. Besides, the Brønsted Acid procedure was also applied to synthesize porous CTF membranes by spreading thin films of the acidic nitrile solution onto flat glass discs and heating at $100\text{ }^\circ\text{C}$.⁷ However, some inherent drawbacks of this methodology restrict its broad feasibility. This includes the high cost of catalyst, use of corrosive and eye irritating carcinogenic chemicals and inapplicability for heteroatomic monomers.

2.2.3. Sulfur-mediated

In 2017, the group of Coskun developed a sulfur-mediated route to make CTFs in the absence of any catalyst or solvent.⁸ S-CTF-1 was formed in the presence of

elemental sulfur via *in-situ* vulcanization at 400 °C. The obtained CTF showed great potential as a cathode material for lithium-sulfur batteries due to the high sulfur content. Partial carbonization at high synthesis temperatures (400 °C) and the presence of large amounts of sulfur in the micropores of the obtained CTFs limit their widespread applications.

2.2.4. Phosphorus pentoxide (P₂O₅)

In another strategy developed by Baek *et al.*, phosphorus pentoxide (P₂O₅) was used as the catalyst to synthesize CTFs.⁹ P₂O₅ can facilitate the direct condensation of aromatic primary amide groups into s-triazine rings. The process includes two steps (i) aromatic primary amide groups [C(=O)–NH₂] conversion into nitriles, and (ii) s-triazine ring formation by consequent condensation. Both aromatic amide and nitrile compounds are available to synthesize CTFs using the P₂O₅ catalyst. The PCTF-1 synthesized by this method showed good crystallinity with a surface area up to 2034 m² g⁻¹ and a total pore volume of 1.04 cm³ g⁻¹. The method is more eco-friendly and the catalyst can be removed easily at the end of the reaction. Still, carbonization is challenging due to the high synthesis temperature (400 °C).

2.2.5. Amidine synthesis based on a polycondensation method

As mentioned above, a variety of approaches has been reported for the preparation of CTFs, (for cyclization of nitrile or amide aromatic building blocks) using ZnCl₂ (ionothermal), P₂O₅ (ionothermal), CF₃SO₃H and AlCl₃ catalysts. However, the high temperature (400-500 °C) of the ionothermal synthetic pathways leads to non-photoactive materials and partial carbonization. On the other hand, the other two catalytic pathways using triflic acid or AlCl₃ only show good results for a limited number of building blocks and amorphous materials are typically obtained.

Recently, Cooper and co-workers developed a novel synthesis strategy involving the condensation reaction of aldehydes and amidines to make CTFs under a relatively milder synthetic procedure.¹⁰ The reaction mechanism for triazine formation in this method is based on a condensation reaction between an aldehyde and an amidine dihydrochloride involving a Schiff base formation followed by a Michael addition. This method provides a great opportunity to design novel porous structures using a variety of building blocks. In this regard, 1,4-benzene-

dialdehyde, 4,4'-biphenyl-dialdehyde, tris(4-formyl-phenyl)-amine, and tris(4-formylbiphenyl)-amine were reacted with terephthalamidine dihydrochloride at 120 °C to produce CTF-HUST-1, CTF-HUST-2, CTF-HUST-3 and CTF-HUST-4, respectively (Figure 2.5). The obtained CTFs with this method always showed layered structures compared to the CTFs produced via the Brønsted acid method. The resulting materials are typically obtained as yellow or orange powders, retaining most of their photophysical properties, while still not being crystalline.

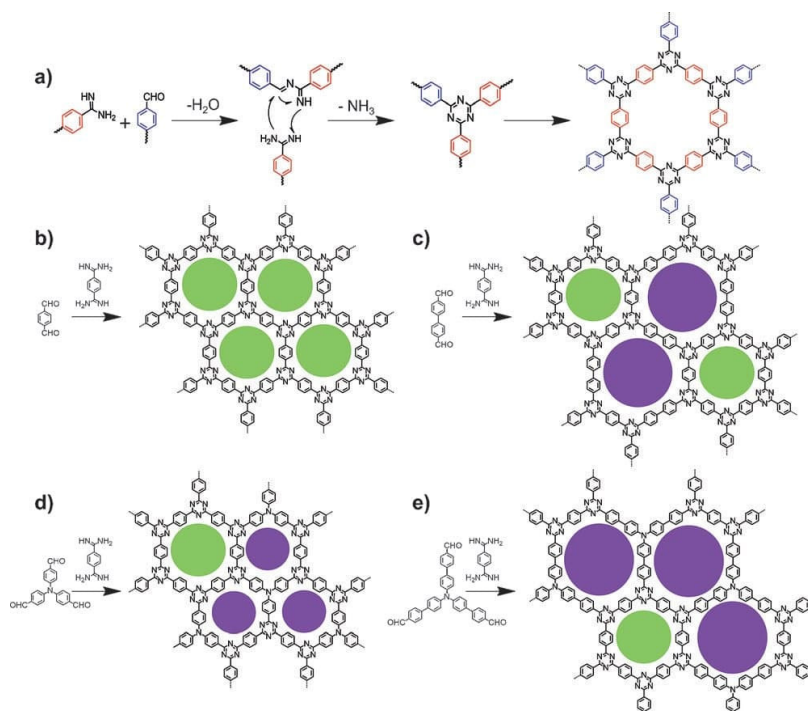


Figure 2.5. (a) Reaction mechanism of the amidine-based polycondensation method for triazine formation in the synthesis of amorphous CTFs. (b-e) Representative structures of CTF-HUST-1, CTF-HUST-2, CTF-HUST-3 and CTF-HUST-4, respectively, were synthesized by different aldehyde monomers. The green and purple circles represent the presence of two types of pores in the structure.¹⁰

Afterward, Tan *and* co-workers found that slowing down the nucleation process through *in-situ* oxidation of alcohol monomers into aldehydes during the polycondensation reaction results in highly crystalline CTFs (Figure 2.6).¹¹ With this strategy, a series of highly crystalline CTFs are prepared using alcohol monomers to evolve into aldehydes. The reaction rates were controlled by performing two reactions simultaneously (i) production of an aldehyde by oxidation of alcohol and (ii) condensation reaction between the produced aldehyde with an amidine dihydrochloride to form triazine. The reaction temperature plays an important role in this polycondensation method. To control the *in-situ* formation of aldehyde and nucleation rate, it is very crucial to keep the polymerization reaction at a low temperature in the initial step. Afterward, an increase in the temperature promotes crystal growth and improves the crystallization of CTFs. Additionally, this method expands the monomer scope to make numerous CTF with a wide range of available alcohols and provides a platform for the large-scale production of CTFs.

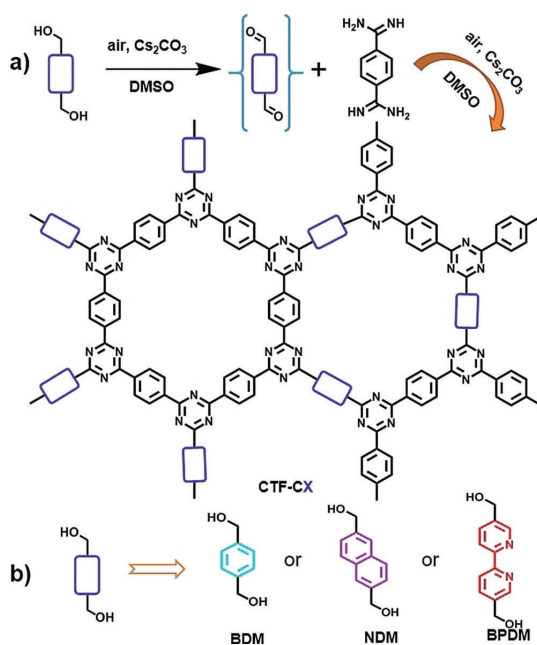


Figure 2.6. (a) The general strategy of *in-situ* aldehyde formation by slow oxidation of alcohol to control the nucleation rate for the formation of CTF. (b) Range of monomers applied within this method.¹¹

Furthermore, to achieve highly crystalline CTFs another method was developed by Tan and co-workers. In this approach, the crystallinity of CTFs was enhanced via direct controlling the monomer feeding rate. The slow feeding rate of the aldehyde monomers controlled the nucleation and crystal growth, which resulted in long-range order and crystalline CTFs.¹²

2.3. Application of CTFs

CTFs have been applied for a wide range of applications such as gas sorption and separation, catalysis, proton conduction, sensing, supercapacitors and adsorption of toxic pollutants.² In the scope of this thesis, the focus will be on heterogeneous (photo) catalysis and sensing applications of novel CTFs. In the following, we will mainly focus on the application of CTFs in heterogeneous (photo) catalysis and sensing.

2.3.1. Catalysis

CTFs with well-defined structures and distinct pores are very interesting for catalysis. As catalyst supports, the skeletons and pore walls of CTFs are the main domains for accommodating the catalytic active centers.¹³⁻¹⁵ The high surface area, porosity and tunable surface properties of CTFs provide a confined space for mass transport in the catalytic process. Due to their insolubility in solvents, CTFs are great platforms for heterogeneous catalysis by having several advantages over homogeneous catalysts such as easy separation, reusability, and potential in continuous flow systems. Furthermore, the high thermal and chemical stability of CTFs even under harsh conditions, provide a possible reactivation for cycle use.² Wide structural diversity and pre-designable platforms enable the incorporation of different catalytic systems into the CTFs skeleton to apply them as a metal-free catalyst or as support.¹⁶ These features allow targeting various types of catalytic reactions such as asymmetric catalysis, photocatalysis, electrocatalysis and metal-based catalysis.^{2, 17}

The heteroatom functionalities in CTFs (N, O, S, etc.) can effectively stabilize various metal complexes and metal nanoparticles. This offers steric restriction to confine the particles, resulting in a high catalytic performance and durability.¹⁸

In 2009, Thomas and co-workers developed Pt-based CTFs as active and efficient catalysts for methane oxidation to methanol using SO₃ in concentrated sulfuric

acid.¹⁸ The CTF support was synthesized through trimerization of 2,6-dicyanopyridine monomer using $ZnCl_2$ under ionothermal conditions (Figure 2.7). The nitrogen sites in the CTF were used to immobilize Pt precursor by pre- and post-modification methods. The resulting Pt-CTF/ $K_2[PtCl_4]$ -CTF catalyst showed very good activity with a high turnover number (TON) up to 300 even after five recycling steps.

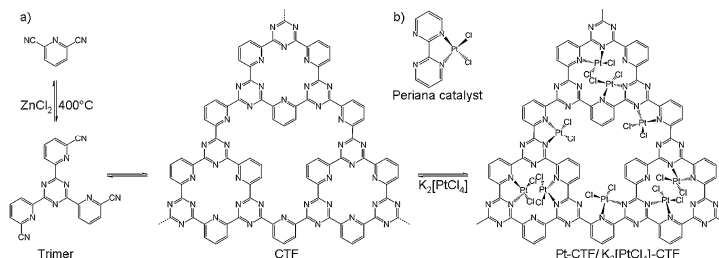


Figure 2.7. (a) Trimerization of 2,6-dicyanopyridine in molten $ZnCl_2$, conversion to a CTF and subsequent platinum coordination (Pt-CTF), (b) Periana's platinum bipyrimidine complex.¹⁸

In another study, they immobilized Pd NPs onto N-heterocyclic moieties of the CTF materials.¹⁹ The performance of the resulting Pd/CTF catalyst was compared with the commercial Pd/AC (activated carbon) for the oxidation of glycerol in a liquid phase reaction system. The Pd/CTF catalyst was found to be highly active and selective even more than the Pd/AC catalyst toward the glycerate and showed high stability up to three cycles. This was attributed to the high N content in the CTFs and great stabilization of the nanoparticles.

Gascon and co-workers showed the influence of porosity on the catalytic efficiency.²⁰ They synthesized CTFs using 2,6-pyridinedicarbonitrile and 4,4'-biphenyldicarbonitrile monomers with a ratio of 1:2. The modified CTF with an $Ir^{III}Cp^*$ complex was applied to produce hydrogen from formic acid. The presence of mesopores results in smooth mass transport during the catalytic process. Besides, the contribution of free pyridinic nitrogen sites for formic acid activation resulted in high rates of hydrogen production.

Later, the same group studied the catalytic performance of CTF composites with other porous materials. In this report, the polymerization of CTFs was performed directly on the surface of a cordierite monolith.²¹ The resulting CTF composite was

modified with two different homogeneous catalysts: (1) an Ir^{III}Cp*⁺-based catalyst for the hydrogen generation from formic acid and (2) a Pt^{II}-based catalyst for the direct activation of methane via Periana chemistry (Figure 2.8). The monolith-supported CTFs showed higher activity compared to the pristine CTFs due to the better mass transport from the liquid to the coated channel wall. Their results introduced a method to alleviate internal and external mass transport limitations. To make the recyclability of the CTF catalysts easier, a facile one-step method was reported by Gascon and co-workers to shape CTFs.²² The large size spherical CTFs were prepared by using polyimide Matrimid as a binder in a microfluidic device. The obtained spheres showed high mechanical and thermal stability with accessible CTF porosity. After anchoring with an Ir^{III}Cp*⁺ complex, the catalysts were employed for the CO₂ hydrogenation to formic acid with high activity and good recyclability.

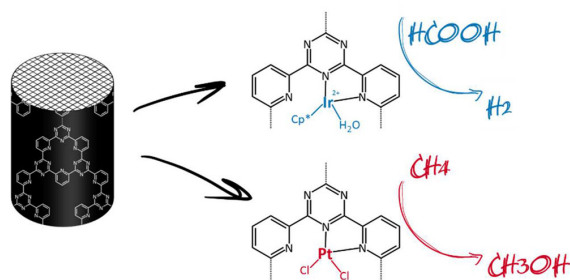


Figure 2.8. Schematic representation of the Ir@CTF and Pt@CTF catalysts.²¹

Palkovits and co-workers developed Ru/CTF catalysts for the selective aerobic oxidation of 5-hydroxymethylfurfural (HMF) to 2,5-diformylfuran.²³⁻²⁴ Various dinitrile monomers were used to synthesize porous CTFs that contain numerous N moieties, which allowed the coordination of RuCl₃·xH₂O precursor before reduction under H₂ atmosphere. This procedure allowed a narrow particle size distribution of the Ru NPs on the solid support. In comparison to other supports such as activated carbon, γ-Al₂O₃, hydrotalcite, or MgO, the Ru clusters supported on the CTF showed excellent selectivity and superior catalytic activity. The obtained results revealed the importance of N-content and the inherent polarity of the CTF catalysts besides the large surface area and porosity. The same materials were also employed as a selective catalyst for the conversion of xylitol to glycols with up to

80% yield.²⁵ The reported study showed that the increased N-content in CTF-supported Ru catalysts suppressed the decarbonylation reactions, leading to a high glycol selectivity.

Hydrogenation is one of the most important transformations in the organic synthesis which can be performed via direct hydrogenation using H₂ gas or through the transfer hydrogenation (TH) reaction. TH reaction is an attractive alternative to direct hydrogenation of organic compounds referring to the addition of hydrogen to a molecule from a non-H₂ source.²⁶ In this regard, Chen and co-workers employed CTF-1 loaded with 4 wt% Pd as a catalyst for the hydrogenation process of N-heterocycle molecules.²⁷ The Pd/CTF catalyst showed 3.6 times higher catalytic efficiency compared to the Pd/activated carbon. The higher catalytic activity was ascribed to the intensified electronic interaction between Pd and the electron-rich nitrogen sites in the CTF. In another study, an Ir^{III}Cp* complex was anchored to a CTF and applied for isomerization of allylic alcohols to saturated ketones (intramolecular TH reaction).²⁸ The catalyst showed very good activity with 98% conversion and 82% yield towards the target product and was fully recyclable.

In another example, after the deposition of Pd nanoparticles onto a CTF, the resulting material catalyzed the reduction of a wide range of nitroarenes to arylamines with up to 99% yield and high chemoselectivity (up to 99%) within 2.5 h.²⁹ The obtained results outperform the previous reports in terms of reaction time and temperature.³⁰⁻³¹

CTFs have been also applied as efficient catalytic systems to promote the steam- and oxygen-free dehydrogenation (DDH) of ethylbenzene to styrene. In this regard, a pyridine-based CTF was employed as a catalyst for the dehydrogenation of ethylbenzene to styrene.³² The CTF showed superior activity and stability compared to the benchmark systems such as K-Fe₂O₃. The high activity is due to the chemically accessible surface basicity revealed by chemical-physical analysis. In another study, due to the high stability of CTFs in acidic and basic media, bipyridine-based CTF was modified with Ir and Rh half-sandwich complexes as active heterogeneous catalysts for the aqueous-phase hydrogenation of carbonyl compounds. The highest turnover frequency (TOF) was obtained at optimized acidic medium reaction conditions (pH 3.5), in which most of the MOFs and other transition metal-based oxide catalysts are unstable.³³

Another interesting feature of CTFs is their high affinity towards CO₂ which makes them outstanding candidates in the capture and conversion of CO₂.³⁴ For example, the di(4-cyanophenyl)ethyne-based CTF (CTF-DCE) reported by Zhang and co-workers can uptake 4.3 mmol g⁻¹ CO₂ at 273 K and 1 bar.³⁵ The deposition of Ag nanoparticles into the obtained CTF (Ag@CTF) catalyzed the direct carboxylation of terminal alkynes using CO₂. The applied mild reaction conditions and good reusability are promising for their application in synthetic chemistry.

Later, Yoon and co-workers utilized the N-heterocyclic carbene-based CTFs as support for Ir complexes which were used in the conversion of CO₂ to formate under mild conditions and in the presence of triethylamine as the base.³⁶ The obtained catalyst showed great activity with TOF up to 16 000 h⁻¹ and TON up to 24 300 h⁻¹, which is one of the highest reported values to date.

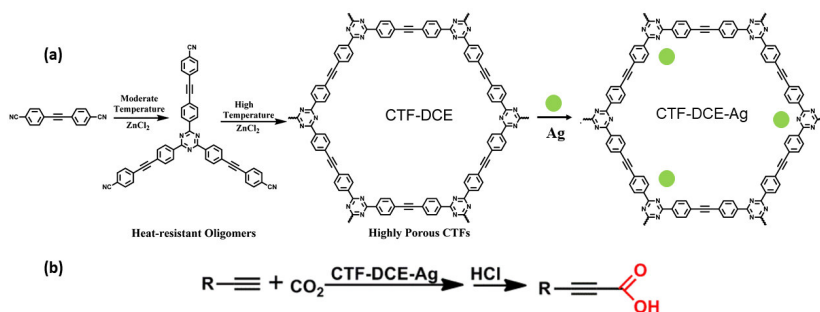


Figure 2.9. (a) Schematic representation of the CTF-DCE-Ag catalyst, (b) Direct carboxylation of terminal alkynes with CO₂.³⁵

2.3.2. Photocatalysis

High nitrogen content, tunable functionality, thermochemical stability, robust conjugated structure and visible light absorption features make CTFs attractive candidates in photocatalytic reactions. Theoretical calculation results showed that CTFs have suitable bandgaps for visible light adsorption. For instance, CTF-1 with intrinsic donor–acceptor properties has a bandgap of 2.42 eV. The semiconductor behavior of CTFs is approved by the study on the density of states of triazine-based frameworks using first-principles calculations. Additionally, a vast number of functional groups and heteroatoms can be incorporated into the backbone of CTFs

to adjust photophysical properties and donor or acceptor units.³⁷ Accordingly, CTFs have shown great potential for several photocatalytic reactions such as water splitting, pollutants degradation, organic transformation, CO₂ reduction and many more. However, due to the high carbonization degree of CTFs synthesized through the ionothermal method under harsh synthetic conditions (>400 °C), the conjugated structures and the semiconductor properties of CTFs can be destroyed resulting in low photocatalytic efficiency. Hence, it is highly important to make CTFs under milder conditions (reduced temperatures) to prevent carbonization and improve photocatalytic activity.³⁸ In this regard, Lotsch and co-workers reported the synthesis of phenyl-triazine oligomers through an ionothermal method at lower temperatures (300–350 °C) and higher reaction time (>150 hours).³⁸ The photocatalytic efficiency of the resulting oligomers with Pt as a cocatalyst was improved compared to the archetypal CTF-1 and showed hydrogen evolution rates of 1076 μmol h⁻¹ g⁻¹. The authors suggested that the absence of activity in CTF-1 is due to the incipient carbonization, where light absorption by carbon limits photon absorption by the framework, consequently reducing the photocatalytic activity. This study revealed the influence of the synthesis procedure on the photophysical properties of CTFs and subsequently on the photocatalytic performance.

In another study, Thomas and co-workers combined the trifluoromethanesulfonic (TFMS) acid catalysis and ionothermal methods.³⁹ This method combines the initial synthesis of CTF in Brønsted and Lewis acidic media at ambient temperatures followed by the transformation of this amorphous pre-CTF into an ordered CTF in molten ZnCl₂ (Figure 2.10a). The effect of reaction time was investigated, and samples were obtained after 2.5-30 min. Figure 2.10b displays the photographs and XRD patterns of all materials. The color of the CTFs is changing from light yellow for pre-CTF and CTF-1-2.5 min to red-brown for CTF-1-15 min, confirming that extended conjugated frameworks are formed after short reaction times. However, the darkening after only 20 min shows that partial carbonization has occurred. PXRD also confirms the formation of more extended two-dimensional frameworks over time, as the intensity of the peak at 7.51 increases visibly with reaction time. Also, while the long-time reaction (40 h) yields a material with a high surface area of 910 m² g⁻¹, no detectable surface area was obtained for all CTF-1-X with X = 2.5-30 min, which is due to the lower polymerization degree and structural order of these materials. The obtained CTFs were loaded with Pt and

used for hydrogen evolution under visible light irradiation (Figure 2.10c). The maximum activity was achieved for the CTF-1-10 material, showing an average hydrogen evolution rate of $1072 \mu\text{mol h}^{-1} \text{g}^{-1}$. However, with increasing the reaction time in molten salt, the hydrogen evolution rate decreased significantly ($138 \mu\text{mol h}^{-1} \text{g}^{-1}$ for CTF-1-30).

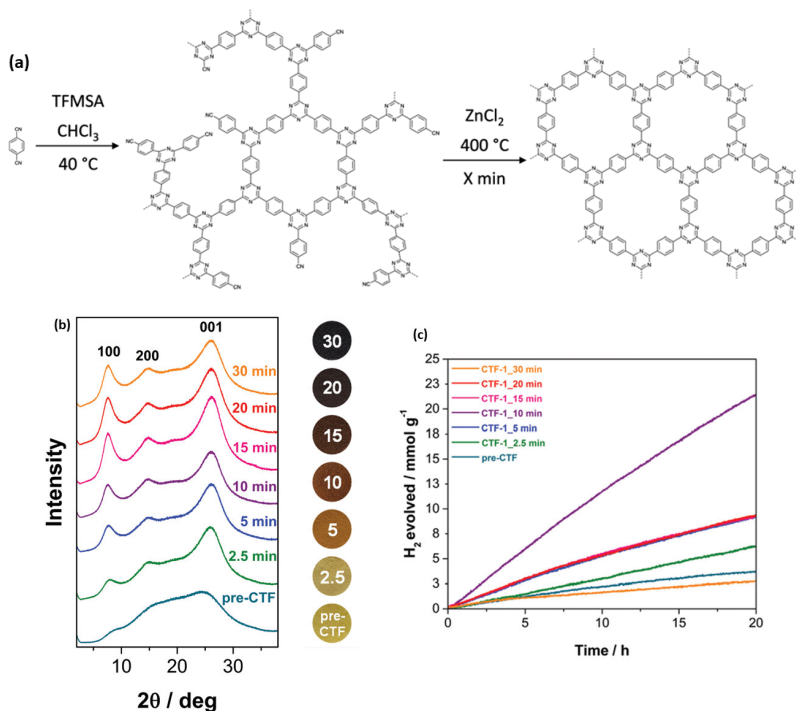


Figure 2.10. (a) Two-step synthesis of CTF-1-X materials, (b) Powder XRD patterns and photographs of pre-CTF and CTF-1-X materials with $X = 2.5\text{--}30$ min, (c) Photocatalytic H_2 evolution of pre-CTF and CTF-1-X materials under visible light irradiation.³⁹

In pursuit of alternative methods for the ZnCl_2 method to synthesize CTFs under mild conditions to make photoactive CTFs, Wu and co-workers synthesized CTF-T1 using the Brønsted acid method. After the dispersion of Pt nanoparticles, CTF-T1 exhibited comparable photocatalytic H_2 evolution activity compared to $\text{g-C}_3\text{N}_4$ (graphitic carbon nitride) under visible light irradiation (wavelength = 420 nm).⁴⁰ By

applying the same method, Janiak and co-workers synthesized PCTF-8 using a tetra(4-cyanophenyl)ethylene monomer which showed high thermal stability (>400 °C) and a high photoluminescence performance.⁴¹ The PCTF-8 photocatalyst exhibited a moderate H₂ evolution value of 2370 μmol g⁻¹ due to the lack of long-range order.

MoS₂ is a well-known photocatalyst, especially for H₂ evolution. To enhance the photoactivity, MoS₂ quantum dots (QDs)-modified CTF (MoS₂/CTF) composites were synthesized through an *in-situ* photo-deposition method. The microporous nature of CTF is suitable for confining the MoS₂ to produce quantum dots and increase stability. The interactions between the MoS₂ and CTFs promoted interfacial charge transfer and separation. Accordingly, the obtained H₂ evolution rates were higher than the MoS₂/g-C₃N₄ materials.³⁴

Heteroatom doping can adjust the photocatalytic activity of a photoactive material by providing more active sites and changing the charge distribution of the system. As reported, a sulfur-doped CTF exhibited a higher hydrogen evolution performance from water up to 2000 μmol h⁻¹ g⁻¹ under visible light irradiation, which is much higher than that of pristine CTFs (without sulfur) and g-C₃N₄. The high photocatalytic performance of CTF-S_x (X = 5, 10, 20, 30 wt%) is attributed to the sulfur-doping in the frameworks, which results in enhanced absorption ability of visible light, reduced recombination of free charge carriers and rapid electron–holes separation and transportation.⁴² Subsequently, Wu and co-workers utilized a chemical doping strategy to introduce phosphorus heteroatom into the framework of CTF-1. In the resulting P-doped CTF, the optical and electronic properties are enhanced by promoting photoinduced electron-hole pairs generation, separation and migration. Consequently, PCTF-1 showed a higher H₂ evolution rate compared to the pristine CTF-1 and P-doped g-C₃N₄.⁴³

As an elegant example for a greener oxidation pathway, a thiophene-based CTF has been developed as a metal-free and photoactive catalyst for the selective aerobic oxidation of alcohols.⁴⁴ As shown in Figure 2.11a, through the cyclization polymerization of 2,5-dicyanothiophene (DCT) linker under TfOH vapor, a thiophene-containing CTF (CTF-Th) was directly synthesized onto mesoporous silica SBA-15, providing the photoactive CTF-Th@SBA-15 catalyst. The presence of the thiophene units into the CTF provides a low HOMO level that is desirable for a great photooxidation potential. Furthermore, applying mesoporous silica as the

support for CTF could increase the active area in the photocatalytic reaction. The CTF-Th@SBA-15 catalyst showed a high conversion of benzyl alcohol (99%) towards benzaldehyde under blue light irradiation and oxygen at room temperature. After 4 h, benzaldehyde was obtained as the sole product (99% selectivity) which is comparable with the reported metal and non-metal catalytic systems. A series of control experiments were done to obtain insights into the reaction mechanism. More specifically, the addition of benzoquinone (superoxide scavenger), ammonium oxalate (hole scavenger) and NaN_3 (singlet oxygen scavenger) decreased the conversion of benzyl alcohol. These observations confirmed that the oxidation is associated with a combined action of superoxide ($\cdot\text{O}_2^-$) and singlet oxygen ($^1\text{O}_2$) which are produced under light irradiation. The proposed reaction mechanism (Figure 2.11b) is based on the molecular oxygen activation into its activated forms ($\cdot\text{O}_2^-$ and $^1\text{O}_2$) followed by the activation of benzyl alcohol and the formation of benzaldehyde.

Moreover, Zhang and co-workers employed the same process to synthesize CTFs with a template of SiO_2 , and the resulting CTFs presented an outstanding performance in the photoreduction of 4-nitrophenol to 4-aminophenol.⁴⁵

In 2018, Wang *et al.* reported a very promising new strategy to synthesize CTFs via the amidines polycondensation with a wide variety of monomers at low temperatures. The conjugated structure and configuration of CTFs prepared according to this approach can be preserved perfectly. The CTFs synthesized with this strategy were scaled up to gram quantities. Based on the reaction between the aldehyde and amidine, the final CTFs were found to be promising photocatalysts for sacrificial photocatalytic hydrogen evolution. The CTF-HUST-2 showed excellent hydrogen evolution performance up to $2647 \mu\text{mol h}^{-1} \text{g}^{-1}$, which was the highest reported value for CTFs at that time.¹⁰

The ordered crystalline structure can boost the efficient charge transfer and enhance photocatalytic activity. In this regard, Tan and co-workers applied the amidines polycondensation method and developed an *in-situ* oxidation approach to construct crystalline CTFs through the oxidation of alcohol monomers followed by reaction with amidine linkers.¹¹ The resulting CTFs with a highly crystalline structure showed a photocatalytic hydrogen evolution performance of $5100 \mu\text{mol h}^{-1} \text{g}^{-1}$ and even after 5 cycles, the average of the hydrogen evolution activity was

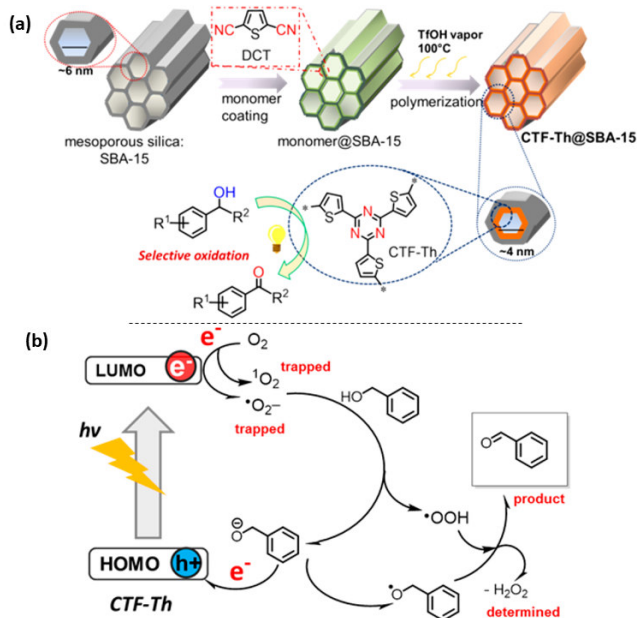


Figure 2.11. (a) Schematic representation of thiophene-based CTF formation pathway on SBA-15, (b) Proposed reaction mechanism for the selective oxidation of benzyl alcohol using CTF-Th@SBA-15 photocatalyst.⁴⁴

3880 $\mu\text{mol h}^{-1} \text{g}^{-1}$, which is 2.6 times higher than that of the amorphous CTFs. This method is very simple and convenient which offers a promising route for the large-scale industrial production of crystalline CTFs.

Using the amidines polycondensation method, the photocatalytic performance of catalysts can be boosted by enhancing charge transfer/separation. More specifically, the donors can be easily tuned via substituting various heteroatoms in a series of donor–acceptor CTFs. Therefore, optimal energy levels and improved electron transfer and charge separation ability can be obtained. Using the same acceptor triazine rings in a series of CTFs, the donor ability was tailored by changing the heteroatoms (N, S, and O) in a fluorene-like structure as demonstrated in Figure 2.12.⁴⁶ The results showed that carbazole has the strongest donor ability in this work and the resulting CTF-N presented the highest hydrogen evolution activity of 538 $\mu\text{mol h}^{-1}$ which was the highest reported value of porous organic polymers (POPs) at that time.

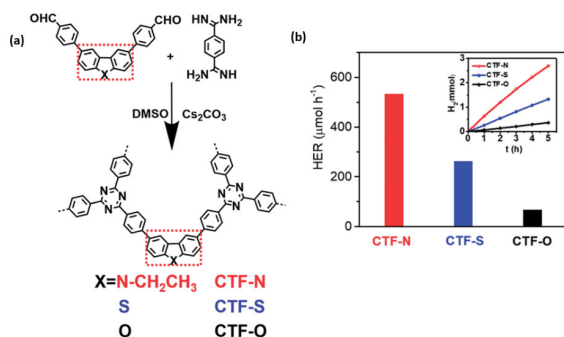


Figure 2.12. (a) Schematic representation of heteroatom-containing CTFs, (b) Hydrogen evolution performance of CTFs with the time course (inset).⁴⁶

The photocatalytic oxygen evolution is another half-reaction of water splitting and is more difficult than the hydrogen evolution. Only once the HOMO value is higher than 1.23 eV, the oxidation of water to O₂ could be possible dynamically. Wang *et al.* conducted the oxygen evolution reaction using CTFs loaded with Co as the co-catalyst and this work demonstrated the great potential of CTFs in overall water splitting.⁴⁷ Tang and co-workers developed ordered CTFs through a microwave-assisted synthesis method and the target CTFs exhibited an oxygen evolution rate of 140 μmol h⁻¹ g⁻¹ which was 20 times higher than that of the g-C₃N₄.⁴⁸

2.3.3. Luminescence and sensing applications

The inherent porous network of CTFs makes them interesting for other applications. CTFs can be applied as sensors based on their fluorescence properties.⁴⁹ CTFs are sensitive to nitroaromatic analytes and heavy metal ions (Hg²⁺) because their coordination to the nitrogen sites quenches the fluorescence intensity of CTFs.⁴⁹ A highly photoluminescent (PL) porous CTF (PCTF-8) was synthesized from the tetra(4-cyanophenyl)ethylene monomer by using trifluoromethanesulfonic acid as the catalyst at low temperature (Figure 2.13a).⁴¹ The photoluminescence properties, as well as the sensing behavior of PCTF-8, was examined towards nitroaromatics. In the presence of 2,4,6-trinitrophenol (TNP), the fluorescence emission intensity of the PCTF-8 material was quenched by ca. 71% (Figure 2.13b).⁴¹

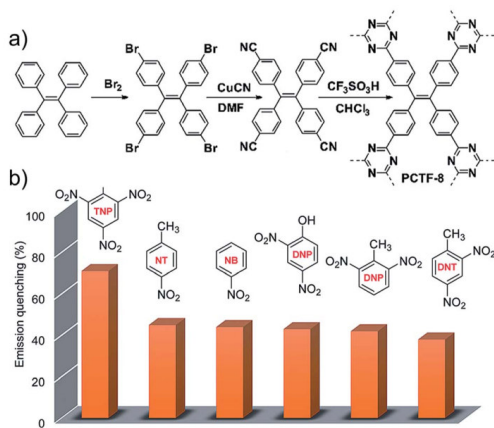


Figure 2.13. (a) Synthesis procedure to make PCTF-8, (b) the fluorescence quenching performance of PCTF-8.⁴¹

Fan and co-workers showed that the layered structures of CTF-1 can be rapidly exfoliated and cut into N-doped carbon quantum dots (CQDs).⁵⁰ The obtained CTFQDs were utilized as an efficient PL probe for Hg^{2+} sensing due to their unique chemical structure and luminescent properties. Experiments and density functional theory (DFT) calculations confirmed that the fluorescence of the resulting CTFQDs mainly originate from the intrinsic state emission induced by localized $\pi-\pi^*$ transitions and the contribution of the defect state emission. In another report, a CTF with a tetraphenylthiophene (TTPT) backbone was synthesized by AlCl_3 -catalyzed Friedel–Crafts reaction of 2,4,6-trichloro-1,3,5-triazine and tetraphenylthiophene in dichloromethane. The surface area of the TTPT-CTF material was $315.5 \text{ m}^2 \text{ g}^{-1}$. Taking advantage of its large surface area and strong fluorescence, TTPT-CTF showed very fast responses and high sensitivity towards o-nitrophenol with the limit of detection (LOD) around $2.18 \times 10 \text{ mol L}^{-1}$. The remarkable fluorescence response of TTPT-CTF is due to the rigid micropore environment and π -conjugated skeleton of the material.⁵¹

Primary aromatic amines, as a class of persistent and highly toxic organic pollutants, are a tremendous threat to human health and the environment. In this context, a fluorescent CTF (F-CTF-3) was synthesized by the condensation reaction between the 4,4'-(benzo[c][1,2,5]thiadiazole-4,7-diyl)dibenzaldehyde

(BTDD) monomer and phenamidine hydrochloride (PAHC) (Figure 2.14a). The F-CTF-3 exhibited high sensitivity and selectivity for primary aromatic amines detection through fluorescence quenching. F-CTF-3 showed low detection limits of 11.7 and 1.47 nM towards phenylamine (PA) and p-phenylenediamine (PDA), respectively. The high sensitivity of F-CTF-3 towards PAA detection could be attributed to the static quenching process and formation of a ground-state fluorescence-quenched complex via hydrogen bonding interactions between F-CTF-3 and PAAs (Figure 2.14b).⁵²

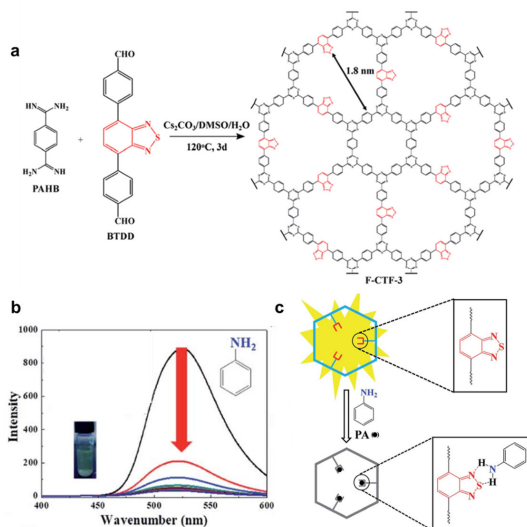


Figure 2.14. (a) Synthesis route to make F-CTF-3, (b) The emission spectra of F-CTF-3 dispersed in water upon the addition of PA, and (c) Representation of the mechanism for the selective fluorescence response of F-CTF-3 to PA.

2.4. Objectives

Based on the above discussion, we can conclude that CTFs and COFs represent a new field of rapidly growing research in recent years. Still, these materials are in their infancy and there is countless unexplored potential. The unique properties of these materials have made them very promising for various applications particularly from the perspective of green chemistry.

One of the main objectives targeted in this thesis is to apply different synthesis strategies to design novel CTFs. Detailed attention is given to the characterization of these materials and their structural properties as these are critical factors in recognizing the role of chemical functionalities for the corresponding application. Accordingly, we applied ionothermal synthesis to make CTFs with various nitrogen functionalities. This strategy provides materials with high surface areas which is beneficial for post-synthesis modification with active metal sites for heterogeneous catalysis. Moreover, the presence of defective nitrogen functionalities boosts the catalytic activity of the final material. Different types of defects can play an important role in the functional properties of materials. The defects in materials may open up a new concept for modulating structures and properties in some cases and providing materials with enhanced performances. For example, defects have been introduced into MOFs structures to obtain materials with new functionalities and properties (e.g., ion motion, active sites for catalysis, photoluminescence, sensing and many other applications). Therefore, it seems that rationally introducing defects into COFs/CTFs may be a good strategy for broadening their functionalities and applications. Different strategies have been employed to create defects such as the monomer-truncation strategy to create defects for functionalization of COFs, precise control over the reaction solvent and conditions to obtain defective COFs and carbonization to generate different nitrogen species in the framework.

Besides, the defects in materials have an impact on various properties such as increased surface areas and the creation mesoporosity next to the expected microporosity. In addition, different nitrogen species (pyridinic, pyrrolic, quaternary, and oxidized N-O) can be generated under certain reaction conditions, a typical example is the harsh ionothermal synthesis route that creates a lot of defects, oxidized species and carbonization. Furthermore, these defects can narrow the band gap and facilitate the separation of photogenerated charge carriers, thus promoting photocatalytic activity. Based on reports, defects can have positive effects both on the adsorption and photocatalytic properties. With respect to adsorption, it has been demonstrated that various defected nitrogen sites display a high affinity to organic pollutants which results in enhanced removal efficiency. Regarding photocatalysis, defects also play a vital role in accelerating the

photoinduced charge carrier mobility through perturbation of the conformation. Accordingly, the synergistic effect of CTFs as catalyst support is investigated in detail. Although CTFs prepared under ionothermal conditions have unique advantages in heterogeneous catalysis, the harsh synthesis procedure can limit their application in green chemistry. Therefore, another synthesis approach was targeted in which CTFs are designed under mild reaction conditions. The CTFs prepared in mild conditions can retain most of their photophysical properties. Therefore, we applied the mild synthesis strategy to make metal-free photoactive catalysts. Besides, we present a novel application of CTFs as photoluminescent materials. The highly crystalline CTFs with bipyridine docking sites allow an easy and controlled grafting of lanthanide complexes, which open up a new avenue for designing LnCTF-based ratiometric luminescent thermometers.

2.5. References:

1. Geng, K. Y.; He, T.; Liu, R. Y.; Dalapati, S.; Tan, K. T.; Li, Z. P.; Tao, S. S.; Gong, Y. F.; Jiang, Q. H.; Jiang, D. L., Covalent Organic Frameworks: Design, Synthesis, and Functions. *Chem Rev* **2020**, *120* (16), 8814-8933.
2. Liu, M. Y.; Guo, L. P.; Jin, S. B.; Tan, B. E., Covalent triazine frameworks: synthesis and applications. *J Mater Chem A* **2019**, *7* (10), 5153-5172.
3. Kuhn, P.; Antonietti, M.; Thomas, A., Porous, covalent triazine-based frameworks prepared by ionothermal synthesis. *Angew Chem Int Edit* **2008**, *47* (18), 3450-3453.
4. Kuhn, P.; Thomas, A.; Antonietti, M., Toward Tailorable Porous Organic Polymer Networks: A High-Temperature Dynamic Polymerization Scheme Based on Aromatic Nitriles. *Macromolecules* **2009**, *42* (1), 319-326.
5. Zhang, W.; Li, C.; Yuan, Y. P.; Qiu, L. G.; Xie, A. J.; Shen, Y. H.; Zhu, J. F., Highly energy- and time-efficient synthesis of porous triazine-based framework: microwave-enhanced ionothermal polymerization and hydrogen uptake. *J Mater Chem* **2010**, *20* (31), 6413-6415.
6. Ren, S. J.; Bojdys, M. J.; Dawson, R.; Laybourn, A.; Khimyak, Y. Z.; Adams, D. J.; Cooper, A. I., Porous, Fluorescent, Covalent Triazine-Based Frameworks Via Room-Temperature and Microwave-Assisted Synthesis. *Adv Mater* **2012**, *24* (17), 2357-2361.
7. Zhu, X.; Tian, C. C.; Mahurin, S. M.; Chai, S. H.; Wang, C. M.; Brown, S.; Veith, G. M.; Luo, H. M.; Liu, H. L.; Dai, S., A Superacid-Catalyzed Synthesis of Porous Membranes Based on Triazine Frameworks for CO₂ Separation. *Journal of the American Chemical Society* **2012**, *134* (25), 10478-10484.
8. Je, S. H.; Kim, H. J.; Kim, J.; Choi, J. W.; Coskun, A., Perfluoroaryl-Elemental Sulfur SNAr Chemistry in Covalent Triazine Frameworks with High Sulfur Contents for Lithium-Sulfur Batteries. *Adv Funct Mater* **2017**, *27* (47).
9. Yu, S. Y.; Mahmood, J.; Noh, H. J.; Seo, J. M.; Jung, S. M.; Shin, S. H.; Im, Y. K.; Jeon, I. Y.; Baek, J. B., Direct Synthesis of a Covalent Triazine-Based Framework from Aromatic Amides. *Angew Chem Int Edit* **2018**, *57* (28), 8438-8442.
10. Wang, K. W.; Yang, L. M.; Wang, X.; Guo, L. P.; Cheng, G.; Zhang, C.; Jin, S. B.; Tan, B.; Cooper, A., Covalent Triazine Frameworks via a Low-Temperature Polycondensation Approach. *Angew Chem Int Edit* **2017**, *56* (45), 14149-14153.

11. Liu, M. Y.; Huang, Q.; Wang, S. L.; Li, Z. Y.; Li, B. Y.; Jin, S. B.; Tan, B., Crystalline Covalent Triazine Frameworks by InSitu Oxidation of Alcohols to Aldehyde Monomers. *Angew Chem Int Edit* **2018**, *57* (37), 11968-11972.
12. Liu, M. Y.; Jiang, K.; Ding, X.; Wang, S. L.; Zhang, C. X.; Liu, J.; Zhan, Z.; Cheng, G.; Li, B. Y.; Chen, H.; Jin, S. B.; Tan, B., Controlling Monomer Feeding Rate to Achieve Highly Crystalline Covalent Triazine Frameworks. *Adv Mater* **2019**, *31* (19).
13. Abednatanzi, S.; Derakhshandeh, P. G.; Tack, P.; Muniz-Miranda, F.; Liu, Y. Y.; Everaert, J.; Meledina, M.; Vanden Bussche, F.; Vincze, L.; Stevens, C. V.; Van Speybroeck, V.; Vrielinck, H.; Callens, F.; Leus, K.; Van Der Voort, P., Elucidating the promotional effect of a covalent triazine framework in aerobic oxidation. *Appl Catal B-Environ* **2020**, *269*.
14. Jena, H. S.; Krishnaraj, C.; Wang, G. B.; Leus, K.; Schmidt, J.; Chaoui, N.; Van der Voort, P., Acetylacetone Covalent Triazine Framework: An Efficient Carbon Capture and Storage Material and a Highly Stable Heterogeneous Catalyst. *Chem Mater* **2018**, *30* (12), 4102-4111.
15. Tahir, N.; Muniz-Miranda, F.; Everaert, J.; Tack, P.; Heugebaert, T.; Leus, K.; Vincze, L.; Stevens, C. V.; Van Speybroeck, V.; Van der Voort, P., Immobilization of Ir(I) complex on covalent triazine frameworks for C-H borylation reactions: A combined experimental and computational study. *J Catal* **2019**, *371*, 135-143.
16. Abednatanzi, S.; Derakhshandeh, P. G.; Leus, K.; Vrielinck, H.; Callens, F.; Schmidt, J.; Savateev, A.; Van der Voort, P., Metal-free activation of molecular oxygen by covalent triazine frameworks for selective aerobic oxidation. *Sci Adv* **2020**, *6* (14).
17. Krishnaraj, C.; Jena, H. S.; Leus, K.; Van der Voort, P., Covalent triazine frameworks - a sustainable perspective. *Green Chem* **2020**, *22* (4), 1038-1071.
18. Palkovits, R.; Antonietti, M.; Kuhn, P.; Thomas, A.; Schuth, F., Solid Catalysts for the Selective Low-Temperature Oxidation of Methane to Methanol. *Angew Chem Int Edit* **2009**, *48* (37), 6909-6912.
19. Chan-Thaw, C. E.; Villa, A.; Katekomol, P.; Su, D. S.; Thomas, A.; Prati, L., Covalent Triazine Framework as Catalytic Support for Liquid Phase Reaction. *Nano Lett* **2010**, *10* (2), 537-541.
20. Bavykina, A. V.; Goesten, M. G.; Kapteijn, F.; Makkee, M.; Gascon, J., Efficient production of hydrogen from formic acid using a Covalent Triazine Framework supported molecular catalyst. *ChemSuschem* **2015**, *8* (5), 809-812.
21. Bavykina, A. V.; Olivos-Suarez, A. I.; Osadchii, D.; Valecha, R.; Franz, R.; Makkee, M.; Kapteijn, F.; Gascon, J., Facile Method for the Preparation of Covalent Triazine Framework coated Monoliths as Catalyst Support: Applications in C1 Catalysis. *Acs Appl Mater Inter* **2017**, *9* (31), 26060-26065.
22. Bavykina, A. V.; Rozhko, E.; Goesten, M. G.; Wezendonk, T.; Seoane, B.; Kapteijn, F.; Makkee, M.; Gascon, J., Shaping Covalent Triazine Frameworks for the Hydrogenation of Carbon Dioxide to Formic Acid. *Chemcatchem* **2016**, *8* (13), 2217-2221.
23. Artz, J.; Palkovits, R., Base-Free Aqueous-Phase Oxidation of 5-Hydroxymethylfurfural over Ruthenium Catalysts Supported on Covalent Triazine Frameworks. *ChemSuschem* **2015**, *8* (22), 3832-3838.
24. Artz, J.; Mallmann, S.; Palkovits, R., Selective Aerobic Oxidation of HMF to 2,5-Diformylfuran on Covalent Triazine Frameworks-Supported Ru Catalysts. *ChemSuschem* **2015**, *8* (4), 672-679.
25. Beine, A. K.; Kruger, A. J. D.; Artz, J.; Weidenthaler, C.; Glotzbach, C.; Hausoul, P. J. C.; Palkovits, R., Selective production of glycols from xylitol over Ru on covalent triazine frameworks - suppressing decarbonylation reactions. *Green Chem* **2018**, *20* (6), 1316-1322.
26. Wang, D.; Astruc, D., The Golden Age of Transfer Hydrogenation. *Chem Rev* **2015**, *115* (13), 6621-6686.
27. He, T.; Liu, L.; Wu, G. T.; Chen, P., Covalent triazine framework-supported palladium nanoparticles for catalytic hydrogenation of N-heterocycles. *J Mater Chem A* **2015**, *3* (31), 16235-16241.

28. Bavykina, A. V.; Mautscke, H. H.; Makkee, M.; Kapteijn, F.; Gascon, J.; Xamena, F. X. L. I., Base free transfer hydrogenation using a covalent triazine framework based catalyst. *Crystengcomm* **2017**, *19* (29), 4166-4170.
29. Li, J.; Zhang, L. H.; Liu, X. T.; Shang, N. Z.; Gao, S. T.; Feng, C.; Wang, C.; Wang, Z., Pd nanoparticles supported on a covalent triazine-based framework material: an efficient and highly chemoselective catalyst for the reduction of nitroarenes. *New J Chem* **2018**, *42* (12), 9684-9689.
30. Jagadeesh, R. V.; Natte, K.; Junge, H.; Beller, M., Nitrogen-Doped Graphene-Activated Iron-Oxide-Based Nanocatalysts for Selective Transfer Hydrogenation of Nitroarenes. *Acs Catal* **2015**, *5* (3), 1526-1529.
31. Datta, K. J.; Rathi, A. K.; Gawande, M. B.; Ranc, V.; Zoppellaro, G.; Varma, R. S.; Zboril, R., Base-Free Transfer Hydrogenation of Nitroarenes Catalyzed by Micro-Mesoporous Iron Oxide. *Chemcatchem* **2016**, *8* (14), 2351-2355.
32. Tuci, G.; Pilaski, M.; Ba, H.; Rossin, A.; Luconi, L.; Caporali, S.; Pham-Huu, C.; Palkovits, R.; Giambastiani, G., Unraveling Surface Basicity and Bulk Morphology Relationship on Covalent Triazine Frameworks with Unique Catalytic and Gas Adsorption Properties. *Adv Funct Mater* **2017**, *27* (7).
33. Sudakar, P.; Gunasekar, G. H.; Baek, I. H.; Yoon, S., Recyclable and efficient heterogenized Rh and Ir catalysts for the transfer hydrogenation of carbonyl compounds in aqueous medium. *Green Chem* **2016**, *18* (24), 6456-6461.
34. Buyukcakir, O.; Je, S. H.; Talapaneni, S. N.; Kim, D.; Coskun, A., Charged Covalent Triazine Frameworks for CO₂ Capture and Conversion. *Acs Appl Mater Inter* **2017**, *9* (8), 7209-7216.
35. Dang, Q. Q.; Liu, C. Y.; Wang, X. M.; Zhang, X. M., Novel Covalent Triazine Framework for High-Performance CO₂ Capture and Alkyne Carboxylation Reaction. *Acs Appl Mater Inter* **2018**, *10* (33), 27972-27978.
36. Gunasekar, G. H.; Park, K.; Ganesan, V.; Lee, K.; Kim, N. K.; Jung, K. D.; Yoon, S., A Covalent Triazine Framework, Functionalized with Ir/N-Heterocyclic Carbene Sites, for the Efficient Hydrogenation of CO₂ to Formate. *Chem Mater* **2017**, *29* (16), 6740-6748.
37. Jiang, X.; Wang, P.; Zhao, J. J., 2D covalent triazine framework: a new class of organic photocatalyst for water splitting. *J Mater Chem A* **2015**, *3* (15), 7750-7758.
38. Schwinghammer, K.; Hug, S.; Mesch, M. B.; Senker, J.; Lotsch, B. V., Phenyl-triazine oligomers for light-driven hydrogen evolution. *Energ Environ Sci* **2015**, *8* (11), 3345-3353.
39. Kuecken, S.; Acharjya, A.; Zhi, L. J.; Schwarze, M.; Schomacker, R.; Thomas, A., Fast tuning of covalent triazine frameworks for photocatalytic hydrogen evolution. *Chemical Communications* **2017**, *53* (43), 5854-5857.
40. Bi, J. H.; Fang, W.; Li, L. Y.; Wang, J. Y.; Liang, S. J.; He, Y. H.; Liu, M. H.; Wu, L., Covalent Triazine-Based Frameworks as Visible Light Photocatalysts for the Splitting of Water. *Macromol Rapid Comm* **2015**, *36* (20), 1799-1805.
41. Bhunia, A.; Esquivel, D.; Dey, S.; Fernandez-Teran, R.; Goto, Y.; Inagaki, S.; Van der Voort, P.; Janiak, C., A photoluminescent covalent triazine framework: CO₂ adsorption, light-driven hydrogen evolution and sensing of nitroaromatics. *J Mater Chem A* **2016**, *4* (35), 13450-13457.
42. Li, L. Y.; Fang, W.; Zhang, P.; Bi, J. H.; He, Y. H.; Wang, J. Y.; Su, W. Y., Sulfur-doped covalent triazine-based frameworks for enhanced photocatalytic hydrogen evolution from water under visible light. *J Mater Chem A* **2016**, *4* (32), 12402-12406.
43. Cheng, Z.; Fang, W.; Zhao, T. S.; Fang, S. Q.; Bi, J. H.; Liang, S. J.; Li, L. Y.; Yu, Y.; Wu, L., Efficient Visible-Light-Driven Photocatalytic Hydrogen Evolution on Phosphorus-Doped Covalent Triazine-Based Frameworks. *Acs Appl Mater Inter* **2018**, *10* (48), 41415-41421.
44. Huang, W.; Ma, B. C.; Lu, H.; Li, R.; Wang, L.; Landfester, K.; Zhang, K. A. I., Visible-Light-Promoted Selective Oxidation of Alcohols Using a Covalent Triazine Framework. *Acs Catal* **2017**, *7* (8), 5438-5442.

45. Huang, W.; Wang, Z. J.; Ma, B. C.; Ghasimi, S.; Gehrig, D.; Laquai, F.; Landfester, K.; Zhang, K. A. I., Hollow nanoporous covalent triazine frameworks via acid vapor-assisted solid phase synthesis for enhanced visible light photoactivity. *J Mater Chem A* **2016**, *4* (20), 7555-7559.
46. Guo, L. P.; Niu, Y. L.; Xu, H. T.; Li, Q. W.; Razzaque, S.; Huang, Q.; Jin, S. B.; Tan, B., Engineering heteroatoms with atomic precision in donor- acceptor covalent triazine frameworks to boost photocatalytic hydrogen production. *J Mater Chem A* **2018**, *6* (40), 19775-19781.
47. Lan, Z. A.; Fang, Y. X.; Zhang, Y. F.; Wang, X. C., Photocatalytic Oxygen Evolution from Functional Triazine-Based Polymers with Tunable Band Structures. *Angew Chem Int Edit* **2018**, *57* (2), 470-474.
48. Xie, J. J.; Shevlin, S. A.; Ruan, Q. S.; Moniz, S. J. A.; Liu, Y. R.; Liu, X.; Li, Y. M.; Lau, C. C.; Guo, Z. X.; Tang, J. W., Efficient visible light-driven water oxidation and proton reduction by an ordered covalent triazine-based framework. *Energ Environ Sci* **2018**, *11* (6), 1617-1624.
49. Wang, X. Y.; Zhang, C.; Zhao, Y.; Ren, S. J.; Jiang, J. X., Synthetic Control and Multifunctional Properties of Fluorescent Covalent Triazine-Based Frameworks. *Macromol Rapid Comm* **2016**, *37* (4), 323-329.
50. Zhu, Y. Z.; Qiao, M.; Peng, W. C.; Li, Y.; Zhang, G. L.; Zhang, F. B.; Li, Y. F.; Fan, X. B., Rapid exfoliation of layered covalent triazine-based frameworks into N-doped quantum dots for the selective detection of Hg²⁺ ions. *J Mater Chem A* **2017**, *5* (19), 9272-9278.
51. Geng, T. M.; Zhang, W. Y.; Zhu, Z. M.; Chen, G. F.; Ma, L. Z.; Ye, S. N.; Niu, Q. Y., A covalent triazine-based framework from tetraphenylthiophene and 2,4,6-trichloro-1,3,5-triazine motifs for sensing o-nitrophenol and effective I-2 uptake. *Polym Chem-Uk* **2018**, *9* (6), 777-784.
52. Tang, Y. Z.; Huang, H. L.; Peng, B.; Chang, Y. J.; Li, Y.; Zhong, C. L., A thiadiazole-based covalent triazine framework nanosheet for highly selective and sensitive primary aromatic amine detection among various amines. *J Mater Chem A* **2020**, *8* (32), 16542-16550.

Abstract

The heterogenization of an iridium(III) complex is accomplished via the modification of a nanoporous gallium-based metal-organic framework (MOF), denoted as COMOC-4. The introduction of the iridium complex was performed successfully through two different strategies (post- and pre-functionalization). The obtained iridium-based MOF materials were compared in terms of the iridium loading, specific surface area, and crystallinity. In this case, the pre-functionalization approach was a powerful synthetic way which led to a higher iridium loading and surface area while preserving the formation of the desired MOF topology. The Ir(III)Cp*Cl@COMOC-4 material exhibits a good catalytic performance in the oxidation of benzyl alcohol using molecular oxygen as a clean oxidant. Furthermore, the stability and reusability were examined showing that the Ir(III)Cp*Cl@COMOC-4 material could be reused for at least 4 cycles with no decrease in activity and selectivity. Additionally, no significant leaching of the Ir and Ga species or loss of the crystallinity was observed.

3.1. Introduction

The selective oxidation of alcohols to carbonyl compounds is one of the most fundamental and important organic transformations, especially in environmentally benign organic synthesis and fine chemical industry.¹⁻² In particular, aldehydes are essential as they are the starting materials for many functional groups.

From an environmental point of view, it is of paramount importance to develop stable catalysts which use molecular oxygen as a clean and cheap oxidant to realize a so-called green oxidation process.³ It is well known that compounds containing transition metals, such as Pd, Pt, and Ru, are able to catalyze the oxidation of alcohols using oxygen as oxidant.⁴⁻⁶ Nevertheless, in some Pd-catalyzed aerobic oxidation of alcohols, the homogeneous catalysts undergo decomposition.⁷ These findings have drawn considerable attention to the design of new stable catalysts that undergo similar "green oxidations". Within this context, the application of iridium(III) complexes is less explored in comparison to other transition metals. However, iridium complexes have already shown to be promising catalysts in severe thermal or basic conditions.⁸ Since the initial successes with iridium-catalyzed hydrogenation reactions,⁹⁻¹⁰ considerable efforts have been devoted to the development of efficient iridium oxidation catalysts. Within this regard, different Cp*Ir complexes (Cp*=1,2,3,4,5-pentamethylcyclopentadienyl) bearing bipyridine- or N-heterocyclic carbene (NHC)-based ligands have been synthesized.¹¹⁻¹⁵ Most of these catalysts have been employed for the Oppenauer-type alcohol oxidation in which acetone acts as the oxidant.

The first application on the use of iridium-based catalysts in the aerobic oxidation of alcohols was reported by Gabrielsson and co-workers in 2006.¹⁶ Moreover, mechanistic investigations demonstrated the applicability of iridium complexes in the aerobic oxidation of primary and secondary alcohols.¹⁷ However, so far very few studies were conducted using iridium-based catalysts in aerobic oxidation reactions.¹⁸⁻¹⁹ Moreover, these homogeneous catalysts exhibit fundamental drawbacks in which high catalyst loadings (5-10 mol % [Ir]) or a large excess of oxygen as oxidant are required as well as problems associated with the catalysts recovery.¹⁶⁻¹⁹

In recent years, there has been an increasing trend towards a minimization of the amount of produced waste by using supported reagents and catalysts.²⁰⁻²¹ Therefore, the separation of catalysts or products from the reaction mixture is crucial. In this respect, the use of supported catalysts through immobilization of soluble transition metal complexes has many advantages because of easier work-up, recyclability and stability of active components compared to their homogeneous counterparts.²² Although significant efforts have been paid to the synthesis of new homogeneous iridium catalysts, the catalyst recovery, and recycling, as well as the deactivation of the active sites, are still the most important problems and difficulties especially with respect to the cost of iridium complexes.²³

Metal-organic frameworks (MOFs) have received tremendous attention because of their large specific surface area with regular and accessible pores and especially their structural variety that make them outstanding candidates to act as support for various active centers.²⁴⁻²⁶ Moreover, the ability to introduce a large variety of functional groups into the framework by utilizing the modified ligands directly in the solvothermal synthesis (pre-functionalization) or chemical modification of the framework after synthesis (post-synthetic modification) is an extra advantage to obtain advanced MOF materials suitable for more specialized applications.²⁷⁻²⁹ In this regard, we have developed a Ga-based MOF, known as COMOC-4 (COMOC = Center for Ordered Materials, Organometallics, and Catalysis, Ghent University) to anchor a variety of different active complexes in order to prepare heterogeneous catalysts with enhanced catalytic activity in oxidation reactions.³⁰⁻³²

In the present study, we report on the immobilization of an Ir(III) complex onto a MOF support to obtain a new heterogenized iridium catalyst for the oxidation of benzyl alcohol. For this purpose, the gallium 2,2'-bipyridine-5,5'-dicarboxylate (H₂bpydc) MOF, Ga(OH)(bpydc), denoted as COMOC-4 was applied as host matrix to develop a MOF supported iridium catalyst. To the best of our knowledge, there is no report on the preparation and characterization of a heterogeneous Ir complex for the oxidation of alcohols. So far, there is only one report on supported iridium (oxide) nanoparticles on CeO₂.³³ The activity of this catalyst could be addressed to both CeO₂ as support which

plays an important role in the catalytic activity and the iridium oxide centers. Furthermore, this catalyst suffers from a severe deactivation process caused by the formation of benzoic acid through the free-radical (auto)oxidation of benzaldehyde. Here, $[\text{IrCp}^*\text{Cl}_2]_2$, was utilized as an iridium precursor to tether onto the bipyridine moiety of the 2,2'-bipyridine-5,5'-dicarboxylate linkers via pre-functionalization and post-synthetic modification routes. The covalent attachment of the complex onto a stable MOF support is an efficient strategy to prevent leaching of the metal ions and therefore to create a truly heterogenized catalyst. The catalytic activity of the prepared Ir(III)Cp*Cl@COMOC-4 material was examined in the oxidation of benzyl alcohol. Furthermore, the recyclability and stability of the heterogeneous catalyst were investigated during 4 successive cycles.

3.2. Results and Discussion

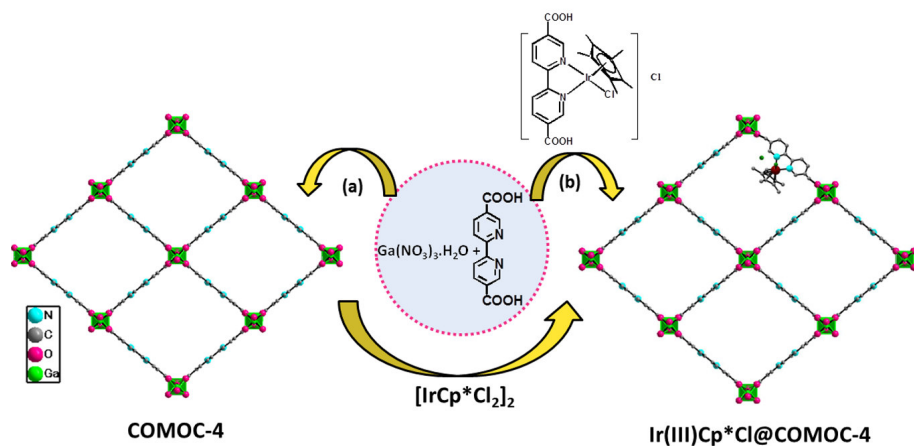
3.2.1. Synthesis and structural information

The pristine COMOC-4 is a gallium-based framework with 1D microporous channels. The bipyridine sites of the H_2bpydc linkers are located on the walls of the channels, allowing the coordination of a second metal site. In general, MOFs can be functionalized with transition metal complexes via a post- or pre-functionalization approach.

Direct synthesis of MOFs using pre-functionalized ligands is challenging since decomposition of the transition metal complexes under the applied reaction conditions can occur. Furthermore, finding the appropriate reaction conditions for forming a particular MOF structure is indispensable. As a result, very few papers report on the modification of MOFs using the pre-functionalized method while there are many reports considering the classical post-synthetic modification route to incorporate functional groups.

Therefore, we applied two different strategies (post- and pre-functionalization) to generate new Ir-based catalysts (see Scheme 1). The iridium-containing catalyst through the pre-functionalization approach was obtained via 2 steps (see Scheme 1, route b). As reviewed previously³⁴ the chloro-bridged dinuclear complexes $[\text{LMCl}_2]_2$ ($\text{M} = \text{Rh(III)}, \text{Ir(III)}$) are very useful precursors for the preparation of a variety of derivatives. Addition of 2,2'-bipyridine

to $[\text{LMCl}_2]_2$ leads to the complexes $[\text{LM}(\text{bpy})\text{Cl}]\text{Cl}$ ($\text{L} = \text{Cp}^*$ for $\text{M} = \text{Rh}, \text{Ir}$). Therefore, the $[\text{IrCp}^*\text{Cl}_2]_2$ complex was stirred in a suspension of the H_2bpydc ligand which resulted in the covalent attachment of the iridium complex to the bipyridine sites (the ^1H NMR spectrum of the metallo-linker is shown in Figure S3.1). In a second step, the use of both functionalized and unfunctionalized H_2bpydc linkers as the organic building blocks followed by the addition of gallium(III) nitrate generated the modified COMOC-4 framework. In the second approach (see Scheme 1, route a), the $[\text{IrCp}^*\text{Cl}_2]_2$ complex was immobilized onto the framework after the formation of the COMOC-4.



Scheme 1. Schematic illustration for the preparation of Ir(III)Cp*Cl@COMOC-4 via (a) post-functionalization, and (b) pre-functionalization.

3.2.2. Characterization of Ir(III)Cp*Cl@COMOC-4

3.2.2.1. X-ray diffraction, nitrogen adsorption and thermogravimetric analysis

In order to immobilize the $[\text{IrCp}^*\text{Cl}_2]_2$ complex onto the COMOC-4 framework following the post-synthetic modification approach the influence of the applied reaction time on the resulting Ir loading was investigated. Therefore, 2 different reaction times were examined, more specifically 3 h and 15 h. The wt % of the obtained Ir loadings is presented in Table

3.1. As can be seen from Table 3.1, the Ir loading of the Ir(III)Cp*Cl@COMOC-4 materials synthesized via the pre-functionalization and post-functionalization (15 h) route are relatively similar and significantly higher than the post-functionalized (3 h) Ir(III)Cp*Cl@COMOC-4. CHN analysis revealed 22 %, 20 % and 10% occupation of bipyridine moieties with the iridium complex in the pre-functionalized and post-functionalized (15 h and 3 h) samples respectively.

The phase purity and crystallinity of all bulk samples were examined by powder XRD measurements (Figure 3.1). The structure of the Ir(III)Cp*Cl@COMOC-4 remained intact after the post-synthetic modification showing the stability of the framework during the modification process. Moreover, the powder XRD pattern of the Ir(III)Cp*Cl@COMOC-4 sample prepared by pre-functionalization strategy revealed the successful synthesis of the framework upon using the iridium metallo-linker.

The textural properties of the pristine COMOC-4 and Ir(III)Cp*Cl@COMOC-4 samples were investigated by means of N₂ adsorption/desorption analyses. The adsorption isotherms of the samples are shown in Figure 3.2. The pristine COMOC-4 maintains a permanent microporosity, as demonstrated by a type IV isotherm and exhibits a Langmuir surface of 980 m²/g and BET surface of 725 m²/g. After the introduction of the iridium complex via the pre-functionalization route, the Langmuir surface area of COMOC-4 drops very moderately and the corresponding pore volume is slightly lower than the pristine COMOC-4 due to the presence of the iridium complex. In contrast to the Ir(III)Cp*Cl@COMOC-4 prepared via the pre-functionalization route, the Ir(III)Cp*Cl@COMOC-4 samples synthesized by the post-synthetic modification strategy show a significant decrease in the Langmuir surface area (502 and 381 m²/g) and pore volume in comparison to the parent COMOC-4 as can be seen from Table 3.1.

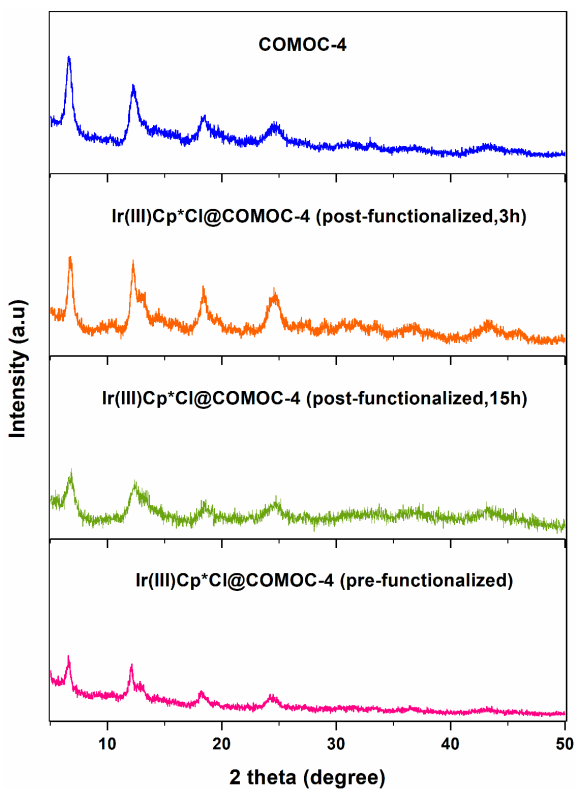


Figure 3.1. Powder XRD patterns of the COMOC-4 and Ir(III)Cp*Cl@COMOC-4 materials.

The obtained results demonstrate that the pre-functionalization approach is a powerful synthetic way which can lead to a higher metal loading and surface area while preserving the formation of the desired MOF. Iridium complex with dimensions of about $5.8 \times 9.3 \text{ \AA}$ has the appropriate size to diffuse through the accessible pores present in the COMOC-4 framework (13 \AA) via the post-functionalization. However, insertion of one iridium complex inside the pore rules out the possibility of the second iridium complex to pass through the first one. Therefore, regarding the fundamental drawbacks of the post-synthetic modification approach such as diffusion limitations which can limit the number

of anchored groups and also pore blocking, we achieved a better control over the porosity as well as the Ir loading using the pre-functionalization strategy. The higher metal loading and surface area are reasonable evidence to confirm the advantage of the pre-functionalized route compared to the post-synthetic modification.

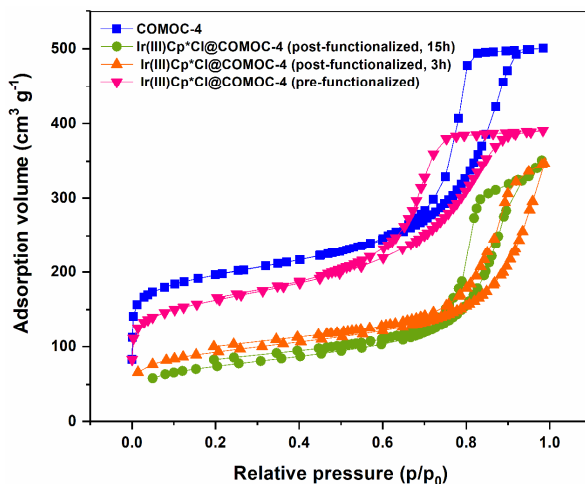


Figure 3.2. Nitrogen adsorption and desorption isotherms of the COMOC-4, and Ir(III)Cp*Cl@COMOC-4 materials.

Thermal gravimetric analyses (TGA) were performed in order to investigate the local structure of the catalyst upon temperature increase. TGA profile of the Ir-H₂bpydc metallo-linker shows two weight losses at 226 °C and 276 °C before decomposition which is in consistent with the H₂bpydc decomposition (see Figure S3.2). After these initial losses, the molecule decomposes in two steps at 326 and 376 °C resulting in a final weight loss of 62 %. In the TGA curve of the Ir(III)Cp*Cl@COMOC-4 catalyst, the main weight loss between 250 and 450 °C might be attributed to the loss of the iridium complex together with the bipyridine linkers of the framework which reveal a slightly reduced thermal stability compared to COMOC-4. As can be seen from Figure S3.3, the pristine COMOC-4 is thermally stable up to 300 °C, above which a weight loss of

about 68 % is observed indicating the decomposition of the framework. The H₂bpydc linker shows a thermal stability up to 310 °C and after that the molecule starts decomposition.

Table 3.1. Properties of the Ir(III)Cp*Cl@COMOC-4 materials.

Catalyst	Ir (mmol g ⁻¹)	S _{lang} (m ² g ⁻¹)	Pore volume (cm ³ g ⁻¹)
Ir(III)Cp*Cl@COMOC-4 functionalization)	(pre- 0.67	767	0.6
Ir(III)Cp*Cl@COMOC-4 (post-functionalization, 15h)	0.61	381	0.54
Ir(III)Cp*Cl@COMOC-4 functionalization, 3h)	(post- 0.27	502	0.53
COMOC-4	-	980	0.94

3.2.2.2. Spectroscopic analysis

In order to confirm the modification of the COMOC-4 framework, far-infrared spectra were recorded (see Figure 3.3). As can be seen from Figure 3.3, the homogeneous Ir-H₂bpydc metallo-linker exhibits characteristic bands at approximately 190-210 cm⁻¹ and 260 cm⁻¹ which can be ascribed to the Ir-N and Ir-Cl stretching vibrations respectively.³⁵ These vibrations can also be seen in the far-infrared spectrum of the pre-functionalized Ir(III)Cp*Cl@COMOC-4 and post-functionalized Ir(III)Cp*Cl@COMOC-4 materials which clearly confirm the immobilization of the iridium complex to the bipyridine sites.

The DRIFT spectra of the COMOC-4 and Ir(III)Cp*Cl@COMOC-4 materials are presented in Figure S3.4. In the DRIFT spectrum of COMOC-4, the absorption bands in the region 1597–1616 cm⁻¹ and 1415–1463 cm⁻¹ can be assigned to the asymmetric and symmetric -CO₂ stretching vibrations respectively. Furthermore, the vibration bands due to the benzene ring appear in the region 1510–1450 cm⁻¹ (aromatic ring stretch), and 1225–950 cm⁻¹ (aromatic C-H bend). All these characteristic vibrations of the framework are preserved in the post-functionalized and pre-functionalized Ir(III)Cp*Cl@COMOC-4 materials demonstrating once more the framework stability.

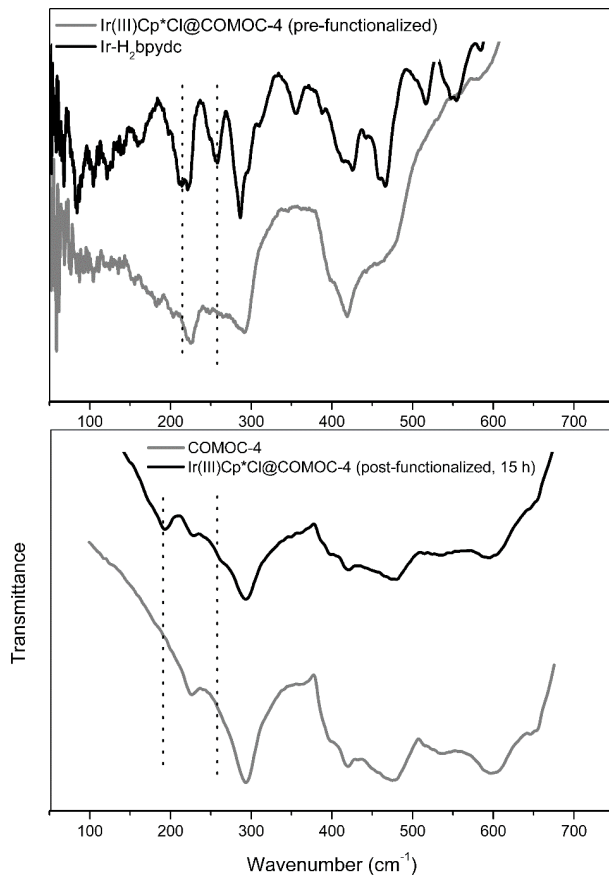


Figure 3.3. Far-IR spectra of the COMOC-4, Ir-H₂bpydc metallo-linker, and Ir(III)Cp*Cl@COMOC-4 materials.

3.3. Catalytic tests

The surface area, as well as the distribution of the active sites within the framework, has a direct impact on the catalytic properties. In this aspect, we have employed the pre-

functionalized Ir(III)Cp*Cl@COMOC-4 material during the catalytic tests while the aerobic oxidation of benzyl alcohol was used as a benchmark reaction. In a typical catalytic test, a catalyst loading of 1 mol % or 3 mol % was used and the catalyst/substrate/base ratio was 1:100:120. Iodobenzene was added as the co-oxidant based on the study of Yan *et al.*³⁶ In the latter study, it was seen that the combination of Ir-based catalysts, nitrogen ligand, and iodobenzene is critical for achieving excellent catalytic activity in the aerobic oxidation of alkylarenes. The Ir complex may promote the decomposition of iodobenzene to release the phenyl radical and initiate the auto-oxidation process.³⁶ In the proposed mechanism by Gabrielsson for the aerobic oxidation of benzyl alcohol¹⁶ substitution of the halide by the alcohol produces an alcohol complex and deprotonation results in an alkoxide complex which rapidly undergoes β -hydride elimination to yield a hydride. Deprotonation of the hydride generates Cp*Ir(bpy). Oxidation followed by solvation returns the alcohol complex. The reoxidation of the Ir^I complexes probably forms a peroxide species (Figure S3.7). Since this work introduces a promising approach toward aerobic oxidation of alcohols in the presence of iodobenzene future work will provide the mechanistic investigation of the iridium(III)-catalyzed aerobic oxidation of alcohols in the presence of iodobenzene.

The results of catalytic performance of the Ir(III)Cp*Cl@COMOC-4 material are given in Table 3.2. In the absence of the catalyst no conversion of benzyl alcohol was observed (< 1% after 24 h). In the presence of the Ir(III)Cp*Cl@COMOC-4 material the selectivity towards benzaldehyde was 100% during each catalytic test indicating that the iridium catalyst exhibits an excellent product selectivity.

In an attempt to explore the role of the applied base, different bases were examined. The conversion of benzyl alcohol improves in the presence of K₂CO₃ and Cs₂CO₃ (Table 3.2, entries 1-4) while in the presence of Na₂CO₃ and Et₃N almost no activity was observed. Further tests were carried out to determine the influence of the reaction temperature on the catalytic properties of the Ir(III)Cp*Cl@COMOC-4. The reaction temperature has a strong impact on the catalyst performance. When the reaction was done at 130 and 100 °C poor catalytic activity was observed. Increasing the catalyst amount from 1 mol % [Ir] to 3 mol % [Ir] resulted in a higher benzyl alcohol conversion of 37 % and 54 % in the

Chapter 3: Direct synthesis of an Iridium(III)-bipyridine-Metal-Organic Framework as heterogeneous catalyst for aerobic alcohol oxidation

presence of Cs_2CO_3 while a conversion of 24 % and 38 % was obtained when K_2CO_3 was added (Table 3.2, entries 1-4).

Table 3.2. Catalytic performance of $\text{Ir(III)Cp}^*\text{Cl@COMOC-4}$ in the oxidation of benzyl alcohol.

Entry	Catalyst ^[a]	Base	Conv. ^[b] (%)	Sel. ^[c] (%)
1	$\text{Ir(III)Cp}^*\text{Cl@COMOC-4}^{[d]}$ 1 mol %	K_2CO_3	24	> 99
2	$\text{Ir(III)Cp}^*\text{Cl@COMOC-4}^{[d]}$ 3 mol %	K_2CO_3	37	> 99
3	$\text{Ir(III)Cp}^*\text{Cl@COMOC-4}^{[d]}$ 1 mol %	Cs_2CO_3	38	> 99
4	$\text{Ir(III)Cp}^*\text{Cl@COMOC-4}^{[d]}$ 3 mol %	Cs_2CO_3	54	> 99
5 ^[e]	$\text{Ir(III)Cp}^*\text{Cl@COMOC-4}^{[d]}$ 3 mol %	Cs_2CO_3	27	> 99
6	COMOC-4	Cs_2CO_3	< 1	-
7	-	K_2CO_3	< 1	-
8	$\text{Ir(III)Cp}^*\text{Cl@COMOC-4}^{[d]}$ 3 mol %	Na_2CO_3	< 1	-
9	$\text{Ir(III)Cp}^*\text{Cl@COMOC-4}^{[d]}$ 3 mol %	Et_3N	< 1	-

Reaction conditions: Benzyl alcohol (0.33 mmol), base (0.4 mmol), iodobenzene (0.4 mmol), solvent (330 μl), 24h.

^[a] Based on iridium, ^[b] GC yield based on starting substrate, ^[c] Selectivity toward the formation of benzaldehyde, ^[d] the pre-functionalized $\text{Ir(III)Cp}^*\text{Cl@COMOC-4}$ was applied. ^[e] No iodobenzene was added.

In Table 3.3 a comparison of the catalytic performance of the $\text{Ir(III)Cp}^*\text{Cl@COMOC-4}$ to other Ir-based homogeneous and heterogeneous catalyst systems is summarized. The homogeneous Ir-based catalysts display a moderate to good activity in the aerobic oxidation of benzyl alcohol depending on the applied reaction conditions. For instance, using Et_3N with a high Ir loading resulted in a high catalytic activity (Table 3.3, entry 1). Moreover, it was shown that the presence of a Cp^*Ir complex bearing α -hydroxypyridine ligand improves the catalytic activity (Table 3.3, entry 3 compared to 4). So far, there is only one report on the preparation of a supported iridium catalyst (Table 3.3, entry 5). However, this catalyst suffers from an extreme deactivation process due the formation of benzoic acid through the free-radical (auto)oxidation of benzaldehyde. From this table, one

can conclude that the Ir(III)Cp*Cl@COMOC-4 exhibits a comparable catalytic performance (54%) in comparison to the Ir/CeO₂ catalyst reported in the literature. Even in comparison to some other homogeneous based Ir catalysts this catalyst performs equally or better in terms of activity.

Table 3.3. Comparison of the results obtained for the aerobic oxidation of benzyl alcohol catalyzed by different iridium catalysts.

Entry	Catalyst	Reaction conditions	Conv. (%)	TOF ^[a] (h ⁻¹)	Ref.
1	[IrCp*Cl ₂] ₂	5 mol % [Ir], Et ₃ N, 80 °C	82	1.36	17
2	[IrCp*Cl ₂] ₂	1mol % [Ir], buffer, 100 °C	34 ^[b]	1.41	19
3	[Ir(bpy)(H ₂ O)Cp*](OTF) ₂	0.5 mol % [Ir], 100 °C	25	2.5	14
4	[Ir(OH- bpy)(H ₂ O)Cp*](OTF) ₂	1.5 mol % [Ir], 100 °C	92	3.06	14
5	Ir/CeO ₂	0.5 mol % [Ir], 90 °C	54.8	36.5	33
6	Ir(III)Cp*Cl@COMOC-4	3 mol % [Ir], Cs ₂ CO ₃ , 150 °C	54	0.75	-

^[a] Calculated as mmol of product formed per mmol of iridium in the catalyst per time, ^[b] Based on GC yield.

3.4. Stability and regenerability tests

In order to assess the heterogeneity of the Ir(III)Cp*Cl@COMOC-4 material, a hot filtration experiment was performed. The reaction mixture was filtered after 12 h reaction time and the filtrate was allowed to react further for an additional 12 h. After the removal of the catalyst, the benzaldehyde formation stopped immediately indicating that the catalysis occurs truly heterogeneous (Figure 3.4). Furthermore, to examine the recyclability of the Ir(III)Cp*Cl@COMOC-4, the catalyst was separated from the reaction mixture, washed with toluene and then used directly for the subsequent runs applying the same reaction conditions. KCl was added to provide the correct counter ion. The results of the reusability tests are depicted in Figure 3.5.

Chapter 3: Direct synthesis of an Iridium(III)-bipyridine-Metal-Organic Framework as heterogeneous catalyst for aerobic alcohol oxidation

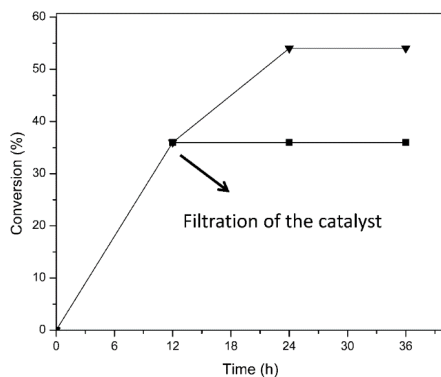


Figure 3.4. Hot filtration test for the Ir(III)Cp*Cl@COMOC-4 catalyst.

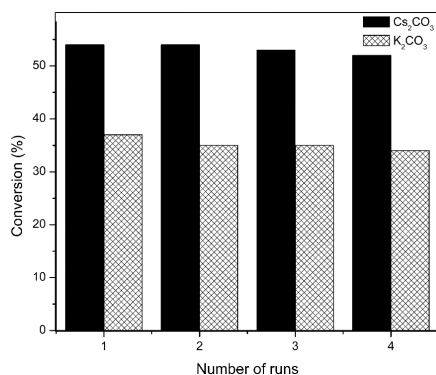


Figure 3.5. Recyclability of the Ir(III)Cp*Cl@COMOC-4 catalyst in the presence of KCl. Reaction conditions: Benzyl alcohol (0.33 mmol), base (0.4 mmol), iodobenzene (0.4 mmol), KCl (0.4 mmol), toluene (330 μ l) (The recycle tests are just an indication and not definitive proof of catalyst stability).

The recovered catalyst was reused at least 4 times for the oxidation of benzyl alcohol and as can be seen from this figure the recovered Ir(III)Cp*Cl@COMOC-4 catalyst maintains similar activity after 4 recycles with a 100% selectivity towards benzaldehyde. It should

be noted that in the absence of KCl a reduced activity was observed in the additional runs (Figure S3.5). ICP-OES analyses of the filtrate after each catalytic test (see Table S3.1) showed no significant leaching of Ir and Ga during the 4 successive runs. Additional proof for the stability of the framework was obtained by powder XRD measurements. The similarity of the XRD patterns of Ir(III)Cp*Cl@COMOC-4 before catalysis and after each run clearly indicates the catalyst stability under the applied reaction conditions (Figure 3.6).

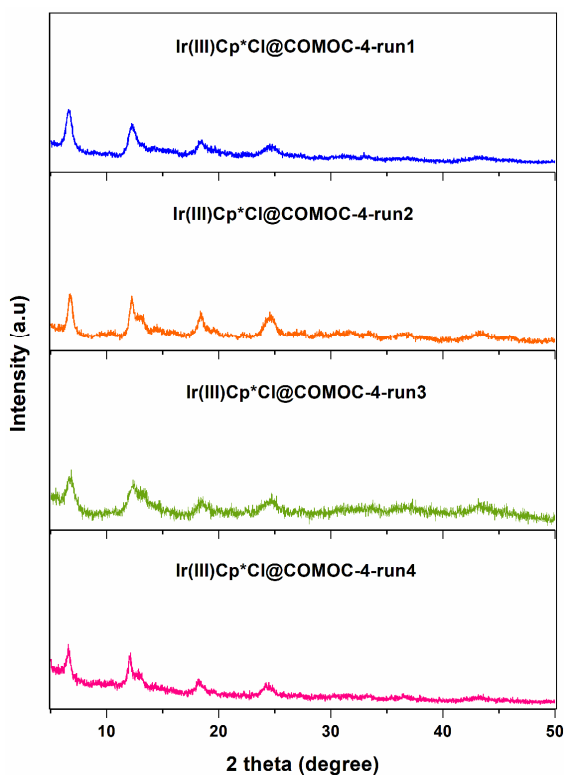


Figure 3.6. Powder XRD patterns of the Ir(III)Cp*Cl@COMOC-4 catalyst after each catalytic run.

3.5. Conclusions

In the present work, we succeeded in designing a new heterogeneous iridium catalyst using COMOC-4 as solid support. Modification of the framework was successfully conducted by immobilization of the $[\text{IrCp}^*\text{Cl}_2]_2$ complex *via* two different routes (post- and pre-functionalization). The obtained results revealed the importance of the different functionalization routes for the introduction of metal complexes into MOFs and the effect on the properties of the materials. The $\text{Ir(III)Cp}^*\text{Cl@COMOC-4}$ catalyst exhibited a good catalytic performance in the aerobic oxidation reaction of benzyl alcohol with a selectivity up to 100 % towards benzaldehyde. This work is an important first step toward the heterogenization of iridium complexes to design an effective heterogeneous catalyst in the selective oxidation of alcohols.

3.6. Experimental Section

3.6.1. Materials and instrumentation

For details please see Appendix.

3.6.2. Synthesis of the $\text{Ir(III)Cp}^*\text{Cl@COMOC-4}$ materials

3.6.2.1. Post-synthetic modification approach

The synthesis of COMOC-4 was carried out according to our previously published procedure.³⁰ Typically, 1.2 g (4.4 mmol) of $\text{Ga}(\text{NO}_3)_3 \cdot \text{H}_2\text{O}$ and 1.22 g (5 mmol) of H_2bpydc were added to 120 mL DMF and stirred at 150 °C for 48 h. The green precipitate was filtered off and washed with DMF, methanol, and acetone respectively. Afterward, the solid sample was stirred in DMF at 80 °C for 2 h to remove the unreacted linkers followed by a soxhlet extraction in methanol for 48 h at 120 °C. Hereafter, the obtained COMOC-4 material was dried under vacuum overnight (Calcd for $\text{Ga}(\text{OH})(\text{C}_{12}\text{H}_6\text{N}_2\text{O}_4) \cdot 2.7\text{H}_2\text{O}$: C, 38.36; H, 3.27; N, 7.46 %; Found: C, 38.31; H, 3.21; N, 7.40 %). The post-modification of the COMOC-4 was performed in a glovebox as follows: $[\text{IrCp}^*\text{Cl}_2]_2$ (9.32 mg, 0.011 mmol) was added to 45 mL dry THF and stirred for 15 minutes to give a clear orange solution. Afterward, 0.1 g COMOC-4 material was added and stirred for 3 h or 15 h at room

temperature (7.8 mol % [Ir]). The Ir(III)Cp*Cl@COMOC-4 was filtered, washed thoroughly with acetone, and dried under vacuum overnight (Found for post- functionalized Ir(III)Cp*Cl@COMOC-4, 3 h: C, 40.71; H, 1.87; N, 7.30 %; Found for post-functionalized Ir(III)Cp*Cl@COMOC-4, 15 h: C, 39.69; H, 1.90; N, 7.54 %).

3.6.2.2. Pre-functionalization approach

The functionalization of the H₂bpydc linker with the iridium complex was achieved following the procedure described in the literature.³⁷ In a glovebox, [IrCp*Cl₂]₂ (398.5 mg, 0.5 mmol) was added to H₂bpydc linker (244 mg, 1 mmol) in dry DMF (60 mL). The resulting suspension was stirred at room temperature for 24 h. Then, Et₂O (60 mL) was added to the obtained clear orange solution and stirred at room temperature for an additional 15 minutes after which an orange solid precipitation was formed. The prepared metallo-linker was filtered, washed with Et₂O and pentane and dried under vacuum (630 mg, 82 %, Calcd for C₂₂H₂₃Cl₂IrN₂O₄ linker: C, 40.17; H, 3.96; N, 4.36 %; Found: C, 39.80; H, 3.13; N, 5.00 %).

In a second step, the metallo-linker was used as the building block for the synthesis of the COMOC-4 material using the original reaction conditions of the pristine COMOC-4 framework. For 7.8 mol % [Ir] loading, H₂bpydc (65 mg, 0.268 mmol), metallo-linker (84 mg, 0.132 mmol) and Ga(NO₃)₃.H₂O (96 mg, 0.352 mmol) were suspended in dry DMF (9.6 mL). The mixture was stirred at 150 °C for 48 h after which the green precipitate was filtered off and washed. Finally, a soxhlet extraction with methanol was performed for 48 h at 120 °C to remove the unreacted organic species. Hereafter, the sample was dried under vacuum overnight (Found for pre-functionalized Ir(III)Cp*Cl@COMOC-4: C, 37.67; H, 2.07; N, 6.45 %).

3.6.3. Catalytic setup

The oxidation of benzyl alcohol was carried out in a 20 mL Schlenk tube. During a typical catalytic test, the Ir(III)Cp*Cl@COMOC-4 (21 mg, 1 mol % [Ir]; 63 mg, 3 mol % [Ir]), K₂CO₃ (55.28 mg, 0.4 mmol) or Cs₂CO₃ (130.33 mg, 0.4 mmol) as base, dodecane as internal standard (37.5 µl, 0.165 mmol), benzyl alcohol (34.3 µl, 0.33 mmol), toluene (330 µl) and

Chapter 3: Direct synthesis of an Iridium(III)-bipyridine-Metal-Organic Framework as heterogeneous catalyst for aerobic alcohol oxidation

iodobenzene (44.6 μl , 0.4 mmol) as co-oxidant were added to the Schlenk tube. The tube was filled with pure oxygen, sealed and heated to 150 $^{\circ}\text{C}$ for 24 h. K_2CO_3 and Cs_2CO_3 were placed in a porous membrane during the catalytic tests in order to separate our solid catalyst from the base.

The Ir(III) $\text{Cp}^*\text{Cl@COMOC-4}$ materials were activated under vacuum overnight prior to catalysis. After each catalytic run, the catalyst was recovered by filtration, washed with toluene, and then used directly for the subsequent runs. For the additional runs, KCl (29.82 mg, 0.4 mmol) was added to the porous membrane which contained the base.

3.7. References

1. Sheldon, R. A.; Arends, I. W. C. E.; Dijkstra, A., New developments in catalytic alcohol oxidations for fine chemicals synthesis. *Catal Today* **2000**, *57* (1-2), 157-166.
2. Bai, C. H.; Li, A. Q.; Yao, X. F.; Liu, H. L.; Li, Y. W., Efficient and selective aerobic oxidation of alcohols catalysed by MOF-derived Co catalysts. *Green Chem* **2016**, *18* (4), 1061-1069.
3. Punniyamurthy, T.; Velusamy, S.; Iqbal, J., Recent advances in transition metal catalyzed oxidation of organic substrates with molecular oxygen. *Chem Rev* **2005**, *105* (6), 2329-2363.
4. Sheldon, R. A.; Arends, I. W. C. E.; Ten Brink, G. J.; Dijkstra, A., Green, catalytic oxidations of alcohols. *Accounts Chem Res* **2002**, *35* (9), 774-781.
5. Piera, J.; Backvall, J. E., Catalytic oxidation of organic substrates by molecular oxygen and hydrogen peroxide by multistep electron transfer - A biomimetic approach. *Angew Chem Int Edit* **2008**, *47* (19), 3506-3523.
6. Lu, T. L.; Du, Z. T.; Liu, J. X.; Ma, H.; Xu, J., Aerobic oxidation of primary aliphatic alcohols over bismuth oxide supported platinum catalysts in water. *Green Chem* **2013**, *15* (8), 2215-2221.
7. Steinhoff, B. A.; Guzei, I. A.; Stahl, S. S., Mechanistic characterization of aerobic alcohol oxidation catalyzed by Pd(OAc)₂/pyridine including identification of the catalyst resting state and the origin of nonlinear [catalyst] dependence. *J Am Chem Soc* **2004**, *126* (36), 11268-11278.
8. Suzuki, T., Organic Synthesis Involving Iridium-Catalyzed Oxidation. *Chem Rev* **2011**, *111* (3), 1825-1845.
9. Henbest, H. B.; Trochagr, J., Aspects of Catalysis .4. Hydrogen Transfer from Propan-2-OI to Alpha,Beta-Unsaturated Ketones Catalyzed by a Soluble Hydridoiridium Complex - Isolation of Compound Containing a Carbon-Iridium Bond and a Chelated Keto-Group. *J Chem Soc Perk T 1* **1974**, (5), 601-603.
10. Zassinovich, G.; Camus, A.; Mestroni, G., Enantioselective Hydrogen Transfers from Isopropanol to Prochiral Ketones, Using Iridium Complexes with Nitrogen Donor Ligands as Catalyst Precursors. *J Mol Catal* **1980**, *9* (3), 345-347.
11. Hanasaka, F.; Fujita, K. I.; Yamaguchi, R., Cp*Ir complexes bearing N-heterocyclic carbene ligands as effective catalysts for Oppenauer-type oxidation of alcohols. *Organometallics* **2004**, *23* (7), 1490-1492.
12. Hanasaka, F.; Fujita, K.; Yamaguchi, R., Synthesis of new iridium N-heterocyclic carbene complexes bearing a functionalized Cp* ligand and their high catalytic activities in the Oppenauer-type oxidation of alcohol. *Organometallics* **2006**, *25* (19), 4643-4647.

13. Hanasaka, F.; Fujita, K.; Yamaguchi, R., Synthesis of new cationic Cp*Ir N-heterocyclic carbene complexes and their high catalytic activities in the Oppenauer-type oxidation of primary and secondary alcohols. *Organometallics* **2005**, *24* (14), 3422-3433.
14. Kawahara, R.; Fujita, K.; Yamaguchi, R., Dehydrogenative Oxidation of Alcohols in Aqueous Media Using Water-Soluble and Reusable Cp*Ir Catalysts Bearing a Functional Bipyridine Ligand. *J Am Chem Soc* **2012**, *134* (8), 3643-3646.
15. Jimenez, M. V.; Fernandez-Tornos, J.; Modrego, F. J.; Perez-Torrente, J. J.; Oro, L. A., Oxidation and beta-Alkylation of Alcohols Catalysed by Iridium(I) Complexes with Functionalised N-Heterocyclic Carbene Ligands. *Chem-Eur J* **2015**, *21* (49), 17877-17889.
16. Gabrielsson, A.; van Leeuwen, P. W. N. M.; Kaim, W., Acidic iridium hydrides: Implications for aerobic and Oppenauer oxidation of alcohols. *Chem Commun* **2006**, (47), 4926-4927.
17. Jiang, B.; Feng, Y.; Ison, E. A., Mechanistic Investigations of the Iridium(III)-Catalyzed Aerobic Oxidation of Primary and Secondary Alcohols. *J Am Chem Soc* **2008**, *130* (44), 14462-+.
18. Arita, S.; Koike, T.; Kayaki, Y.; Ikariya, T., Aerobic oxidation of alcohols with bifunctional transition-metal catalysts bearing C-N chelate ligands. *Chem-Asian J* **2008**, *3* (8-9), 1479-1485.
19. Gunay, A.; Mantell, M. A.; Field, K. D.; Wu, W. B.; Chin, M.; Emmert, M. H., Oxidation catalysis in air with Cp*Ir: influence of added ligands and reaction conditions on catalytic activity and stability. *Catal Sci Technol* **2015**, *5* (2), 1198-1205.
20. Wight, A. P.; Davis, M. E., Design and preparation of organic-inorganic hybrid catalysts. *Chem Rev* **2002**, *102* (10), 3589-3613.
21. Choplin, A.; Quignard, F., From supported homogeneous catalysts to heterogeneous molecular catalysts. *Coordin Chem Rev* **1998**, *178*, 1679-1702.
22. de Miguel, Y. R.; Brule, E.; Margue, R. G., Supported catalysts and their applications in synthetic organic chemistry. *J Chem Soc Perk T* **2001**, (23), 3085-3094.
23. Ajjou, A. N., First example of water-soluble transition-metal catalysts for Oppenauer-type oxidation of secondary alcohols. *Tetrahedron Lett* **2001**, *42* (1), 13-15.
24. Long, J. R.; Yaghi, O. M., The pervasive chemistry of metal-organic frameworks. *Chem Soc Rev* **2009**, *38* (5), 1213-1214.
25. Zhou, H. C.; Long, J. R.; Yaghi, O. M., Introduction to Metal-Organic Frameworks. *Chem Rev* **2012**, *112* (2), 673-674.
26. Moon, H. R.; Lim, D. W.; Suh, M. P., Fabrication of metal nanoparticles in metal-organic frameworks. *Chem Soc Rev* **2013**, *42* (4), 1807-1824.
27. Abednatanzi, S.; Abbasi, A.; Masteri-Farahani, M., Enhanced catalytic activity of nanoporous Cu-3(BTC)(2) metal-organic framework via immobilization of oxidiperoxo molybdenum complex. *New J Chem* **2015**, *39* (7), 5322-5328.
28. Wang, Z. Q.; Cohen, S. M., Postsynthetic modification of metal-organic frameworks. *Chem Soc Rev* **2009**, *38* (5), 1315-1329.
29. Yang, D.; Odoh, S. O.; Borycz, J.; Wang, T. C.; Farha, O. K.; Hupp, J. T.; Cramer, C. J.; Gagliardi, L.; Gates, B. C., Tuning Zr-6 Metal-Organic Framework (MOF) Nodes as Catalyst Supports: Site Densities and Electron-Donor Properties Influence Molecular Iridium Complexes as Ethylene Conversion Catalysts. *Acs Catal* **2016**, *6* (1), 235-247.
30. Liu, Y. Y.; Decadt, R.; Bogaerts, T.; Hemelsoet, K.; Kaczmarek, A. M.; Poelman, D.; Waroquier, M.; Van Speybroeck, V.; Van Deun, R.; Van Der Voort, P., Bipyridine-Based Nanosized Metal-Organic Framework with Tunable Luminescence by a Postmodification with Eu(III): An Experimental and Theoretical Study. *J Phys Chem C* **2013**, *117* (21), 11302-11310.
31. Liu, Y. Y.; Leus, K.; Bogaerts, T.; Hemelsoet, K.; Bruneel, E.; Van Speybroeck, V.; Van Der Voort, P., Bimetallic-Organic Framework as a Zero-Leaching Catalyst in the Aerobic Oxidation of Cyclohexene. *Chemcatchem* **2013**, *5* (12), 3657-3664.

Chapter 3: Direct synthesis of an Iridium(III)-bipyridine-Metal-Organic Framework as heterogeneous catalyst for aerobic alcohol oxidation

32. Leus, K.; Liu, Y. Y.; Meledina, M.; Turner, S.; Van Tendeloo, G.; Van der Voort, P., A Mo-VI grafted Metal Organic Framework: Synthesis, characterization and catalytic investigations. *J Catal* **2014**, *316*, 201-209.
33. Hammond, C.; Schumperli, M. T.; Conrad, S.; Hermans, I., Hydrogen Transfer Processes Mediated by Supported Iridium Oxide Nanoparticles. *Chemcatchem* **2013**, *5* (10), 2983-2990.
34. Koelle, U., Organometallic Aqua Ions of the Transition-Metals. *Coordin Chem Rev* **1994**, *135*, 623-650.
35. Lai, S. H.; Ling, J. W.; Huang, Y. M.; Huang, M. J.; Cheng, C. H.; Chen, I. C., Characterization of Ir(ppy)(3) and [Ir(ppy)(2) bpy](+) by infrared, Raman spectra and surface-enhanced Raman scattering. *J Raman Spectrosc* **2011**, *42* (3), 332-338.
36. Yan, Y. Y.; Chen, Y. Y.; Yan, M.; Li, X. S.; Zeng, W., Iridium-catalyzed aerobic oxidation of alkylarenes with excellent turnover numbers. *Catal Commun* **2013**, *35*, 64-67.
37. Platero-Prats, A. E.; Gomez, A. B.; Samain, L.; Zou, X. D.; Martin-Matute, B., The First One-Pot Synthesis of Metal-Organic Frameworks Functionalised with Two Transition-Metal Complexes. *Chem-Eur J* **2015**, *21* (2), 861-866.

3.8. Supporting Information

$[\text{IrCp}^*(\text{H}_2\text{bpydc})\text{Cl}]\text{Cl}$

^1H NMR (400 MHz, $\text{DMSO}-d_6$): δ 9.28 (2 H, d, J 1.5), 9.01 (2 H, d, J 8.4), 8.75 (2 H, dd, J 8.3, 1.7), 1.68 (15 H, s).

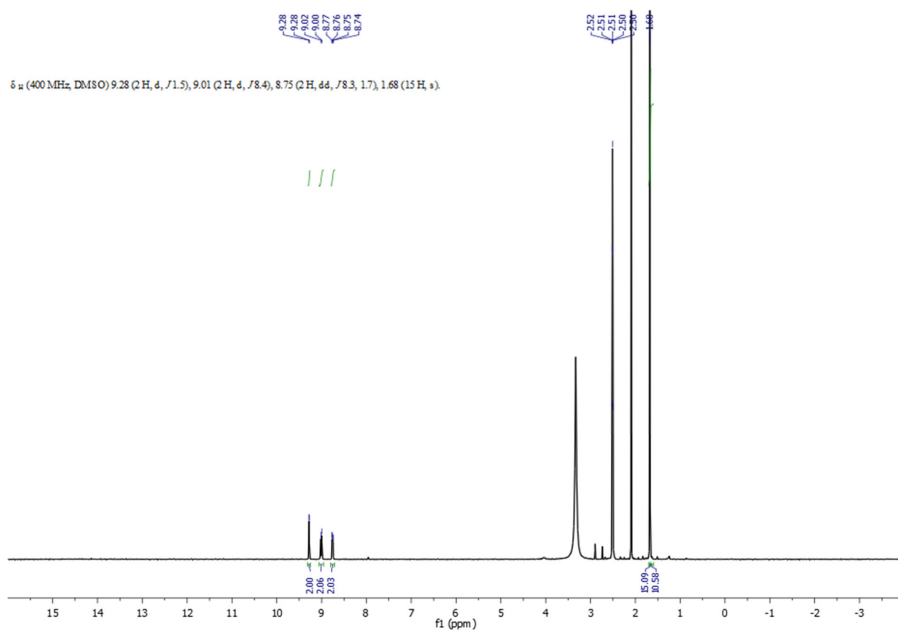


Figure S3.1. ^1H NMR spectrum of the Ir- H_2bpydc metallo-linker.

Chapter 3: Direct synthesis of an Iridium(III)-bipyridine-Metal-Organic Framework as heterogeneous catalyst for aerobic alcohol oxidation

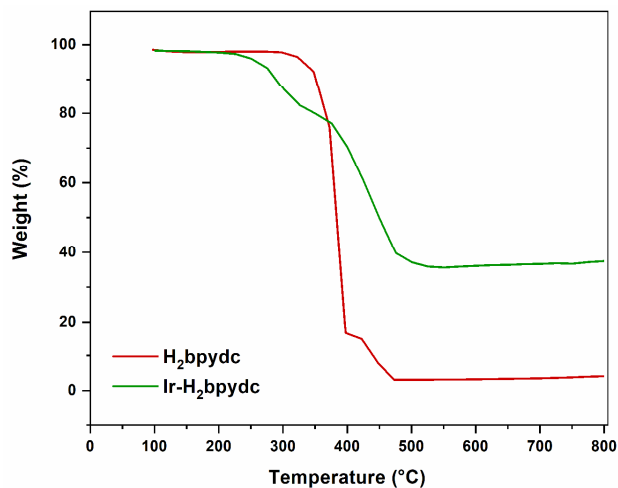


Figure S3.2. TGA curves of the H₂bpydc and Ir-H₂bpydc metallo-linker.

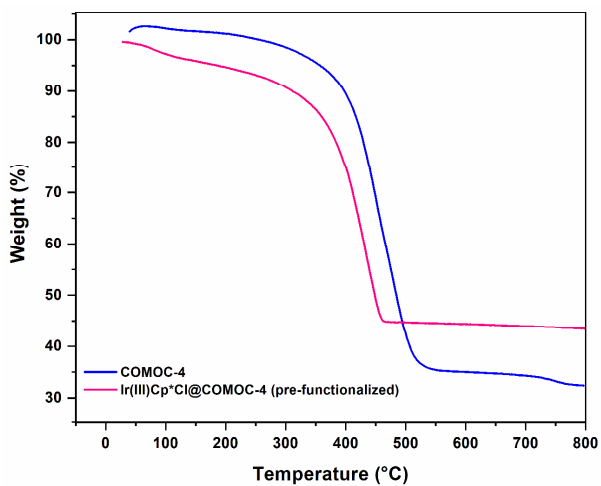


Figure S3.3. TGA curves of the COMOC-4, and Ir(III)Cp*Cl@COMOC-4 materials.

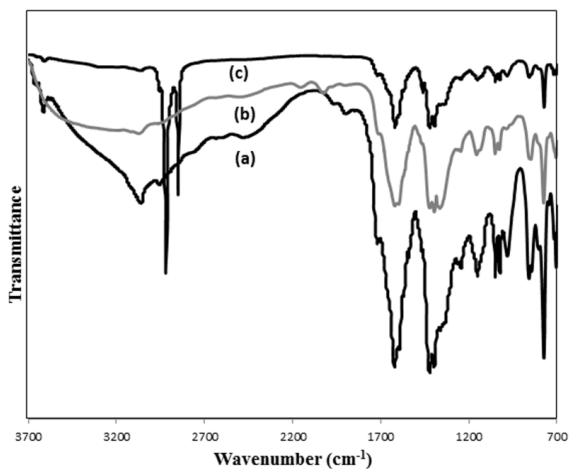


Figure S3.4. DRIFT spectra of (a) COMOC-4, (b) Ir(III)Cp*Cl@COMOC-4 (pre-functionalized), (c) Ir(III)Cp*Cl@COMOC-4 (post-functionalized, 15 h).

Table S3.1. Total metal amount leached from the Ir(III)Cp*Cl@COMOC-4 catalyst in the successive runs.

Runs	Ga (wt%)	Ir (wt%)
1	0.00024	0.0000057
2	0.000023	0.0000050
3	0.000043	0
4	0.000021	0

Chapter 3: Direct synthesis of an Iridium(III)-bipyridine-Metal-Organic Framework as heterogeneous catalyst for aerobic alcohol oxidation

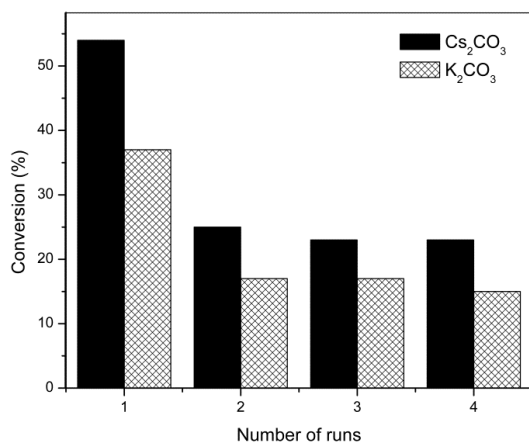


Figure S3.5. Recyclability of the Ir(III)Cp*Cl@COMOC-4 catalyst in the absence of KCl.

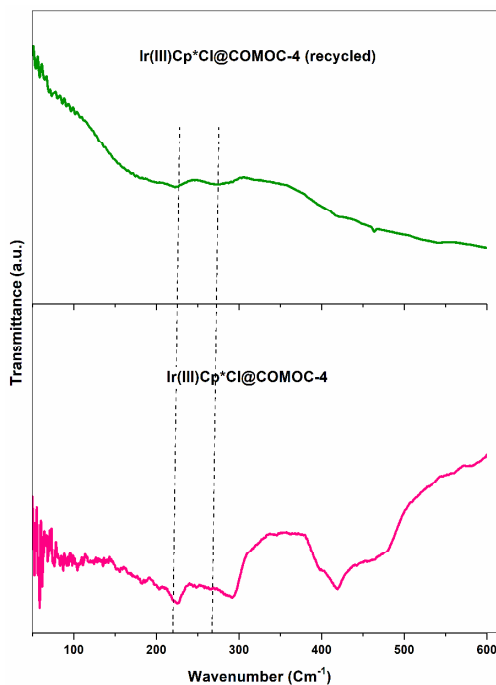


Figure S3.6. Far-IR spectra of the Ir(III)Cp*Cl@COMOC-4, and Ir(III)Cp*Cl@COMOC-4 (recycled) materials.

The mechanism for Homogeneous Ir-catalyzed aerobic oxidation of benzyl alcohol is presented in Figure S3.7. In the catalytic system for the COMOC-4 material grafted with Ir the presence of iodobenzene as the co-oxidant is vital. However, the exact mechanism of Ir complexes in the presence of iodobenzene for oxidation reactions is still not known. Since this work introduces a promising approach toward aerobic oxidation of alcohols in the presence of iodobenzene, the mechanistic study of the iridium(III)-catalyzed aerobic oxidation of alcohols in the presence of iodobenzene is under investigation.

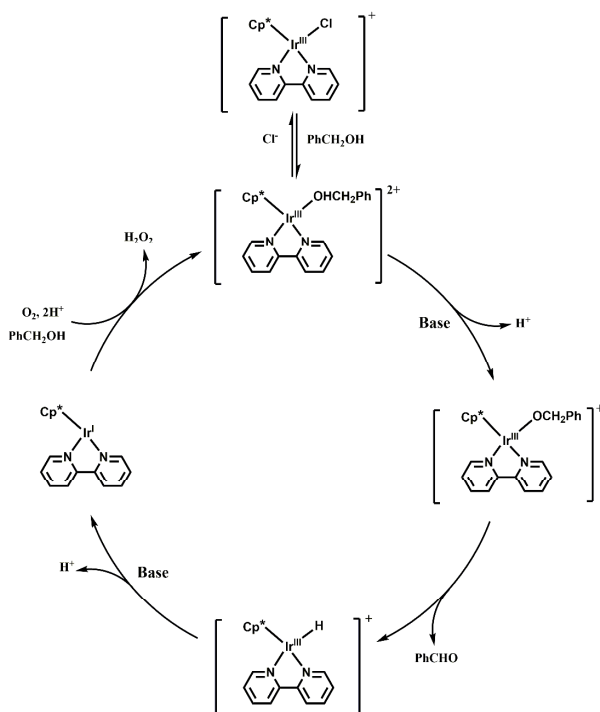


Figure S3.7. Proposed mechanism for the Ir-catalyzed aerobic oxidation of benzyl alcohol.

CHAPTER 4

Ce(III)-BASED FRAMEWORKS: FROM 1D CHAIN TO 3D POROUS METAL- ORGANIC FRAMEWORK



The results of this chapter were published in:

P. Gohari Derakhshandeh, S. Abednatanzi, K. Leus, J. Janczak R. Van Deun, P. Van Der Voort, K. Van Hecke. Ce(III)-Based Frameworks: From 1D Chain to 3D Porous Metal-Organic Framework. **Crystal Growth & Design**, 19, **2019**, 7096-7105.

Abstract

The reaction of pyridine-2,4-dicarboxylic acid (H₂pydc) with Ce(NO₃)₃·6H₂O, by applying only minor changes to the reaction conditions, generated a series of new one-, two-, and three-dimensional coordination polymers namely, [Ce(pydc)(Hpydc)(H₂O)₄]_n (**1**), [Ce(pydc)(Hpydc)(H₂O)₂]_n (**2**), and {[Ce₃(pydc)₄(H₂O)₂NO₃].4H₂O]_n (**3**). The ancillary ligand interaction as well as the reaction conditions determine the specific coordination modes for the Hpydc⁻ and pydc²⁻ ligands and, in turn, discriminate between 1D, 2D, and 3D frameworks. Characterization of the prepared materials was performed using single-crystal and powder X-ray diffraction analysis, Fourier transform infrared, CHN elemental analysis, thermogravimetric analysis and nitrogen adsorption/desorption techniques. Compound **1** consists of 1D chains, that compose of Ce³⁺ ions bridged by Hpydc⁻ and pydc²⁻ ligands, which further link via non-covalent interactions to form a 3D supramolecular architecture. Compound **2** assembles into 2D sheets with 1D channels. Similarly, via hydrogen bonding interactions between two adjacent sheets, the 2D layers are further stacked into the final 3D supramolecular structure. Compound **3** is a 3D metal-organic framework (MOF), showing 1D helical channels. The progressive skeletal variation from the 1D chains (**1**) to 2D sheets (**2**) and 3D framework (**3**) is attributed to the flexibility of both the Ce(III) coordination sphere and coordination modes of the Hpydc⁻ and pydc²⁻ ligands under different reaction conditions. The three compounds illustrate how the tuning of the coordination geometry of Ce(III) translates into different dimensionality, which is readily influenced by reaction temperature and ancillary ligand presence. Moreover, the porosity of MOF **3** was confirmed by N₂ and CO₂ gas adsorption/desorption. Finally, the catalytic activity of MOF **3** was examined in acetalization reactions in a series of aromatic aldehydes with methanol.

4.1. Introduction

Metal-organic frameworks (MOFs) as a class of nanoporous solids have received tremendous attention in various applications such as catalysis,¹⁻³ gas storage,⁴⁻⁵ magnetism,⁶⁻⁷ sensing⁸⁻¹⁰ and drug delivery.¹¹ Within this context, the design of coordination polymers (CPs) and MOFs have gained widespread interest during the last decades due to the vast diversity of organic ligands and metal nodes that can be incorporated in such compounds to construct intriguing architectures and topologies. Numerous attempts have been geared for the design of CPs and MOFs, using the local geometry of metal ions and functional ligands. Nevertheless, it is still challenging to control the dimensionality of the target compounds, structural topology and pore dimensions to obtain advanced MOF materials, suitable for more specialized applications.¹²⁻¹⁵

Lanthanide (Ln) CPs have attracted current research efforts due to their high and significant flexibility in coordination modes and numbers, as they can incorporate various modular and adjustable multi-dimensional framework materials.¹⁶⁻²² The combination of lanthanide luminescence, magnetic, and Lewis acid properties, with the diversity and features of CPs, can potentially be applied in heterogeneous catalysis,²³⁻²⁵ luminescent molecular thermometers,²⁶⁻²⁸ sensors,²⁹⁻³² and magnetic compounds.³³ The coordination modes in transition metals are mostly controlled by d-orbital directional features. In contrast, due to the shielded valence orbitals in lanthanide ions, they do not display specific coordination geometries and show significant flexibility in both coordination numbers and geometries. Therefore, design and control over the coordination sphere of lanthanide frameworks appears to be challenging, due to the effect of several factors, such as metal-ligand interactions, auxiliary ligand nature, outer-sphere counter ion, hydrogen bonding groups and reaction conditions (temperature, solvent, pH, etc.). So far, very few studies have reported the rational design and synthesis of rare earth CPs and MOFs. The report of Ayhan *et al.* described the structural coordination chemistry of two new Ce(III)-based MOFs. In this case, small changes to the reaction conditions resulted in distinctive structures.³⁴ Another study demonstrated the formation of tubular Ln-based frameworks depending on the reaction conditions as well as the counterion. In the

presence of Cl^- or NO_3^- anions, a tubular structure was formed, while by using BF_4^- and OAc^- anions, a zigzag 2D compound was obtained.³⁵

Since Ln coordination compounds display significant flexibility in both coordination numbers and geometries, we targeted Ce(III)-based frameworks as promising candidates for designing new structures.³⁶⁻³⁷ The large ionic radius of Ce(III) ions allows to adjust coordination modes by adapting reaction conditions to produce distinctive structures. In this work, we report the design and synthesis of three new Ce(III)-based frameworks using 2,4-pyridinedicarboxylic acid as a linker. Small changes to the reaction conditions led to three different structures ranging from a one-dimensional coordination polymer to a three-dimensional porous MOF. Moreover, the catalytic properties of 3D MOF in acetalization reactions of different aldehydes with methanol were investigated.

4.2. Results and Discussion

4.2.1. Synthesis and Preliminary Characterization

CP **1**, $[\text{Ce}(\text{pydc})(\text{Hpydc})(\text{H}_2\text{O})_4]_n$, was synthesized by conventional heating of $\text{Ce}(\text{NO}_3)_3 \cdot 6\text{H}_2\text{O}$ and 2,4- H_2pydc in a molar ratio of 2:3 in water at 100 °C. After slow evaporation within 5 weeks, pale-yellow single crystals of **1** were obtained. In addition, a yellow precipitation of **1** can be obtained in a shorter time by refluxing a more concentrated solution for 3 h in water. CP **2**, $[\text{Ce}(\text{pydc})(\text{Hpydc})(\text{H}_2\text{O})_2]_n$, was synthesized with the same reaction mixture as **1** but using a hydrothermal condition at 100 °C. After cooling of the mixture during 24 h to room temperature, light-yellow crystals of **2** were prepared. MOF **3**, $\{[\text{Ce}_3(\text{pydc})_4(\text{H}_2\text{O})_2\text{NO}_3] \cdot 4\text{H}_2\text{O}\}_n$, was synthesized under the same conditions as **2**. However, nicotinamide was added as an ancillary ligand, which gives the yellow single crystals of **3**, suitable for the X-ray analysis. Although the nicotinamide ligand is not coordinated in the product, its presence is crucial for the growth of the crystalline 3D MOF **3**, since without it the 2D CP **2** is obtained. The presence of trace amounts of disordered nicotinamide in **3** was confirmed during the refinement of the crystal structure, as well as by observing some discrepancy between calculated and

experimental results of elemental analysis. All of the prepared compounds are stable in air.

The IR spectra of all compounds show characteristic strong and broad bands for the coordinated carboxylate groups (COO^-) of the 2,4-pydc ligands in the ranges of $1587\text{--}1604\text{ cm}^{-1}$ and $1371\text{--}1402\text{ cm}^{-1}$, for the asymmetric and symmetric stretching vibrations, respectively. In addition, the characteristic broad peaks of the O-H vibration of water and/or carboxylic acid groups centered at around 3241 cm^{-1} (**1**), 3318 cm^{-1} (**2**) and 3305 cm^{-1} (**3**) (Figure S4.1).

The thermal stability of **1**, **2** and **3** was determined by means of thermogravimetric analysis (TGA). The CP **1** is stable up to $148\text{ }^\circ\text{C}$ and then starts to completely decompose till $722\text{ }^\circ\text{C}$ with a mass loss of 63.18% (calc. 67.7%). The exothermic peak at $473\text{--}548\text{ }^\circ\text{C}$ in the DTA curve shows that compound **1** is fully decomposed. CP **2** reveals three mass loss steps after $172.6\text{ }^\circ\text{C}$. The coordination framework is thermally stable up to $397\text{ }^\circ\text{C}$ and at higher temperature, with an exothermic peak at $397\text{--}522\text{ }^\circ\text{C}$, the decomposition appears with a mass loss of 63.3% (calc. 66.0%). The TGA profile for MOF **3** shows a first weight loss step of 11.8% up to $148.8\text{ }^\circ\text{C}$, which is probably attributed to the loss of four water molecules and a nitrate anion (calc. 10.7%). The second mass loss of 2.8% occurs at $224\text{ }^\circ\text{C}$ which may be due to the loss of two coordinated water molecules (calc. 2.9%). On further heating, the decomposition of the organic components in **3** are observed, showing an exothermic peak at $393\text{--}498\text{ }^\circ\text{C}$ (Figure S4.2).

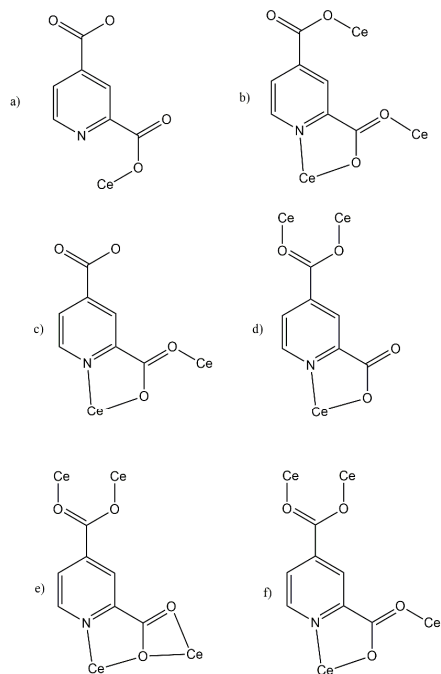
The experimental powder XRD patterns for compounds **1**, **2** and **3** are in good agreement with the corresponding simulated ones (Figure S4.3).

4.2.2. Structural Analysis

The reactions of the 2,4- H_2pydc ligand with $\text{Ce}(\text{NO}_3)_3 \cdot 6\text{H}_2\text{O}$ led to the formation of three 1D, 2D and 3D coordination frameworks. The structures of these compounds were characterized by single-crystal X-ray diffraction. The crystallographic data and structure refinement parameters for all materials are summarized in Table 4.1. The corresponding bond lengths and angles in the coordination sphere of the Ce(III) cations are listed in

Table S4.1. The coordination modes of the pydc ligand in compounds **1**, **2** and **3** are presented in scheme 4.1.

Table 4.1. Crystal data and refinement details for 1 , 2 and 3 .			
Empirical formula	C₁₄H₁₅CeN₂O₁₂ (1)	C₁₄H₁₇CeN₂O₁₀ (2)	C₂₈H₂₄Ce₃N₅O₂₅ (3)
Formula weight	543.40 g/mol	507.37 g/mol	1250.88 g/mol
Temperature	100.0 K	100.0 K	100.0 K
Wavelength	1.5418 Å	0.71073 Å	0.71073 Å
Crystal system	triclinic	triclinic	tetragonal
Space group	<i>P</i> -1	<i>P</i> -1	<i>P</i> 4 ₃ 2 ₁ 2
Unit cell dimensions	<i>a</i> = 6.3729(4) Å <i>b</i> = 6.6115(2) Å <i>c</i> = 19.9859(6) Å α = 82.857(3)° β = 81.281(4)° γ = 81.673(4)°	<i>a</i> = 6.2373(2) Å <i>b</i> = 9.3746(5) Å <i>c</i> = 14.2072(5) Å α = 72.685(4)° β = 84.587(3)° γ = 71.604(4)°	<i>a</i> = 9.6303(6) Å <i>b</i> = 9.6303(6) Å <i>c</i> = 52.293(3) Å α = 90° β = 90° γ = 90°
Volume	819.06(6) Å ³	752.55(6) Å ³	4849.8(7) Å ³
Z	2	2	4
Density (calculated)	2.203 Mg/m ³	2.239 Mg/m ³	1.697 Mg/m ³
Absorption coefficient	22.211 mm ⁻¹	3.091 mm ⁻¹	2.894 mm ⁻¹
F(000)	534.0	494.0	2356
Crystal size	0.18 x 0.07 x 0.068 mm ³	0.294 x 0.147 x 0.089 mm ³	0.17 x 0.18 x 0.19 mm ³
Theta range for data collection	9.00 to 150.706°	4.77 to 59.36°	2.4 to 29.5°
Index ranges	-7 ≤ <i>h</i> ≤ 7 -8 ≤ <i>k</i> ≤ 7 -22 ≤ <i>l</i> ≤ 25	-8 ≤ <i>h</i> ≤ 8 -12 ≤ <i>k</i> ≤ 12 -18 ≤ <i>l</i> ≤ 19	-12 ≤ <i>h</i> ≤ 13 -12 ≤ <i>k</i> ≤ 12 -69 ≤ <i>l</i> ≤ 66
Reflections collected	10829	16655	52792
Independent reflections	3285 [<i>R</i> (int) = 0.0632]	3837 [<i>R</i> (int) = 0.0818]	6251 [<i>R</i> (int) = 0.050]
Absorption correction	Numerical	Numerical	Numerical
Refinement method	Full-matrix least-squares on <i>F</i> ²	Full-matrix least-squares on <i>F</i> ²	Full-matrix least-squares on <i>F</i> ²
Data / restraints / parameters	3285 / 13 / 289	3837 / 6 / 257	6251 / 0 / 272
Goodness-of-fit on <i>F</i>²	1.042	1.044	1.006
Final <i>R</i>. [<i>I</i> > 2σ(<i>I</i>)]	<i>R</i> ₁ = 0.0422, <i>wR</i> ₂ = 0.1088	<i>R</i> ₁ = 0.0383, <i>wR</i> ₂ = 0.0681	<i>R</i> ₁ = 0.0478, <i>wR</i> ₂ = 0.1142
<i>R</i> indices (all data)	<i>R</i> ₁ = 0.0445, <i>wR</i> ₂ = 0.1114	<i>R</i> ₁ = 0.0509, <i>wR</i> ₂ = 0.0735	<i>R</i> ₁ = 0.0520, <i>wR</i> ₂ = 0.1164
Flack parameter	-	-	-0.014(15)
Largest diff. peak, hole	1.41 and -1.35 e.Å ⁻³	1.08 and -1.19 e.Å ⁻³	1.75 and -1.57 e.Å ⁻³



Scheme 4.1. The coordination modes of the 2,4-pydc ligands in the (a, b) structure **1**, (c,d) structure **2** and (e,f) structure **3**.

Crystal structure of 1. CP **1** crystallizes in the triclinic centrosymmetric space group $P\bar{1}$. The asymmetric unit of **1** contains one Ce(III) cation coordinated by one pydc²⁻ and one Hpydc⁻ anionic ligands and four coordinated water molecules. The central Ce(III) ion is nine-coordinated to eight oxygen atoms, from four water molecules, four carboxylate groups, and one nitrogen atom of a pydc²⁻ ligand (Figure 4.1a). In **1**, two Ce(III) centers are connected via two pydc²⁻ ligands to produce a binuclear unit. These units are connected to each other by carboxylic groups to make a one-dimensional channel (Figure 4.1b and 4.1c). In fact, each pydc²⁻ ligand acts as a tetradentate bridging ligand and is coordinated to one Ce(III) in a bidentate fashion through the pyridine nitrogen atom and a carboxylate oxygen atom and two more Ce(III) ions in a monodentate fashion through

single carboxylate oxygen atoms. Furthermore, a Hpydc⁻ ligand is bound to each Ce(III) center through a single carboxylate oxygen atom. As shown in scheme 1a and 1b, in compound **1** two different coordination modes of pydc are observed, which are coordinated to 1 and 3 distinct Ce(III) ions, respectively. Extensive non-covalent interactions such as $\pi \cdots \pi$ stacking interactions and strong O–H \cdots O hydrogen bonds exist between two neighboring chains. The $\pi \cdots \pi$ stacking interactions (with centroid-centroid distances of 3.712 Å) between single 1D chains, as illustrated in Figure 4.1d, plays an important role in the final framework. Furthermore, the coordinated water molecules contribute to the formation of intermolecular hydrogen bonds involving carboxylate O atoms (Table S4.2). As a result, the 1D chains are further assembled into a 3D supramolecular network (Figure 4.1d and 4.1e). To describe the 1D architecture of **1** more clearly, the TOPOS program³⁸ was used to analyze the topological structure. If every Ce ion is regarded as a node and each Hpydc⁻ and pydc²⁻ ligands serves as a linker, CP **1** could simplify as a 3-c net (uninodal net) topological structure, characterized by $\{4^2.6\}$ point symbol (Figure 4.4a).

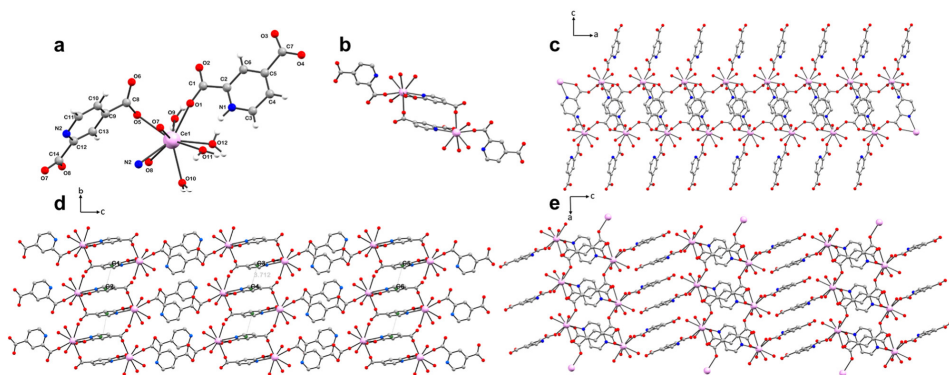


Figure 4.1. (a) Coordination environment of the Ce(III) cation in **1**. (b, c) Fragment of the 1D coordination polymer chain of **1**. (d, e) Fragment of the 3D supramolecular framework of **1**.

Crystal structure of 2. CP **2** crystallizes in the triclinic centrosymmetric space group *P*-1 and the asymmetric unit consists of a Ce(III) cation, one pydc²⁻ and one Hpydc⁻ ligands

and two coordinated water molecules. Here, the Hpydc⁻ ligand has a protonated carboxyl group instead of a protonated pyridine nitrogen atom. The Ce(III) center is coordinated to five pydc²⁻ units and two water molecules to form an overall nine-coordinated local geometry of the metal center (Figure 4.2a). Three pydc²⁻ units are monodentately coordinated to the Ce(III) center through a single carboxylate atom and two remaining pydc²⁻ units are coordinated in a bidentate fashion, similar to the one seen in CP **1**, through a carboxylate oxygen atom and a pyridine nitrogen atom. As indicated in scheme 1c and 1d in compound **2** also two different coordination modes of pydc²⁻ are observed, which are coordinated to 2 and 3 distinct Ce(III) ions, respectively. Finally, two water molecules are bound to complete the nine-coordination of the Ce(III). Viewing down the a-axis reveals that the Ce(III) metal ions are linked via a carboxylate group, from one of the pydc²⁻ linkages. Furthermore, another carboxylate group is bridging the Ce(III) ions to complete the overall 2D structure (Figure 4.2b-2d). Similar to the CP **1**, extensive face-to-face $\pi\cdots\pi$ stacking interactions of pyridyl rings with centroid-centroid distances of 3.937 Å exist between the neighboring layers. In addition, strong O–H \cdots O hydrogen bonds of the coordinated water molecules and protonated carboxylate O atoms in collaboration with $\pi\cdots\pi$ stacking serves to connect 2D sheets of **2** into a 3D supramolecular framework (Figure 4.2e-f). Corresponding hydrogen bonding distances and angles are listed in Table S4.2. For better insight into this intricate net of the 2D coordinating polymer, a topological analysis of compound **2** was performed. Its structure consists of layers parallel to (001) with a thickness of 9.22 Å and can also be simplified to simple node-and-linker net using topology approach. The CP **2** structure could simplify as a 3,5-c net with stoichiometry (3-c)(5-c); 2-nodal net characterized by $\{4^2.6^7.8\}\{4^2.6\}$ point symbol (Figure 4.4b).

Metal- and Covalent Organic Frameworks for Advanced Applications: Heterogeneous Catalysis and Sensing

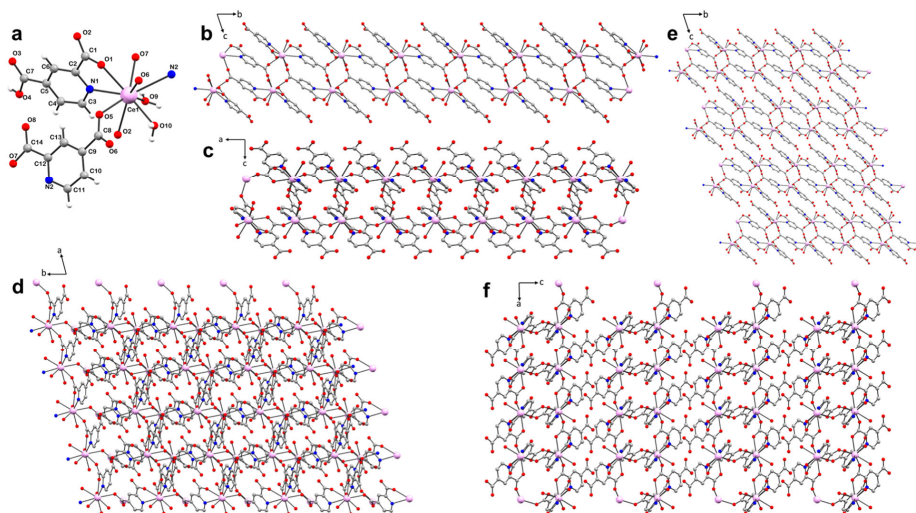


Figure 4.2. (a) Coordination environment of the Ce(III) cation in **2**. (b, c and d) Fragment of the 2D coordination polymer grid of **2**. (e, f) Fragment of the 3D supramolecular framework of **2**.

Crystal structure of 3. MOF **3** crystallizes in the tetragonal non-centrosymmetric space group $P4_32_12$ and the asymmetric unit contains two crystallographically independent Ce1 and Ce2 centers, two pydc²⁻ ligands, one and half of coordinated water, one half of coordinated nitrate ion and four halves of non-coordinated water molecules that are disordered (Figure 4.3a). The Ce2 center is found on a special position (2-fold axis), while the nitrate anion is observed in half occupancy. In **3**, the Ce1 is eight-coordinated whereas the Ce2 is nine-coordinated similar to those in **1** and **2**. The Ce1 coordinates to five pydc²⁻ ligands and statistically to one nitrate anion or water molecule to form the overall 8-coordinate local geometry of the metal center. Three pydc²⁻ units are bound to the Ce(III) ion though a single carboxylate oxygen atom. The two other pydc²⁻ ligands are bound to the Ce1 center in a bidentate mode via a carboxylate oxygen atom and pyridine nitrogen atom. A nitrate anion or a water molecule (both with the occupation factor of 0.5) is bound to complete the coordination sphere of the Ce1 (CeO₆N₂) (See Figure 4.3b). The Ce2 coordinates to four pydc²⁻ in a monodentate fashion through a single oxygen atom of

carboxylate groups and two other pydc^{2-} in a bidentate mode via their carboxylate groups. Finally, one oxygen atom of a water molecule is coordinated to complete the nine-coordination of the Ce2 (CeO_9) (Figure 4.3b).

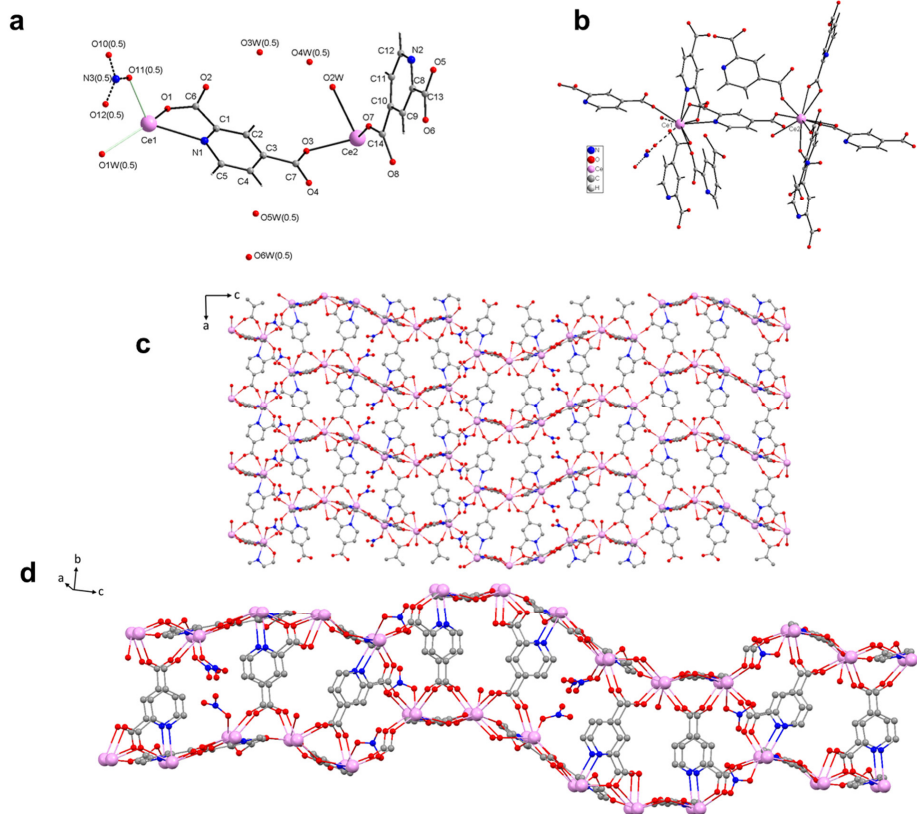
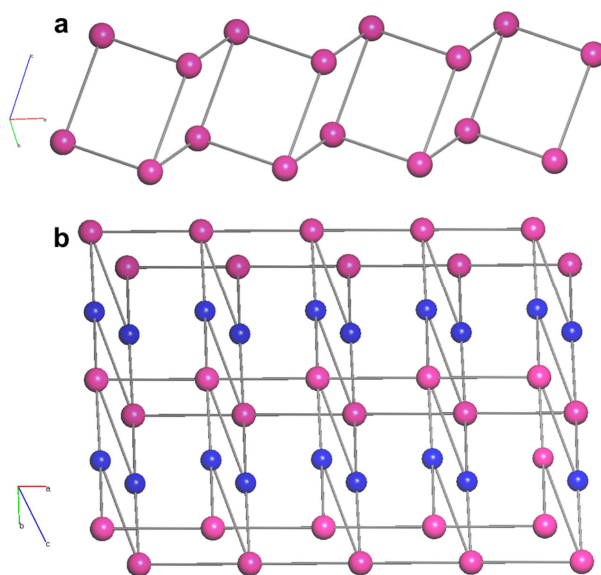


Figure 4.3. (a) Asymmetric unit of **3**. (b) Coordination environment of Ce1 and Ce2. (c) Fragment of the 3D network of **3**. (d) View of helical channel in **3**.

As it can be seen in scheme 1e and 1f, in compound **3** again two different coordination modes of pydc^{2-} are observed, which are coordinated to 4 and 4 separate Ce(III) ions respectively. Viewing down the b-axis shows that the Ce1 and Ce2 centers are connected

through bridging carboxylate groups to form the overall 3D network consisting of a helical channel with diagonal distance of $9.630 \times 9.630 \text{ \AA}^2$ determined via the Ce ions distance (Figure 4.3c-d). Disordered water molecules as solvent molecules that have been localized, as well as disordered nicotinamide molecules, highly disordered, which have not been modeled, fill the channels in the structure. Note that due to the wavelike structure, the channels are not elongated. In order to better identify the intricate net of the 3D MOF, suitable connectors can be defined by using topological approach. As exhibited in Figure 4.4c, Ce ion (pink) is regarded as a node and each pydc²⁻ ligand serves as a linker, MOF **3** could simplify as a 8-c net (uninodal net) characterized by $\{3^6.4^{16}.5^6\}$ point symbol.



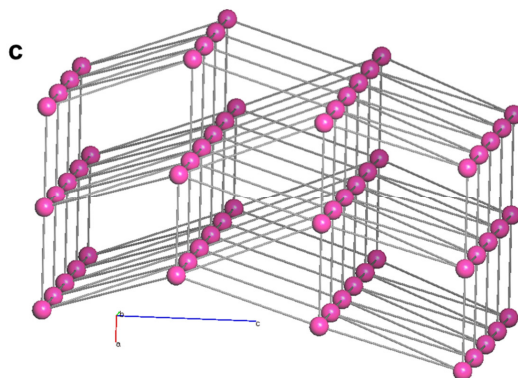


Figure 4.4. View of (a) the 3-c net topological structure of **1**, (b) the 3,5-c net with stoichiometry (3-c)(5-c) of **2** (color codes: blue codes represent the center ring of the 3-connected Hpydc⁻ and pydc²⁻ ligands and pink codes represent Ce³⁺ ions) and (c) the 8-c net topological structure of **3**.

The adsorption characteristics of the frameworks in MOF **3** was investigated, and its porosity was confirmed by the N₂ and CO₂ adsorption isotherms at 77 and 298 K, respectively. As demonstrated in Figure 4.5, after desolvation the framework maintains a permanent porosity and exhibits a Langmuir surface area (S_{lang}) of 310 m² g⁻¹ with a pore volume of 0.15 cm³ g⁻¹. Gas adsorption measurement at 1 bar was performed to investigate the CO₂ uptake capacities of **3**, which is shown in Figure S4.4 in Supporting Information. After activation at 120 °C under vacuum overnight, the adsorption capacities of MOF **3** for CO₂ was 0.81 mmol g⁻¹ at room temperature.

The 1D Compound **1** is formed by refluxing the reaction mixture, while the same reaction mixture under hydrothermal condition resulted in the 2D structure **2**. This may be due to the higher reaction temperature in the closed system which plausibly leads to various coordination modes of the pydc ligand. Furthermore, by adding the nicotinamide to the identical reaction mixture under the same conditions as material **2** the 3D compound **3** is obtained. Although the nicotinamide ligand does not coordinate to the Ce centers, it can facilitate the coordination of pydc to the metal centers through deprotonating 2,4-H₂pydc and also via non-covalent interactions. From these observations it can be concluded that

the applied reaction conditions have a direct impact on the obtained structures. Furthermore, an ancillary ligand can conduct the obtained product to a specific structure even without being in the final framework.

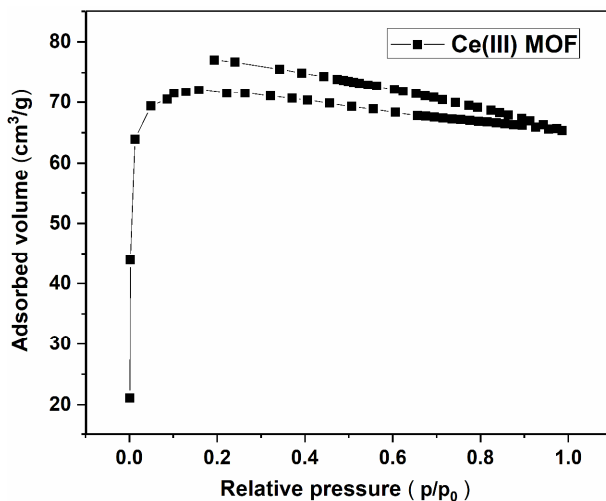


Figure 4.5. Nitrogen sorption isotherm of MOF 3.

So far there are a few reported lanthanide-based coordination polymers using 2,4- H_2pydc as the ligand.³⁹⁻⁴² However, these structures are bimetallic or oxalate was used as the ancillary ligand. To the best of our knowledge, the only Ce-based coordination polymer with 2,4- H_2pydc ligand is reported by Lush *et. al.*⁴³ In this compound, the Ce(III) cation is nine-coordinated (CeNO_8) and formed by three pydc anions, one oxalate anion, and three water molecules. The oxalate and pydc ligands bridge the Ce(III) cations, forming a two-dimensional coordination polymer. The pydc^{2-} ligand acts as a tetradentate bridging ligand similar the coordination mode observed in our 1D coordination polymer (scheme 1b) and is coordinated to one Ce(III) in a bidentate fashion through the pyridine nitrogen atom and a carboxylate oxygen atom and two more Ce(III) ions in a monodentate fashion through single carboxylate oxygen atoms.

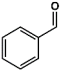
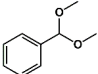
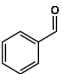
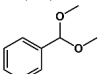
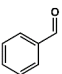
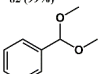
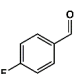
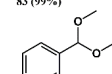
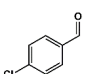
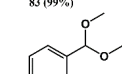
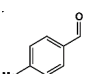
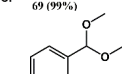
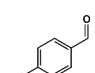
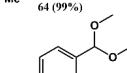
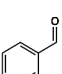
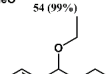
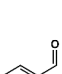

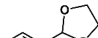
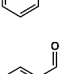

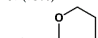
4.2.3. Catalytic acetalization reaction

Lewis acid metal sites are known to promote the acetalization reaction of aldehydes.⁴⁴⁻⁴⁶ Therefore, the catalytic activity of MOF **3** was investigated for the acetalization reaction of benzaldehyde and methanol as model reactants. The obtained results are given in Table 4.2. In the presence of benzaldehyde and methanol as the substrates and MOF **3** catalyst, a good conversion of 80% with 99% selectivity towards benzaldehyde dimethyl acetal as the desired product was observed. In order to clarify the general applicability of the MOF **3** catalyst, various substrates and different alcohols such as ethanol, ethylene glycol and 1,3-propanediol were tested and the obtained results are listed in Table 4.2. In general, the catalyst showed a good activity for all types of examined substrates as well as complete selectivity towards the related product. Additionally, the catalytic activity of compound **1** (1D) and compound **2** (2D) were investigated for the acetalization reaction of benzaldehyde and methanol under the same reaction conditions. The catalysts showed good catalytic activity with conversions of 82 and 83% respectively (Table 4.2, entry 2 and 3).

Based on the work of Kanai and co-workers⁴⁷ the possible reaction mechanism is illustrated in Figure S4.7. As shown, the removal of water molecules of the framework creates open coordination sites capable of attaching to organic molecules. Hereafter, the interaction of both benzaldehyde and methanol with the Ce center and coordinated oxygens can facilitate the nucleophilic addition of the OH group in methanol on the carbon atom of the aldehyde group in benzaldehyde to give the hemiacetal derivative analogous. Afterward, the hemiacetal reacts with another methanol molecule, most likely with the assistance of the Ce-MOF catalyst, to give the corresponding acetal derivative.

The recyclability of MOF **3** was examined after separation of the catalyst from reaction mixture at the end of the reaction. The recovered catalyst was reused at least 3 times for the acetalization reaction of benzaldehyde with methanol and the obtained results are given in Figure S4.5. As can be observed, the recovered MOF **3** maintains similar activity after 3 recycles. Further evidence of the stability of the catalyst was confirmed by powder XRD analysis after 3 times reuse (Figure S4.6).

Table 4.2. Catalytic performance of the MOF 3 catalyst towards the acetalization reaction of various benzaldehyde derivatives with alcohols.

Entry	Benzaldehyde derivatives	Alcohol	Product
1		CH ₃ OH	 79 (99%)
2 ^a		CH ₃ OH	 82 (99%)
3 ^b		CH ₃ OH	 83 (99%)
4 ^c		CH ₃ OH	 83 (99%)
5 ^c		CH ₃ OH	 69 (99%)
6 ^c		CH ₃ OH	 64 (99%)
7 ^c		CH ₃ OH	 54 (99%)
8 ^d		CH ₃ CH ₂ OH	 54 (99%)
9 ^e			 87 (78%)
10 ^f			 98 (99%)

Reaction conditions: 0.33 mmol benzaldehyde, 0.008 mmol catalyst (10 mg), 0.5 ml methanol, 0.2 mmol dodecane, 40 °C, 24 h, Conversions are determined based on GC-MS, Selectivity is towards the related acetal. Conversion and selectivity are reported respectively in parenthesis.

^a Compound 1 (1D) was used as the catalyst (0.008 mmol, 4.3 mg). ^b Compound 2 (2D) was used as the catalyst (0.008 mmol, 4 mg). ^c 60 °C. ^d Ethanol, ^e Ethylene glycol and ^f 1,3-Propanediol were used as the solvent, respectively.

4.3. Conclusion

In summary, we have developed three new 1D, 2D and 3D Ce(III)-based frameworks by small changes in the synthetic routes. The obtained results revealed the importance of the reaction conditions as well as the ancillary ligand for the preparation of distinctive structures and the effect on the properties of the materials. This shows that the lanthanide ions do not have the preference for a specific coordination geometry because of their valence orbitals which are buried inside. Therefore, the nature of coordination modes in lanthanide ions is controlled by a subtle interplay between metal-ligand and inter-ligand steric interactions depending on the reaction conditions. These findings demonstrate that Ce(III) ions are outstanding candidates to adopt distinct coordination environments due to their adjustable coordination modes which is an important step towards the design of Ce(III)-based frameworks for more specialized applications. The MOF **3** showed good activity and selectivity in acetalization reaction and could be recycled without loss of activity or selectivity.

4.4. Experimental Section

4.4.1. Materials and instrumentation

For details please see Appendix.

4.4.2. Synthesis

$[Ce(pydc)(Hpydc)(H_2O)_4]_n$ (**1**). A mixture of $Ce(NO_3)_3 \cdot 6H_2O$ (0.218 g, 0.5 mmol) and 2,4- H_2pydc (0.126 g, 0.75 mmol) was refluxed for 1 h in 5 mL of water. The resulting solution was filtered and left to stand at room temperature. Pale-yellow single crystals, suitable for

X-ray crystallography, were obtained by slow evaporation after five weeks (yield 63%). Elemental Anal. Calcd for $C_{14}H_{15}CeN_2O_{12}$: C, 30.94; H, 2.78; N, 5.15%. Found: C, 31.51; H, 3.34; N, 4.87%. IR (cm^{-1}): 3249 br/m, 1677 w, 1587 s, 1548 m, 1479 w, 1440 w, 1392 m, 1371 s, 1280 m, 1093 w, 1012 w, 777 m.

$[Ce(pydc)(Hpydc)(H_2O)_2]_n$ (**2**). A mixture of $Ce(NO_3)_3 \cdot 6H_2O$ (0.218 g, 0.5 mmol) and 2,4- H_2pydc (0.126 g, 0.75 mmol) in 3 mL of H_2O was placed in a 12 mL Teflon-lined stainless steel autoclave. The mixture was heated to 100 °C within 15 min, then kept at this temperature for 1 h and cooled to ambient temperature within 24 h. Light-yellow crystals of **2** were filtered off, washed with water and dried in air (yield 60%). Elemental Anal. Calcd for $C_{14}H_{11}CeN_2O_{10}$: C, 33.11; H, 2.18; N, 5.51%. Found: C, 32.89; H, 2.16; N, 5.11%. IR (cm^{-1}): 3326 br/m, 3120 br, 1693 m, 1666 w, 1604 s, 1562 m, 1471 m, 1427 m, 1371 m, 1276 m, 1249m, 1191 w, 1093 w, 1006 w, 939 w, 875 w, 771 s, 707 s.

$\{[Ce_3(pydc)_4(H_2O)_2NO_3] \cdot 4H_2O\}_n$ (**3**). A mixture of $Ce(NO_3)_3 \cdot 6H_2O$ (0.218 g, 0.5 mmol), 2,4- H_2pydc (0.126 g, 0.75 mmol) and nicotinamide (0.062 g, 0.5 mmol) in 3 mL of H_2O was placed in a 12 mL Teflon-lined stainless steel autoclave. The mixture was heated to 100 °C within 15 min, then kept at this temperature for 1 h and cooled to ambient temperature within 24 h. Yellow crystals of **3** were filtered off, washed with water and dried in air (yield 51%). Elemental Anal. Calcd for $C_{28}H_{24}Ce_3N_5O_{25}$: C, 26.88; H, 1.93; N, 5.59%. Found: C, 30.31; H, 2.30; N, 5.35%. IR (cm^{-1}): 3305 br/m, 1645 s, 1592 vs, 1481 s, 1454 s, 1402 vs, 1305 w, 1245 w, 1095 w, 1014 m, 883 w, 831 w, 788s, 725s.

In addition, compound **3** can also be obtained by performing the reaction at 150 °C instead of 100 °C and without the addition of nicotinamide, however in this case the crystals were not suitable for the X-ray single crystal analysis.

4.4.3. General procedure for the acetalization reaction of benzaldehyde

During a typical catalytic test, MOF **3** (0.008mmol, 10 mg), dodecane as an internal standard (0.2 mmol), benzaldehyde (0.33 mmol) and methanol (0.5 ml) were added into a Schlenk tube. The tube was sealed and then heated to 40 °C for 24 h. After each catalytic run, the catalyst was recovered by filtration, washed with methanol and used

directly in the subsequent runs. Samples were withdrawn after 24 h reaction, and after cooling and dilution with the solvent, were analyzed using an ultra-fast gas chromatograph (Thermo, Interscience) equipped with a flame ionization detector (FID).

4.5. References

1. Abednatanzi, S.; Leus, K.; Derakhshandeh, P. G.; Nahra, F.; De Keukeleere, K.; Van Hecke, K.; Van Driessche, I.; Abbasi, A.; Nolan, S. P.; Van Der Voort, P., POM@IL-MOFs - inclusion of POMs in ionic liquid modified MOFs to produce recyclable oxidation catalysts. *Catal Sci Technol* **2017**, *7* (7), 1478-1487.
2. Abednatanzi, S.; Derakhshandeh, P. G.; Abbasi, A.; Van der Voort, P.; Leus, K., Direct Synthesis of an Iridium(III) Bipyridine Metal-Organic Framework as a Heterogeneous Catalyst for Aerobic Alcohol Oxidation. *Chemcatchem* **2016**, *8* (23), 3672-3679.
3. Huang, Y. B.; Liang, J.; Wang, X. S.; Cao, R., Multifunctional metal-organic framework catalysts: synergistic catalysis and tandem reactions. *Chem Soc Rev* **2017**, *46* (1), 126-157.
4. Wang, H. H.; Shi, W. J.; Hou, L.; Li, G. P.; Zhu, Z. H.; Wang, Y. Y., A Cationic MOF with High Uptake and Selectivity for CO₂ due to Multiple CO₂-Philic Sites. *Chem-Eur J* **2015**, *21* (46), 16525-16531.
5. Zhang, Y. B.; Furukawa, H.; Ko, N.; Nie, W. X.; Park, H. J.; Okajima, S.; Cordova, K. E.; Deng, H. X.; Kim, J.; Yaghi, O. M., Introduction of Functionality, Selection of Topology, and Enhancement of Gas Adsorption in Multivariate Metal Organic Framework-177. *J Am Chem Soc* **2015**, *137* (7), 2641-2650.
6. Chuang, Y. C.; Ho, W. L.; Sheu, C. F.; Lee, G. H.; Wang, Y., Crystal engineering from a 1D chain to a 3D coordination polymer accompanied by a dramatic change in magnetic properties. *Chem Commun* **2012**, *48* (87), 10769-10771.
7. Bauer, W.; Schlamp, S.; Weber, B., A ladder type iron(II) coordination polymer with cooperative spin transition. *Chem Commun* **2012**, *48* (82), 10222-10224.
8. Mukherjee, S.; Desai, A. V.; More, Y. D.; Inamdar, A. I.; Ghosh, S. K., A Bifunctional Metal-Organic Framework: Striking CO₂-Selective Sorption Features along with Guest-Induced Tuning of Luminescence. *Chempluschem* **2016**, *81* (8), 702-707.

9. Pal, S.; Bharadwaj, P. K., A Luminescent Terbium MOF Containing Hydroxyl Groups Exhibits Selective Sensing of Nitroaromatic Compounds and Fe(III) Ions. *Cryst Growth Des* **2016**, *16* (10), 5852-5858.
10. Gao, R. C.; Guo, F. S.; Bai, N. N.; Wu, Y. L.; Yang, F.; Liang, J. Y.; Li, Z. J.; Wang, Y. Y., Two 3D Isostructural Ln(III)-MOFs: Displaying the Slow Magnetic Relaxation and Luminescence Properties in Detection of Nitrobenzene and Cr2O7²⁻. *Inorg Chem* **2016**, *55* (21), 11323-11330.
11. An, J. Y.; Geib, S. J.; Rosi, N. L., Cation-Triggered Drug Release from a Porous Zinc-Adeninate Metal-Organic Framework. *J Am Chem Soc* **2009**, *131* (24), 8376-+.
12. Zhang, J. P.; Zhang, Y. B.; Lin, J. B.; Chen, X. M., Metal Azolate Frameworks: From Crystal Engineering to Functional Materials. *Chem Rev* **2012**, *112* (2), 1001-1033.
13. Kitagawa, S.; Kitaura, R.; Noro, S., Functional porous coordination polymers. *Angew Chem Int Edit* **2004**, *43* (18), 2334-2375.
14. Yaghi, O. M.; O'Keeffe, M.; Ockwig, N. W.; Chae, H. K.; Eddaoudi, M.; Kim, J., Reticular synthesis and the design of new materials. *Nature* **2003**, *423* (6941), 705-714.
15. Furukawa, H.; Cordova, K. E.; O'Keeffe, M.; Yaghi, O. M., The Chemistry and Applications of Metal-Organic Frameworks. *Science* **2013**, *341* (6149), 974-+.
16. Cui, Y. J.; Yue, Y. F.; Qian, G. D.; Chen, B. L., Luminescent Functional Metal-Organic Frameworks. *Chem Rev* **2012**, *112* (2), 1126-1162.
17. Duan, J. G.; Higuchi, M.; Foo, M. L.; Horike, S.; Rao, K. P.; Kitagawa, S., A Family of Rare Earth Porous Coordination Polymers with Different Flexibility for CO₂/C₂H₄ and CO₂/C₂H₆ Separation. *Inorg Chem* **2013**, *52* (14), 8244-8249.
18. Guo, H. L.; Zhu, Y. Z.; Qiu, S. L.; Lercher, J. A.; Zhang, H. J., Coordination Modulation Induced Synthesis of Nanoscale Eu(1-x)Tb(x)-Metal-Organic Frameworks for Luminescent Thin Films. *Adv Mater* **2010**, *22* (37), 4190-+.
19. Le Natur, F.; Calvez, G.; Daiguebonne, C.; Guillou, O.; Bernot, K.; Ledoux, J.; Le Polles, L.; Roiland, C., Coordination Polymers Based on Heterohexanuclear Rare Earth Complexes: Toward Independent Luminescence Brightness and Color Tuning. *Inorg Chem* **2013**, *52* (11), 6720-6730.
20. Freslon, S.; Luo, Y.; Calvez, G.; Daiguebonne, C.; Guillou, O.; Bernot, K.; Michel, V.; Fan, X., Influence of Photoinduced Electron Transfer on Lanthanide-Based

Coordination Polymer Luminescence: A Comparison between Two Pseudoisoreticular Molecular Networks. *Inorg Chem* **2014**, *53* (2), 1217-1228.

21. Derakhshandeh, P. G.; Soleimannejad, J.; Janczak, J., Sonochemical synthesis of a new nano-sized cerium(III) coordination polymer and its conversion to nanocerium. *Ultrason Sonochem* **2015**, *26*, 273-280.

22. Derakhshandeh, P. G.; Soleimannejad, J.; Janczak, J.; Kaczmarek, A. M.; Van Hecke, K.; Van Deun, R., Mechanochemically synthesized crystalline luminescent 2D coordination polymers of La³⁺ and Ce³⁺, doped with Sm³⁺, Eu³⁺, Tb³⁺, and Dy³⁺: synthesis, crystal structures and luminescence. *Crystengcomm* **2016**, *18* (35), 6738-6747.

23. Xiong, Y. H.; Chen, S. H.; Ye, F. G.; Su, L. J.; Zhang, C.; Shen, S. F.; Zhao, S. L., Synthesis of a mixed valence state Ce-MOF as an oxidase mimetic for the colorimetric detection of biothiols. *Chem Commun* **2015**, *51* (22), 4635-4638.

24. Ji, P. F.; Sawano, T.; Lin, Z. K.; Urban, A.; Boures, D.; Lin, W. B., Cerium-Hydride Secondary Building Units in a Porous Metal-Organic Framework for Catalytic Hydroboration and Hydrophosphination. *J Am Chem Soc* **2016**, *138* (45), 14860-14863.

25. Lin, A.; Ibrahim, A. A.; Arab, P.; El-Kaderi, H. M.; El-Shall, M. S., Palladium Nanoparticles Supported on Ce-Metal-Organic Framework for Efficient CO Oxidation and Low-Temperature CO₂ Capture. *Acs Appl Mater Inter* **2017**, *9* (21), 17961-17968.

26. Kaczmarek, A. M.; Liu, Y. Y.; Wang, C.; Laforce, B.; Vincze, L.; Van Der Voort, P.; Van Hecke, K.; Van Deun, R., Lanthanide "Chameleon" Multistage Anti-Counterfeit Materials. *Adv Funct Mater* **2017**, *27* (20).

27. Rao, X. T.; Song, T.; Gao, J. K.; Cui, Y. J.; Yang, Y.; Wu, C. D.; Chen, B. L.; Qian, G. D., A Highly Sensitive Mixed Lanthanide Metal-Organic Framework Self-Calibrated Luminescent Thermometer. *J Am Chem Soc* **2013**, *135* (41), 15559-15564.

28. Cui, Y. J.; Xu, H.; Yue, Y. F.; Guo, Z. Y.; Yu, J. C.; Chen, Z. X.; Gao, J. K.; Yang, Y.; Qian, G. D.; Chen, B. L., A Luminescent Mixed-Lanthanide Metal-Organic Framework Thermometer. *J Am Chem Soc* **2012**, *134* (9), 3979-3982.

29. Hu, Z. C.; Deibert, B. J.; Li, J., Luminescent metal-organic frameworks for chemical sensing and explosive detection. *Chem Soc Rev* **2014**, *43* (16), 5815-5840.

30. Meyer, L. V.; Schonfeld, F.; Muller-Buschbaum, K., Lanthanide based tuning of luminescence in MOFs and dense frameworks - from mono- and multimetal systems to sensors and films. *Chem Commun* **2014**, 50 (60), 8093-8108.
31. Tan, H. L.; Liu, B. X.; Chen, Y., Lanthanide Coordination Polymer Nanoparticles for Sensing of Mercury(II) by Photoinduced Electron Transfer. *Acs Nano* **2012**, 6 (12), 10505-10511.
32. Xu, H.; Hu, H. C.; Cao, C. S.; Zhao, B., Lanthanide Organic Framework as a Regenerable Luminescent Probe for Fe³⁺. *Inorg Chem* **2015**, 54 (10), 4585-4587.
33. Malaestean, I. L.; Kutluca-Alici, M.; Ellern, A.; van Leusen, J.; Schilder, H.; Speldrich, M.; Baca, S. G.; Kogerler, P., Linear, Zigzag, and Helical Cerium(III) Coordination Polymers. *Cryst Growth Des* **2012**, 12 (3), 1593-1602.
34. Ayhan, O.; Malaestean, I. L.; Ellern, A.; van Leusen, J.; Baca, S. G.; Kogerler, P., Assembly of Cerium(III) 2,2'-Bipyridine-5,5'-dicarboxylate-based Metal-Organic Frameworks by Solvent Tuning. *Cryst Growth Des* **2014**, 14 (7), 3541-3548.
35. Ghosh, S. K.; Bharadwaj, P. K., Coordination polymers of La(III) as bunched infinite nanotubes and their conversion into an open-framework structure. *Inorg Chem* **2005**, 44 (9), 3156-3161.
36. Ebrahim, A. M.; Bandosz, T. J., Ce(III) Doped Zr-Based MOFs as Excellent NO₂ Adsorbents at Ambient Conditions. *Acs Appl Mater Inter* **2013**, 5 (21), 10565-10573.
37. Lammert, M.; Glissmann, C.; Reinsch, H.; Stock, N., Synthesis and Characterization of New Ce(IV)-MOFs Exhibiting Various Framework Topologies. *Cryst Growth Des* **2017**, 17 (3), 1125-1131.
38. Blatov, V. A.; Shevchenko, A. P.; Proserpio, D. M., Applied Topological Analysis of Crystal Structures with the Program Package ToposPro. *Cryst Growth Des* **2014**, 14 (7), 3576-3586.
39. Huang, Y. G.; Wu, M. Y.; Wei, W.; Gao, Q.; Yuan, D. Q.; Jiang, F. L.; Hong, M. C., Unprecedented ferromagnetic interaction in an erbium(III)-copper(II) coordination polymer. *J Mol Struct* **2008**, 885 (1-3), 23-27.
40. Min, D.; Lee, S. W., Terbium-oxalate-pyridinedicarboxylate coordination polymers suggesting the reductive coupling of carbon dioxide (Co-2) to oxalate (C₂O₄²⁻): [Tb-2

(3,5-PDC)(2)(H₂O)(4)(C₂O₄)]center dot 2H₂O and [Tb(2,4-PDC) (H₂O) (C₂O₄)(0.5)] (PDC = pyridinedicarboxylate). *Inorg Chem Commun* **2002**, 5 (11), 978-983.

41. An, X. P.; Wang, H. S.; Li, G. C., Structures and Luminescent Properties of Two 2D Coordination Polymers Containing Tb(III) or Dy(III) Ions. *J Fluoresc* **2014**, 24 (2), 425-429.

42. Lush, S. F.; Shen, F. M., Poly[hexaaquaheakis(mu-pyridine-2,4-dicarboxylato)tricopper(II)-dieuropium(III)]. *Acta Crystallogr E* **2010**, 66, M1516-U370.

43. Shen, F. M.; Lush, S. F., Poly[[hexaaqua(mu(2)-oxalato-kappa O-4(1),O-2:O-1',O-2')bis(mu(3)-pyridine-2,4-dicarboxylato-kappa N-4,O-1:O-1':O-4)dicerium(III)] monohydrate]. *Acta Crystallogr E* **2012**, 68, M21-+.

44. Silveira, C. C.; Mendes, S. R.; Ziembowicz, F. I.; Lenardao, E. J.; Perin, G., The Use of Anhydrous CeCl₃ as a Recyclable and Selective Catalyst for the Acetalization of Aldehydes and Ketones. *J Brazil Chem Soc* **2010**, 21 (2), 371-374.

45. Cao, C. C.; Chen, C. X.; Wei, Z. W.; Qiu, Q. F.; Zhu, N. X.; Xiong, Y. Y.; Jiang, J. J.; Wang, D. W.; Su, C. Y., Catalysis through Dynamic Spacer Installation of Multivariate Functionalities in Metal-Organic Frameworks. *J Am Chem Soc* **2019**, 141 (6), 2589-2593.

46. Talebian-Kiakalaieh, A.; Amin, N. A. S.; Najaafi, N.; Tarighi, S., A Review on the Catalytic Acetalization of Bio-renewable Glycerol to Fuel Additives. *Front Chem* **2018**, 6.

47. Kanai, S.; Nagahara, I.; Kita, Y.; Kamata, K.; Hara, M., A bifunctional cerium phosphate catalyst for chemoselective acetalization. *Chem Sci* **2017**, 8 (4), 3146-3153.

48. Dolomanov, O. V.; Bourhis, L. J.; Gildea, R. J.; Howard, J. A. K.; Puschmann, H., OLEX2: a complete structure solution, refinement and analysis program. *J Appl Crystallogr* **2009**, 42, 339-341.

49. Sheldrick, G. M., A short history of SHELX. *Acta Crystallogr A* **2008**, 64, 112-122.

50. Sheldrick, G. M., Crystal structure refinement with SHELXL. *Acta Crystallogr C* **2015**, 71, 3-8.

4.6. Supporting Information

Table S4.1. Selected bond lengths [Å] and angles [°] for **1**, **2** and **3**.

1			
Ce1–O1	2.410(4)	Ce1–O10	2.505(4)
Ce1–O5	2.456(4)	Ce1–O11	2.555(4)
Ce1–O7 ⁱ	2.547(4)	Ce1–O12	2.614(4)
Ce1–O8 ⁱⁱ	2.540(4)	Ce1–N2 ⁱ	2.713(4)
Ce1–O9	2.555(4)		
O1–Ce1–O5	82.44(12)	O7 ⁱ –Ce1–O10	111.91(12)
O1–Ce1–O9	76.64(13)	O7 ⁱ –Ce1–N2 ⁱ	59.57(12)
O1–Ce1–O10	138.55(13)	O7 ⁱ –Ce1–O8 ⁱⁱ	130.17(11)
O1–Ce1–O11	77.10(13)	O8 ⁱⁱ –Ce1–O9	69.88(12)
O1–Ce1–O12	74.36(13)	O8 ⁱⁱ –Ce1–O10	67.17(12)
O1–Ce1–O7 ⁱ	69.80(12)	O8 ⁱⁱ –Ce1–N2 ⁱ	74.60(13)
O1–Ce1–N2 ⁱ	128.86(13)	O8 ⁱⁱ –Ce1–O12	137.02(12)
O1–Ce1–O8 ⁱⁱ	145.18(12)	O8 ⁱⁱ –Ce1–O11	98.48(14)
O5–Ce1–O9	72.52(12)	O9–Ce1–O10	113.74(13)
O5–Ce1–O10	138.83(12)	O9–Ce1–O11	68.11(13)
O5–Ce1–O11	138.75(13)	O9–Ce1–O12	132.56(12)
O5–Ce1–O12	137.65(13)	O9–Ce1–N2 ⁱ	136.67(12)
O5–Ce1–O7 ⁱ	73.18(12)	O10–Ce1–O11	71.21(12)

Chapter 4: Ce(III)-based Frameworks: From 1D Chain to 3D Porous Metal-Organic Framework

O5–Ce1–N2 ⁱ	76.99(12)	O10–Ce1–O12	69.92(13)
O5–Ce1–O8 ⁱⁱ	78.76(12)	O10–Ce1–N2 ⁱⁱ	72.33(12)
O7 ⁱ –Ce1–O12	65.76(12)	O11–Ce1–N2 ⁱ	142.59(12)
O7 ⁱ –Ce1–O11	129.53(13)	O11–Ce1–O12	69.33(14)
O7 ⁱ –Ce1–O9	134.35(12)	O12–Ce1–N2 ⁱ	90.56(12)

Symmetry codes: (i) 1-x, 1-y, 1-z; (ii) 2-x, 1-y, 1-z;

2

Ce1–O1	2.501(3)	Ce1–O7 ⁱⁱ	2.495(3)
Ce1–O5	2.487(3)	Ce1–N2 ⁱⁱ	2.752(4)
Ce1–O9	2.507(3)	Ce1–O2 ^{iv}	2.549(3)
Ce1–O10	2.529(3)	Ce1–O6 ^v	2.516(3)
Ce1–N1	2.681(3)		
O1–Ce1–O5	72.19(9)	O9–Ce1–N2 ⁱⁱ	77.53(10)
O1–Ce1–O9	128.95(9)	O2 ^{iv} –Ce1–O9	68.48(10)
O1–Ce1–O10	136.31(9)	O6 ^v –Ce1–O9	142.81(10)
O1–Ce1–N1	62.30(9)	O10–Ce1–N1	143.40(10)
O1–Ce1–O7 ⁱⁱ	68.27(9)	O7 ⁱⁱ –Ce1–O10	135.15(9)
O1–Ce1–N2 ⁱⁱ	104.34(9)	O10–Ce1–N2 ⁱⁱ	75.39(9)
O1–Ce1–O2 ^{iv}	125.58(9)	O2 ^{iv} –Ce1–O10	71.71(9)
O1–Ce1–O6 ^v	67.74(9)	O6 ^v –Ce1–O10	73.19(9)
O5–Ce1–O9	136.14(10)	O7 ⁱⁱ –Ce1–N1	77.42(10)

Metal- and Covalent Organic Frameworks for Advanced Applications: Heterogeneous Catalysis and Sensing

O5-Ce1-O10	81.18(9)	N1-Ce1-N2 ⁱⁱ	137.53(9)
O5-Ce1-N1	77.08(9)	O2 ^{iv} -Ce1-N1	73.09(9)
O5-Ce1-O7 ⁱⁱ	139.55(9)	O6 ^v -Ce1-N1	128.71(9)
O5-Ce1-N2 ⁱⁱ	140.55(8)	O7 ⁱⁱ -Ce1-N2 ⁱⁱ	60.64(9)
O2 ^{iv} -Ce1-O5	68.70(9)	O2 ^{iv} -Ce1-O7 ⁱⁱ	130.94(9)
O5-Ce1-O6 ^v	77.59(9)	O6 ^v -Ce1-O7 ⁱⁱ	94.87(9)
O9-Ce1-O10	94.19(9)	O2 ^{iv} -Ce1-N2 ⁱⁱ	129.88(9)
O9-Ce1-N1	81.95(10)	O6 ^v -Ce1-N2 ⁱⁱ	65.52(9)
O7 ⁱⁱ -Ce1-O9	69.28(9)	O2 ^{iv} -Ce1-O6 ^v	134.13(8)

Symmetry codes: (i) 1+x, +y, +z; (ii) 2-x, 1-y, -z; (iii) +x, -1+y, +z; (iv) -1+x, +y, +z; (v) +x, 1+y, +z

3

Ce1-O1	2.599(5)	Ce2-O2W	2.609(10)
Ce1-O1W	2.643(12)	Ce2-O3	2.452(6)
Ce1-O11	2.485(12)	Ce2-O7	2.425(6)
Ce1-N1	2.698(8)	Ce2-O1 ⁱⁱ	2.668(5)
Ce1-O5 ⁱ	2.475(6)	Ce2-O2 ⁱⁱ	2.638(6)
Ce1-N2 ⁱ	2.685(7)	Ce2-O1 ^x	2.668(5)
Ce1-O4 ⁱⁱⁱ	2.436(6)	Ce2-O2 ^x	2.638(6)
Ce1-O8 ⁱⁱⁱ	2.544(9)	Ce2-O3 ^{xi}	2.452(6)
Ce1-O6 ^{viii}	2.434(5)	Ce2-O7 ^{xi}	2.425(6)
O1-Ce1-O1W	135.3(3)	O1 -Ce1 -O8 ⁱⁱⁱ	66.0(2)

Chapter 4: Ce(III)-based Frameworks: From 1D Chain to 3D Porous Metal-Organic Framework

O5 ⁱ -Ce1-O8 ⁱⁱⁱ	125.9(3)	O4 ⁱⁱⁱ -Ce1-O6 ^{viii}	147.1(2)
O1-Ce1-O11	110.0(3)	O1-Ce1-O6 ^{viii}	130.36(18)
O5 ⁱ -Ce1-O6 ^{viii}	68.60(19)	O6 ^{viii} -Ce1-O8 ⁱⁱⁱ	72.3(3)
O1-Ce1-N1	60.1(2)	O1W-Ce1-O11	87.9(4)
O4 ⁱⁱⁱ -Ce1-N2 ^j	75.4(2)	O2W-Ce2-O3	73.6(2)
O1-Ce1-O5 ^j	117.20(19)	O1W-Ce1-N1	133.0(3)
O8 ⁱⁱⁱ -Ce1-N2 ^j	132.1(3)	O2W-Ce2-O7	67.9(2)
O1-Ce1-N2 ^j	69.46(19)	O1W-Ce1-O5 ⁱⁱⁱ	61.3(3)
O6 ^{viii} -Ce1-N2 ^j	130.9(2)	O1 ⁱⁱ -Ce2-O2W	130.95(12)
O1-Ce1-O4 ⁱⁱⁱ	72.74(19)	O1W-Ce1-N2 ^j	72.3(3)
O4 ⁱⁱⁱ -Ce1-O8 ⁱⁱⁱ	106.4(3)	O2 ⁱⁱ -Ce2-O2W	137.8(2)
O1W-Ce1-O4 ⁱⁱⁱ	75.9(3)	O11-Ce1-N1	133.4(3)
O1 ^x -Ce2-O2W	130.95(12)	O5 ^j -Ce1-O11	132.7(3)
O1W-Ce1-O8 ⁱⁱⁱ	155.5(3)	O11-Ce1-N2 ^j	143.7(3)
O2 ^x -Ce2-O2W	137.8(2)	O4 ⁱⁱⁱ -Ce1-O11	70.3(3)
O1W-Ce1-O6 ^{viii}	92.5(3)	O8 ⁱⁱⁱ -Ce1-O11	70.7(3)
O2W-Ce2-O3 ^{xi}	73.6(2)	O6 ^{viii} -Ce1-O11	78.7(3)
O5 ^j -Ce1-N1	72.6(3)	O4 ⁱⁱⁱ -Ce1-O5 ^j	126.8(2)
N1-Ce1-N2 ^j	79.4(3)	O7-Ce2-O7 ^{xi}	135.9(2)
O4 ⁱⁱⁱ -Ce1-N1	131.8(2)	O1 ⁱⁱ -Ce2-O2 ⁱⁱ	49.14(17)
O8 ⁱⁱⁱ -Ce1-N1	63.9(3)	O2W-Ce2-O7 ^{xi}	67.9(2)
O6 ^{viii} -Ce1-N1	78.3(2)	O3-Ce2-O7	86.0(2)
O5 ^j -Ce1-N2 ^j	63.1(2)	O1 ⁱⁱ -Ce2-O3	81.33(18)

Metal- and Covalent Organic Frameworks for Advanced Applications: Heterogeneous Catalysis and Sensing

O2 ⁱⁱ -Ce2-O3	130.43(18)	O2 ^x -Ce2-O7	138.68(19)
O1 ^x -Ce2-O3	121.45(19)	O3 ^{xi} -Ce2-O7	81.8(2)
O2 ^x -Ce2-O3	76.8(2)	O1 ⁱ -Ce2-O1 ^x	98.09(17)
O3-Ce2-O3 ^{xi}	147.1(2)	O1 ⁱ -Ce2-O2 ^x	71.54(17)
O3-Ce2-O7 ^{xi}	81.8(2)	O1 ⁱ -Ce2-O3 ^{xi}	121.45(19)
O1 ⁱⁱ -Ce2-O7	68.9(2)	O1 ⁱ -Ce2-O7 ^{xi}	148.5(2)
O2 ⁱⁱ -Ce2-O7	78.8(2)	O1 ^x -Ce2-O2 ⁱⁱ	71.54(17)
O1 ^x -Ce2-O7	148.5(2)	O2 ⁱⁱ -Ce2-O2 ^x	84.43(18)
O2 ⁱⁱ -Ce2-O3 ^{xi}	76.8(2)	O2 ^x -Ce2-O3 ^{xi}	130.43(18)
O2 ⁱⁱ -Ce2-O7 ^{xi}	138.68(19)	O2 ^x -Ce2-O7 ^{xi}	78.8(2)
O1 ^x -Ce2-O2 ^x	49.14(17)	O3 ^{xi} -Ce2-O7 ^{xi}	86.0(2)
O1 ^x -Ce2-O3 ^{xi}	81.33(18)	Ce1-O1-Ce2 ⁱⁱⁱ	127.3(2)
O1 ^x -Ce2-O7 ^{xi}	68.9(2)		

Symmetry codes: (i) $-1+x, 1+y, z$; (ii) $x, -1+y, z$; (iii) $x, 1+y, z$; (viii) $-1/2+x, 3/2-y, 5/4-z$; (x) $-1+y, x, 1-z$; (xi) $y, x, 1-z$

Table S4.2. Hydrogen bonds geometry (Å, °) for **1**, **2** and **3**.

D-H...A	D-H	H...A	D...A	D-H...A
1				
N1-H1...O1	0.88(3)	2.29(5)	2.661(6)	106(5)
N1-H1...O12	0.88(3)	2.10(4)	2.957(6)	163(5)
O9-H9A...O4	0.84(4)	1.94(4)	2.784(5)	179(7)
O9-H9B...O7	0.84(3)	1.96(5)	2.752(5)	156(6)
O10-H10A...O5	0.84(4)	2.29(5)	2.992(5)	142(5)

Chapter 4: Ce(III)-based Frameworks: From 1D Chain to 3D Porous Metal-Organic Framework

O10-H10A...O9	0.84(4)	2.32(4)	2.943(6)	132(5)
O10-H10A...O6	0.84(2)	1.92(2)	2.752(6)	176(6)
O11-H11A...O4	0.84(4)	2.04(3)	2.876(6)	170(8)
O11-H11B...O3	0.84(5)	1.88(4)	2.713(6)	168(8)
O12-H12A...O2	0.84(4)	1.88(4)	2.672(6)	158(7)
O12-H12B...O6	0.85(5)	1.89(5)	2.727(5)	171(7)

D-H...A	D-H	H...A	D...A	D-H...A
2				
O4-H4...O7	0.84	1.74	2.570(4)	168
O9-H9A...O8	0.83(3)	1.91(3)	2.731(4)	169(4)
O9-H9B...O3	0.83(3)	2.14(3)	2.910(4)	153(4)
O10-H10A...O1	0.84(4)	1.87(4)	2.683(4)	161(4)
O10-H10B...O5	0.84(2)	1.96(3)	2.729(4)	152(4)

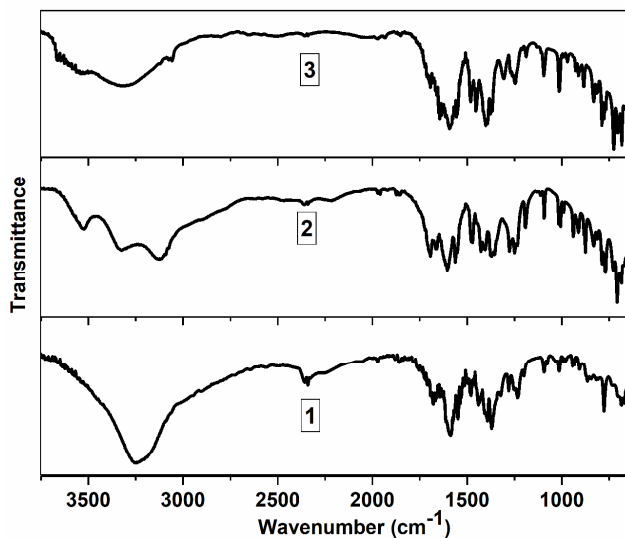
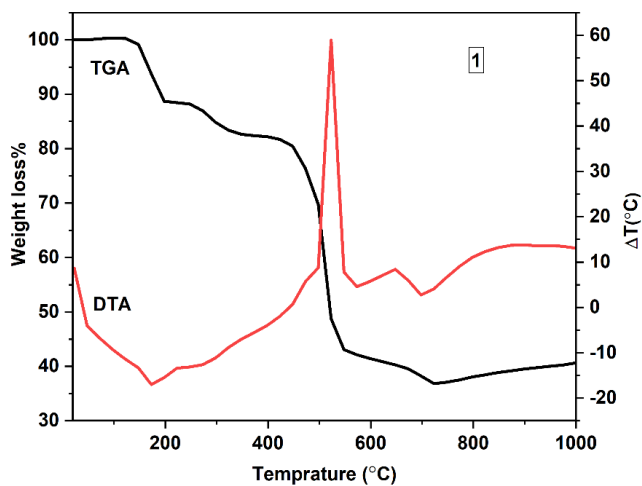


Figure S4.1. DRIFT spectra of compounds 1, 2 and 3.



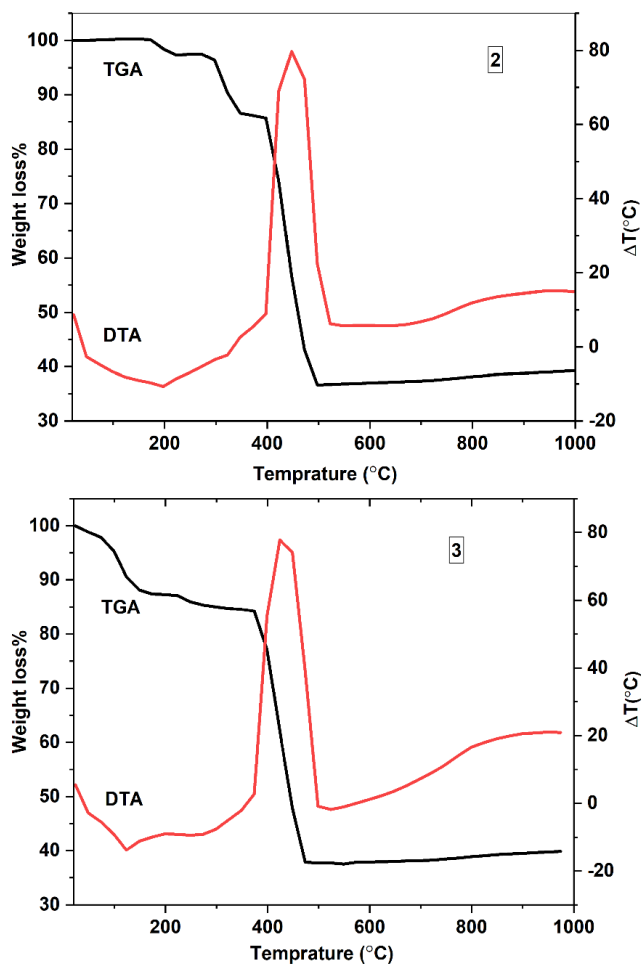


Figure S4.2. TGA and DTA curves of compounds 1, 2 and 3.

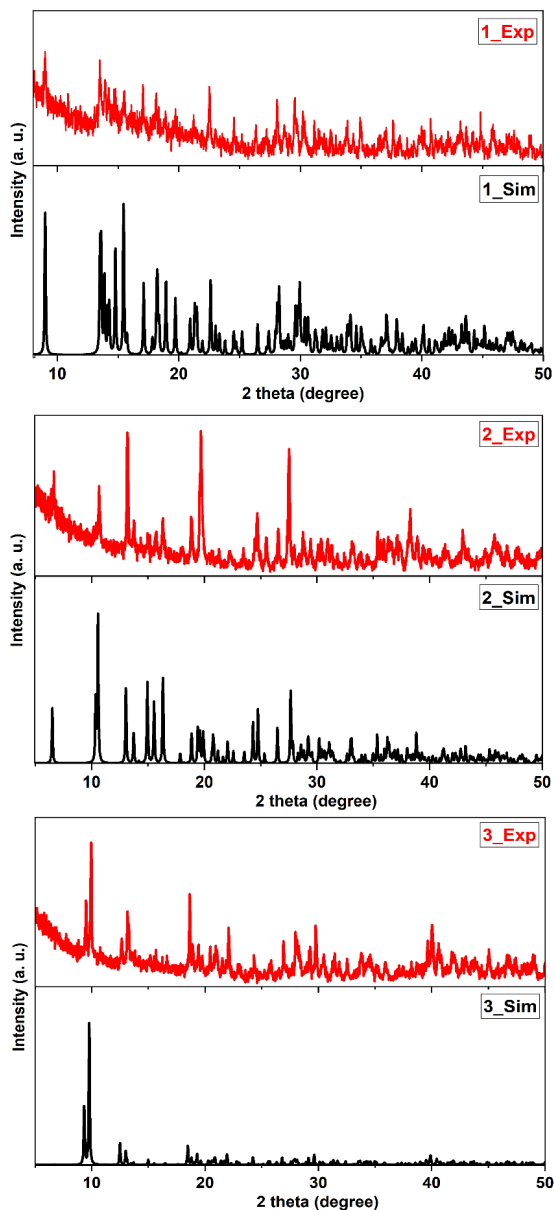


Figure S4.3. XRD patterns of compounds 1, 2 and 3 (Simulated and Experimental).

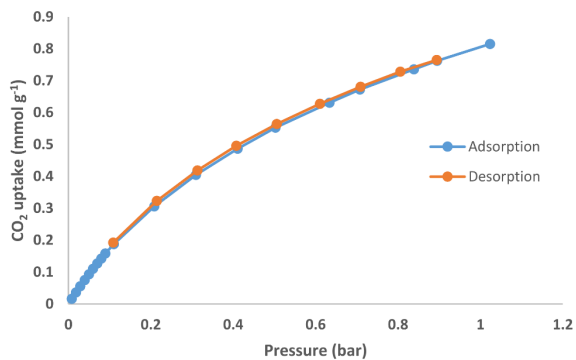


Figure S4.4. CO₂ adsorption isotherm of **3** measured at 298 K.

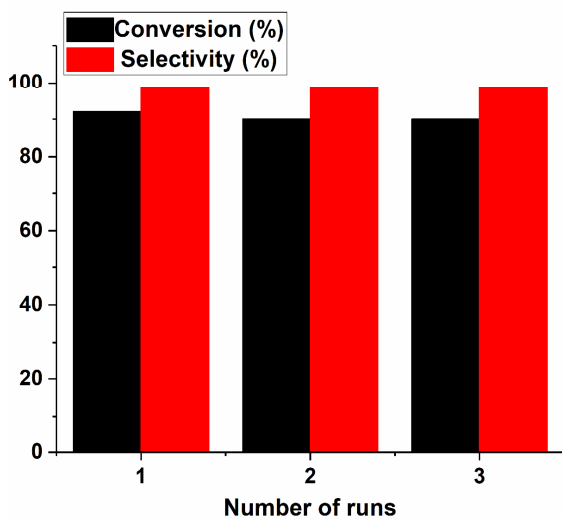


Figure S4.5. Recyclability of the compound **3**.

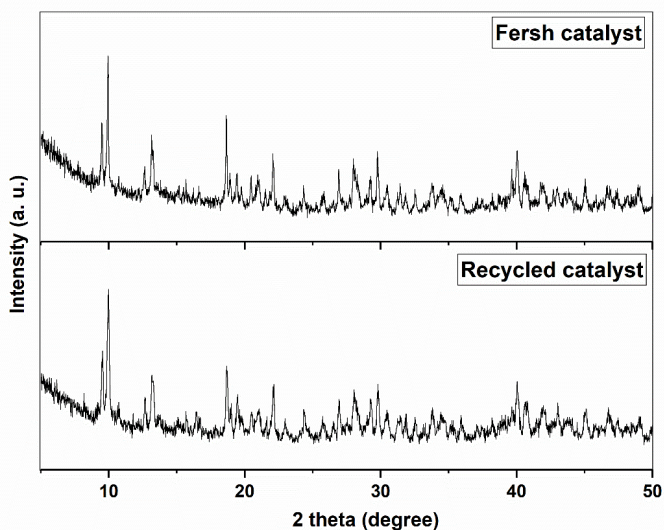


Figure S4.6. XRD patterns of the compound **3** before and after the catalytic reaction.

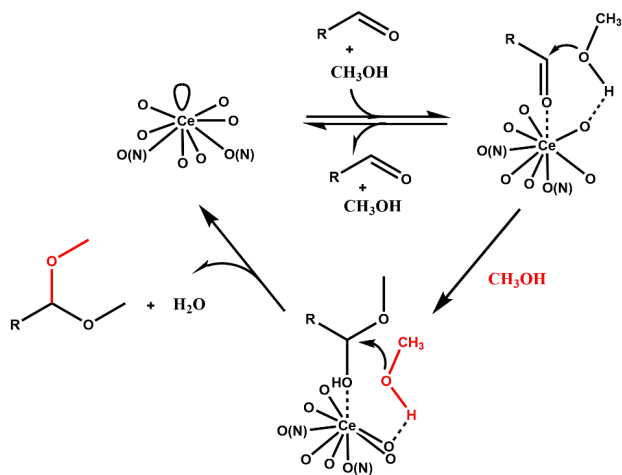
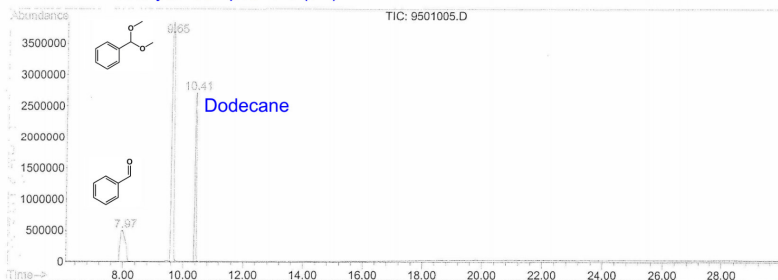


Figure S4.7. Proposed reaction mechanism for the Ce MOF-catalyzed acetalization of benzaldehyde with methanol.

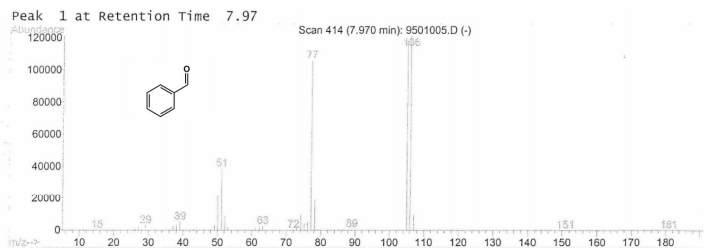
GC-MS analysis

The data of the GC-MS analyses are provided below. In all chromatogram, the peaks are assigned to the related materials. The peak in the retention time of 10.40 min is related to the dodecane. Please see the spectra in the next pages.

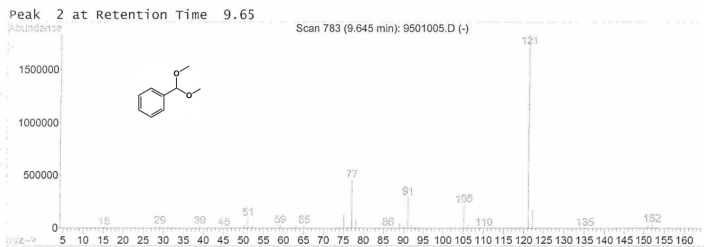
Catalyst: Compound 3 (3D)



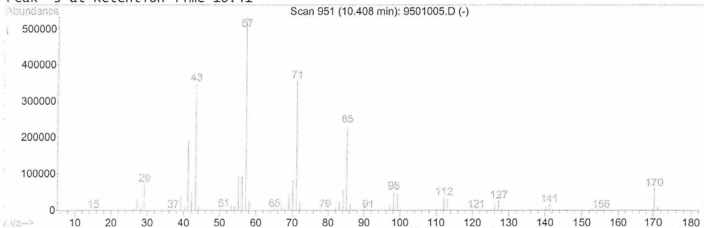
Peak 1 at Retention Time 7.97



Peak 2 at Retention Time 9.65

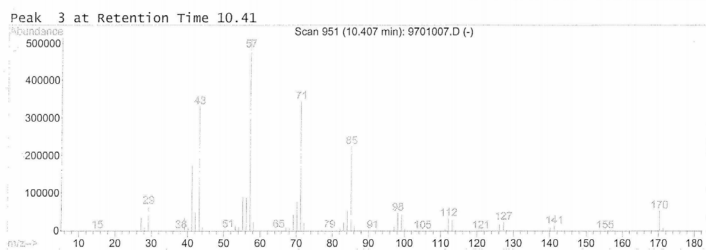
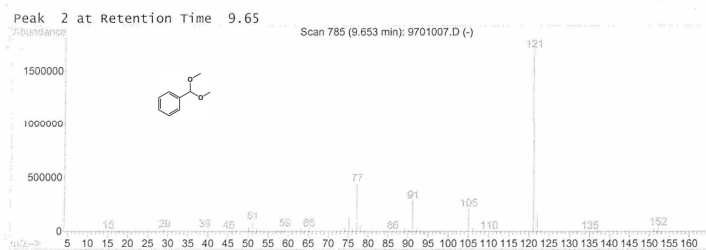
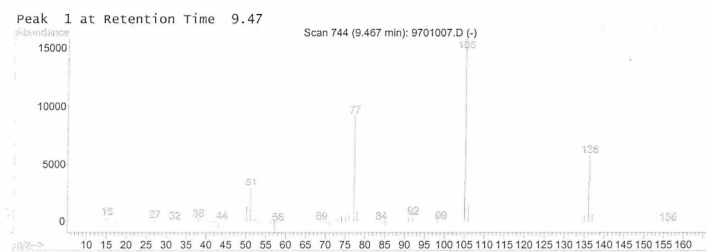
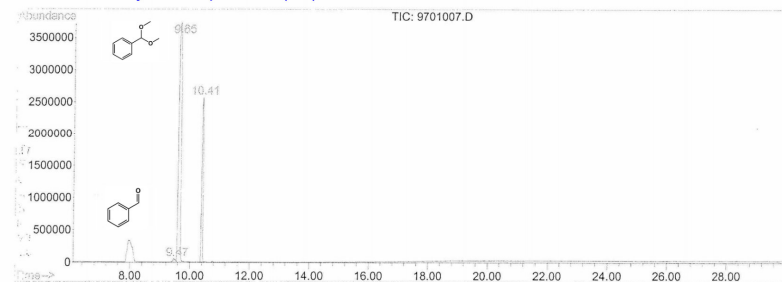


Peak 3 at Retention Time 10.41

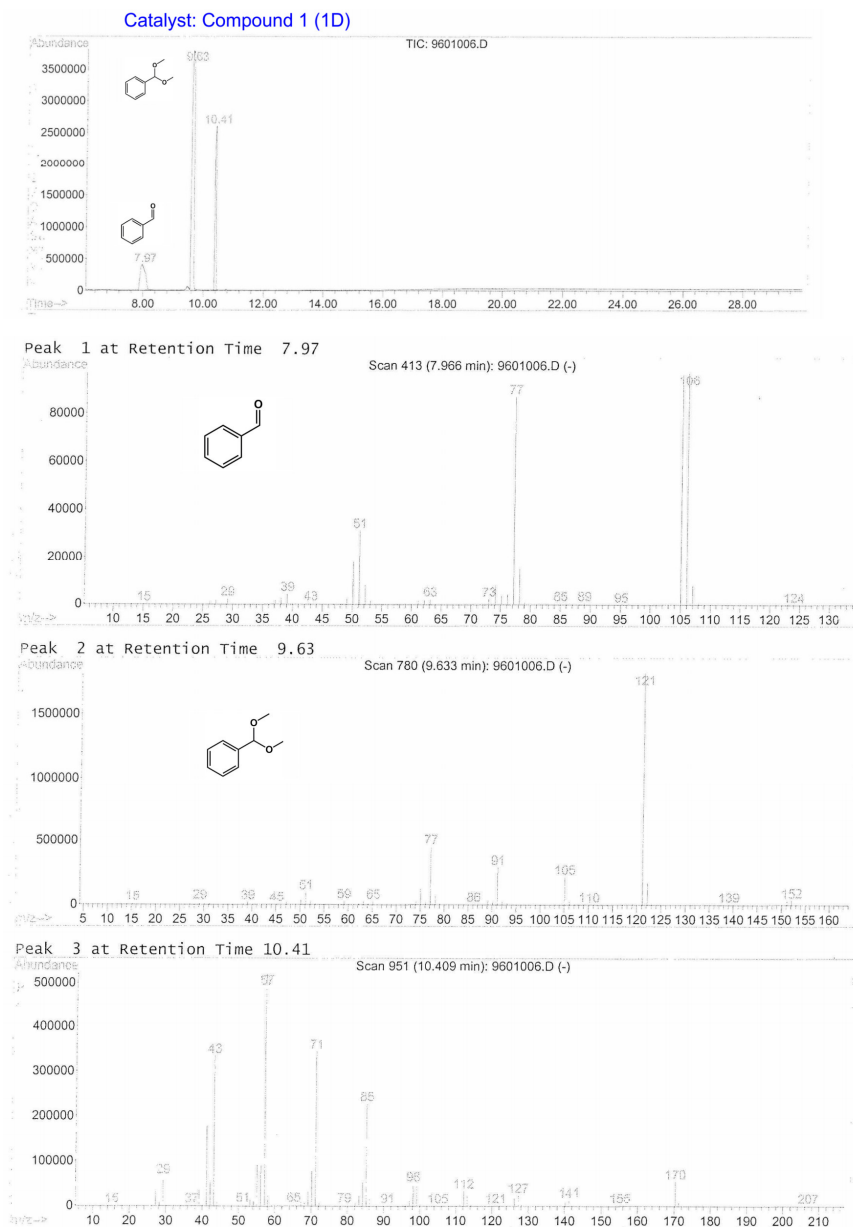


Metal- and Covalent Organic Frameworks for Advanced Applications: Heterogeneous Catalysis and Sensing

Catalyst: Compound 2 (2D)

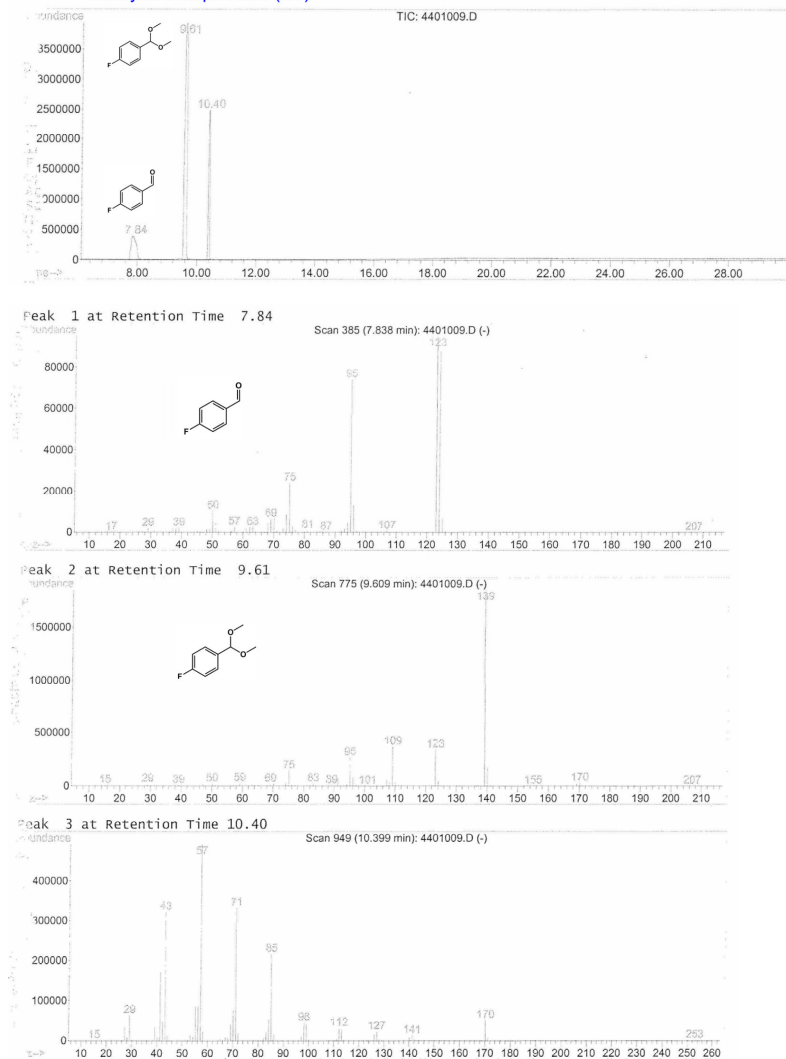


Chapter 4: Ce(III)-based Frameworks: From 1D Chain to 3D Porous Metal-Organic Framework

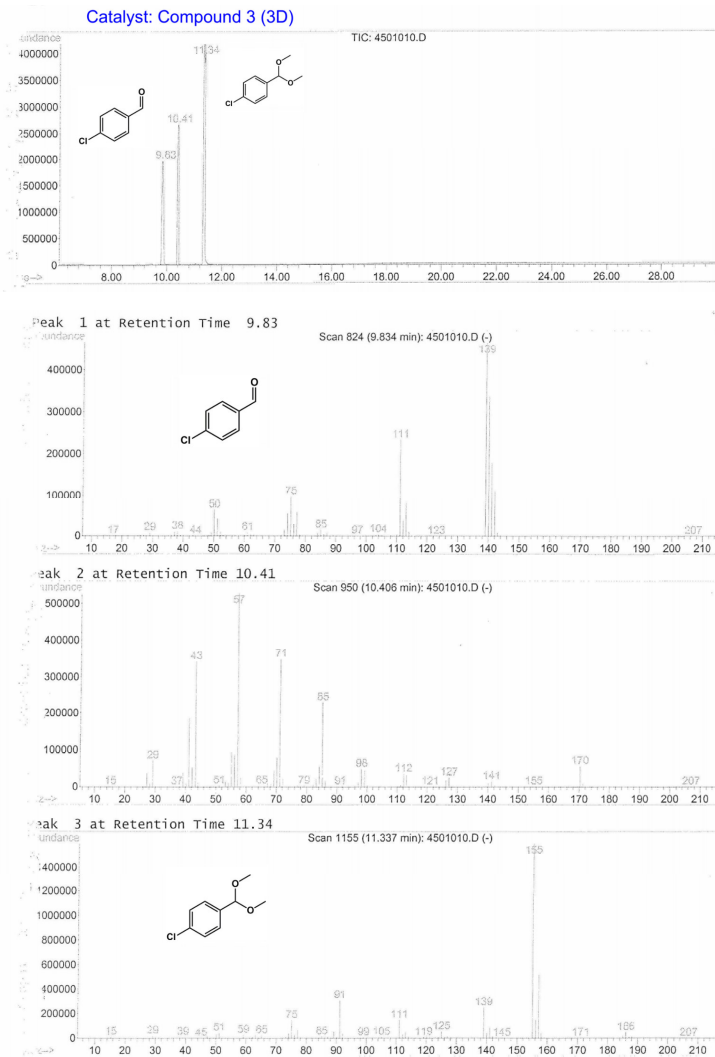


Metal- and Covalent Organic Frameworks for Advanced Applications: Heterogeneous Catalysis and Sensing

Catalyst: Compound 3 (3D)

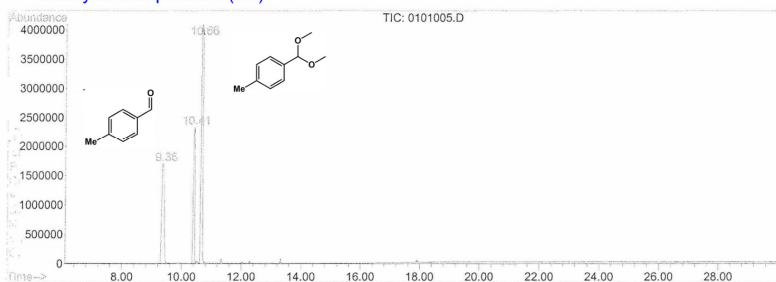


Chapter 4: Ce(III)-based Frameworks: From 1D Chain to 3D Porous Metal-Organic Framework

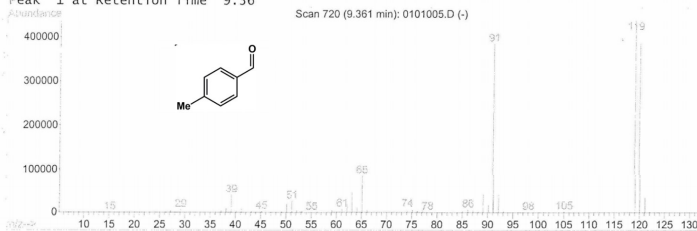


Metal- and Covalent Organic Frameworks for Advanced Applications: Heterogeneous Catalysis and Sensing

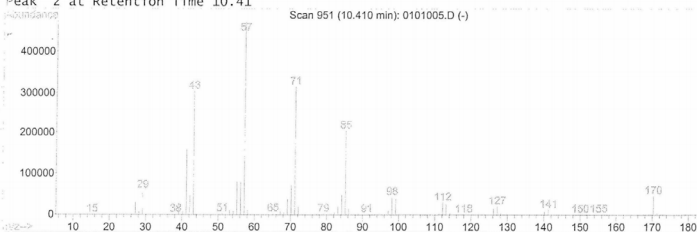
Catalyst: Compound 3 (3D)



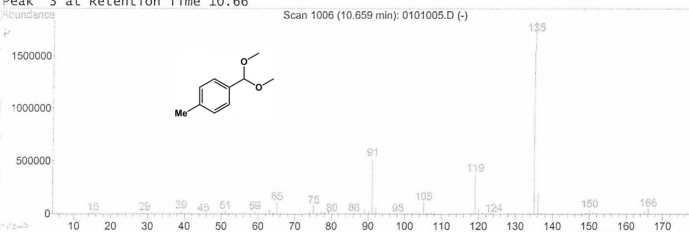
Peak 1 at Retention Time 9.36



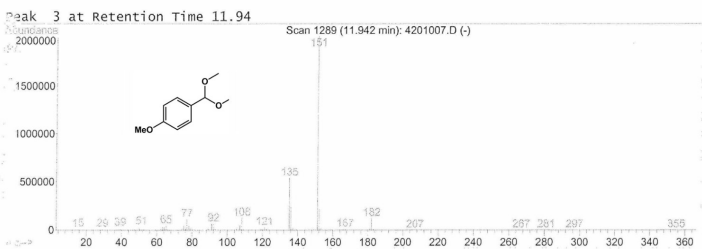
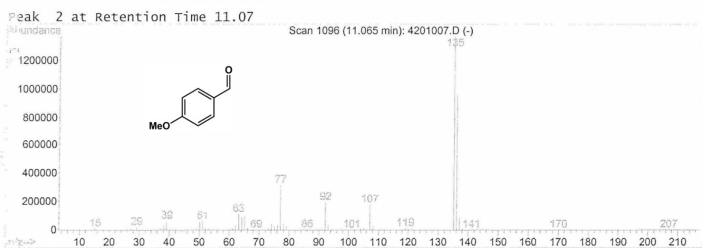
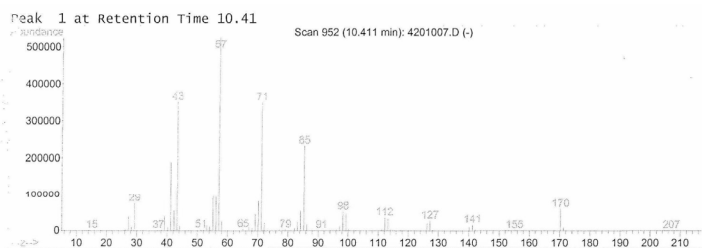
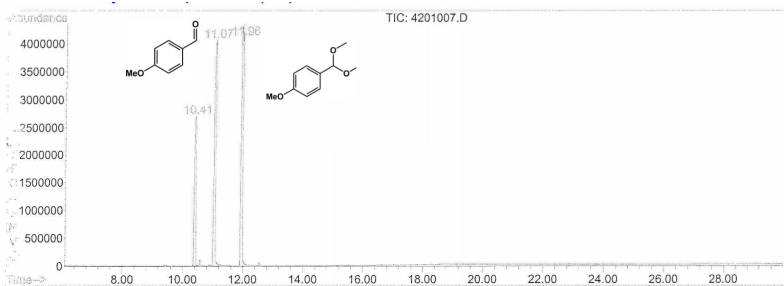
Peak 2 at Retention Time 10.41



Peak 3 at Retention Time 10.66

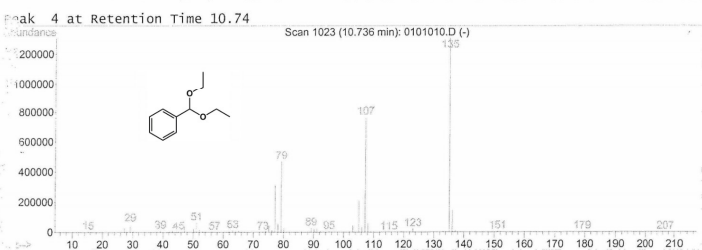
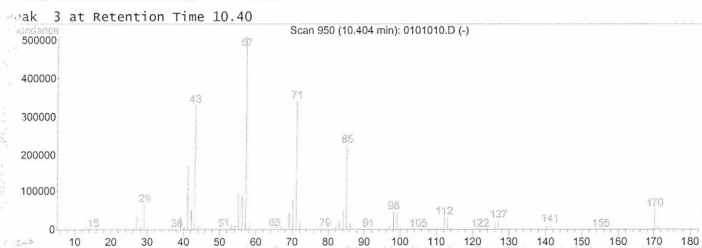
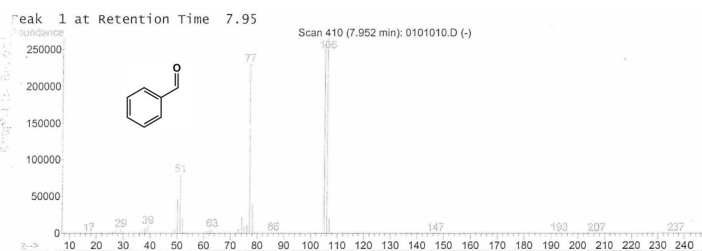
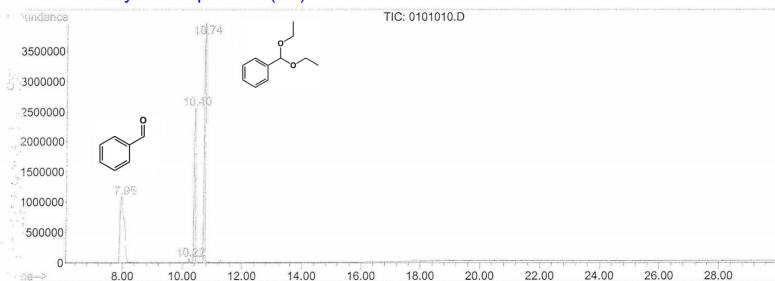


Chapter 4: Ce(III)-based Frameworks: From 1D Chain to 3D Porous Metal-Organic Framework



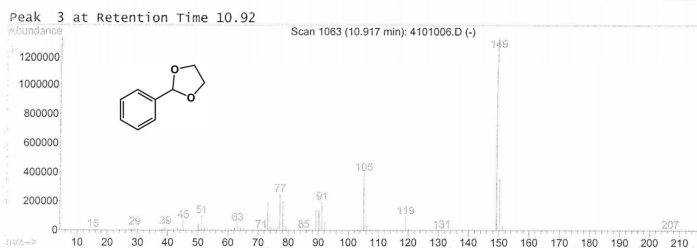
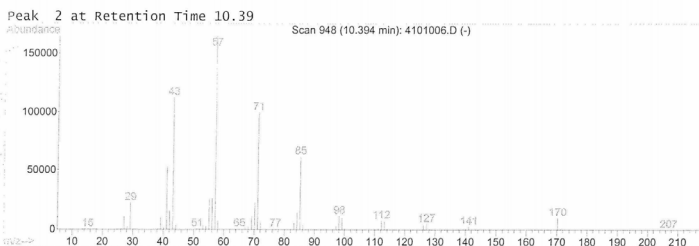
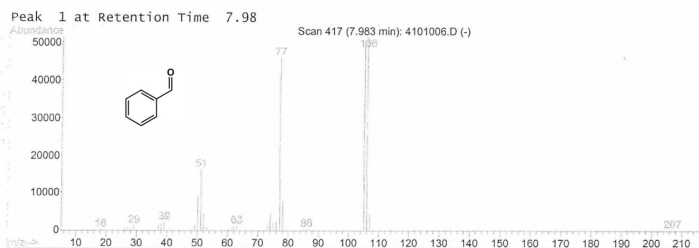
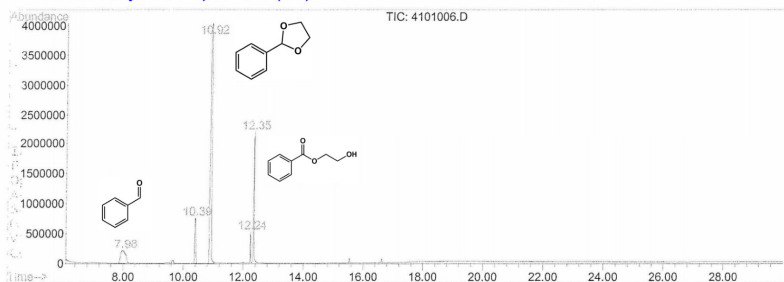
Metal- and Covalent Organic Frameworks for Advanced Applications: Heterogeneous Catalysis and Sensing

Catalyst: Compound 3 (3D)

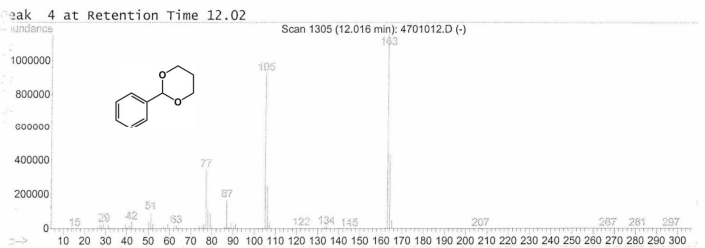
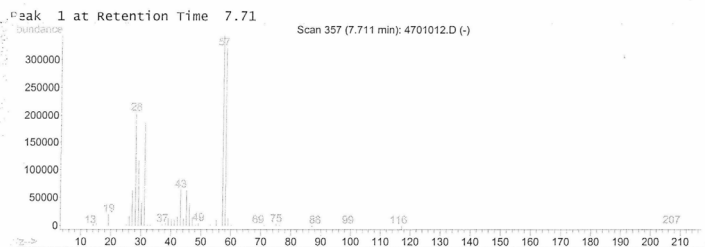
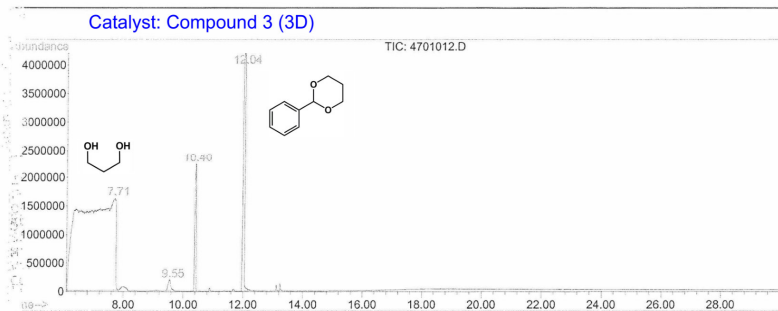
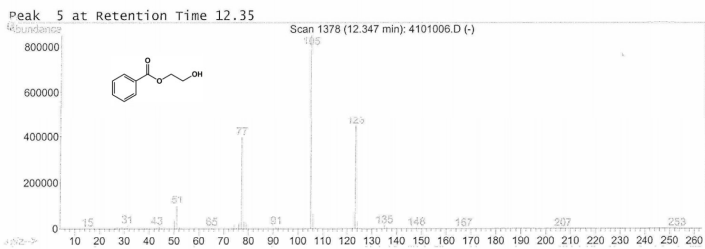


Chapter 4: Ce(III)-based Frameworks: From 1D Chain to 3D Porous Metal-Organic Framework

Catalyst: Compound 3 (3D)

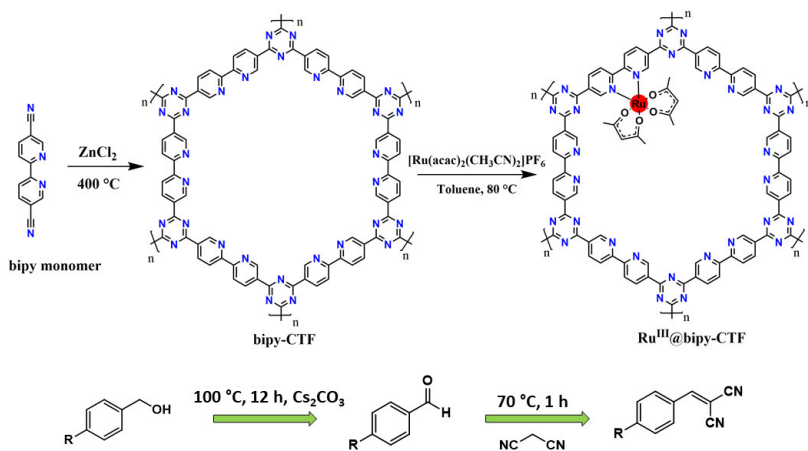


Metal- and Covalent Organic Frameworks for Advanced Applications: Heterogeneous Catalysis and Sensing



CHAPTER 5

A Ru-COMPLEX TETHERED TO A N-RICH COVALENT TRIAZINE FRAMEWORK FOR TANDEM AEROBIC OXIDATION–KNOEVENAGEL CONDENSATION REACTIONS



The results of this chapter were published in:

G. Watson †, **P. Gohari Derakhshandeh** †, S. Abednatanzi, J. Schmidt, K. Leus, P. Van Der Voort. A Ru-complex tethered to a N-Rich Covalent Triazine Framework for Tandem Aerobic Oxidation–Knoevenagel Condensation Reactions. **Molecules** 26, **2021**, 838.

Abstract

Herein, a highly N-rich covalent triazine framework (CTF) is applied as support for a Ru^{III} complex. The bipyridine sites within the CTF provide excellent anchoring points for the [Ru(acac)₂(CH₃CN)₂]PF₆ complex. The obtained robust Ru^{III}@bipy-CTF material was applied for the selective tandem aerobic oxidation–Knoevenagel condensation reaction. The presented system shows a high catalytic performance (>80% conversion of alcohols to α , β -unsaturated nitriles) without the use of expensive noble metals. The bipy-CTF not only acts as the catalyst support but also provides the active sites for both aerobic oxidation and Knoevenagel condensation reactions. This work highlights a new perspective for the development of highly efficient and robust heterogeneous catalysts applying CTFs for cascade catalysis.

5.1. Introduction

Conventional porous materials including silica, zeolite and activated charcoal have attracted extensive interest in large-scale industrial applications, most importantly in heterogeneous catalysis.¹⁻³ However, the poor chemical versatility of their chemical structure has increased the need for alternative porous materials with tailorable properties. In the last few years, the focus in heterogeneous catalysis lies on the development of novel and efficient porous supports with tailor-made functionalities rather than prefabricated materials for targeted liquid phase reactions.⁴⁻⁵ The recently emerging porous materials, particularly metal-organic frameworks (MOFs) and covalent organic frameworks (COFs) have led to excellent progress in the field.⁶⁻⁷ In contrast to MOFs fabricated from inorganic nodes (metal ions/clusters), COFs are purely organic materials and constructed from covalently linking light atoms (C, O, N, P, B, Si).⁸⁻⁹ Covalent triazine frameworks (CTFs) are a class of COFs which are formed through a trimerization reaction followed by subsequent oligomerization of aromatic nitriles.¹⁰⁻¹¹ The robust aromatic covalent bonds endow CTFs with excellent stability compared to coordinative-linked porous materials.¹² Additionally, CTFs contain a high amount of nitrogen functionalities in their networks allowing them to be outstanding candidates as supports for various catalytic active centers.¹³

Over a wide range of catalytic processes, tandem catalysis has attracted increasing research attention.¹⁴ In tandem catalysis, several catalytic reactions occur consecutively in one reaction vessel, using only one multifunctional catalyst. Therefore, there is no need for separation, purification, and transfer of intermediates produced in each step. Tandem catalysis significantly reduces the amount of waste and minimizes the use of harmful solvents.¹⁵ Great efforts have been made to design heterogeneous catalysts for tandem reactions through the immobilization of metal complexes and nanoparticles on the surface of various porous supports.^{14, 16} α , β -unsaturated nitriles are key intermediates for the synthesis of pharmaceuticals and fine chemicals.¹⁷ These intermediates are generally produced through the Knoevenagel condensation of aldehydes or ketones with nitriles catalyzed by common bases.¹⁸ However, the catalytic process suffers from limited substrate scope due to the high price or unavailability of some aldehydes¹⁸. In this regard,

the development of highly efficient multifunctional catalysts to prepare α , β -unsaturated nitriles through tandem aerobic oxidation–Knoevenagel condensation reaction significantly boosts the synthesis efficiency.

Highly efficient oxidation catalysts for the selective conversion of alcohols to aldehydes is the key step in designing an appropriate heterogeneous catalyst for the tandem oxidation–Knoevenagel condensation reaction. Traditional oxidation processes employ stoichiometric amounts of sometimes toxic and expensive inorganic oxidants, mainly iodosylbenzene, sodium hypochlorite and chromium trioxide.^{19–22}

Many papers have appeared on the design of various homogeneous and heterogeneous catalysts containing noble metals, such as Au, Pd, Pt and Ir for the selective aerobic oxidation of alcohols.^{23–26} Ru catalysts are economically attractive in comparison to other noble-metal catalysts that are rather expensive. Ru^{III} complexes are well documented as efficient oxidation catalysts for various substrates, such as alcohols, aldehydes and sulfides. Nevertheless, in almost all studies using ruthenium, either homo- or heterogeneously, the reaction is conducted in the presence of non-green oxidants (3-dichloriodanyl-benzoic acid, periodic acid and iodosylbenzene).^{19, 27–28} Recently, our group reported on the immobilization of a Ru^{III} complex onto a periodic mesoporous organosilica (PMO).²⁹ Although the catalyst was highly active for the selective oxidation of alcohols using periodic acid, no activity was observed using oxygen as the green oxidant. So far, very few studies have been reported on the application of Ru^{III}-based catalysts in the aerobic oxidation of alcohols. Moreover, these catalysts exhibit fundamental drawbacks as high catalyst loadings (5 mol% [Ru]) or a large excess of oxygen (20 atm) as the oxidant is required.^{30–31} Thus, the development of greener and more atom-efficient methods that adopt recyclable catalysts and molecular oxygen as the sole oxidant is a great alternative to the existing systems.

We introduce here an efficient catalytic system for tandem aerobic oxidation–Knoevenagel condensation reaction. A highly N-rich CTF containing bipyridine (bipy) building blocks (bipy-CTF) is used as the catalyst support. The bipy building units provide excellent docking sites for immobilization of a Ru^{III} complex, examined initially in the selective aerobic oxidation of alcohols to aldehydes. The bipy-CTF material not only acts

as anchoring points but also promotes the sequential reaction of aldehydes and nitriles due to the presence of N-rich basic functionalities. Our results indicate that the synergistic effects between the N-rich bipy-CTF and the Ru^{III} complex are beneficial to obtain a highly active and selective catalyst for tandem catalysis in the absence of any co-oxidant.

5.2. Results and Discussion

5.2.1. Synthesis and characterization of the modified bipy-CTF with the Ru Complex (Ru^{III}@bipy-CTF)

We targeted a CTF with free 2,2'-bipyridine building blocks (5,5'-dicyano-2,2'-bipyridine), which forms excellent anchoring points. The bipy-CTF material was synthesized following the typical reported ionothermal procedure.³² After the synthesis, the remaining ZnCl₂ is removed by extensive washing with water followed by refluxing at 120 °C in 1 M HCl. The obtained bipy-CTF material was post-modified with the [Ru(acac)₂(CH₃CN)₂]PF₆ complex through a simple wet impregnation method as depicted in Figure 5.1.

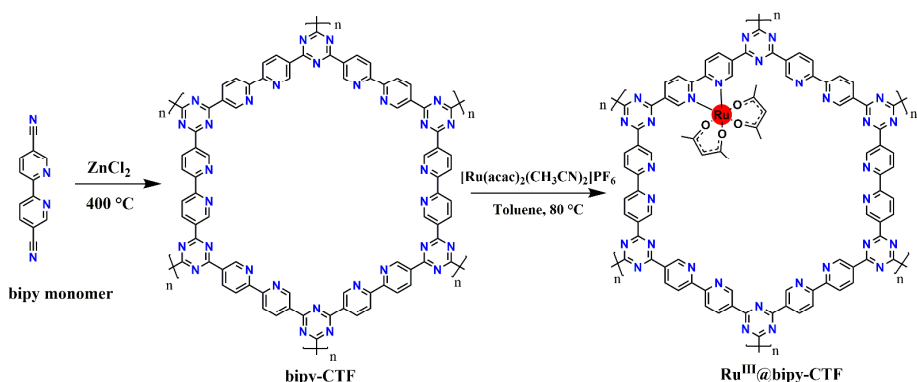


Figure 5.1. Schematic representation of the ideal ordered structure of Ru^{III}@bipy-CTF material.

In the diffuse reflectance infrared Fourier transform (DRIFT) spectrum of the bipy-CTF (Figure 5.2a), the characteristic bands of the triazine fragment appear at 1356 and 1521

cm^{-1} . The absence of the intense nitrile band at around 2330 cm^{-1} demonstrates the complete consumption of monomer and formation of triazine linkages. The doublet band around $1602\text{--}1626 \text{ cm}^{-1}$ is ascribed to the C=N vibrations of the bipy moiety. In the DRIFT spectrum of the $\text{Ru}^{\text{III}}@$ bipy-CTF material, the vibration bands of the bipy moiety are shifted ($\sim 10 \text{ cm}^{-1}$) to lower frequency which can be due to coordination with the Ru complex. A similar observation is reported in previous studies.³³

The pristine bipy-CTF material displays a rapid uptake of N_2 at low relative pressures which is indicative of a highly microporous material (Figure 5.2b). This profile is assigned to a type I isotherm and exhibits a Brunauer–Emmett–Teller (BET) surface area of $787 \text{ m}^2\text{g}^{-1}$. The total pore volume was found to be $0.40 \text{ cm}^3 \text{ g}^{-1}$ at $P/P_0 = 0.99$. After the introduction of the Ru complex, the BET surface area decreases moderately to $556 \text{ m}^2\text{g}^{-1}$, indicating that most of the pores are still accessible.

The powder X-ray diffraction (XRD) patterns of the pristine bipy-CTF and $\text{Ru}^{\text{III}}@$ bipy-CTF are shown in Figure 5.2c. As known from most of the CTFs prepared ionothermally, the bipy-CTF materials were found to be predominantly amorphous. The broad peaks at $2\theta \sim 13$ and 25° are assigned to the 00 l reflection showing a “graphitic” layer stacking. It is important to note that, the exact structure of these amorphous materials cannot be determined since the harsh synthesis conditions result in carbonization and blackening of the material making it difficult to be fully characterized. To estimate the carbonization degree and purity of the materials, we applied elemental analysis (Table 5.1). The CHN data obtained from the bipy-CTF material reveals a C/N ratio of 2.9 and the theoretical value for C/N in the bipy-CTF sample is calculated to be 2.6. Therefore, partial carbonization of around 10 % occurs, while 90 % of the structural composition is preserved.

The thermal stability of both materials was determined by thermogravimetric analysis (TGA). The TGA profile of the bipy-CTF displayed a high thermal stability up to approximately $550 \text{ }^\circ\text{C}$ (Figure 5.2d). A first weight loss of about 8 % below $150 \text{ }^\circ\text{C}$ corresponds to the loss of water and organic solvent molecules. The TGA profile of the modified sample shows that the $\text{Ru}^{\text{III}}@$ bipy-CTF material is thermally stable up to $300 \text{ }^\circ\text{C}$ and gradually decomposes at higher temperatures.

Table 5.1. Elemental analysis of the pristine and modified CTF materials.

Sample	C ^a (Wt.%)	N ^a (Wt.%)	C/N	Ru ^b (mmol g ⁻¹)
bipy-CTF	58.92	20.27	2.9	-
Ru ^{III} @bipy-CTF	59.6	15.7	3.8	0.15

^a Determined by elemental analysis. ^b Determined by ICP-OES analysis.

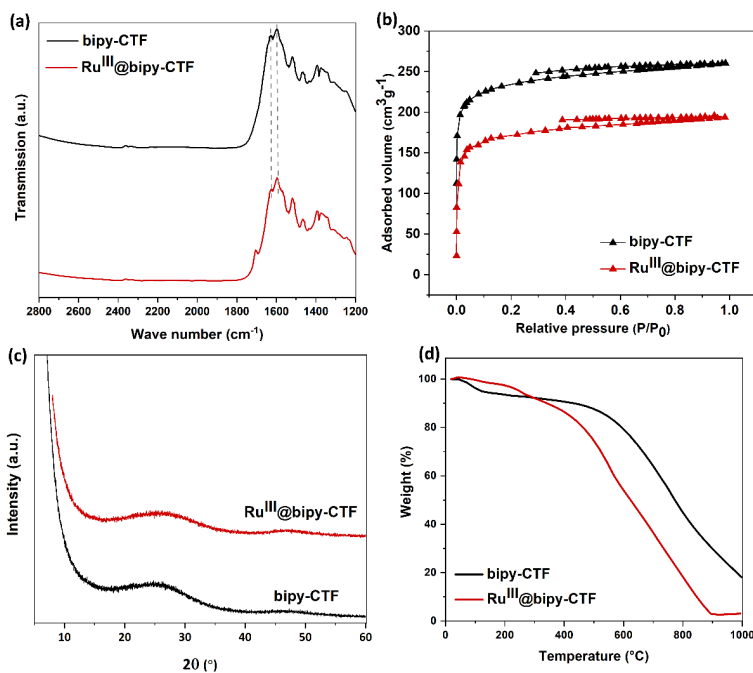


Figure 5.2. Structural characterization of bipy-CTF and Ru^{III}@bipy-CTF materials. (a) DRIFT spectra. (b) Nitrogen adsorption/desorption isotherms. (c) Powder XRD patterns. (d) TGA curves.

Further structural characterization was done by applying x-ray photoelectron spectroscopy (XPS). In the N 1S spectrum of the bipy-CTF material (Figure 5.3a), a peak at 398.39 eV confirms the existence of the pyridinic nitrogen in the framework. Besides,

the peaks at 399.58 and 400.38 eV are attributed to the pyrrolic- and quaternary-N species, respectively. These nitrogen functionalities are formed during the synthesis at high temperatures as reported by Osadchii *et al.*³⁴ In the N 1s spectrum of the Ru^{III}@bipy-CTF material (Figure 5.3b), a peak at higher binding energy is observed for the pyridinic N species which overlaps with the peak of pyrrolic-N sites. Such a N 1s shift towards higher binding energies can be attributed to the slight transfer of electrons to the immobilized Ru complexes.³⁵ The Ru 3p peaks for the Ru^{III}@bipy-CTF are located around 463 and 485 eV, which corresponds to Ru in the (+3) oxidation state (Figure 5.3c).

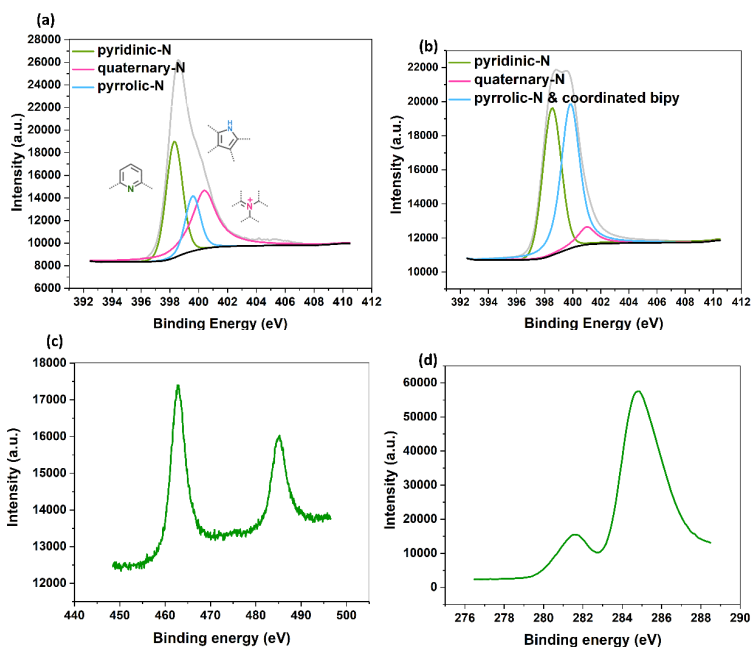


Figure 5.3. Structural characterization of bipy-CTF and Ru^{III}@bipy-CTF materials. (a) N 1S XPS spectrum of the bipy-CTF. (b) N 1s XPS spectrum of the Ru^{III}@bipy-CTF. (c) Ru 3p XPS spectrum of the Ru^{III}@bipy-CTF. (d) Ru 3d XPS spectrum of the Ru^{III}@bipy-CTF.

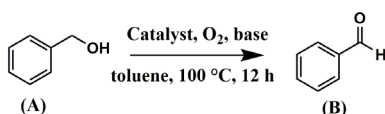
Moreover, the Ru 3d peak is seen at 285 eV (Figure 5.3d). Based on the inductively coupled plasma (ICP) analysis, the loading of Ru in the modified material is 0.15 mmol g⁻¹ and around 3% of the total bipyridine sites are coordinated to the Ru complex.

5.3. Catalytic activity of the Ru^{III}@bipy-CTF catalyst in the tandem aerobic oxidation–Knoevenagel condensation reaction

The catalytic activity of heterogeneous Ru catalysts for oxidation reactions using O₂ or air as green oxidant remains a challenge. Initially, the catalytic activity of the Ru^{III}@bipy-CTF catalyst was tested under aerobic conditions for the selective oxidation of benzyl alcohol to benzaldehyde. The catalytic results are presented in Table 5.2. The Ru^{III}@bipy-CTF catalyst displays a moderate activity with a conversion of 37% using toluene as the reaction medium (Table 5.2, entry 1). To further enhance the catalytic performance of the catalyst, different bases were applied (Table 5.2, entries 2-4). The catalytic conversion of benzyl alcohol increases in the presence of K₂CO₃ and Cs₂CO₃ with conversions of 78 and 99% respectively. Notably, no product of over-oxidation (benzoic acid) was detected, proving the high selectivity of the Ru catalyst towards benzaldehyde. In the absence of the catalyst, no conversion of benzyl alcohol was observed (<1% after 12 h). Moreover, the conversion of benzyl alcohol toward benzaldehyde decreased to 3% under an Ar atmosphere which confirms the essential need for oxygen as the oxidant (entry 7 in Table 5.2). The catalytic activity of the Ru^{III}@bipy-CTF catalyst was further compared with its homogeneous counterpart (Table 5.2, entry 8). Under the same reaction conditions, the [Ru(acac)₂(CH₃CN)₂]PF₆ complex showed lower catalytic conversion (54% using Cs₂CO₃). We also compared the use of a bipyridine linker MOF (UiO-67) instead of the CTF in the same reaction conditions. When the same Ru complex was immobilized on UiO-67 as the solid support, the oxidation of benzyl alcohol proceeded slowly and a conversion of 46% was observed under similar reaction conditions. Although the catalyst based on UiO-67 had a much higher surface area (1158 m²g⁻¹) compared to the one on bipy-CTF, a lower catalytic efficiency was observed in the case of Ru^{III}@UiO-67. The improved activity of the Ru^{III}@bipy-CTF catalyst can be attributed to the contributing role of the bipy-CTF support (see mechanistic studies in the supplementary materials, Table S5.1, Figure S5.1). A control experiment was performed using the pristine bipy-CTF material. A conversion of 39% was obtained using the pristine CTF as the catalyst while UiO-67 showed almost no activity for the conversion of benzyl alcohol to

benzaldehyde under identical reaction conditions (Table 5.2, entry 9). It has been proven that nitrogen-rich carbon materials are effective catalysts for aerobic oxidation reactions³⁶. We recently showed the unique properties of CTFs to proceed aerobic oxidation reactions assisted through nitrogen functionalities.³⁷⁻³⁸ More specifically, CTFs with quaternary N species can activate molecular O₂ to generate oxygen radicals (superoxide) which further promote the oxidation reaction.

Table 5.2. Catalytic performance of different catalysts in the oxidation of benzyl alcohol.



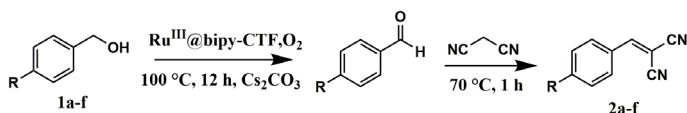
Entry	Catalyst	Base	Conversion (%)	TON ^a
1	Ru ^{III} @bipy-CTF	No base	37	37
2	Ru ^{III} @bipy-CTF	Na ₂ CO ₃	41	41
3	Ru ^{III} @bipy-CTF	K ₂ CO ₃	78	78
4	Ru ^{III} @bipy-CTF	Cs ₂ CO ₃	99	99
5	Ru ^{III} @bipy-CTF ^b	Cs ₂ CO ₃	64	267
6	No catalyst	Cs ₂ CO ₃	< 1	-
7	Ru ^{III} @bipy-CTF ^c	Cs ₂ CO ₃	3	3
8	[Ru(acac) ₂ (CH ₃ CN) ₂]PF ₆	Cs ₂ CO ₃	54	54
9	bipy-CTF ^d	Cs ₂ CO ₃	39	39

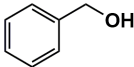
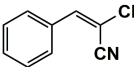
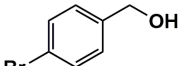
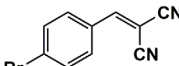
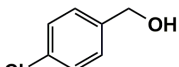
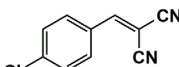
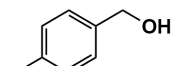
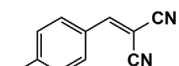
Reaction conditions: 1 mol% catalyst (based on Ru, obtained from ICP-OES analysis), 0.33 mmol benzyl alcohol, 0.4 mmol base, 500 μ l toluene, O₂, 100 $^\circ$ C, 12 h. ^ammol of product formed per mmol of Ru in the catalyst. ^b0.24 mol% catalyst was used. ^cUnder Ar atmosphere. ^d17 mg catalyst was used. All catalysts displayed >99% selectivity toward benzaldehyde.

Our further studies focused on the catalytic performance of the Ru^{III}@bipy-CTF catalyst for the tandem aerobic oxidation–Knoevenagel condensation reaction. For this purpose, the optimized reaction condition for the oxidation of benzyl alcohol was selected (1 mol%

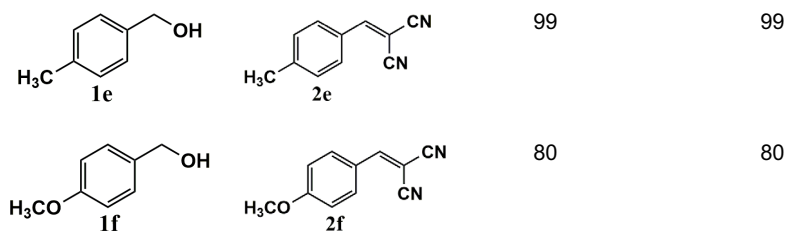
$\text{Ru}^{\text{III}}@bipy\text{-CTF}$, Cs_2CO_3 , O_2 , $100\text{ }^\circ\text{C}$, 12 h). Different substituted benzyl alcohols and malononitrile were examined and the obtained results are listed in Table 5.3. No product was formed in the absence of the catalyst. As shown in Table 5.3, the $\text{Ru}^{\text{III}}@bipy\text{-CTF}$ catalyst was found to be highly active in the Knoevenagel condensation reaction under mild reaction conditions. A high conversion was obtained for all substrates at low temperature ($70\text{ }^\circ\text{C}$) and only after 1 h. Moreover, complete selectivity was observed towards the corresponding product.

Table 5.3. Catalytic performance of $\text{Ru}^{\text{III}}@bipy\text{-CTF}$ catalyst in tandem aerobic oxidation–Knoevenagel condensation reaction.



Substrate	Product	Conv. of 1a-f (%)	Yield of 2a-f (%)
 1a	 2a	99	99
 1b	 2b	99	99
 1c	 2c	99	99
 1d	 2d	97	97

Metal- and Covalent Organic Frameworks for Advanced Applications: Heterogeneous Catalysis and Sensing



Reaction conditions: 1 mol% catalyst (based on Ru, obtained from ICP-OES analysis), 0.33 mmol alcohol, 0.4 mmol Cs₂CO₃, 500 μ l toluene, 0.33 mmol malononitrile, O₂, 100 °C, 12 h (1st step) and 70 °C, 1 h (2nd step). All substrates displayed >99% selectivity toward the corresponding product.

The recyclability of the Ru^{III}@bipy-CTF catalyst was investigated for the tandem aerobic oxidation–Knoevenagel condensation reaction. The recyclability studies showed that the Ru^{III}@bipy-CTF catalyst maintains almost its full catalytic performance after four consecutive cycles with no obvious loss of activity or selectivity. Moreover, the recycled catalyst showed no detectable Ru leaching (analyzed by ICP-OES).

A comparison of the catalytic performance of the presented system is made with various catalysts for the tandem aerobic oxidation–Knoevenagel condensation reaction. It is challenging to make a fair comparison since in almost all the studies no turnover number (TON) or turnover frequency (TOF) values were reported. Therefore, a comparison can only be made in terms of conversion to provide an overall overview. As can be seen from Table 5.4, a high yield of benzylmalononitrile is obtained over the Ru^{III}@bipy-CTF catalyst using O₂ as the green oxidant and in the absence of any co-oxidant. Moreover, the present system has the advantage of high catalytic performance without the use of expensive noble metals.

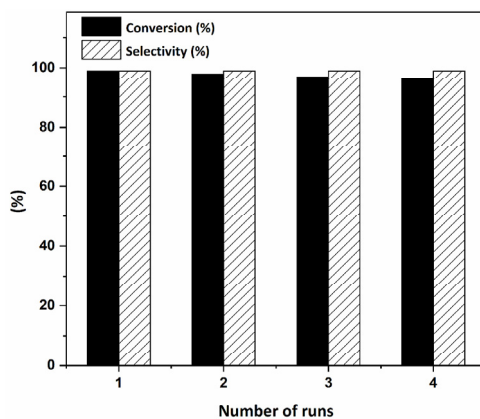


Figure 5.4. Recyclability of the Ru^{III}@bipy-CTF catalyst (1 mol% catalyst, 0.33 mmol benzyl alcohol, 0.4 mmol Cs₂CO₃, 500 μl toluene, 0.33 mmol malononitrile, O₂, 100 °C, 12 h (1st step) and 70 °C, 1 h (2nd step).

Table 5.4. Comparison of the Ru^{III}@bipy-CTF catalyst with other heterogeneous catalysts for selective tandem oxidation–Knoevenagel condensation reaction.

Entry	Catalyst	Oxidant/Temp. (°C)	Time (h) ^a	Conv./Yield (%)	Ref
1	Au@Cu(II)-MOF	Air/110	15 + 7	99/99	39
2	Au@MIL-53(NH ₂)	O ₂ /100	13	99/99	40
3	UoB-2 (Ni-MOF)	TBHP/65	1.5	94	41
4	Cu ₃ TATAT-3 MOF	O ₂ , TEMPO/75	12	95/95	42
5	Pd/COF-TaPa-Py	O ₂ /80	4 + 1.5	98/98	43
6	5CoOx/tri-g-C ₃ N ₄	O ₂ /80	6	96.4/96.4	44
7	Ru ^{III} @bipy-CTF	O ₂ /100	12 + 1	99/99	This work

^a “m + n” refers to a step-by-step reaction without separation of benzaldehyde as the intermediate.

5.4. Conclusions

In conclusion, an efficient heterogeneous catalyst is developed by applying a highly N-rich covalent triazine framework. The presence of bipyridine docking sites within the CTF provides excellent anchoring centers for the $[\text{Ru}(\text{acac})_2(\text{CH}_3\text{CN})_2]\text{PF}_6$ complex. The potential application of the obtained $\text{Ru}^{\text{III}}@\text{bipy-CTF}$ catalyst was studied in the selective tandem aerobic oxidation–Knoevenagel condensation reaction. The catalyst showed very high conversion of various benzyl alcohol derivatives (80–99%) with full selectivity towards the corresponding α , β -unsaturated nitriles using O_2 as the sole oxidant. The existence of N-rich functionalities not only act as basic sites for Knoevenagel condensation reaction but also promote the aerobic oxidation of alcohols through oxygen activation. The obtained results revealed the high catalytic performance of the $\text{Ru}^{\text{III}}@\text{bipy-CTF}$ catalyst exceeding its homogeneous counterpart. To the best of our knowledge, this is one of the rare reports on the application of Ru-based catalysts for tandem oxidation catalysis using O_2 as the sole oxidant.

5.5. Experimental Section

5.5.1. Materials and instrumentation

For details please see Appendix.

5.5.2. Synthesis of bipy-CTFs and $\text{Ru}^{\text{III}}@\text{bipy-CTF}$ materials

The preparation of the bipy-CTF material was achieved following the standard procedure described in literature applying the typical ionothermal conditions³². Typically, a glass ampule was filled with 5,5'-dicyano-2,2'-bipyridine (100 mg, 0.48 mmol) and ZnCl_2 (332 mg, 2.40 mmol) in a glovebox. The ampule was flame-sealed under vacuum and placed in an oven at 400 °C for 48 h with a heating rate of 60 °C/h. After cooling to room temperature, the ampule was opened and the black colored solid was stirred in 120 mL H_2O overnight at 60 °C, filtered and washed with H_2O and acetone. The solid was then

stirred at 120 °C in 1 M HCl (150 mL) overnight, filtered, and subsequently washed with 1 M HCl (3 × 75 mL), H₂O (15 × 75 mL), THF (3 × 75 mL), and acetone (3 × 75 mL). Finally, the powder was dried under vacuum overnight at 90 °C (Found for bipy-CTF: C, 58.92; H, 3.51; N, 20.27 %).

The [Ru(acac)₂(CH₃CN)₂]PF₆ complex was prepared according to the literature method.⁴⁶ For this, [Ru(acac)₃] (400 mg, 1 mmol) was dissolved in 30 mL of CH₃CN and to this solution, 10 mL of a 1% H₂SO₄/CH₃CN solution was slowly added while stirring. The solution was stirred at room temperature until the wine-red solution turned deep blue (approx. 12 h). Next, the solution was concentrated to 3 mL by evaporating the solvent. NH₄PF₆ (0.5 g, 3 mmol) in 5 mL of cold water was added to the deep-blue solution. The resulting deep-blue precipitate was collected by filtration, washed with cold water and n-hexane and dried under vacuum.

The post-modification of the bipy-CTF was performed as follows: [Ru(acac)₂(CH₃CN)₂]PF₆ (13.6 mg, 0.026 mmol) was added to 4 mL dry toluene. Afterward, 120 mg bipy-CTF material was added and stirred for 48 h at 80 °C. The prepared material was collected by filtration and stirred in CH₃CN for 24 h to remove the unreacted residue of the Ru complex. Then, the modified material was filtered, washed thoroughly with CH₃CN and acetone followed by drying under vacuum overnight (Found for Ru^{III}@bipy-CTF, C, 59.6; H, 3.2; N, 15.7 %).

5.5.3. Catalytic reactions

The procedure to perform the tandem reaction is as follows: The oxidation of benzyl alcohol was carried out in a 20 mL Schlenk tube. During a typical catalytic test, the catalyst (1 mol % Ru), Cs₂CO₃ (0.4 mmol, placed in a porous membrane) as base, benzyl alcohol (0.33 mmol), dodecane as internal standard (0.33 mmol) and toluene (500 μl) were added to the Schlenk tube. The tube was purged with pure oxygen, sealed and heated to 100 °C for 12 h. Samples were withdrawn after 12 h. Upon cooling to room temperature and dilution with solvent, the samples were analyzed using a gas chromatograph. Hereafter, the porous membrane containing Cs₂CO₃ was removed and nitrile substrates (0.33 mmol)

were added to the previous reaction mixture. The tube was sealed without purging oxygen. The reaction was heated from room temperature to 70 °C for an additional 1 hour. Upon cooling to room temperature and dilution with toluene, the samples were analyzed using a gas chromatograph. After each catalytic run, the catalyst was recovered by filtration and washed with toluene, water, and acetone. The catalyst was then used directly in the subsequent runs. Conversion, selectivity and yield are calculated through equations S5.1, S5.2 and S5.3 respectively (See section catalytic reactions in the SI, Figure S5.2).

5.6. References

1. Liang, J.; Liang, Z. B.; Zou, R. Q.; Zhao, Y. L., Heterogeneous Catalysis in Zeolites, Mesoporous Silica, and Metal-Organic Frameworks. *Adv Mater* **2017**, *29* (30).
2. Lehman, S. E.; Larsen, S. C., Zeolite and mesoporous silica nanomaterials: greener syntheses, environmental applications and biological toxicity. *Environ Sci-Nano* **2014**, *1* (3), 200-213.
3. Gopinath, K. P.; Vo, D. V. N.; Prakash, D. G.; Joseph, A. A.; Viswanathan, S.; Arun, J., Environmental applications of carbon-based materials: a review. *Environ Chem Lett* **2020**.
4. Huang, N.; Wang, K. C.; Drake, H.; Cai, P. Y.; Pang, J. D.; Li, J. L.; Che, S.; Huang, L.; Wang, Q.; Zhou, H. C., Tailor-Made Pyrazolide-Based Metal-Organic Frameworks for Selective Catalysis. *J Am Chem Soc* **2018**, *140* (20), 6383-6390.
5. Fried, D. I.; Brieler, F. J.; Froba, M., Designing Inorganic Porous Materials for Enzyme Adsorption and Applications in Biocatalysis. *Chemcatchem* **2013**, *5* (4), 862-884.
6. Rogge, S. M. J.; Bavykina, A.; Hajek, J.; Garcia, H.; Olivos-Suarez, A. I.; Sepulveda-Escribano, A.; Vimont, A.; Clet, G.; Bazin, P.; Kapteijn, F.; Daturi, M.; Ramos-Fernandez, E. V.; Xamena, F. X. L. I.; Van Speybroeck, V.; Gascon, J., Metal-organic and covalent organic frameworks as single-site catalysts. *Chem Soc Rev* **2017**, *46* (11), 3134-3184.
7. Thomas, A., Functional Materials: From Hard to Soft Porous Frameworks. *Angew Chem Int Edit* **2010**, *49* (45), 8328-8344.
8. Geng, K. Y.; He, T.; Liu, R. Y.; Dalapati, S.; Tan, K. T.; Li, Z. P.; Tao, S. S.; Gong, Y. F.; Jiang, Q. H.; Jiang, D. L., Covalent Organic Frameworks: Design, Synthesis, and Functions. *Chem Rev* **2020**, *120* (16), 8814-8933.
9. Diercks, C. S.; Yaghi, O. M., The atom, the molecule, and the covalent organic framework. *Science* **2017**, *355* (6328).
10. Kuhn, P.; Antonietti, M.; Thomas, A., Porous, covalent triazine-based frameworks prepared by ionothermal synthesis. *Angew Chem Int Edit* **2008**, *47* (18), 3450-3453.
11. Artz, J., Covalent Triazine-based Frameworks Tailor-made Catalysts and Catalyst Supports for Molecular and Nanoparticulate Species. *Chemcatchem* **2018**, *10* (8), 1753-1771.
12. Wang, H.; Jiang, D. N.; Huang, D. L.; Zeng, G. M.; Xu, P.; Lai, C.; Chen, M.; Cheng, M.; Zhang, C.; Wang, Z. W., Covalent triazine frameworks for carbon dioxide capture. *J Mater Chem A* **2019**, *7* (40), 22848-22870.

13. Chan-Thaw, C. E.; Villa, A.; Katekomol, P.; Su, D. S.; Thomas, A.; Prati, L., Covalent Triazine Framework as Catalytic Support for Liquid Phase Reaction. *Nano Lett* **2010**, *10* (2), 537-541.
14. Jin, R. H.; Zheng, D. S.; Liu, R.; Liu, G. H., Silica-Supported Molecular Catalysts for Tandem Reactions. *Chemcatchem* **2018**, *10* (8), 1739-1752.
15. Cho, H. J.; Xu, B. J., Enabling Selective Tandem Reactions via Catalyst Architecture Engineering. *Trends Chem* **2020**, *2* (10), 929-941.
16. Huang, Y. B.; Liang, J.; Wang, X. S.; Cao, R., Multifunctional metal-organic framework catalysts: synergistic catalysis and tandem reactions. *Chem Soc Rev* **2017**, *46* (1), 126-157.
17. Huang, L. S.; Lai, Y. H.; Yang, C.; Xu, D. Z., Iron-catalyzed one-pot oxidation/Knoevenagel condensation reaction using air as an oxidant. *Appl Organomet Chem* **2019**, *33* (6).
18. Chen, C.; Yang, H. M.; Chen, J. Z.; Zhang, R.; Guo, L.; Gan, H. M.; Song, B. N.; Zhu, W. W.; Hua, L.; Hou, Z. S., One-pot tandem catalytic synthesis of alpha, beta-unsaturated nitriles from alcohol with nitriles in aqueous phase. *Catal Commun* **2014**, *47*, 49-53.
19. Yang, Z. W.; Kang, Q. X.; Quan, F.; Lei, Z. Q., Oxidation of alcohols using iodosylbenzene as oxidant catalyzed by ruthenium complexes under mild reaction conditions. *J Mol Catal a-Chem* **2007**, *261* (2), 190-195.
20. Zhang, Y. C.; Zhou, Q.; Ma, W. C.; Zhao, J. Q., Enantioselective oxidation of racemic secondary alcohols catalyzed by chiral Mn(III)-salen complex with sodium hypochlorite as oxidant. *Catal Commun* **2014**, *45*, 114-117.
21. Lou, J. D.; Xu, Z. N., Selective oxidation of primary alcohols with chromium trioxide under solvent free conditions. *Tetrahedron Lett* **2002**, *43* (35), 6095-6097.
22. Parmeggiani, C.; Matassini, C.; Cardona, F., A step forward towards sustainable aerobic alcohol oxidation: new and revised catalysts based on transition metals on solid supports. *Green Chem* **2017**, *19* (9), 2030-2050.
23. Sheldon, R. A.; Arends, I. W. C. E.; Ten Brink, G. J.; Dijkstra, A., Green, catalytic oxidations of alcohols. *Accounts Chem Res* **2002**, *35* (9), 774-781.
24. Piera, J.; Backvall, J. E., Catalytic oxidation of organic substrates by molecular oxygen and hydrogen peroxide by multistep electron transfer - A biomimetic approach. *Angew Chem Int Edit* **2008**, *47* (19), 3506-3523.
25. Lu, T. L.; Du, Z. T.; Liu, J. X.; Ma, H.; Xu, J., Aerobic oxidation of primary aliphatic alcohols over bismuth oxide supported platinum catalysts in water. *Green Chem* **2013**, *15* (8), 2215-2221.
26. Abednatanzi, S.; Derakhshandeh, P. G.; Abbasi, A.; Van der Voort, P.; Leus, K., Direct Synthesis of an Iridium(III) Bipyridine Metal-Organic Framework as a Heterogeneous Catalyst for Aerobic Alcohol Oxidation. *Chemcatchem* **2016**, *8* (23), 3672-3679.
27. Zeng, X. M.; Chen, J. M.; Yoshimura, A.; Middleton, K.; Zhdankin, V. V., SiO₂-supported RuCl₃·3-(dichloroiodo)benzoic acid: green catalytic system for the oxidation of alcohols and sulfides in water. *Rsc Adv* **2011**, *1* (6), 973-977.
28. Ganesamoorthy, S.; Tamizh, M. M.; Shanmugasundaram, K.; Karvembu, R., Immobilization of Ru(III) complex on silica: a heterogenized catalyst for selective oxidation of alcohols in water at room temperature. *Tetrahedron Lett* **2013**, *54* (51), 7035-7039.
29. Clerick, S.; De Canck, E.; Hendrickx, K.; Van Speybroeck, V.; Van der Voort, P., Heterogeneous Ru(III) oxidation catalysts via 'click' bidentate ligands on a periodic mesoporous organosilica support. *Green Chem* **2016**, *18* (22), 6035-6045.
30. Guo, H. J.; Liu, W. D.; Yin, G. C., Aerobic oxidation of alcohols to aldehydes and ketones using ruthenium(III)/Et₃N catalyst. *Appl Organomet Chem* **2011**, *25* (11), 836-842.
31. Sodhi, R. K.; Paul, S.; Clark, J. H., A comparative study of different metal acetylacetonates covalently anchored onto amine functionalized silica: a study of the oxidation of aldehydes and alcohols to corresponding acids in water. *Green Chem* **2012**, *14* (6), 1649-1656.

32. Hug, S.; Tauchert, M. E.; Li, S.; Pachmayr, U. E.; Lotsch, B. V., A functional triazine framework based on N-heterocyclic building blocks. *J Mater Chem* **2012**, *22* (28), 13956-13964.
33. Bagherzadeh, M.; Karimi, H.; Amini, M., Immobilization of dioxomolybdenum(VI) Schiff base complex on graphene oxide nanosheets and its catalytic activity for oxidation of sulfides. *J Coord Chem* **2017**, *70* (17), 2986-2998.
34. Osadchii, D. Y.; Olivos-Suarez, A. I.; Bavykina, A. V.; Gascon, J., Revisiting Nitrogen Species in Covalent Triazine Frameworks. *Langmuir* **2017**, *33* (50), 14278-14285.
35. Chen, L. Y.; Huang, B. B.; Qiu, X.; Wang, X.; Luque, R.; Li, Y. W., Seed-mediated growth of MOF-encapsulated Pd@Ag core-shell nanoparticles: toward advanced room temperature nanocatalysts. *Chem Sci* **2016**, *7* (1), 228-233.
36. Watanabe, H.; Asano, S.; Fujita, S.; Yoshida, H.; Arai, M., Nitrogen-Doped, Metal-Free Activated Carbon Catalysts for Aerobic Oxidation of Alcohols. *ACS Catal* **2015**, *5* (5), 2886-2894.
37. Abednatanzi, S.; Derakhshandeh, P. G.; Leus, K.; Vrielinck, H.; Callens, F.; Schmidt, J.; Savateev, A.; Van der Voort, P., Metal-free activation of molecular oxygen by covalent triazine frameworks for selective aerobic oxidation. *Sci Adv* **2020**, *6* (14).
38. Abednatanzi, S.; Derakhshandeh, P. G.; Tack, P.; Muniz-Miranda, F.; Liu, Y. Y.; Everaert, J.; Meledina, M.; Vanden Bussche, F.; Vincze, L.; Stevens, C. V.; Van Speybroeck, V.; Vrielinck, H.; Callens, F.; Leus, K.; Van Der Voort, P., Elucidating the promotional effect of a covalent triazine framework in aerobic oxidation. *Appl Catal B-Environ* **2020**, 269.
39. Wang, J. S.; Jin, F. Z.; Ma, H. C.; Li, X. B.; Liu, M. Y.; Kan, J. L.; Chen, G. J.; Dong, Y. B., Au@Cu(II)-MOF: Highly Efficient Bifunctional Heterogeneous Catalyst for Successive Oxidation-Condensation Reactions. *Inorg Chem* **2016**, *55* (13), 6685-6691.
40. Qi, Y.; Luan, Y.; Peng, X.; Yang, M.; Hou, J. Y.; Wang, G., Design and Synthesis of an Au@MIL-53(NH₂) Catalyst for a One-Pot Aerobic Oxidation/Knoevenagel Condensation Reaction. *Eur J Inorg Chem* **2015**, (30), 5099-5105.
41. Aryanejad, S.; Bagherzade, G.; Farrokhi, A., Efficient and recyclable novel Ni-based metal-organic framework nanostructure as catalyst for the cascade reaction of alcohol oxidation-Knoevenagel condensation. *Appl Organomet Chem* **2018**, *32* (2).
42. Miao, Z. C.; Luan, Y.; Qi, C.; Ramella, D., The synthesis of a bifunctional copper metal organic framework and its application in the aerobic oxidation/Knoevenagel condensation sequential reaction. *Dalton T* **2016**, *45* (35), 13917-13924.
43. Sun, Q.; Aguila, B.; Ma, S. Q., A bifunctional covalent organic framework as an efficient platform for cascade catalysis. *Mater Chem Front* **2017**, *1* (7), 1310-1316.
44. Wu, J. Q.; Hua, W. M.; Yue, Y. H.; Gao, Z., A Highly Efficient Bifunctional Catalyst CoOx/tri-g-C(3)N(4) for One-Pot Aerobic Oxidation-Knoevenagel Condensation Reaction. *Catalysts* **2020**, *10* (6).
45. Liao, L. Y.; Kong, X. R.; Duan, X. F., Reductive Couplings of 2-Halopyridines without External Ligand: Phosphine-Free Nickel-Catalyzed Synthesis of Symmetrical and Unsymmetrical 2,2'-Bipyridines. *J Org Chem* **2014**, *79* (2), 777-782.
46. Koiwa, T.; Masuda, Y.; Shono, J.; Kawamoto, Y.; Hoshino, Y.; Hashimoto, T.; Natarajan, K.; Shimizu, K., Synthesis, characterization, and detailed electrochemistry of binuclear ruthenium(III) complexes bridged by bisacetylacetonate. Crystal and molecular structures of [Ru(acac)(2)](2)(tae) (acac=2,4-pentanedionate ion, tae=1,1,2,2-tetraacetylthionate dianion). *Inorg Chem* **2004**, *43* (20), 6215-6223.

5.7. Supporting Information

Mechanistic studies

To obtain an insight of the function of the bipy-CTF material in oxidation catalysis, a set of control experiments was performed (Table S5.1). In this regard, a control experiment was performed using the pristine bipy-CTF material. A conversion of 39% was obtained using the pristine bipy-CTF as the catalyst in the presence of Cs₂CO₃ as the base. (Table S5.1, entry 1). To obtain more insight into the role of the base, the influence of different bases was investigated. The obtained results are outlined in Table S5.1 below. As can be observed, the reaction without any basic additive resulted in no conversion of benzyl alcohol (Table S5.1, entry 2). However, the addition of a variety of bases, such as Na₂CO₃, K₂CO₃, and Cs₂CO₃, improved the catalytic activity, with the highest activity obtained using Cs₂CO₃. In general, carboxylates with bigger counter cations are more dissociated in aprotic solvents and consequently more reactive. Similar trend is observed for the Ru^{III}@bipy-CTF catalyst (Table 5.2, entries 1-4 of the manuscript). We believe that the applied base can facilitate the deprotonation of benzyl alcohol and boosts the catalytic activity. The conversion of benzyl alcohol towards benzaldehyde dramatically lowered to 3% under Ar atmosphere, proving the essential role of oxygen as the oxidant (Table S5.1, entry 5). Another control experiment was done using *p*-benzoquinone (Table S5.1, entry 7). The addition of *p*-benzoquinone as superoxide ([•]O₂⁻) scavenger into the reaction system containing bipy-CTF as the catalyst completely suppressed the oxidation of benzyl alcohol (conversion < 1%). This observation indicates that bipy-CTF activates molecular oxygen to superoxide, which acts as oxidant species in the catalytic cycle.

Table S5.1. Various control experiments to obtain insights into the reaction mechanism for the oxidation of benzyl alcohol.

Entry	Catalyst	base	Conversion (%)
1	bipy-CTF	Cs ₂ CO ₃	39
2	bipy-CTF	No base	3

Metal- and Covalent Organic Frameworks for Advanced Applications: Heterogeneous Catalysis and Sensing

3	bipy-CTF	K_2CO_3	18
4	bipy-CTF	Na_2CO_3	10
5 ^a	bipy-CTF	Cs_2CO_3	3
6 ^b	bipy-CTF	Cs_2CO_3	14
7 ^c	bipy-CTF	Cs_2CO_3	<1

Reaction conditions: 17 mg bipy-CTF, 0.33 mmol benzyl alcohol, 0.4 mmol base, 500 μ l toluene, O_2 , 100 $^\circ C$, 12 h. ^aUnder Ar atmosphere. ^bReaction was done at 50 $^\circ C$. ^c*p*-benzoquinone (0.33 mmol) was added.

So far, many experimental and theoretical investigations have shown the applicability of N-doped carbon-based materials for adsorption and activation of molecular O_2 .¹⁻² Based on our observations and previous reports,³⁻⁴ we propose that the oxygen activation occurs on the surface of bipy-CTF and the generated superoxide reacts with benzyl alcohol to generate $PhCH_2O^-$ and subsequently $PhCH_2O^{\bullet}$ and benzaldehyde. Although the exact mechanism on the aerobic oxidation using $[Ru(acac)_2(CH_3CN)_2]PF_6$ complex has been remained unknown in the previous reports, it can be expected that the generated $PhCH_2O^-$ on the surface of bipy-CTF reacts with the Ru centers in the reaction system. The obtained results thus corroborate each other, unveiling the promotional impact of bipy-CTF in activating oxygen and benzyl alcohol in our reaction system. A reaction mechanism is proposed based on the obtained results and previous studies,³⁻⁴ as shown below.

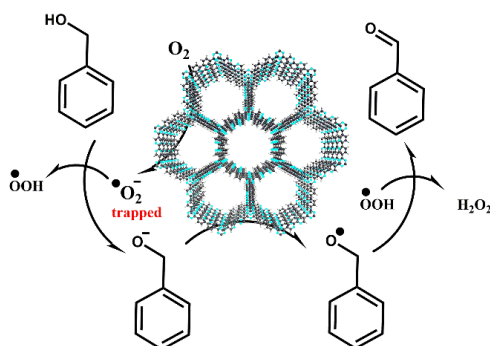


Figure S5.1. Proposed mechanism for bipy-CTF-catalyzed aerobic oxidation of benzyl alcohol.

Catalytic reactions

Conversion, yield and selectivity are calculated through equations S1, S2 and S3 respectively. Dodecane was used as the internal standard. The conversion, yield and selectivity are calculated based on the observed peak area using a TRACE GC × GC (Thermo, Interscience) coupled to a TEMPUS TOFMS detector (Thermo, Interscience). The pure starting material (alcohols) and products (α , β -unsaturated nitriles) were injected to the GC as the reference peaks.

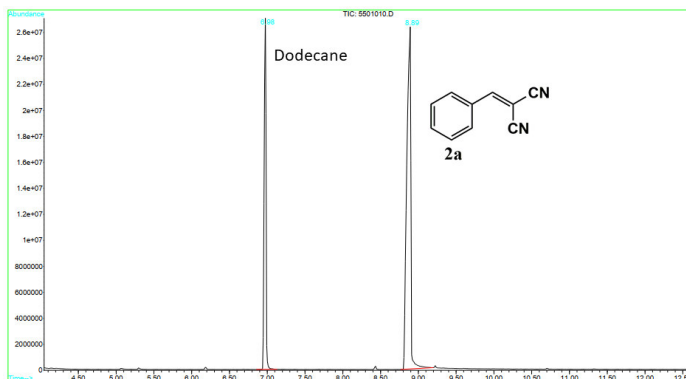
$$(S5.1) \text{ Conversion} = 1 - \left(\frac{\text{Area of IS1}}{\text{Area of S1}} \times \frac{\text{Area of S2}}{\text{Area of IS2}} \right) \times 100$$

$$(S5.2) \text{ Yield} = \frac{\text{mmol of S1} - \text{mmol of S2}}{\text{mmol of S1}} \times 100$$

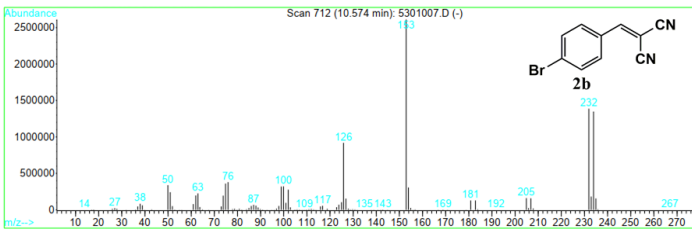
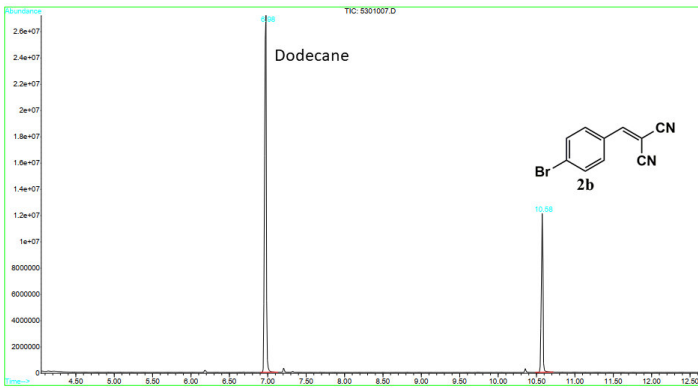
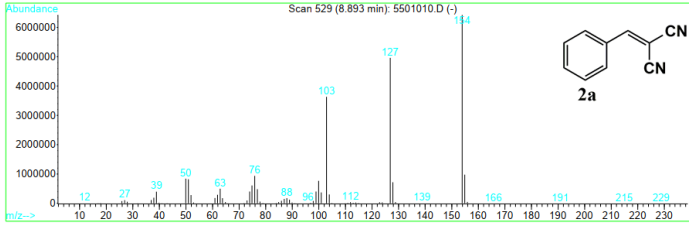
$$(S5.3) \text{ Selectivity} = \frac{\text{Area of Px}}{\text{Area of all products}} \times 100$$

IS1= Internal standard at time zero; S1= Substrate at time zero; S2= Substrate at time X;
IS2= Internal standard at time X; PX= Product X.

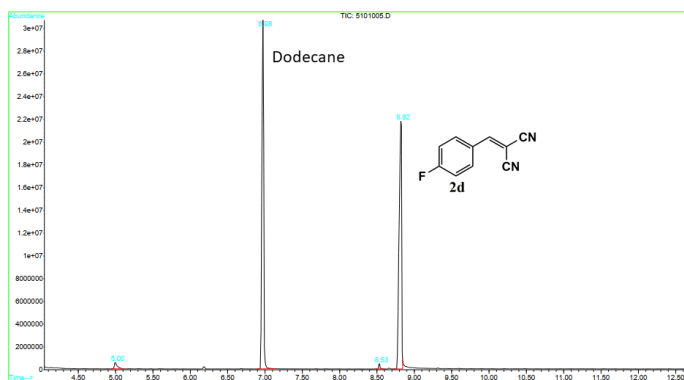
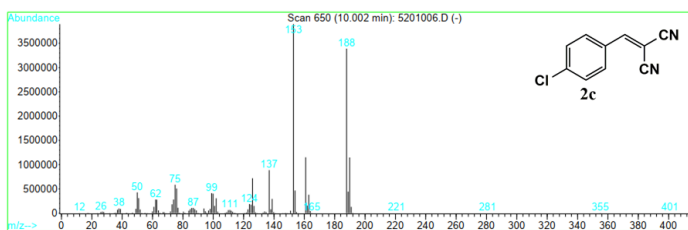
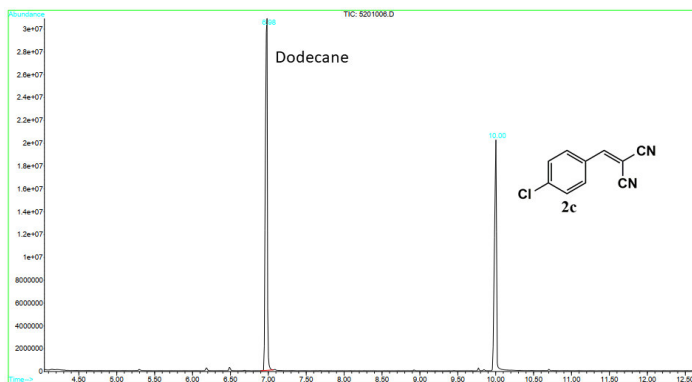
The GC-MS spectra of the α , β -unsaturated nitriles are presented below.



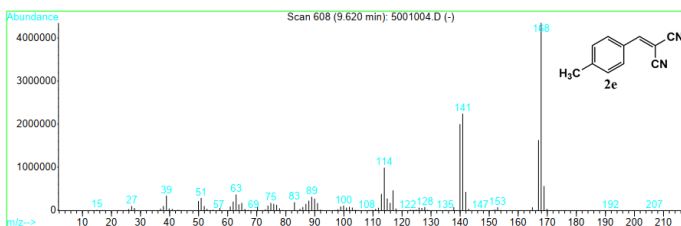
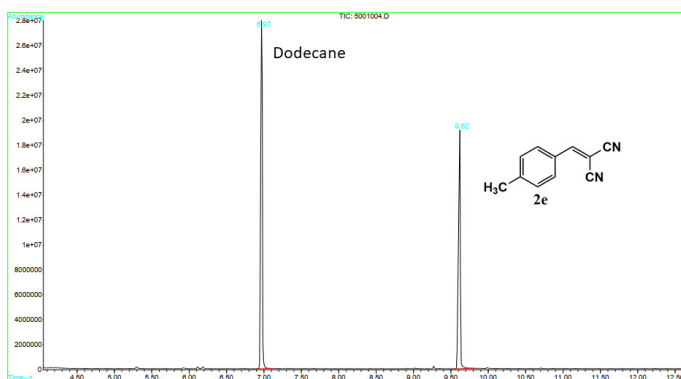
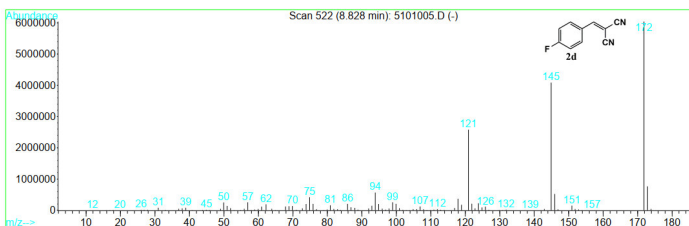
Metal- and Covalent Organic Frameworks for Advanced Applications: Heterogeneous Catalysis and Sensing



Chapter 5: A Ru-complex tethered to a N-Rich Covalent Triazine Framework for Tandem Aerobic Oxidation–Knoevenagel Condensation Reactions



Metal- and Covalent Organic Frameworks for Advanced Applications: Heterogeneous Catalysis and Sensing



Chapter 5: A Ru-complex tethered to a N-Rich Covalent Triazine Framework for Tandem Aerobic Oxidation–Knoevenagel Condensation Reactions

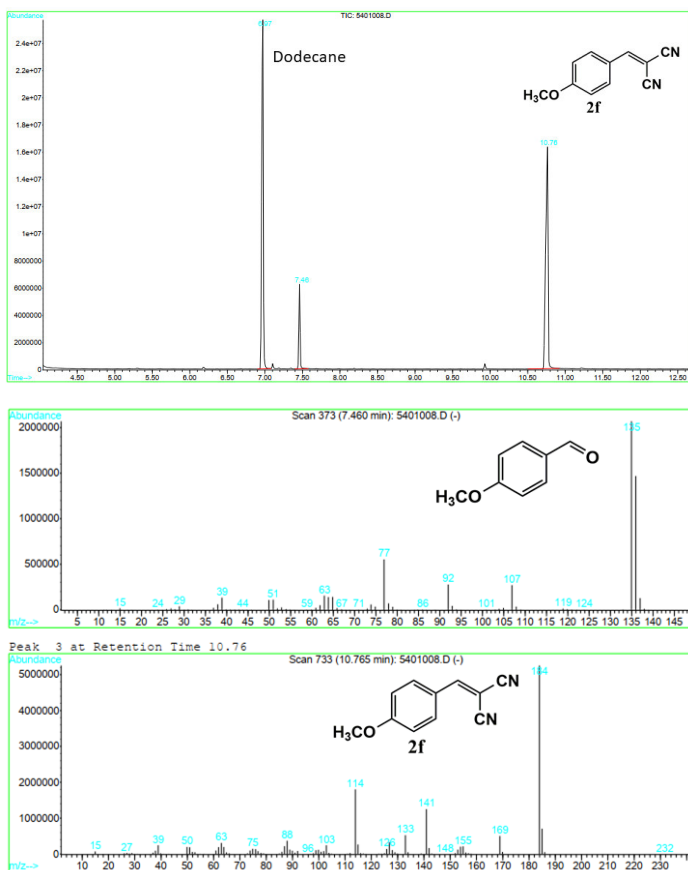


Figure S5.2. The GC-MS spectra of the α , β -unsaturated nitriles.

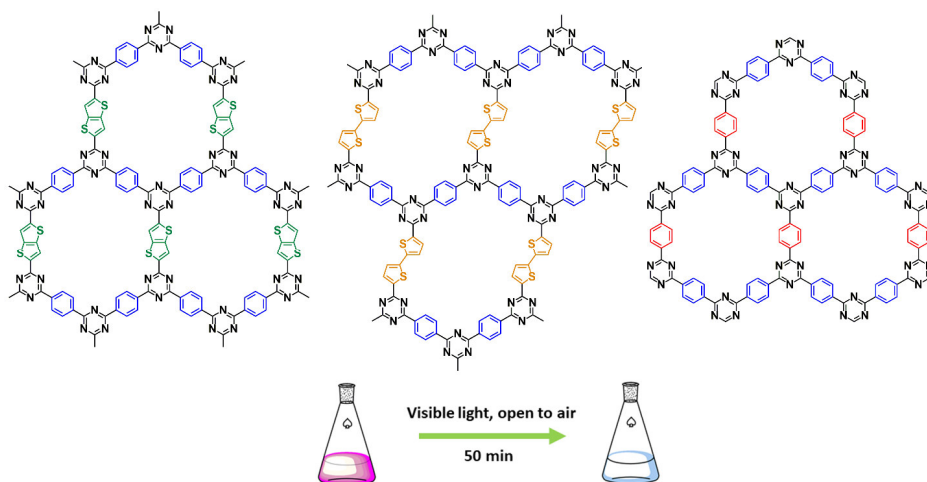
References:

1. Watanabe, H.; Asano, S.; Fujita, S.; Yoshida, H.; Arai, M., Nitrogen-Doped, Metal-Free Activated Carbon Catalysts for Aerobic Oxidation of Alcohols. *Acs Catal* **2015**, 5 (5), 2886-2894.
2. Eisenberg, D; Slot, T.K; Rothenberg, G.; Understanding oxygen activation on metal- and nitrogen-codoped carbon catalysts. *ACS Catal* **2018**, 8, 8618–8629.

3. Abednatanzi, S.; Derakhshandeh, P. G.; Leus, K.; Vrielinck, H.; Callens, F.; Schmidt, J.; Savateev, A.; Van der Voort, P., Metal-free activation of molecular oxygen by covalent triazine frameworks for selective aerobic oxidation. *Sci Adv* **2020**, 6 (14).
4. Abednatanzi, S.; Derakhshandeh, P. G.; Tack, P.; Muniz-Miranda, F.; Liu, Y. Y.; Everaert, J.; Meledina, M.; Vanden Bussche, F.; Vincze, L.; Stevens, C. V.; Van Speybroeck, V.; Vrielinck, H.; Callens, F.; Leus, K.; Van Der Voort, P., Elucidating the promotional effect of a covalent triazine framework in aerobic oxidation. *Appl Catal B-Environ* **2020**, 269.

CHAPTER 6

COVALENT TRIAZINE FRAMEWORKS AS METAL-FREE HETEROGENEOUS PHOTOCATALYSTS FOR POLLUTANT DEGRADATION



The results of this chapter are submitted:

P. Gohari Derakhshandeh, M. Ovisi, S. Abednatanzi, M. Alinia Asli, N. M. Mahmoodi, P. Saadat Esbah Tabaei, R. Morent, N. De Geyter, P. Van Der Voort. Covalent Triazine Frameworks as Metal-Free Heterogeneous Photocatalysts for Pollutant Degradation.

Abstract

The metal-free photocatalytic elimination of organic pollutants under visible light irradiation and ambient conditions is an environmentally friendly and energy-saving approach. However, the photocatalytic performances of most photocatalyst is hindered by limited visible light absorption, insufficient charge transfer and fast charge recombination. Covalent triazine frameworks (CTFs), as tunable porous materials with conjugated structures and high stability, are attractive for photocatalytic removal of organic pollutants. Herein, two new highly N,S-rich CTFs, referred as TT-CTF and BT-CTF, are synthesized via the condensation reaction of aldehydes and amidines in mild conditions. The introduction of S-containing linkers (based on thiophene functionalities) into the structure of donor-acceptor CTFs could effectively expand visible light harvesting and enhance the charge transfer by π -electron delocalization. The prepared CTFs were used as photocatalysts for the degradation of Rhodamine B from aqueous media under visible light irradiation. Our observations prove that different parameters including porosity, heteroatom density, rigidity and donor-acceptor moieties have a direct impact on the photocatalytic activity. The results indicated that the degradation of the best performing catalyst follows a first-order kinetic with a high degradation constant (0.087 min^{-1}). To the best of our knowledge, this is the first report on the application of CTFs for photocatalytic degradation of dyes.

6.1. Introduction

The growing interest in the development of advanced porous materials has inspired the scientific community to design materials with permanent porosity and tunable functionality.¹

Covalent triazine frameworks (CTFs) have received growing interest recently due to their unique properties.²⁻⁵ The ease of synthesis and wide variability in organic linkers provide a great platform to incorporate a range of functionalities into the framework. Therefore, their chemical structure and properties can be tuned based on targeted applications.⁵⁻¹³

The development of high-performance materials is a key step to address challenges in environmental remediation technologies.¹⁴ The release of untreated wastewater into the environment has led to an immense threat to ecological systems and human health. Micropollutants such as pesticides, antibiotics and dyes are one of the most refractory contaminants to be degraded.¹⁵ Among a variety of processes to decompose micropollutants, photocatalysis has been considered as a very promising technology.¹⁶⁻²⁰ This is due to its unique properties including (1) eco-friendly reaction conditions (ambient temperature and pressure); (2) the use of solar energy as a cheap and abundant energy source; (3) strong redox ability. So far, different inorganic and organic materials have been applied as photocatalysts for the removal of organic contaminants.²¹⁻²⁴ However, many of the photocatalytic systems suffer from large bandgaps and inefficient use of the solar spectrum. For instance, TiO_2 is a widely used catalyst due to its stability, low cost, non-toxicity and high photocatalytic activity. Unfortunately, TiO_2 is only active under the UV irradiation because of its large bandgap (3.2 eV).²⁵ Graphitic carbon nitride (g- C_3N_4) is an interesting metal-free photocatalyst which possesses desirable bandgap (2.70 eV).²⁶⁻²⁷ Still, g- C_3N_4 photocatalysts suffer from poor chemical diversity, limited absorption of visible light and fast charge recombination. Besides, various semiconductors such as metal oxides, noble metals and metal-organic frameworks catalysts have been used.²⁸ However, metal catalysts have the drawbacks of post-recovery after water treatment. Therefore, there is an urgent need to design efficient, metal-free photocatalysts with a broad absorption range of the visible-light.

CTFs with tailorable structures, adjustable semiconductive properties, tunable functionality and broad absorption of visible light hold great potential in photocatalysis.^{4, 29-30} Specifically, CTFs are very interesting candidates for metal-free photocatalytic decomposition of micropollutants. The presence of nitrogen-rich functionalities and an extended π -conjugated skeleton are beneficial to obtain promising photocatalytic systems. The energy band-gap and photo induced charge carriers are the main determining factors in the photocatalyst performance.³¹ CTFs can be designed precisely to tune the structural factors that impact the photocatalytic performance.³²

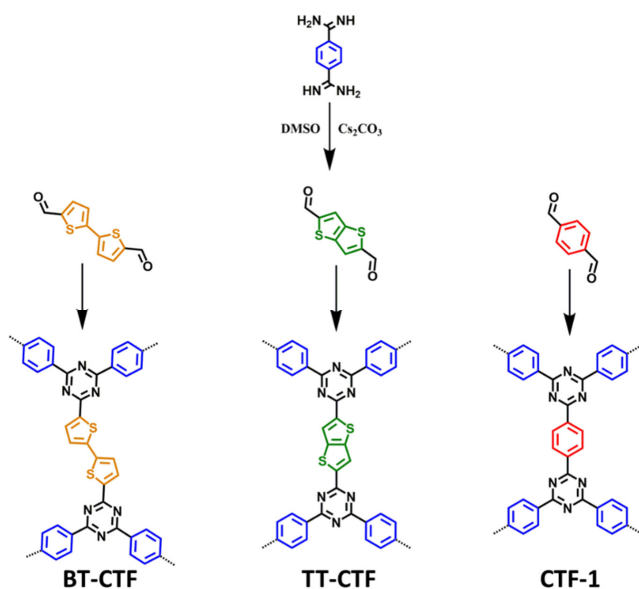
Heteroatom doping is a well-investigated strategy to adjust the band-gap and charge transfer in a photocatalyst.³³⁻³⁷ Compared to the postprocessing doping strategies in carbon materials, CTFs are fabricated directly applying the heteroatom-containing building blocks. Therefore, fine and uniform distribution of heteroatoms is obtained in the final material. The heteroatom-containing functionalities incorporate an electron donor-acceptor feature to the CTF. Accordingly, the electrostatic interactions of donor and acceptor moieties in the CTFs facilitates the charge separation/transfer and further promote the photocatalytic performance.

We present here the design of two new CTFs containing S and N functionalities via the condensation reaction of aldehydes and amidines in mild conditions. For this purpose, two thienothiophene-based bis-heterocyclic precursors were applied and reacted with an amidine linker directly. The CTFs were applied as metal-free photocatalysts for dye degradation. In addition, a basic CTF with only N functionalities, CTF-1, is applied to compare the photocatalytic activity with those containing S and N heteroatoms. Accordingly, the effect of heteroatoms on the physicochemical properties and photocatalytic efficiency is investigated. The obtained results show that accessibility and density of active centers, as well as the highly delocalized π -system boost the photocatalytic performance.

6.2. Results and Discussion

6.2.1. Synthesis and Characterization of heteroatom-embedded CTFs

The CTFs applied in this study are synthesized by the condensation reaction of terephthalamidine dihydrochloride and either thieno[3,2-b]thiophene-2,5-dicarboxaldehyde, 2,2'-bithiophene-5,5'-dicarboxaldehyde or 1,4-phthalaldehyde linkers as depicted in Scheme 6.1 (see detailed procedure in the ESI[†]). The obtained CTFs are named TT-CTF, BT-CTF and CTF-1, respectively. The terephthalamidine dihydrochloride precursor is synthesized following the reported procedure.³⁰ The polycondensation reaction of aldehyde and amidine linkers resulted in the formation of extended porous network having triazine linkages (Figure 6.1).



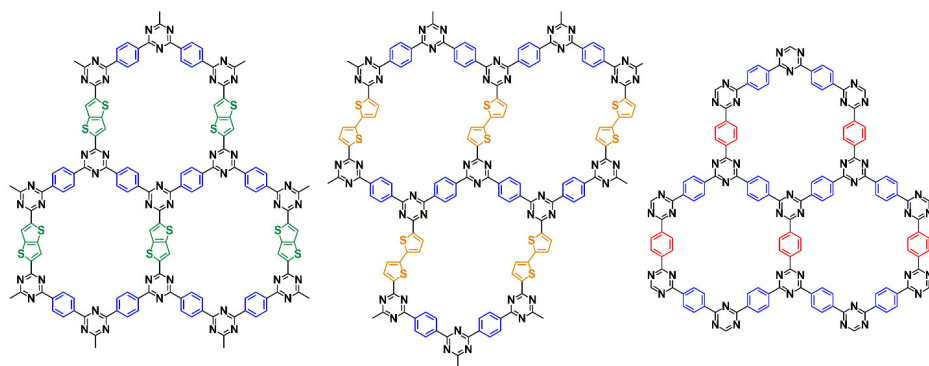


Figure 6.1. Synthesis of covalent triazine frameworks via condensation of different aldehyde monomers with amidine.

The formation of the triazine frameworks was confirmed by Fourier Transform Infrared Spectroscopy (FT-IR). In the FT-IR spectra of BT-CTF, TT-CTF and CTF-1, the vibrational bands at around 1504 cm^{-1} and 1352 cm^{-1} are attributed to the stretching vibrations of C=N and C-N of the triazine units. The FT-IR spectra of the starting linkers are shown in Figure S6.1. The absence of the vibrational peaks at around $1650\text{--}1682\text{ cm}^{-1}$ and $3060\text{--}3299\text{ cm}^{-1}$, characteristic of C=O (from aldehyde linkers) and N-H (from amidine linker) groups indicates the complete consumption of the monomers (Figure 6.2a). Elemental analysis shows the presence of N in all materials and S in BT-CTF and TT-CTF CT which are in good agreement with the theoretical values (Table S6.1). The porosity of materials was investigated by means of N_2 sorption measurement at 77 K (Figure 6.2b). All CTFs display type-I isotherms characteristic of highly microporous frameworks. The specific Brunauer-Emmett-Teller (BET) surface area values for TT-CTF, BT-CTF and CTF-1 are 298, 62 and $613\text{ m}^2\text{g}^{-1}$, with total pore volumes of 0.23, 0.20, and $0.33\text{ cm}^3\text{g}^{-1}$, respectively. The powder XRD patterns of all CTFs display a very broad peak at $2\theta \sim 26^\circ$ attributed to (001) reflection and representing a layer stacking in the materials (Figure 6.2c). The thermal gravimetric analysis (TGA) represents the high thermal stability of the CTF materials. TT-CTF and BT-CTF are thermally stable up to around $300\text{--}350\text{ }^\circ\text{C}$ (Figure 6.2d). CTF-1 is stable up to $500\text{ }^\circ\text{C}$ and decompose at higher temperatures.

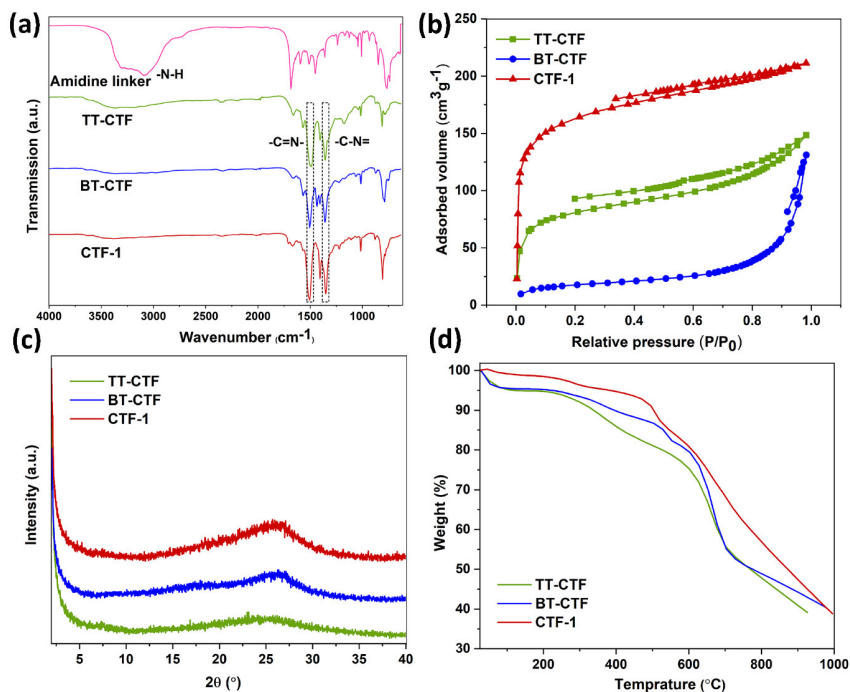


Figure 6.2. (a) DRIFT spectra, (b) Nitrogen adsorption/desorption isotherms, (c) Powder XRD patterns, (d) TGA curves.

TEM imaging (Figures 6.3a-c) was exploited to investigate the morphology and the crystallinity of the CTF materials. TEM images represent a flaky-like morphology. From the images, the layered structure of materials with nanosized pores can be observed. The scanning electron microscopy (SEM) images is shown in Figure S6.2.

Moreover, XPS reveals the elements and bonding types in the CTFs. The N 1s spectra of all CTFs display three peaks centered at around 398.8, 399.8 and 402 eV representing the pyridinic, pyrrolic and pyridine-N-O species (Figure 6.4a-c). The peaks around 398.8 eV for TT-CTF, BT-CTF and CTF-1 were all attributed to pyridine nitrogen of the triazine ring (C=N-C) formation.

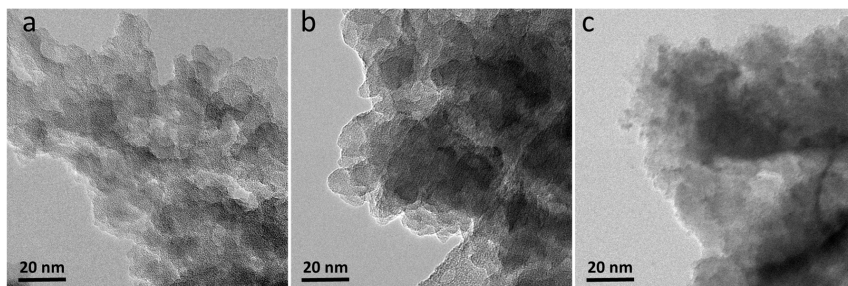


Figure 6.3. (a-c) TEM images of TT-CTF, BT-CTF and CTF-1, respectively.

Moreover, the S 2p spectra of TT-CTF and BT-CTF shows three peaks with the binding energies of 164, 165 and 168.6 eV, characteristic of S 2p_{3/2} and S 2p_{1/2} of thiophene species and oxidized sulfur species (Figure 6.4d-e).

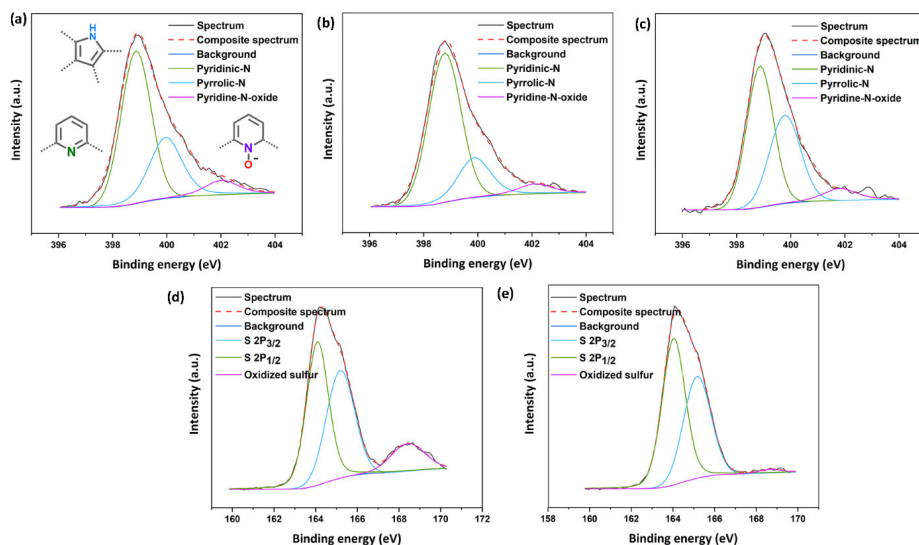


Figure 6.4. XPS high resolution N 1s spectra of TT-CTF (a), BT-CTF (b), CTF-1 (c), and S 2p spectra of TT-CTF (d), and BT-CTF (e).

6.2.2. Catalytic performance of heteroatom-embedded CTFs for the photocatalytic degradation of Rhodamine B (RB)

Dyes are one of the most important chemicals with high production and consumption. The discharge of toxic dye-containing wastewater from different industries has severe impact on aquatic life and human beings.³⁸⁻³⁹ The obtained CTFs were applied to examine their potential application as catalyst in the photocatalytic degradation of rhodamine B (RB) as a model organic pollutant. RB is considerably stable under visible light exposure in the absence of a photocatalyst and the self-photolysis is negligible. Different parameters such as the catalyst amount (2–5 mg), RB concentration (50–80 mg/L) and time (0–60 min) of decolorization were assessed under visible light. Before irradiation with visible light, dark adsorption tests were performed by the addition of the photocatalysts into the RB solution, followed by stirring. Figure 6.5 shows that the applied CTFs exhibit different adsorption capacities towards RB. The RB adsorption on the structures of CTFs is mostly via π - π stacking interaction. The adsorption of RB in the dark was found to be 33%, 8%, and 47% for TT-CTF, BT-CTF and CTF-1, respectively. Generally, the adsorption capacity can be increased in materials with higher surface area, pore volume, and accessible active sites.¹⁶ The observed adsorption ability of the CTFs is in good accordance with their specific BET surface area. More specifically, CTF-1 with the highest specific BET surface area shows the highest adsorption capacity. Afterwards, the visible-light photocatalytic activity of the CTF materials was evaluated and the results are displayed in Figure 6.5. The photocatalytic degradation of RB (50 mg L⁻¹) using various amounts of CTFs (2, 3, 4 and 5 mg) was investigated under visible light irradiation. For all CTFs, the maximum photocatalytic decomposition of RB was achieved by using 5 mg of the photocatalyst. The obtained results display the superior photocatalytic performance of TT-CTF for RB degradation compared to BT-CTF and CTF-1. After only 50 min irradiation under visible light, TT-CTF could fully degrade RB molecules (Figure 6.5a), whereas only 42% and 78% of RB is removed by BT-CTF and CTF-1, respectively. No considerable RB decolorization is observed in the absence of the photocatalyst after 60 min of visible light irradiation. The effect of initial RB concentration (50 to 80 mg/L) on the decolorization using TT-CTF is investigated. Figure 6.5d shows that at an initial RB concentration of 50 mg/L, the maximum degradation occurs.

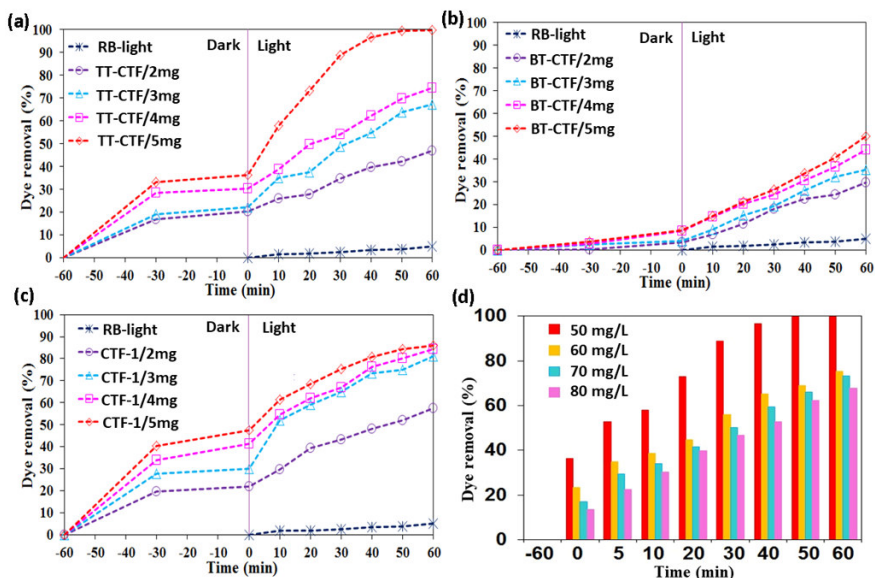


Figure 6.5. Photocatalytic degradation of RB (50 mg L⁻¹) over (a) TT-CTF, (b) BT-CTF and (c) CTF-1 using various amounts of photocatalysts (2, 3, 4 and 5 mg) under visible light irradiation. (d) The degradation efficiency of RB under visible light processes at various pollutant concentrations.

The kinetics of RB degradation was studied using TT-CTF, BT-CTF and CTF-1 materials (Figures S6.3 and Table S6.2). The results showed that the photocatalytic decomposition of RB follows the pseudo-first-order kinetic model at various dosages of catalysts, that is $-\ln(C/C_0) = kt$, where C_0 and C are the initial and actual concentrations of RB and k is the kinetic constant. From Table S6.2, it is obvious that TT-CTF possesses the highest photodegradation efficiency with the rate constant of 0.072 min^{-1} , which is higher than that of BT-CTF (0.009 min^{-1}) and CTF-1 (0.024 min^{-1}). The optical absorption properties of the CTFs were measured by UV-visible diffuse reflectance spectroscopy (DRS) (Figure 6.6). It is observed that all materials absorb a wide range of visible light. The band gap energies of CTFs were calculated to be 2.58, 2.42 and 2.98 eV for TT-CTF, BT-CTF and CTF-1, respectively. The BT-CTF exhibited the narrowest band gap of 2.42 eV.

Although a narrow band gap provides a broader light-responsive range and enhance light absorption, but it is not the only determinant factor for the efficient photocatalytic performance. Based on these observations, we can conclude that the following factors are responsible to boost the photocatalytic activity: 1) High surface area which results in the effective absorption of visible light as well as the adsorption of the dye molecule, 2) The presence of heteroatoms which provides materials with a lower band gap, 3) Rigidity of the framework to minimize intramolecular rotation and therefore enhancing the life-time of excited species, 4) The presence of donor-acceptor functionalities to promote charge carrier transport mobility and 5) Higher density of heteroatoms as the visible-light active centers. Therefore, TT-CTF that possess all these requirements represent the highest photocatalytic activity.

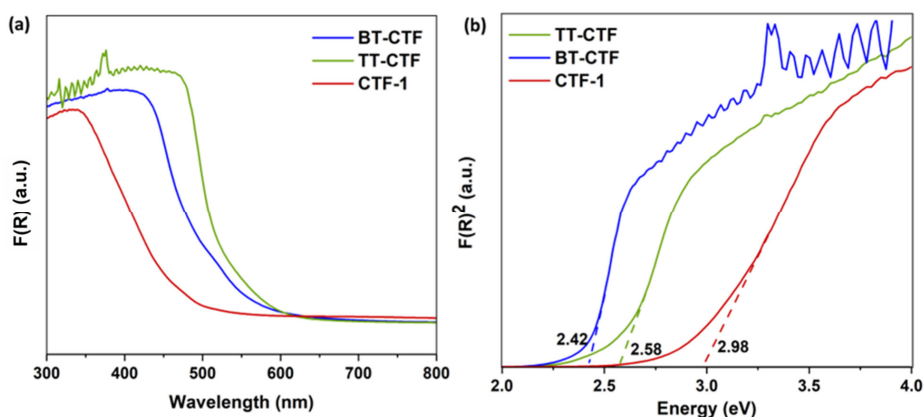


Figure 6.6. (a) Solid state UV-Vis spectra, (b) Tauc plot analyses for bandgap calculations of the CTFs.

6.2.3. Mechanistic studies for the photocatalytic degradation of Rhodamine B over the TT-CTF catalyst

The possible photocatalytic mechanism was investigated by performing various control experiments using the TT-CTF catalyst. For this purpose, different catalytic tests were done using radical trapping agents to identify the active species in the photocatalytic

reaction (Figure 6.7a). The photocatalytic degradation of RB was considerably reduced under Ar atmosphere, indicating the essential role of air to enhance the activity of the TT-CTF. As shown in Figure 6.7a, the RB decomposition is significantly lowered by the addition of tert-butyl alcohol (tBA) and benzoic acid as hydroxyl radical ($\cdot\text{OH}$) scavengers. Besides, in the presence of Tiron as a superoxide radical scavenger ($\text{O}_2^{\cdot-}$), the RB degradation considerably reduced to around 40% after 60 minutes. Furthermore, the photocatalytic degradation efficiency of TT-CTF is decreased by the addition of sodium azide as the singlet oxygen trapping agent. All these control experiments suggest that different reactive oxygen species including superoxide radicals ($\text{O}_2^{\cdot-}$), hydroxyl radicals ($\cdot\text{OH}$) and singlet oxygen ($^1\text{O}_2$) are the main active species in the photodegradation process. Figure 6.7b represents the proposed photocatalytic mechanism for the RB degradation over TT-CTF and under visible light irradiation. Upon excitation of TT-CTF under visible light, reactive oxygen species are generated on the surface of the catalyst. The generated superoxide radicals consequently react with H_2O to form hydroxyl radicals which can efficiently degrade organic pollutants. Moreover, water and RB molecules interact with the created holes and assist in the efficient charge separation.

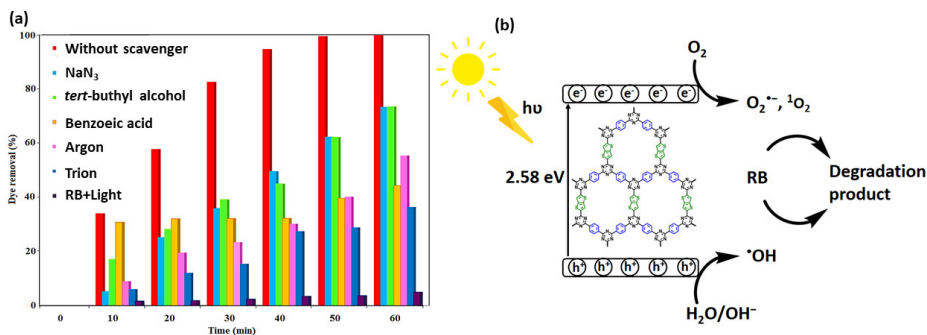


Figure 6.7. (a) Photodegradation of RB over TT-CTF with different scavengers. (b) Schematic illustration of RB photodegradation over TT-CTF under visible light irradiation and in the presence of air (reaction conditions: 5 mg of TT-CTF catalyst, 40 mL of RB solution (50 mg/L), the desired scavenger (0.1 mmol), air, xenon lamp (300 W), 60 minutes).

The recycling tests were carried out to investigate the stability and reusability of the TT-CTF for the degradation of RB. A high photocatalytic performance of the catalyst was obtained (98% removal) after four cycles (Figure 6.8). The TT-CTF catalyst can be effectively reutilized without any major loss of its activity.

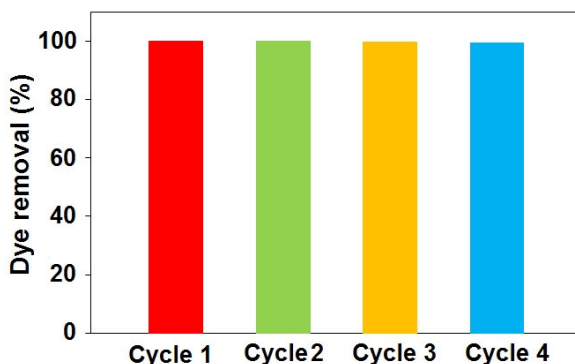


Figure 6.8. Regeneration of the TT-CTF photocatalyst (reaction conditions: 5 mg of TT-CTF catalyst, 40 mL of RB solution (50 mg/L), air, xenon lamp (300 W), 60 minutes).

The photocatalytic activity of the TT-CTF is compared to the commercial TiO₂ nanoparticles (P25) under the same reaction conditions, including the use of visible light only (Figure S6.6). As illustrated, the degradation of RB was only 10 % using the commercial TiO₂ nanoparticles, while 99% of the RB was decomposed using the TT-CTF. These results represent the great photocatalytic performance of the TT-CTF material for the decomposition of organic pollutants and possess great promise for practical applications.

6.3. Conclusions

In summary, three CTFs with photoactive centres were designed and synthesized. The intrinsic advantages of CTFs, particularly high porosity, structural diversity and great stability, were successfully merged with the heteroatom doping strategy to boost the

photocatalytic activity. The photocatalytic degradation of Rhodamine B was studied applying the prepared CTFs. The photocatalytic dye decomposition dramatically increased by introducing the heteroatoms containing linkers within the frameworks. Through rational structural design by tailoring the precursors, TT-CTF showed a superior visible light-harvesting for the photocatalytic dye removal. The TT-CTF catalyst could be recycled for four cycles with no loss of activity and stability. The high photocatalytic performance is assigned to the highly π -conjugated rigid framework in the donor-acceptor CTFs which further reduces the rate of electrons and holes recombination. Furthermore, the photocatalytic activity of our system was compared to the TiO₂ nanoparticles as the typical photocatalyst. The data proved the great activity of TT-CTF since RB was degraded at a significantly higher rate compared to the TiO₂ nanoparticles. This study indicates that CTFs are efficient photocatalysts for degrading organic pollutants from water under visible light as an available and unlimited energy source.

6.4. Experimental Section

6.4.1. Materials and instrumentation

For details please see Appendix.

6.4.2. Synthesis of heteroatom-embedded CTFs

Terephthalamidine dihydrochloride (235.2 mg, 1.0 mmol) and either thieno[3,2-*b*]thiophene-2,5-dicarboxaldehyde (98.1 mg, 0.5 mmol) (for TT-CTF), 2,2'-Bithiophene-5,5'-dicarboxaldehyde (111.1 mg, 0.5 mmol) (for BT-CTF) or 1,4-phthalaldehyde (67.2 mg, 0.5 mmol) for (CTF-1), and cesium carbonate (716.8 mg, 2.2 mmol) were added to a solution of DMSO (15.0 mL) in 25 mL round-bottom flask. The mixture was heated at 100 °C for 24 h, followed by heating at 150 °C for 36 h. After cooling down to room temperature, the resulting precipitate was washed with 1M HCl (3 × 20 mL), water (3 × 30 mL), acetone (3 × 10 mL) and THF (3 × 10 mL). The obtained materials were dried at 80 °C under vacuum for 12 h. Finally, TT-CTF, BT-CTF and CTF1 were obtained as red, orange and yellow powders, respectively.

6.4.3. Photocatalytic dye removal

The photocatalytic performance of the CTFs were examined by degradation of rhodamine B (RB) under visible light irradiation. The visible light source was a 300 W xenon lamp equipped with an optical cutoff filter ($\lambda \geq 420$ nm). Typically, 2, 3, 4 and 5 mg of the synthesized materials were added into 40 mL of RB solution (50 mg/L). Then, the mixture was stirred magnetically for 60 minutes in dark to reach an adsorption–desorption equilibrium before irradiation under Xenon lamp. The samples were collected after a certain time interval and centrifuged to separate the photocatalyst. The resulting mixtures were used for measuring the concentration of contaminant by UV–Vis spectrophotometer at 554 nm. The dye removal percentage of RB was calculated by Equation 1.

$$\% \text{ Dye removal} = \frac{C_0 - C_t}{C_0} \cdot 100$$

Where C_0 = initial dye concentration and C_t (mg/L) = the concentration of dye at time t .

For control tests using scavengers, to a mixture of TT-CTF catalyst (5 mg) and 40 mL of RB solution (50 mg/L), the desired scavenger (0.1 mmol) was added. Then, the mixture was stirred magnetically for 1h in dark to reach an adsorption–desorption equilibrium before irradiation under Xenon lamp for 60 minutes.

6.5. References

1. Diaz, U.; Corma, A., Ordered covalent organic frameworks, COFs and PAFs. From preparation to application. *Coordin Chem Rev* **2016**, *311*, 85-124.
2. Diercks, C. S.; Yaghi, O. M., The atom, the molecule, and the covalent organic framework. *Science* **2017**, *355* (6328).
3. Geng, K. Y.; He, T.; Liu, R. Y.; Dalapati, S.; Tan, K. T.; Li, Z. P.; Tao, S. S.; Gong, Y. F.; Jiang, Q. H.; Jiang, D. L., Covalent Organic Frameworks: Design, Synthesis, and Functions. *Chem Rev* **2020**, *120* (16), 8814-8933.
4. Kuhn, P.; Antonietti, M.; Thomas, A., Porous, covalent triazine-based frameworks prepared by ionothermal synthesis. *Angew Chem Int Edit* **2008**, *47* (18), 3450-3453.
5. Liu, M. Y.; Guo, L. P.; Jin, S. B.; Tan, B. E., Covalent triazine frameworks: synthesis and applications. *J Mater Chem A* **2019**, *7* (10), 5153-5172.
6. Artz, J., Covalent Triazine-based Frameworks Tailor-made Catalysts and Catalyst Supports for Molecular and Nanoparticulate Species. *Chemcatchem* **2018**, *10* (8), 1753-1771.

7. Mukherjee, S.; Das, M.; Manna, A.; Krishna, R.; Das, S., Dual Strategic Approach to Prepare Defluorinated Triazole-Embedded Covalent Triazine Frameworks with High Gas Uptake Performance. *Chem Mater* **2019**, *31* (11), 3929-3940.
8. Abednatanzi, S.; Derakhshandeh, P. G.; Leus, K.; Vrielinck, H.; Callens, F.; Schmidt, J.; Savateev, A.; Van der Voort, P., Metal-free activation of molecular oxygen by covalent triazine frameworks for selective aerobic oxidation. *Sci Adv* **2020**, *6* (14).
9. Abednatanzi, S.; Derakhshandeh, P. G.; Tack, P.; Muniz-Miranda, F.; Liu, Y. Y.; Everaert, J.; Meledina, M.; Vanden Bussche, F.; Vincze, L.; Stevens, C. V.; Van Speybroeck, V.; Vrielinck, H.; Callens, F.; Leus, K.; Van Der Voort, P., Elucidating the promotional effect of a covalent triazine framework in aerobic oxidation. *Appl Catal B-Environ* **2020**, *269*.
10. Laemont, A.; Abednatanzi, S.; Derakhshandeh, P. G.; Verbruggen, F.; Fiset, E.; Qin, Q.; Van Daele, K.; Meledina, M.; Schmidt, J.; Oschatz, M.; Van Der Voort, P.; Rabaey, K.; Antonietti, M.; Breugetmans, T.; Deus, K., Covalent triazine framework/carbon nanotube hybrids enabling selective reduction of CO₂ to CO at low overpotential. *Green Chem* **2020**, *22* (10), 3095-3103.
11. Bhunia, A.; Esquivel, D.; Dey, S.; Fernandez-Teran, R.; Goto, Y.; Inagaki, S.; Van der Voort, P.; Janiak, C., A photoluminescent covalent triazine framework: CO₂ adsorption, light-driven hydrogen evolution and sensing of nitroaromatics. *J Mater Chem A* **2016**, *4* (35), 13450-13457.
12. Tang, Y. Z.; Huang, H. L.; Peng, B.; Chang, Y. J.; Li, Y.; Zhong, C. L., A thiadiazole-based covalent triazine framework nanosheet for highly selective and sensitive primary aromatic amine detection among various amines. *J Mater Chem A* **2020**, *8* (32), 16542-16550.
13. Buyukcakir, O.; Ryu, J.; Joo, S. H.; Kang, J.; Yuksel, R.; Lee, J.; Jiang, Y.; Choi, S.; Lee, S. H.; Kwak, S. K.; Park, S.; Ruoff, R. S., Lithium Accommodation in a Redox-Active Covalent Triazine Framework for High Areal Capacity and Fast-Charging Lithium-Ion Batteries. *Adv Funct Mater* **2020**, *30* (36).
14. Sun, J. K.; Antonietti, M.; Yuan, J. Y., Nanoporous ionic organic networks: from synthesis to materials applications. *Chem Soc Rev* **2016**, *45* (23), 6627-6656.
15. Kosek, K.; Luczkiewicz, A.; Fudala-Ksiazek, S.; Jankowska, K.; Szopinska, M.; Svahn, O.; Tranckner, J.; Kaiser, A.; Langas, V.; Bjorklund, E., Implementation of advanced micropollutants removal technologies in wastewater treatment plants (WWTPs) - Examples and challenges based on selected EU countries. *Environ Sci Policy* **2020**, *112*, 213-226.
16. He, S. J.; Yin, B.; Niu, H. Y.; Cai, Y. Q., Targeted synthesis of visible-light-driven covalent organic framework photocatalyst via molecular design and precise construction. *Appl Catal B-Environ* **2018**, *239*, 147-153.
17. Lv, S. W.; Liu, J. M.; Li, C. Y.; Zhao, N.; Wang, Z. H.; Wang, S., Two novel MOFs@COFs hybrid-based photocatalytic platforms coupling with sulfate radical-involved advanced oxidation processes for enhanced degradation of bisphenol A. *Chemosphere* **2020**, *243*.
18. Liu, F. Y.; Nie, C. Y.; Dong, Q. Q.; Ma, Z. Y.; Liu, W.; Tong, M. P., AgI modified covalent organic frameworks for effective bacterial disinfection and organic pollutant degradation under visible light irradiation. *J Hazard Mater* **2020**, *398*.
19. Zhou, C. Y.; Lai, C.; Zhang, C.; Zeng, G. M.; Huang, D. L.; Cheng, M.; Hu, L.; Xiong, W. P.; Chen, M.; Wang, J. J.; Yang, Y.; Jiang, L. B., Semiconductor/boron nitride composites: Synthesis, properties, and photocatalysis applications. *Appl Catal B-Environ* **2018**, *238*, 6-18.
20. Yi, H.; Yan, M.; Huang, D. L.; Zeng, G. M.; Lai, C.; Li, M. F.; Huo, X. Q.; Qin, L.; Liu, S. Y.; Liu, X. G.; Li, B. S.; Wang, H.; Shen, M. C.; Fu, Y. K.; Guo, X. Y., Synergistic effect of artificial enzyme and 2D nano-structured Bi₂WO₆ for eco-friendly and efficient biomimetic photocatalysis. *Appl Catal B-Environ* **2019**, *250*, 52-62.
21. Jaiswal, R.; Patel, N.; Dashora, A.; Fernandes, R.; Yadav, M.; Edla, R.; Varma, R. S.; Kothari, D. C.; Ahuja, B. L.; Miotello, A., Efficient Co-B-codoped TiO₂ photocatalyst for degradation of organic water pollutant under visible light. *Appl Catal B-Environ* **2016**, *183*, 242-253.

22. Safajou, H.; Khojasteh, H.; Salavati-Niasari, M.; Mortazavi-Derazkola, S., Enhanced photocatalytic degradation of dyes over graphene/Pd/TiO₂ nanocomposites: TiO₂ nanowires versus TiO₂ nanoparticles. *J Colloid Interf Sci* **2017**, *498*, 423-432.
23. Wang, F. L.; Chen, P.; Feng, Y. P.; Xie, Z. J.; Liu, Y.; Su, Y. H.; Zhang, Q. X.; Wang, Y. F.; Yao, K.; Lv, W. Y.; Liu, G. G., Facile synthesis of N-doped carbon dots/g-C₃N₄ photocatalyst with enhanced visible-light photocatalytic activity for the degradation of indomethacin. *Appl Catal B-Environ* **2017**, *207*, 103-113.
24. Fu, J. W.; Yu, J. G.; Jiang, C. J.; Cheng, B., g-C₃N₄-Based Heterostructured Photocatalysts. *Adv Energy Mater* **2018**, *8* (3).
25. Nakata, K.; Fujishima, A., TiO₂ photocatalysis: Design and applications. *J Photoch Photobio C* **2012**, *13* (3), 169-189.
26. Markushyna, Y.; Smith, C. A.; Savateev, A., Organic Photocatalysis: Carbon Nitride Semiconductors vs. Molecular Catalysts. *Eur J Org Chem* **2020**, *2020* (10), 1294-1309.
27. Zhang, L. H.; Jin, Z. Y.; Lu, H.; Lin, T. Q.; Ruan, S. C.; Zhao, X. S.; Zeng, Y. J., Improving the Visible-Light Photocatalytic Activity of Graphitic Carbon Nitride by Carbon Black Doping. *ACS Omega* **2018**, *3* (11), 15009-15017.
28. Wang, X. N.; Zhang, X. C.; Zhang, Y.; Wang, Y.; Sun, S. P.; Wu, W. D.; Wu, Z. X., Nanostructured semiconductor supported iron catalysts for heterogeneous photo-Fenton oxidation: a review. *J Mater Chem A* **2020**, *8* (31), 15513-15546.
29. Liu, M. Y.; Jiang, K.; Ding, X.; Wang, S. L.; Zhang, C. X.; Liu, J.; Zhan, Z.; Cheng, G.; Li, B. Y.; Chen, H.; Jin, S. B.; Tan, B., Controlling Monomer Feeding Rate to Achieve Highly Crystalline Covalent Triazine Frameworks. *Adv Mater* **2019**, *31* (19).
30. Wang, K. W.; Yang, L. M.; Wang, X.; Guo, L. P.; Cheng, G.; Zhang, C.; Jin, S. B.; Tan, B.; Cooper, A., Covalent Triazine Frameworks via a Low-Temperature Polycondensation Approach. *Angew Chem Int Edit* **2017**, *56* (45), 14149-14153.
31. Wang, H.; Wang, H.; Wang, Z. W.; Tang, L.; Zeng, G. M.; Xu, P.; Chen, M.; Xiong, T.; Zhou, C. Y.; Li, X. Y.; Huang, D. N.; Zhu, Y.; Wang, Z. X.; Tang, J. W., Covalent organic framework photocatalysts: structures and applications. *Chem Soc Rev* **2020**, *49* (12), 4135-4165.
32. Guo, L. P.; Niu, Y. L.; Xu, H. T.; Li, Q. W.; Razaque, S.; Huang, Q.; Jin, S. B.; Tan, B., Engineering heteroatoms with atomic precision in donor-acceptor covalent triazine frameworks to boost photocatalytic hydrogen production. *J Mater Chem A* **2018**, *6* (40), 19775-19781.
33. Paraknowitsch, J. P.; Thomas, A.; Schmidt, J., Microporous sulfur-doped carbon from thienyl-based polymer network precursors. *Chem Commun* **2011**, *47* (29), 8283-8285.
34. Huang, W.; Byun, J.; Rorich, I.; Ramanan, C.; Blom, P. W. M.; Lu, H.; Wang, D.; da Silva, L. C.; Li, R.; Wang, L.; Landfester, K.; Zhang, K. A. I., Asymmetric Covalent Triazine Framework for Enhanced Visible-Light Photoredox Catalysis via Energy Transfer Cascade. *Angew Chem Int Edit* **2018**, *57* (27), 8316-8320.
35. Wang, X. Y.; Chen, L. J.; Chong, S. Y.; Little, M. A.; Wu, Y. Z.; Zhu, W. H.; Clowes, R.; Yan, Y.; Zwijnenburg, M. A.; Sprick, R. S.; Cooper, A. I., Sulfone-containing covalent organic frameworks for photocatalytic hydrogen evolution from water. *Nat Chem* **2018**, *10* (12), 1180-1189.
36. Wu, W. T.; Zhang, Q. G.; Wang, X. K.; Han, C. C.; Shao, X. D.; Wang, Y. X.; Liu, J. L.; Li, Z. T.; Lu, X. Q.; Wu, M. B., Enhancing Selective Photooxidation through Co-Nx-doped Carbon Materials as Singlet Oxygen Photosensitizers. *ACS Catal* **2017**, *7* (10), 7267-7273.
37. Nguyen, B. S.; Xiao, Y. K.; Shih, C. Y.; Nguyen, V. C.; Chou, W. Y.; Teng, H. S., Electronic structure manipulation of graphene dots for effective hydrogen evolution from photocatalytic water decomposition. *Nanoscale* **2018**, *10* (22), 10721-10730.
38. Crini, G.; Badot, P. M., Application of chitosan, a natural aminopolysaccharide, for dye removal from aqueous solutions by adsorption processes using batch studies: A review of recent literature. *Prog Polym Sci* **2008**, *33* (4), 399-447.

Metal- and Covalent Organic Frameworks for Advanced Applications: Heterogeneous Catalysis and Sensing

39. Alatalo, S. M.; Makila, E.; Repo, E.; Heinonen, M.; Salonen, J.; Kukk, E.; Sillanpaa, M.; Titirici, M. M., Meso- and microporous soft templated hydrothermal carbons for dye removal from water. *Green Chem* **2016**, *18* (4), 1137-1146.

6.6. Supporting Information

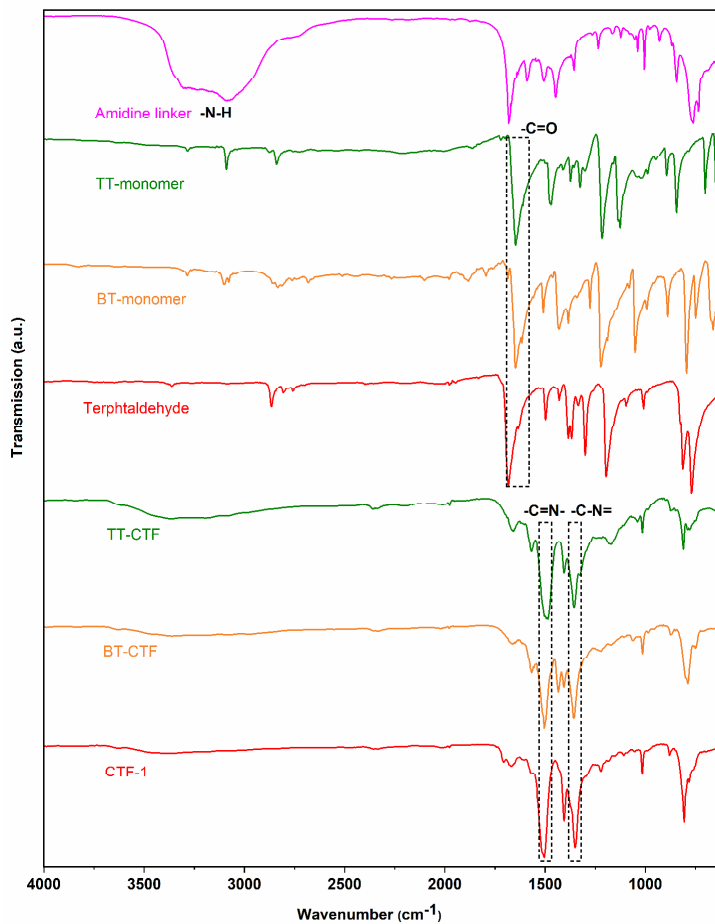


Figure S6.1. FT-IR spectra of the precursors and the obtained CTFs.

Table S6.1. Elemental analysis results of CTFs.

CTFs		C%	H%	N%	S%
TT-CTF	Cal.				
	Exp.	58.3	2.9	14.6	14.5
BT-CTF	Cal.				
	Exp.	62.0	3.0	13.6	14.4
CTF-1	Cal.				-
	Exp.	68.9	3.7	17.7	-

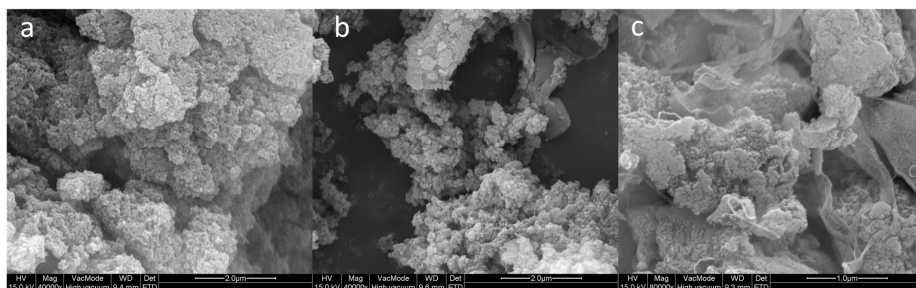


Figure S6.2. SEM images of (a) TT-CTF, (b) BT-CTF and (c) CTF-1.

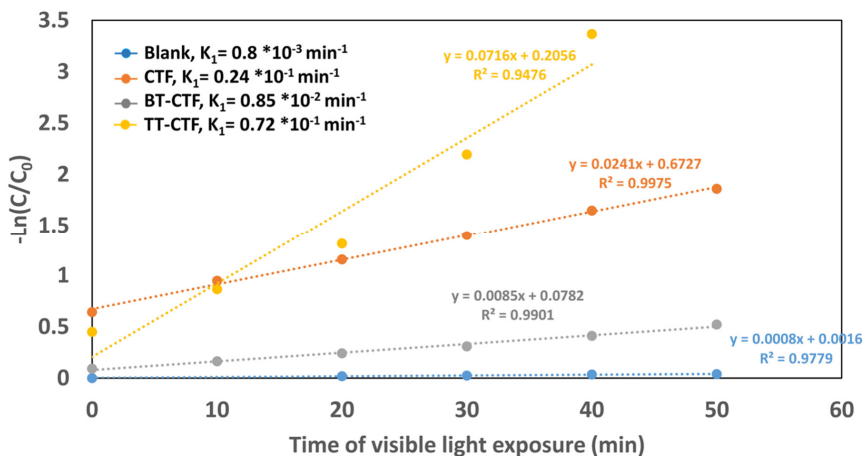


Figure S6.3. First-order visible light dye degradation of (a) TT-CTF, (b) BT-CTF and (c) CTF-1.

In the figure S6.3, it is clear that all catalysts show a nice linear pattern for the first order rate kinetics. The TT-CTF shows slightly more noisy data, but all other catalysts and the blank show excellent linearity. The rate constants have been recalculated in the thesis.

Table S6.2. The dye degradation kinetics constants of the synthesized CTFs.

Catalyst	First-order	
	$\ln(C/C_0) = -k_1t$	
	k_1	R^2
TT-CTF	0.071	0.95
BT-CTF	0.0085	0.99
CTF-1	0.024	0.99
RB-visible light	0.0008	0.98

C_0 =initial dye concentration; C = dye concentration at any time;; k_1 = first-order kinetic constant;
 R^2 = correlation coefficient

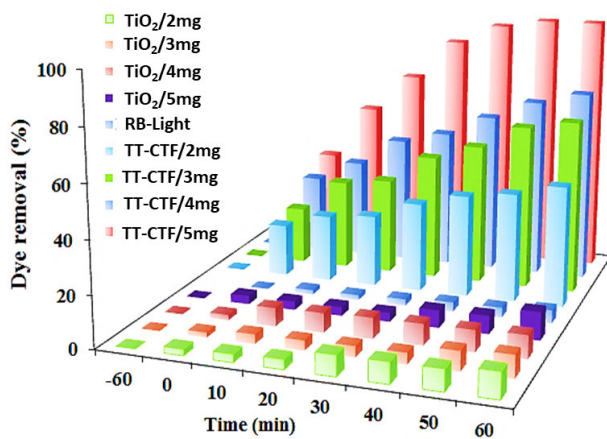
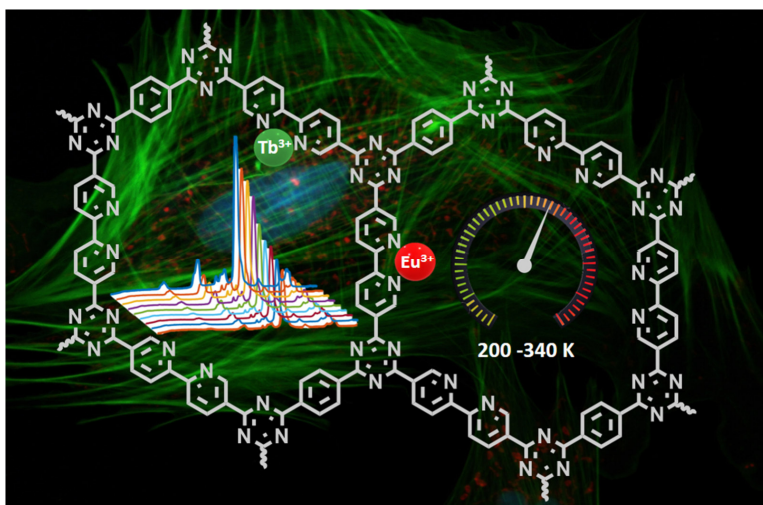


Figure S6.6. Comparison of the degradation percentage of RB as organic pollutant with commercial TiO₂ nanoparticles and TT-CTF.

CHAPTER 7

A LANTHANIDE-FUNCTIONALIZED COVALENT TRIAZINE FRAMEWORK AS PHYSIOLOGICAL MOLECULAR THERMOMETER



The results of this chapter were published in:

P. Gohari Derakhshandeh, S. Abednatanzi, L. Bourda, S. Dalapati, A. Abalymov, M. Meledina, Y.-Y. Liu, A. G. Skirtach, K. Van Hecke, A. M. Kaczmarek, P. Van Der Voort. Lanthanide Functionalized Covalent Triazine Framework as Physiological Molecular Thermometer, **J. Mater. Chem. C**, **2021**, DOI: 10.1039/d1tc00999k.

Abstract

Crystalline covalent triazine frameworks (CTFs) with intrinsic porosity and high stability are excellent platforms for engineering luminescence properties, as their building blocks and guest ions are all potential actors in light emission. Herein, a highly crystalline bipyridine-based CTF (Bipy-CTF) is synthesized in mild conditions. The controlled tethering of lanthanide ions ($\text{Ln} = \text{Eu}^{3+}$ and Tb^{3+}) onto Bipy-CTF combined with a selective photoexcitation results in a ratiometric luminescent thermometer (LnCTF). This LnCTF thermometer exhibits an excellent linear response in the solid state over a wide range of temperatures (200 to 340 K), with a temperature uncertainty below 0.2% and a very good reusability (up to 98.5% repeatability). Moreover, the suspended material in water shows a temperature sensitivity down to 253 K ($-20\text{ }^{\circ}\text{C}$), which is a very important finding for monitoring the physiological processes within biological and biochemical systems during freezing/thawing treatment with precise temperature measurements. We also studied and confirmed the low cytotoxicity of the LnCTF towards cells opening prospects for future *in vivo* applications. This work thus highlights a new application of LnCTF materials as ratiometric luminescent molecular thermometers with excellent sensitivity in the physiological temperature range.

7.1. Introduction

COFs have been designed for diverse applications including gas adsorption and separation, luminescence and sensing, catalysis, optoelectronics, drug delivery, water purification, CO₂ capture, energy storage and energy conversion.¹⁻¹¹ Current strategies to design crystalline COFs involve reversible covalent bond formation, referred to as the “error-correcting” reversible bond formation approach. On the downside, COFs synthesized by highly reversible bond formations often show a poor stability. While COFs based on an imine linkage (C=N) are more robust than those with B-O bonds, they still suffer hydrolysis under acidic conditions.¹²⁻¹³ CTFs, on the other hand, form highly conjugated and stable materials, but often show moderate to poor crystallinity.

Up to date, a variety of approaches has been reported for the preparation of CTFs, such as the cyclization of nitrile or amide aromatic building blocks, using ZnCl₂ (ionothermal), P₂O₅ (ionothermal), CF₃SO₃H and AlCl₃ as catalysts.¹⁴⁻¹⁸ However, the high temperature (400-500 °C) of the ionothermal synthetic pathways leads to non-photoactive materials due to a partial carbonization. On the other hand, the other two catalytic pathways using triflic acid or AlCl₃ only show good results for a limited number of building blocks and amorphous materials are typically obtained. Recently, Cooper *et al.* developed a novel synthesis strategy involving the condensation reaction of aldehydes and amidines to make CTFs under relatively mild conditions.¹⁹ This method provides a great opportunity to design novel porous structures using a variety of building blocks.²⁰⁻²⁴ The resulting materials are typically obtained as yellow or orange powders, retaining most of their photophysical properties, while still not being crystalline. Tan *et al.* found that slowing down the nucleation process through in situ oxidation of alcohol monomers into aldehydes during the polycondensation reaction results in highly crystalline CTFs.²⁵ By introducing metal coordination sites, such as in the case of 2,2'-bipyridine-based CTF (Bipy-CTF), metal complexes can be tethered onto the CTFs. Such materials have already shown great results in heterogeneous catalysis.²⁶ Clearly, also photoactive CTFs can be synthesized in this way.

Temperature is a fundamental thermodynamic parameter, the measurement of which is crucial in both science and industrial applications. Generally, traditional thermometers such as thermistors, thermocouples and liquid-filled thermometers are not applicable at the submicrometer scale. Therefore, precise temperature measurement is still challenging in the fields of nanotechnology and nanomedicine, but it is essential for biomedical applications, for example intracellular release.²⁷ This has encouraged scientists to develop new temperature sensors to measure temperature with micrometric and nanometric precision. Luminescent luminometers are of great interest due to their brilliant color visibility and temperature-dependent luminescence features. High sensitivity, instant response, noninvasive functioning and applicability in strong magnetic or electric fields are some of the important benefits of luminescent thermometers compared to other molecular thermometers. The trivalent lanthanides (Ln^{3+}) have attracted comprehensive attention and are often used in luminescence due to their unique spectroscopic characteristics, particularly, narrow band emission, long lifetime, and high quantum yield values.

The integration of lanthanide ions or complexes with organic bridging linkers is a well-studied methodology to overcome the low absorption coefficients of lanthanides. We and others have prepared lanthanide tethered metal-organic frameworks (MOFs), coordination polymers (CPs) and periodic mesoporous organosilicas (PMOs).²⁸⁻³² Still, some of these materials such as LnMOFs and CPs suffer from low stability and low water dispersibility and are cytotoxic. As COFs have a very low biological toxicity,³³⁻³⁴ the immobilization of lanthanide (Ln) ions onto COFs can result in excellent temperature sensors arising from their multiple luminescence centers and highly tunable luminescence properties.³⁵⁻³⁸ However, most of the COFs are non-luminescent, because of non-radiative deactivation arising from intramolecular bond rotation and aggregation-caused quenching (ACQ) driven by the π - π stacking in the structure. In this regard, the confinement of intramolecular bond rotation and/or the construction of relatively rigid frameworks is one approach to enhance the photoluminescence activity by minimizing non-radiative deactivation. This is the main reason that we targeted CTFs, as they have a rigid framework built by triazine linkages and show minimal intramolecular rotation by 'exocyclic' covalent bonds. Besides, the organic donor-acceptor pairs and crystalline

structure of the Bipy-CTF greatly improve the delocalization of π electrons to overcome ACQ. These features make Bipy-CTF an excellent candidate for photoluminescent applications.¹²⁻¹³

In this work, we present a novel application of CTFs as photoluminescent materials. For this purpose, we designed a bipyridine-based CTF via the polycondensation reaction of Bipy containing monomers and 1,4-benzenedimethanol. The nitrogen-rich material provides excellent docking sites for immobilization of various guests, examined for two different lanthanide guests (Eu^{3+} and Tb^{3+}). The Bipy sites not only act as anchoring points for lanthanides but also enable the excitation of Ln^{3+} ions through intramolecular energy transfer known as the “antenna effect”. The obtained materials exhibit excellent temperature sensing properties in the physiological range. The Bipy-CTF before and after immobilization with lanthanides showed low cytotoxicity to human fibroblastic cells even at high concentration and showed excellent temperature sensing properties, also in water. To the best of our knowledge, this is the first report on the applicability of LnCTFs as photoluminescent materials for physiological molecular thermometers.

7.2. Results and Discussion

7.2.1. Synthesis and Characterization of Ln@Bipy-CTF

The Bipy-CTF material was synthesized by condensation of 2,2'-bipyridine-5,5'-diamidine dihydrochloride with 1,4-benzenedimethanol (Figure 7.1A and 7.1B). The successful formation of the triazine frameworks was confirmed by diffuse reflectance infrared Fourier transform spectroscopy (DRIFTS) analysis, revealing the characteristic stretching vibrations from the triazine units at ~ 1516 and 1351 cm^{-1} for Bipy-CTF (Figure 7.1 C). Also, the disappearance of the intense aldehyde band ($\sim 1716\text{ cm}^{-1}$) and broad O-H band ($\sim 3300\text{ cm}^{-1}$) is indicative of the complete consumption of the monomers to form triazine linkages. The carbon and nitrogen contents obtained from elemental analysis are in close agreement to the theoretical values (Table S7.1).

The experimental and simulated structural X-ray diffraction (XRD) patterns of Bipy-CTF are shown in Figure 7.1D and 7.1E. Powder XRD was used to characterize the crystalline

nature of the synthesized material. Bipy-CTF exhibits two major peaks, one is centered at 5.5° , which is assigned to the combination of the (110) and (200) reflection and a broad peak at 26.8° , indicative for the d-spacing between layers or (001) reflection. Some smaller peaks matching with predicted Bragg peaks could also be observed in the background corrected pattern, namely the combined (310) and (220) reflections centered at 9.9° and the (420) reflection at 14.6° . For the Bipy-CTF the eclipsed (AA) and staggered (AB) structures were compared (Figure 7.1D and S7.14). The eclipsed stacking structure matches best with the theoretical XRD pattern and with the experimental pattern. Subsequently, Pawley refinements were carried out for the eclipsed structure of Bipy-CTF and an optimized structure assigned to the *Cmmm* space group with unit cell parameters of $a = 30.95 \text{ \AA}$, $b = 20.79 \text{ \AA}$ and $c = 3.50 \text{ \AA}$ with a refined parameter of $R_p = 1.51\%$ and $wR_p = 2.22\%$. The diffractograms point at a good crystallinity for the Bipy-CTF material, rarely observed for the previously reported CTFs.

The porosity of the Bipy-CTF was determined by N_2 sorption measurements at 77 K. As shown in Figure 7.1F, the Bipy-CTF displayed typical type I isotherm, indicative for a microporous material. The Bipy-CTF exhibited Brunauer–Emmett–Teller (BET) and Langmuir surface area of 439 and $635 \text{ m}^2\text{g}^{-1}$, respectively. The total pore volume is $0.23 \text{ cm}^3\text{g}^{-1}$ at $P/P_0 = 0.98$. As shown in Figure 7.1G, the ^{13}C CP/MAS solid-state NMR spectrum of Bipy-CTF exhibits five well-resolved signals at 121, 130, 137.5, 149.9, and 157.5 ppm, which can be assigned to the Bipy carbons. Furthermore, the appearance of a peak at 169.8 ppm is characteristic of the carbon signal from triazine rings which clearly confirms the formation of triazine units in the Bipy-CTF.^{19, 25} The thermogravimetric analysis (TGA) reveals excellent thermal stability of the Bipy-CTF material with no weight loss up to $\sim 600^\circ\text{C}$ (Figure 7.1H). Furthermore, scanning electron microscopy (SEM) shows micrometer-sized particles with no particular shape (Figure S7.1).

Metal- and Covalent Organic Frameworks for Advanced Applications: Heterogeneous Catalysis and Sensing

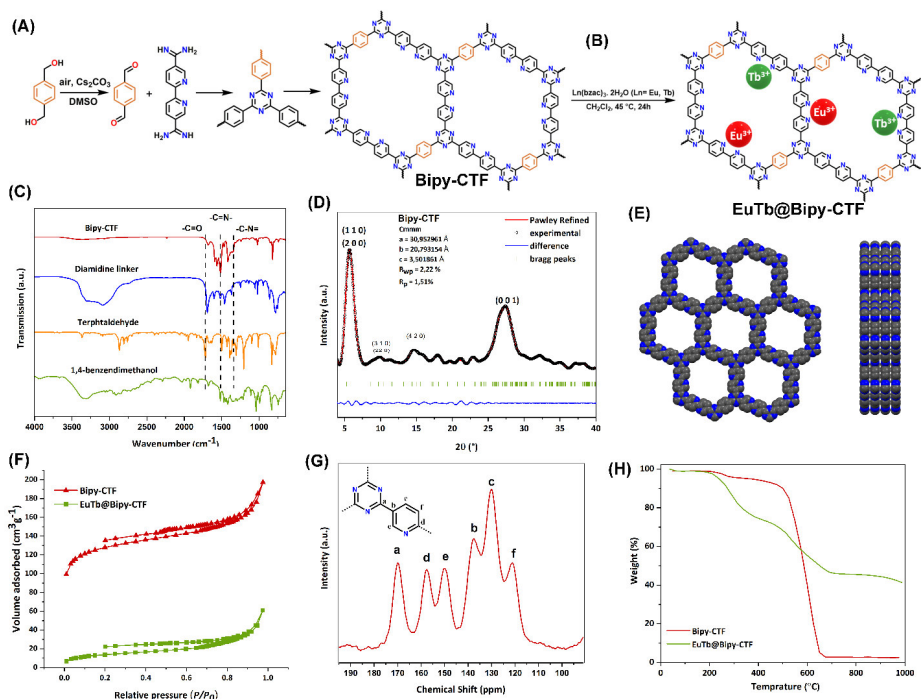


Figure 7.1. A) Scheme showing the triazine framework synthesis through in situ formation of aldehyde monomers by controlled oxidation of alcohol monomers and condensation with amidine, and B) LnCTF ($\text{Ln} = \text{Eu}, \text{Tb}$) synthesis. C) DRIFTS of Bipy-CTF, diamidine linker, terephthalaldehyde and 1,4-benzendimethanol. D) Background corrected experimental (black) and Pawley refined (red) XRD patterns of Bipy-CTF AA stacking, accompanied with the difference plot (blue) and Bragg peak positions (green) of the model. E) Top and side views of the Bipy-CTF structure, carbon is shown in grey, nitrogen in blue, hydrogens were omitted for clarity. F) Nitrogen (N_2) adsorption/desorption isotherms of Bipy-CTF (black) and EuTb@Bipy-CTF (red). G) Solid-state ^{13}C CP/MAS NMR spectra of Bipy-CTF. H) TGA data of Bipy-CTF (black) and EuTb@Bipy-CTF (red) measured under air atmosphere.

Transmission electron microscopic (TEM) and high resolution (HR)-TEM images were taken to further investigate the microscopic structures of the Bipy-CTF. The layered and

crystalline structure of Bipy-CTF with ordered lattice structure is visible in ADF-STEM and HR-TEM images (Figure 7.2A and S7.2).

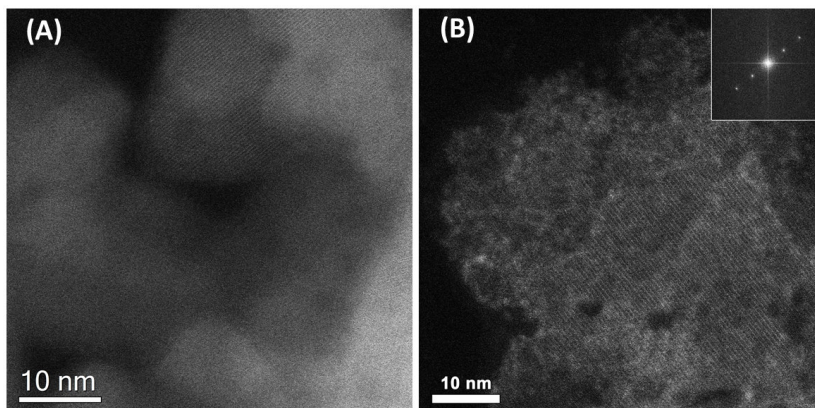


Figure 7.2. ADF-STEM image of A) pristine Bipy-CTF B) Bipy-CTF after loading together with corresponding FFT in the inset revealing the crystallinity of the materials.

As mentioned above, the key to resolve the limitations of photoluminescent materials lies in the development of crystalline porous material with limited intramolecular rotation and delocalized π electrons system while the stability is still preserved. Accordingly, the crystalline, stable, porous Bipy-CTF material was applied to examine its potential application as luminescent molecular thermometer in the physiological temperature range. The Bipy-CTF material comprises numerous N functionalities, including triazine and bipyridine edges that form ideal docking sites for grafting of Eu^{3+} and Tb^{3+} complexes simultaneously *via* a post-modification procedure (Figure 7.1B). The immobilization of Eu^{3+} and Tb^{3+} complexes on the Bipy-CTF was confirmed by DRIFTS analysis (Figure S7.3). In the DRIFTS spectra of the Eu,Tb@Bipy-CTF samples, the intense bands at 1599 cm^{-1} (C=O) and 1569 cm^{-1} (C=C) are observed, which are attributed to the vibrations of C=O and C=C of the lanthanide complexes in the framework. Moreover, the bands around $2850\text{-}3060\text{ cm}^{-1}$ are related to $\nu(\text{C-H})$ and also present in the EuTb@Bipy-CTF sample. Additionally, because of its coordination to the lanthanides, the C=N peak of the

bipyridine linker shifts from 1685 to 1675 cm^{-1} in the EuTb@Bipy-CTF . In addition, the overall N_2 uptake of EuTb@Bipy-CTF decreased upon grafting, indicating the successful immobilization of lanthanides within the porous channel of CTF framework (Figure 7.1F). The BET and Langmuir surface area of Eu,Tb@Bipy-CTF decreased notably to 50 and 89 m^2g^{-1} , respectively, and the total pore volume reduced to 0.06 cm^3g^{-1} . The crystallinity of the hosting network is also clearly visualized by means of ADF-STEM (Figure 7.2b). TEM-EDX analysis of LnCTF was carried out to check the presence of the Eu and Tb elements in the Bipy-CTF after post-modification (Figures S7.4). The observed results revealed that both Eu and Tb ions are well distributed within the EuTb@Bipy-CTF skeletons.

7.2.2. Luminescence Thermometry of Ln@Bipy-CTF

The optical absorption property of the yellowish pristine Bipy-CTF sample was measured by Diffuse Reflectance (DR)-UV-visible spectrophotometry. It was observed that the material could absorb a wide range of visible light (Figure S7.5). The luminescence properties of the pristine Bipy-CTF were first investigated at room temperature (Figure S7.6). Upon excitation with UV light, the Bipy-CTF shows broad emission in the range of 450 - 750 nm, with a peak maximum centered at 575 nm. The luminescence properties of the materials were also studied after grafting with lanthanide complexes. Figure 7.3A demonstrates a picture of the four samples, Tb@Bipy-CTF (1), Eu@Bipy-CTF (2), 3% Eu ,97% Tb@Bipy-CTF (3) and 5% Eu ,95% Tb@Bipy-CTF (4) upon exposing to a UV lamp at 302 nm excitation wavelength. It can be observed that the emitted colors are green, red and yellow respectively (with different yellow undertones).

All four compounds show strong visible emission with the characteristic f-f transitions of the lanthanides upon exciting into the maximum of the broad linker band originating from the pristine CTF (250 - 400 nm) (Figure 7.3). The labelled peaks in the spectra are assigned in the SI (Table S7.2-S7.5). The decay times of the compounds are also presented in the SI (Figures S7.7-S7.9). In addition, we studied the temperature dependence luminescence characteristics of two Eu-Tb co-doped compounds, as it is known that this lanthanide pair can be used for developing optical thermometers.

Ratiometric thermometers are thermometers based on the intensity (wavelength) ratio of two transitions (Eu^{3+} and Tb^{3+} in this case) that suffer from certain limitations such as fluctuations of the excitation source. Here, the emission spectra of the samples were measured at various temperatures, from 200 – 340 K (Figure 7.4).

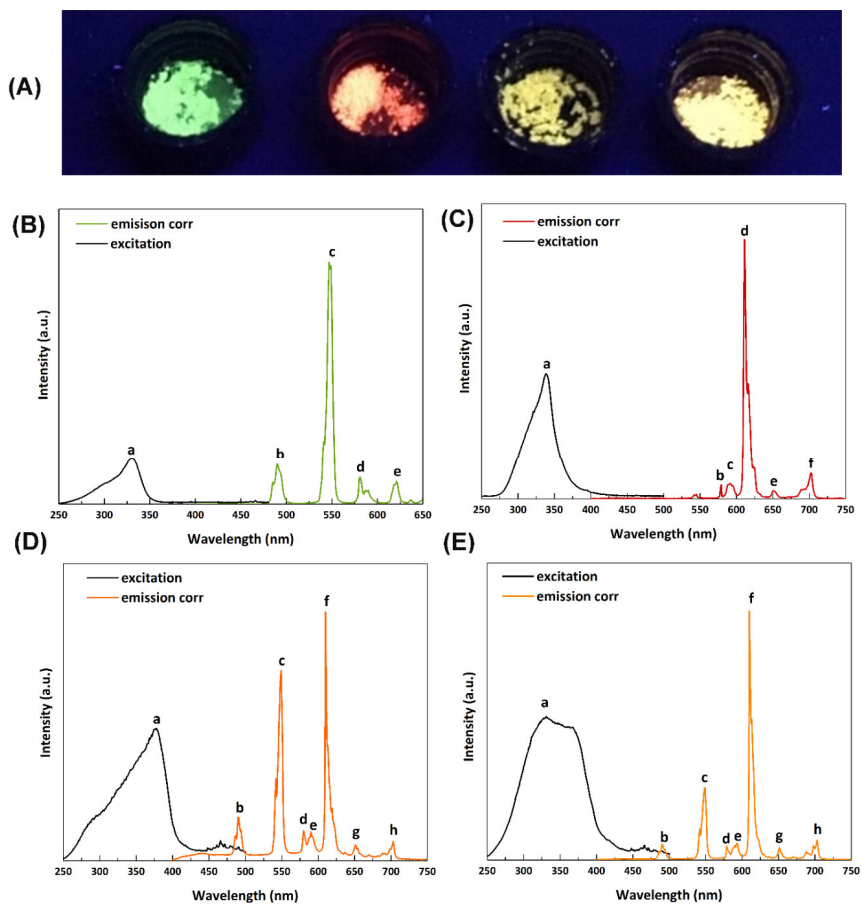


Figure 7.3. A) Photo taken when placing **1**, **2**, **3** and **4** (from left to right) samples under a UV lamp (302 nm excitation). Combined excitation-emission spectra of B) **1**, C) **2**, D) **3** and E) **4** compounds. The labeled peaks have been assigned in the SI (Table S7.2-S7.5).

For compound **3** the I_{549}/I_{610} ratio of the integrated areas was calculated (Tb³⁺: 530 – 565; Eu³⁺: 605-630) for the 200 - 340 K temperature range (Figure 7.4A). The obtained data points could be fitted excellently using the equation for Δ ($R^2 = 0.996$) yielding $\Delta E = 1203 \text{ cm}^{-1}$ (Figure 7.4B). The nonradiative deactivation energies might be involved the ligand triplet level and the ⁵D₄ level of Tb³⁺ (the triplet level of the Bipy-CTF has been determined and is presented in the Figures S7.10-S7.11). Figure 7.4B represents the plot that shows the calibration curve. The maximum number of the relative temperature sensitivity (Sr) was determined to be 2.30% K⁻¹ (240 K) (Figure 7.4C). For compound **4** also, the I_{549}/I_{610} ratio of the integrated areas was calculated (Tb³⁺: 530 – 565; Eu³⁺: 605-630). The emission map recorded at different temperatures (253 – 333 K) is presented in Figure 7.4D. These data points could be well fitted employing the equation for Δ ($R^2 = 0.985$) yielding $\Delta E = 948 \text{ cm}^{-1}$ (Figure 7.4E). Also, in the case of this material the nonradiative deactivation energies probably involve the ligand triplet level and the ⁵D₄ level of Tb³⁺. The plot, showing the calibration curve, is presented in Figure 7.4E. The maximum value of Sr was determined to be 2.12% K⁻¹ (253 K) (Figure 7.4F). Both materials show quite good thermometric performance in the extended physiological range. For both compounds additionally the uncertainty was calculated and was determined to be very low, below 0.2%, which means these thermometers show very good performance in the solid state (Figure 7.4G, H). To additionally prove that they can be reused for several measurement runs the compound **3** was tested for its recyclability. It showed up to 98.5% repeatability (Figure 7.4I).

Inspired by the good performance of the LnCTF thermometers in the physiological temperature range, we further investigated their performance in water. Moreover, we performed cytotoxicity tests on human cells. The sample **3** was also selected for studying the thermometric properties in water. For the temperature-dependent luminescence measurements, a suspension was prepared by adding 1 mg of the sample in 1 mL of distilled water. The suspension demonstrated a light red emission color when illuminated by a UV lamp (302 nm). The thermometric properties of the Eu,Tb@Bipy-CTF compound were measured over 283.15 - 323.15 K, with a step size of 5 K. The emission map of the material is presented in Figure 7.5A. The data points are well fitted by using the equation for Δ ($R^2 = 0.992$) giving $\Delta E = 1506 \text{ cm}^{-1}$ (Figure 7.5B). The maximum relative sensitivity

Sr was calculated to be 2.70 % K⁻¹ (283.15 K) (Figure 7.5C). Due to the stronger influence of signal-to-noise ratio in the measurements performed in water, we have included error bars on the plots of Delta and Sr. This result is somewhat higher than that reported for powder samples. This can be explained by the fact that the sample is solvatochromic and in water the ratio of Tb-to-Eu may change compared to the powder, which influences the final thermometric performance of the material. The temperature uncertainty δT has been plotted in Figure 7.5D. The increase in δT is due to a weaker signal of the material when measured in water compared to solid state. However, at maximum, it only reaches up to 0.3 K, which is a very good value. This additional dataset indicates that the lanthanide grafted CTF materials show good performance in colloidal water suspension, confirming its potential application as biological thermometers.

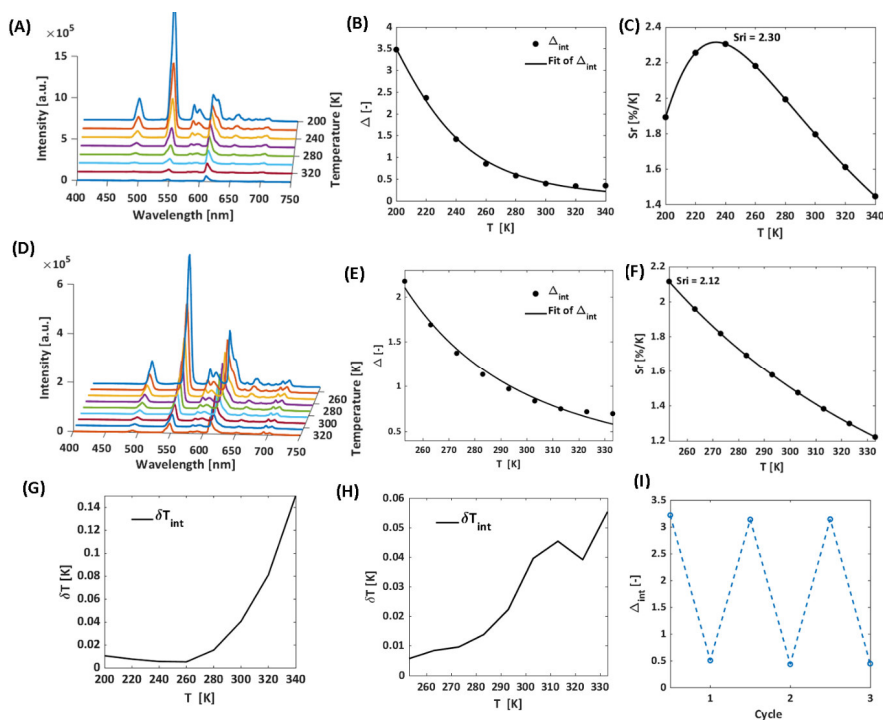


Figure 7.4. A) Emission map of **3** recorded between 200–340 K with a step size of 20K. B) Plot presenting the calibration curve of **3** when the equation for Δ is employed. The points show the

experimental delta parameters and the solid line presents the best fit of the experimental points. C) Plot presenting the relative sensitivity S_r values at varied temperatures (200-340 K) for compound **3**. D) Emission map of **4** recorded between 253-333 K with a step size of 10K. E) Plot presenting the calibration curve of **4** when the equation for Δ is employed. The points show the experimental delta parameters and the solid line presents the best fit of the experimental points; F) Plot presenting the relative temperature sensitivity S_r values at varied temperatures (253-333 K) for compound **4**. The solid line is a guide to increase visibility. G) Graph presenting the temperature uncertainty for compound **3** and H) compound **4**. I) Cycle test showing reusability of the compound **3** thermometer material (98.5% repeatability).

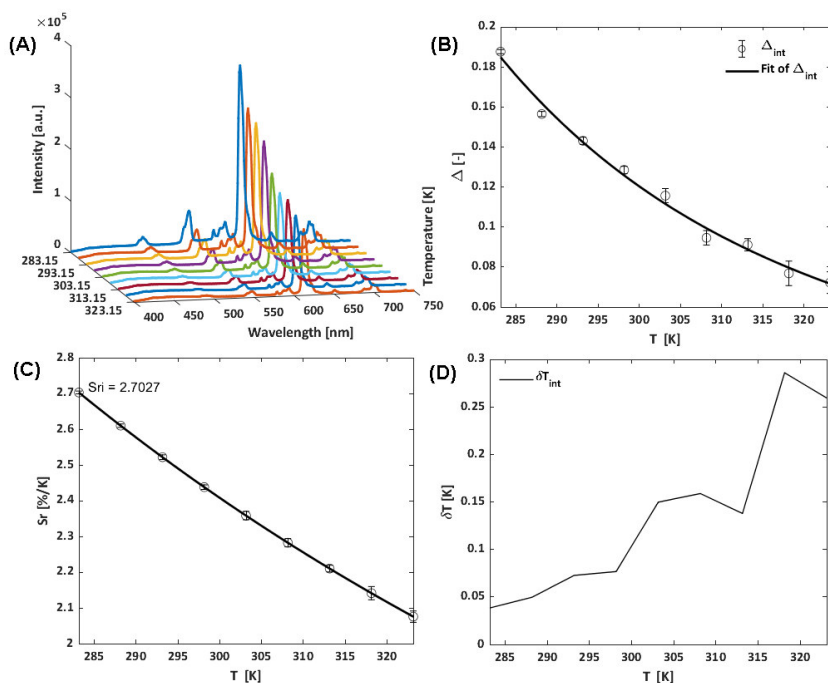


Figure 7.5. A) Emission map of sample **3** recorded between 283.15-323.15 K with a step size of 5 K in a water suspension. B) Plot presenting the calibration curve of compound **3** when the equation for Δ is employed. The points show the experimental delta parameters and the solid line presents the best fit of the experimental points. C) Plot presenting the relative sensitivity S_r values at varied temperatures (283.15-323.15 K) for compound **3** in water suspension. D) Graph presenting the temperature uncertainty for **3** measured in water suspension.

To fully evaluate the suitability of these materials for employing in biomedical systems, it is essential to investigate their cytotoxicity towards living cells. Accordingly, we carried out experiments using normal human dermal fibroblastic cells (NHDF cells). The viability tests of the cells demonstrated that the Bipy-CTF and Ln@Bipy-CTF materials are non-toxic at lower concentrations (Figure 7.6A). The particle toxicity towards fibroblastic cells occurred only at very high concentrations of 1 and 0.5 mg per well for Bipy-CTF and Ln@Bipy-CTF, respectively, that might be due to the mechanical pressure of the particles on the cells. The fluorescence images show the morphology of cells after incubation with the particles (Figure 7.6B). The fusiform morphology of cells incubated with Bipy-CTF and Ln@BipyCTF at 0.1 mg/ml and lower concentrations are comparable to control which fully correlates with the cell viability test. High stability, very good thermometric performance in solid-state and water and, nontoxicity to human cells make these compounds very promising to be used in the biological systems.

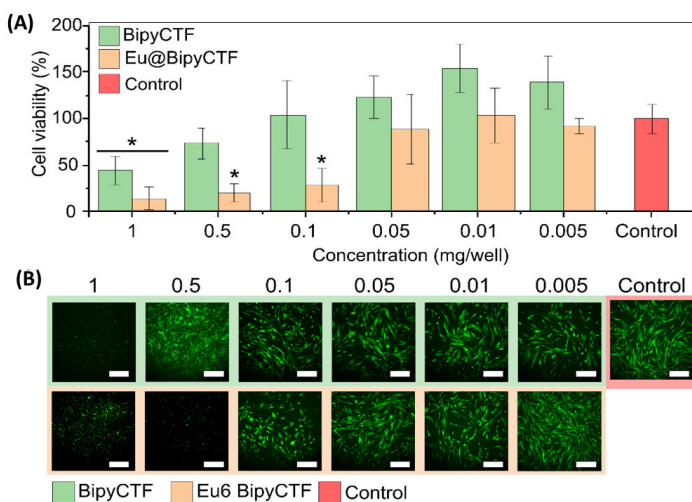


Figure 7.6. A) Graph presenting the cell viability (%) after exposure to different concentrations of the BipyCTF and compound **2** particles. An asterisk (*) indicates significant differences from the control cell group. The statistical analysis was performed by ANOVA followed by the Tukey test ($p < 0.05$). B) Fluorescence microscopy images of the cells at different compound concentrations (cells are green). Scale bar is 250 μ m.

7.3. Conclusions

Here, we report the synthesis of a new bipyridine-based CTF, where the bipyridine linker was purposefully introduced for the selective docking of lanthanide ions. We successfully synthesized a highly crystalline, porous and robust Bipy-CTF *via* in situ generation of an aldehyde intermediate. We applied a polycondensation strategy by using a simple bipyridine amidine monomer, which opens immense possibilities of monomers design for synthesizing new crystalline CTFs under mild conditions. The organic donor-acceptor pairs and ordered structure of the conjugated Bipy-CTF moiety greatly improve the delocalization of π electrons to overcome nonradiative energy dissipation. With these collective advantages of crystalline and porous Bipy-CTF in hand, docking various lanthanide ions not only enable luminescence color tuning but also facilitating the excitation of lanthanide ions through antenna effect. The presence of bipyridine docking sites within the porous channel-wall of the Bipy-CTF allows an easy and controlled grafting of lanthanide complexes, which open up a new avenue for designing LnCTF based ratiometric luminescent thermometers. The EuTb@Bipy-CTF thermometer exhibited excellent linear response over wide range of temperature from 200 to 340 K, with a temperature uncertainty below 0.2% and very good reusability (up to 98.5% repeatability). Moreover, the thermometer also exhibited excellent performance in the physiological temperature range when dispersed in water. High crystallinity and stability, outstanding thermometric performance in the solid-state as well as in water and nontoxicity to human fibroblastic cells make this LnCTF material a very promising candidate as physiological molecular thermometer.

7.4. Experimental Section

7.4.1. Materials and instrumentation

For details please see Appendix.

7.4.2. Synthesis of 2,2'-bipyridine-5,5'-diamidine dihydrochloride

To a solution of 2,2'-bipyridine-5,5'-dicyanide (0.412 g, 2.0 mmol) in 8 mL THF, 8 mL of 1 M LiN(SiMe₃)₂ solution was added dropwise over the time of 30 min at 0 °C. The mixture was stirred at 25 °C for 24 h and then cooled to 0 °C. The reaction was quenched by careful addition of 6 M HCl–EtOH (8 mL) and the mixture was left overnight. The solid sample was then filtered and washed with diethyl ether. Hereafter, the solid was recrystallized from H₂O–EtOH mixture. Yield: (0.767 g, 96%). ¹H NMR (400MHz, DMSO-d₆): δ = 9.80 (s, 4H, NH), 9.53 (s, 4H, NH), 9.18 (d, 2H, aromatic H), 8.63 (d, 2H, aromatic H), 8.47 (d, 2H, aromatic H), ¹³C NMR (75 MHz, D₂O) δ = 164.36, 158.19, 148.30, 138.15, 125.65, 122.81.

7.4.3. Synthesis of Bipy-CTF

1,4-Benzenedimethanol (0.069 mg, 0.5 mmol), 2,2'-bipyridine-5,5'-diamidine dihydrochloride (0.311 g, 1.0 mmol), and cesium carbonate (0.700 g, 2.2 mmol) were added to a DMSO solution (15.0 mL) in a round-bottom flask (100 mL). The mixture was heated at 100 °C for 24 h, then the temperature was raised to 150 °C for 36 h. The precipitate of the yellow suspension was washed with diluted HCl (1M, 3 × 20 mL) to remove residual cesium carbonate, and further washed with water (3 × 30 mL), EtOH (3 × 30 mL), and THF (3 × 20 mL). The filtered solids were freeze-dried for 24 h to yield Bipy-CTF as a yellow powder (150 mg, 84% yield).

7.4.4. Synthesis of Ln@Bipy-CTF

The samples were prepared by weighting of 0.005 mmol of the Bipy-CTF and 0.005 mmol of Ln(bzac)₃·2H₂O (bzac = benzoylacetone) complexes and both powders were placed in a Pyrex tube. After the addition of dichloromethane (5 mL), the sealed tube was placed in an ultrasound bath for 10 minutes. Then, the tube was heated on a heating block at 45 °C for 24 h. Afterwards, the filtered powder was washed with tiny amount of methanol and dried at 80 °C (Ln loading 160 mg/g).

7.5. References

1. Zhu, X.; Tian, C. C.; Veith, G. M.; Abney, C. W.; Dehaut, J.; Dai, S., In Situ Doping Strategy for the Preparation of Conjugated Triazine Frameworks Displaying Efficient CO₂ Capture Performance. *J Am Chem Soc* **2016**, *138* (36), 11497-11500.
2. Abednatanzi, S.; Derakhshandeh, P. G.; Leus, K.; Vrielinck, H.; Callens, F.; Schmidt, J.; Savateev, A.; Voort, P. V. D., Metal-free activation of molecular oxygen by covalent triazine frameworks for selective aerobic oxidation. *Sci. Adv.* **2020**, *6* (14), eaaz2310.
3. Wang, X. Y.; Chen, L. J.; Chong, S. Y.; Little, M. A.; Wu, Y. Z.; Zhu, W. H.; Clowes, R.; Yan, Y.; Zwijnenburg, M. A.; Sprick, R. S.; Cooper, A. I., Sulfone-containing covalent organic frameworks for photocatalytic hydrogen evolution from water. *Nat Chem* **2018**, *10* (12), 1180-1189.
4. Rogge, S. M. J.; Bavykina, A.; Hajek, J.; Garcia, H.; Olivos-Suarez, A. I.; Sepulveda-Escribano, A.; Vimont, A.; Clet, G.; Bazin, P.; Kapteijn, F.; Daturi, M.; Ramos-Fernandez, E. V.; Xamena, F. X. L. I.; Van Speybroeck, V.; Gascon, J., Metal-organic and covalent organic frameworks as single-site catalysts. *Chem Soc Rev* **2017**, *46* (11), 3134-3184.
5. Guan, X. Y.; Chen, F. Q.; Fang, Q. R.; Qiu, S. L., Design and applications of three dimensional covalent organic frameworks. *Chem Soc Rev* **2020**, *49* (5), 1357-1384.
6. Wang, Z. F.; Zhang, S. N.; Chen, Y.; Zhang, Z. J.; Ma, S. Q., Covalent organic frameworks for separation applications. *Chem Soc Rev* **2020**, *49* (3), 708-735.
7. Liu, X. G.; Huang, D. L.; Lai, C.; Zeng, G. M.; Qin, L.; Wang, H.; Yi, H.; Li, B. S.; Liu, S. Y.; Zhang, M. M.; Deng, R.; Fu, Y. K.; Li, L.; Xue, W. J.; Chen, S., Recent advances in covalent organic frameworks (COFs) as a smart sensing material. *Chem Soc Rev* **2019**, *48* (20), 5266-5302.
8. Dogru, M.; Bein, T., On the road towards electroactive covalent organic frameworks. *Chem Commun* **2014**, *50* (42), 5531-5546.
9. Mandal, A. K.; Mahmood, J.; Baek, J. B., Two-Dimensional Covalent Organic Frameworks for Optoelectronics and Energy Storage. *Chemnanomat* **2017**, *3* (6), 373-391.
10. Ascherl, L.; Evans, E. W.; Hennemann, M.; Di Nuzzo, D.; Hufnagel, A. G.; Beetz, M.; Friend, R. H.; Clark, T.; Bein, T.; Auras, F., Solvatochromic covalent organic frameworks. *Nat Commun* **2018**, *9*.
11. Haldar, S.; Chakraborty, D.; Roy, B.; Banappanavar, G.; Rinku, K.; Mullangi, D.; Hazra, P.; Kabra, D.; Vaidyanathan, R., Anthracene-Resorcinol Derived Covalent Organic Framework as Flexible White Light Emitter. *J Am Chem Soc* **2018**, *140* (41), 13367-13374.
12. Geng, K.; He, T.; Liu, R.; Dalapati, S.; Tan, K. T.; Li, Z.; Tao, S.; Gong, Y.; Jiang, Q.; Jiang, D., Covalent Organic Frameworks: Design, Synthesis, and Functions. *Chemical Reviews* **2020**.
13. Li, X. L.; Zhang, C. L.; Cai, S. L.; Lei, X. H.; Altoe, V.; Hong, F.; Urban, J. J.; Ciston, J.; Chan, E. M.; Liu, Y., Facile transformation of imine covalent organic frameworks into ultrastable crystalline porous aromatic frameworks. *Nat Commun* **2018**, *9*.
14. Kuhn, P.; Antonietti, M.; Thomas, A., Porous, covalent triazine-based frameworks prepared by ionothermal synthesis. *Angew Chem Int Edit* **2008**, *47* (18), 3450-3453.
15. Je, S. H.; Kim, H. J.; Kim, J.; Choi, J. W.; Coskun, A., Perfluoroaryl-Elemental Sulfur SNAR Chemistry in Covalent Triazine Frameworks with High Sulfur Contents for Lithium-Sulfur Batteries. *Adv Funct Mater* **2017**, *27* (47).
16. Puthiaraj, P.; Cho, S. M.; Lee, Y. R.; Ahn, W. S., Microporous covalent triazine polymers: efficient Friedel-Crafts synthesis and adsorption/storage of CO₂ and CH₄. *J Mater Chem A* **2015**, *3* (13), 6792-6797.

17. Ren, S. J.; Bojdy, M. J.; Dawson, R.; Laybourn, A.; Khimyak, Y. Z.; Adams, D. J.; Cooper, A. I., Porous, Fluorescent, Covalent Triazine-Based Frameworks Via Room-Temperature and Microwave-Assisted Synthesis. *Adv Mater* **2012**, *24* (17), 2357-2361.
18. Yu, S. Y.; Mahmood, J.; Noh, H. J.; Seo, J. M.; Jung, S. M.; Shin, S. H.; Im, Y. K.; Jeon, I. Y.; Baek, J. B., Direct Synthesis of a Covalent Triazine-Based Framework from Aromatic Amides. *Angew Chem Int Edit* **2018**, *57* (28), 8438-8442.
19. Wang, K. W.; Yang, L. M.; Wang, X.; Guo, L. P.; Cheng, G.; Zhang, C.; Jin, S. B.; Tan, B.; Cooper, A., Covalent Triazine Frameworks via a Low-Temperature Polycondensation Approach. *Angew Chem Int Edit* **2017**, *56* (45), 14149-14153.
20. Tang, Y. Z.; Huang, H. L.; Xue, W. J.; Chang, Y. J.; Li, Y.; Guo, X. Y.; Zhong, C. L., Rigidifying induced fluorescence enhancement in 2D porous covalent triazine framework nanosheets for the simultaneously luminous detection and adsorption removal of antibiotics. *Chem Eng J* **2020**, *384*.
21. Li, J.; Liu, P.; Tang, Y. Z.; Huang, H. L.; Cui, H. Z.; Mei, D. H.; Zhong, C. L., Single-Atom Pt-N-3 Sites on the Stable Covalent Triazine Framework Nanosheets for Photocatalytic N-2 Fixation. *Acs Catal* **2020**, *10* (4), 2431-2442.
22. Guo, L. P.; Niu, Y. L.; Xu, H. T.; Li, Q. W.; Razzaque, S.; Huang, Q.; Jin, S. B.; Tan, B., Engineering heteroatoms with atomic precision in donor- acceptor covalent triazine frameworks to boost photocatalytic hydrogen production. *J Mater Chem A* **2018**, *6* (40), 19775-19781.
23. Jiang, Y.; Oh, I.; Joo, S. H.; Buyukcakir, O.; Chen, X.; Lee, S. H.; Huang, M.; Seong, W. K.; Kim, J. H.; Rohde, J. U.; Kwak, S. K.; Yoo, J. W.; Ruoff, R. S., Organic Radical-Linked Covalent Triazine Framework with Paramagnetic Behavior. *Acs Nano* **2019**, *13* (5), 5251-5258.
24. Guo, L. P.; Niu, Y. L.; Razzaque, S.; Tan, B.; Jin, S. B., Design of D-A(1)-A(2) Covalent Triazine Frameworks via Copolymerization for Photocatalytic Hydrogen Evolution. *Acs Catal* **2019**, *9* (10), 9438-9445.
25. Liu, M. Y.; Huang, Q.; Wang, S. L.; Li, Z. Y.; Li, B. Y.; Jin, S. B.; Tan, B., Crystalline Covalent Triazine Frameworks by InSitu Oxidation of Alcohols to Aldehyde Monomers. *Angew Chem Int Edit* **2018**, *57* (37), 11968-11972.
26. Abednatanzi, S.; Derakhshandeh, P. G.; Tack, P.; Muniz-Miranda, F.; Liu, Y.-Y.; Everaert, J.; Meledina, M.; Bussche, F. V.; Vincze, L.; Stevens, C. V.; Speybroeck, V. V.; Vrielandt, H.; Callens, F.; Leus, K.; Voort, P. V. D., Elucidating the promotional effect of a covalent triazine framework in aerobic oxidation. *Applied Catalysis B: Environmental* **2020**, *269*, 118769.
27. Skirtach, A. G.; Javier, A. M.; Kreft, O.; Kohler, K.; Alberola, A. P.; Mohwald, H.; Parak, W. J.; Sukhorukov, G. B., Laser-induced release of encapsulated materials inside living cells. *Angew Chem Int Edit* **2006**, *45* (28), 4612-4617.
28. Rao, X. T.; Song, T.; Gao, J. K.; Cui, Y. J.; Yang, Y.; Wu, C. D.; Chen, B. L.; Qian, G. D., A Highly Sensitive Mixed Lanthanide Metal-Organic Framework Self-Calibrated Luminescent Thermometer. *J Am Chem Soc* **2013**, *135* (41), 15559-15564.
29. Cui, Y. J.; Song, R. J.; Yu, J. C.; Liu, M.; Wang, Z. Q.; Wu, C. D.; Yang, Y.; Wang, Z. Y.; Chen, B. L.; Qian, G. D., Dual-Emitting MOF superset of Dye Composite for Ratiometric Temperature Sensing. *Adv Mater* **2015**, *27* (8), 1420-+.
30. Zhao, S. N.; Li, L. J.; Song, X. Z.; Zhu, M.; Hao, Z. M.; Meng, X.; Wu, L. L.; Feng, J.; Song, S. Y.; Wang, C.; Zhang, H. J., Lanthanide Ion Codoped Emitters for Tailoring Emission Trajectory and Temperature Sensing. *Adv Funct Mater* **2015**, *25* (9), 1463-1469.
31. Cui, Y. J.; Xu, H.; Yue, Y. F.; Guo, Z. Y.; Yu, J. C.; Chen, Z. X.; Gao, J. K.; Yang, Y.; Qian, G. D.; Chen, B. L., A Luminescent Mixed-Lanthanide Metal-Organic Framework Thermometer. *J Am Chem Soc* **2012**, *134* (9), 3979-3982.
32. Kaczmarek, A. M.; Maegawa, Y.; Abalymov, A.; Skirtach, A. G.; Inagaki, S.; Van Der Voort, P., Lanthanide-Grafted Bipyridine Periodic Mesoporous Organosilicas (BPy-PMOs) for Physiological Range and Wide Temperature Range Luminescence Thermometry. *Acs Appl Mater Inter* **2020**, *12* (11), 13540-13550.

Metal- and Covalent Organic Frameworks for Advanced Applications: Heterogeneous Catalysis and Sensing

33. Vyas, V. S.; Vishwakarma, M.; Moudrakovski, I.; Haase, F.; Savasci, G.; Ochsenfeld, C.; Spatz, J. P.; Lotsch, B. V., Exploiting Noncovalent Interactions in an Imine-Based Covalent Organic Framework for Quercetin Delivery. *Adv Mater* **2016**, *28* (39), 8749-8754.
34. Wang, P.; Zhou, F.; Zhang, C.; Yin, S. Y.; Teng, L. L.; Chen, L. L.; Hu, X. X.; Liu, H. W.; Yin, X.; Zhang, X. B., Ultrathin two-dimensional covalent organic framework nanoprobe for interference-resistant two-photon fluorescence bioimaging. *Chem Sci* **2018**, *9* (44), 8402-8408.
35. Krishnaraj, C.; Kaczmarek, A. M.; Jena, H. S.; Leus, K.; Chaoui, N.; Schmidt, J.; Van Deun, R.; Van der Voor, P., Triggering White-Light Emission in a 2D Imine Covalent Organic Framework Through Lanthanide Augmentation. *Acs Appl Mater Inter* **2019**, *11* (30), 27343-27352.
36. Wang, J. M.; Lian, X.; Yan, B., Eu³⁺-Functionalized Covalent Organic Framework Hybrid Material as a Sensitive Turn-On Fluorescent Switch for Levofloxacin Monitoring in Serum and Urine. *Inorg Chem* **2019**, *58* (15), 9956-9963.
37. Li, J.; Zhang, C. Y.; Yin, M. Y.; Zhang, Z.; Chen, Y. J.; Deng, L.; Wang, S., Surfactant-Sensitized Covalent Organic Frameworks-Functionalized Lanthanide-Doped Nanocrystals: An Ultrasensitive Sensing Platform for Perfluorooctane Sulfonate. *Acs Omega* **2019**, *4* (14), 15947-15955.
38. Kaczmarek, A. M.; Liu, Y. Y.; Kaczmarek, M. K.; Liu, H. S.; Artizzu, F.; Carlos, L. D.; Van Der Voort, P., Developing Luminescent Ratiometric Thermometers Based on a Covalent Organic Framework (COF). *Angew Chem Int Edit* **2020**, *59* (5), 1932-1940.
39. Kaczmarek, A. M.; Van Deun, R.; Kaczmarek, M. K., TeSen - tool for determining thermometric parameters in ratiometric optical thermometry. *Sensor Actuat B-Chem* **2018**, *273*, 696-702.

7.6. Supporting Information

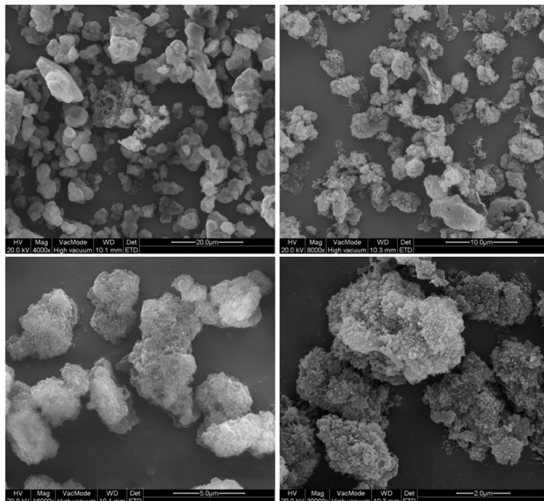


Figure S7.1. SEM image of Bipy-CTF presented at different magnifications.

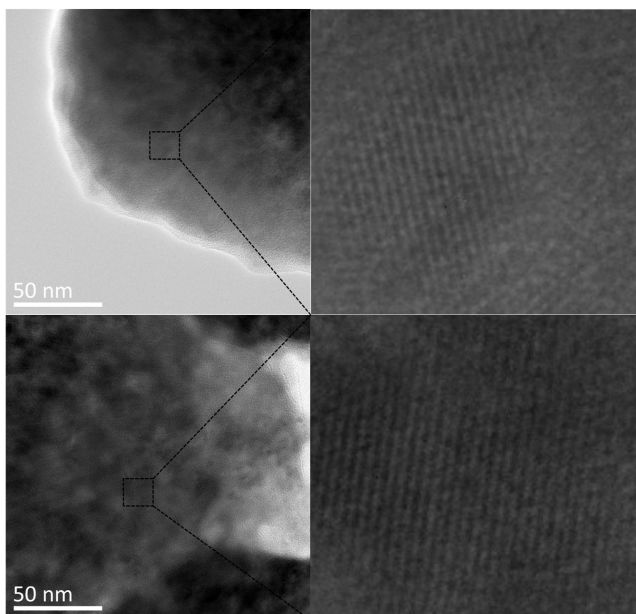


Figure S7.2. TEM image and higher-magnification HR-TEM image of Bipy-CTF.

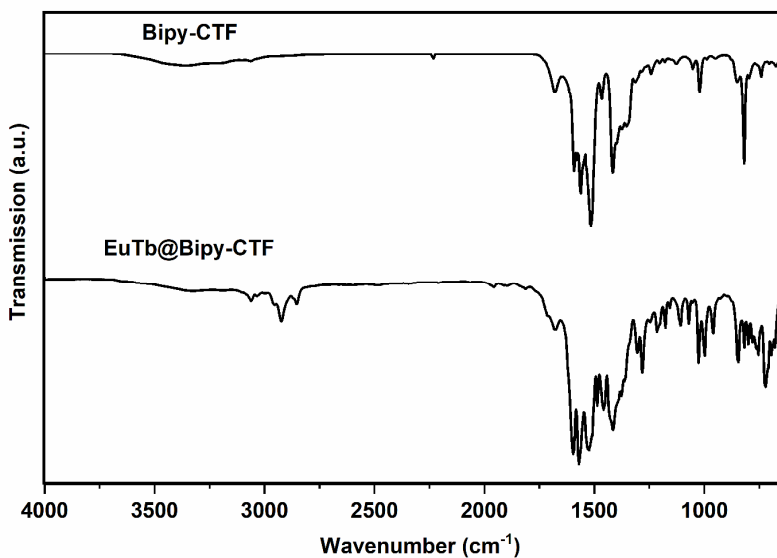


Figure S7.3. DRIFT spectra of Bipy-CTF and EuTb@BipyCTF.

Table S7.1. Elemental analysis of Bipy-CTF.

Sample	Cal.			Exp.		
	N%	C%	H%	N%	C%	H%
Bipy-CTF	25.9	71.0	3.1	20.87	64.11	3.40

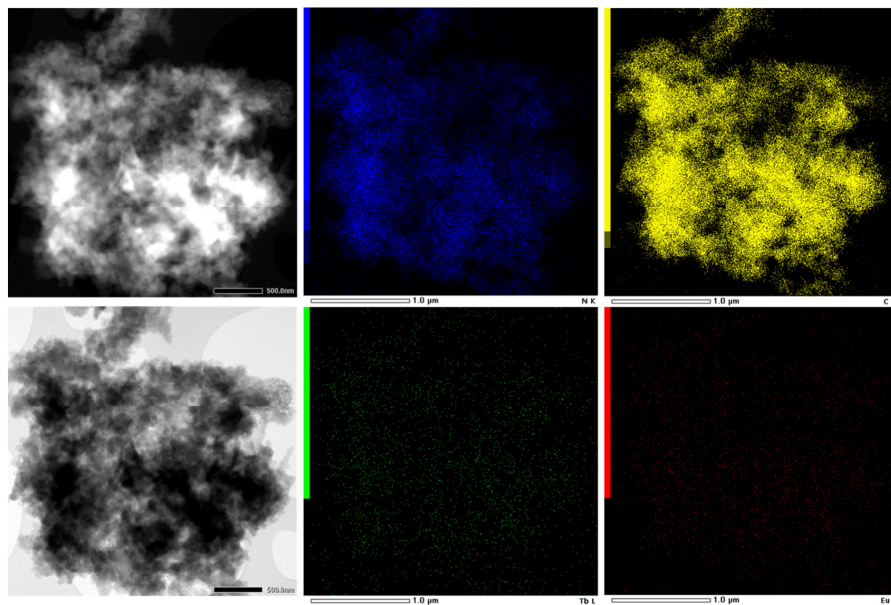


Figure S7.4. Dark-field TEM image of EuTb@Bipy-CTF and corresponding EDX elemental mapping of Eu (red) and Tb (green).

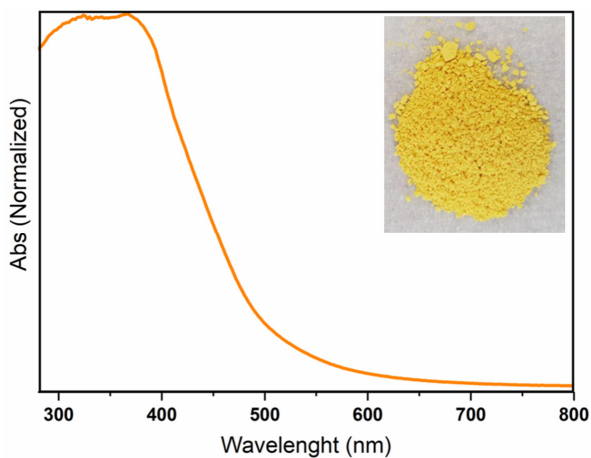


Figure S7.5. UV-Visible spectra and photo of the pristine Bipy-CTF.

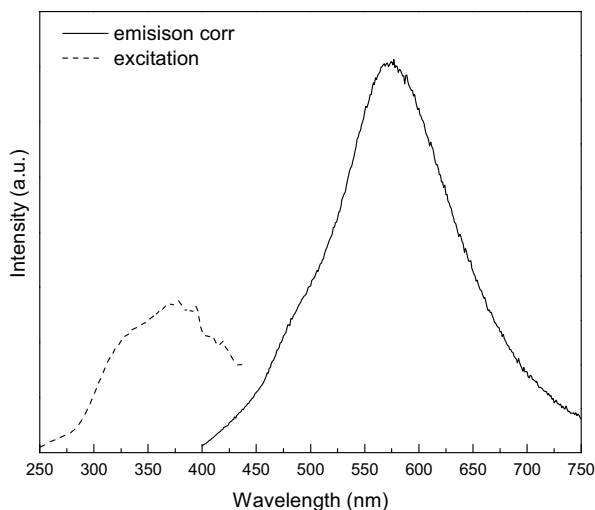


Figure S7.6. Combined excitation-emission spectrum of the pristine Bipy-CTF.

Table S7.2. Assignment of peaks for compound 1.

	Wavelength (nm)	Transitions
excitation		
a	377.0	$\pi \rightarrow \pi^*$
emission		
b	490.0	${}^5D_4 \rightarrow {}^7F_6$
c	549.0	${}^5D_4 \rightarrow {}^7F_5$
d	580.0	${}^5D_4 \rightarrow {}^7F_4$
e	619.0	${}^5D_4 \rightarrow {}^7F_3$

Table S7.3. Assignment of peaks for compound 2.

	Wavelength (nm)	Transitions
excitation		
a	354.0	$\pi \rightarrow \pi^*$
b	395.0	${}^5L_6 \leftarrow {}^7F_0$
emission		
c	579.0	${}^5D_0 \rightarrow {}^7F_0$

d	594.0	$^5D_0 \rightarrow ^7F_1$
e	612.0	$^5D_0 \rightarrow ^7F_2$
f	651.0	$^5D_0 \rightarrow ^7F_3$
g	700.0	$^5D_0 \rightarrow ^7F_4$

Table S7.4. Assignment of peaks for compound **3**.

Wavelength (nm)	Transitions
excitation	
327.0	$\pi \rightarrow \pi^*$
emission	
a	$^5D_4 \rightarrow ^7F_6$ (Tb)
b	$^5D_4 \rightarrow ^7F_5$ (Tb)
c	$^5D_4 \rightarrow ^7F_4$ (Tb)
d	$^5D_0 \rightarrow ^7F_1$ (Eu)
e	$^5D_0 \rightarrow ^7F_2$ (Eu)
f	$^5D_0 \rightarrow ^7F_3$ (Eu)
g	$^5D_0 \rightarrow ^7F_4$ (Eu)

Table S7.5. Assignment of peaks for compound **4**.

Wavelength (nm)	Transitions
excitation	
a	$\pi \rightarrow \pi^*$
emission	
b	$^5D_4 \rightarrow ^7F_6$ (Tb)
c	$^5D_4 \rightarrow ^7F_5$ (Tb)
d	$^5D_4 \rightarrow ^7F_4$ (Tb)
e	$^5D_0 \rightarrow ^7F_1$ (Eu)
f	$^5D_0 \rightarrow ^7F_2$ (Eu)
g	$^5D_0 \rightarrow ^7F_3$ (Eu)
h	$^5D_0 \rightarrow ^7F_4$ (Eu)

Metal- and Covalent Organic Frameworks for Advanced Applications: Heterogeneous Catalysis and Sensing

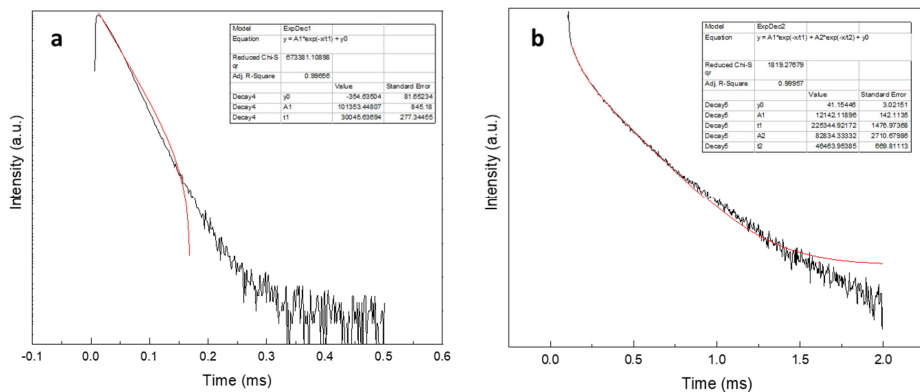


Figure S7.7. a) Decay profile of sample 1 recorded at RT. b) Decay profile of sample 2 recorded at RT.

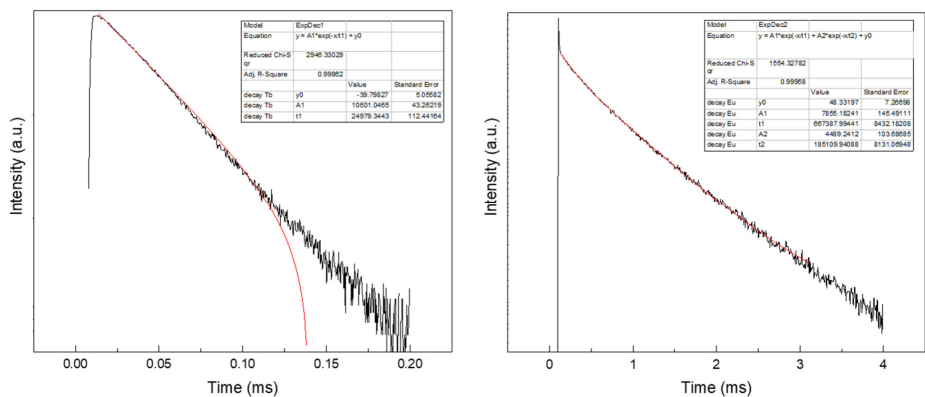


Figure S7.8. Decay profile of 3 recorded at RT (top recorded when observing Tb³⁺, bottom recorded when observing Eu³⁺).

Chapter 7: Lanthanide Functionalized Covalent Triazine Framework as Physiological Molecular Thermometer

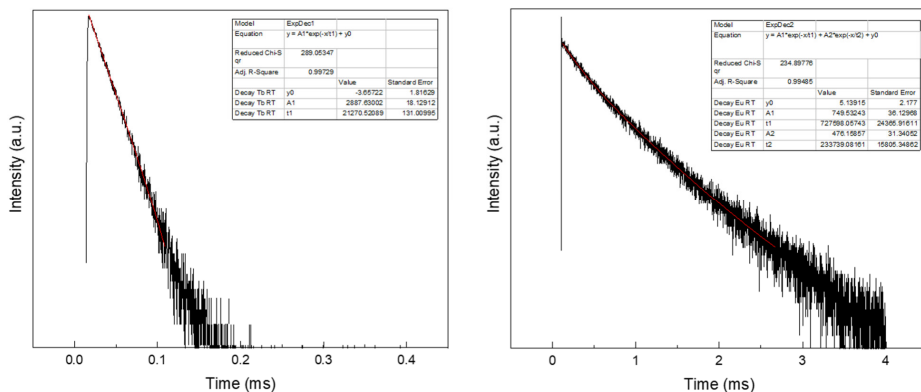


Figure S7.9. Decay profile of **4** recorded at RT (top recorded when observing Tb³⁺, bottom recorded when observing Eu³⁺).

For better understanding of the energy transfer mechanism in the material the triplet level in the Bipy-CTF grafted with GdCl₃ material has been determined at 77 K in ethanol/methanol mixture (4:1). The analysis is depicted in Figure S7.10. In gadolinium complexes, the energy at the triplet level of the ligand is not transferred to the Gd³⁺ metal, as the resonance level of Gd³⁺ lies far above the triplet level. Subsequently, we have recorded the decay time at its maximum and observed microsecond range lifetimes, confirming the band belongs to the triplet level of the material (Figure S7.11). The triplet level of Bipy-CTF grafted with GdCl₃ corresponds to the high-energy edge of this band, the lowest triplet level is therefore located at 460 nm (21740 cm⁻¹). The triplet level lies above the energy level of the ⁵D₄ accepting level of Tb³⁺ allowing successful energy transfer to Tb³⁺ and energy can further be transferred to the accepting levels of Eu³⁺.

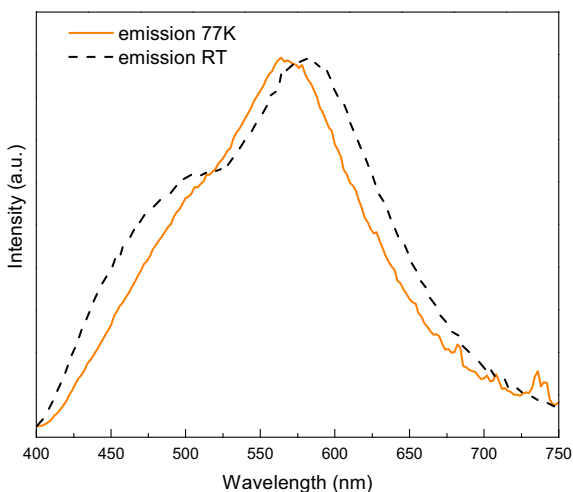


Figure S7.10. Emission spectra of Bipy-CTF grafted with $GdCl_3$, measured in ethanol: methanol (4:1) solution at RT and at 77 K.

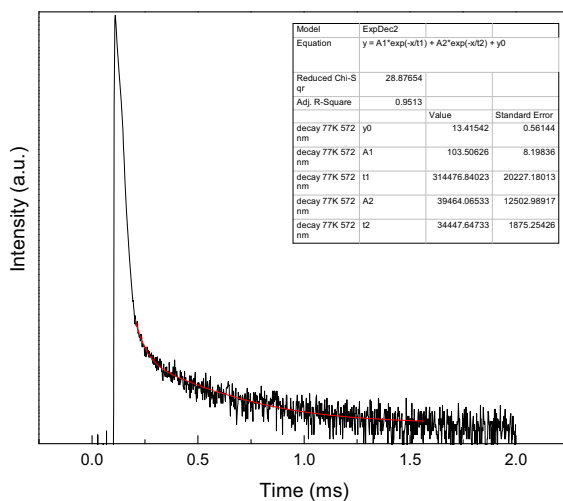


Figure S7.11. Decay time of Bipy-CTF grafted with $GdCl_3$, measured at 460 nm.

Table S7.6. An overview of the relative sensitivity S_r (highest value) for the reported luminescent thermometers (MOFs and coordination polymers) compared to the EuTb@BipyCTF materials (Entry 1 and 2) operating in physiological temperature range.

Entry	Materials	Temp. range [K]	Max. S_r [%K ⁻¹]	Ref.
1	Compound 3	200-340	2.30 (240K)	This work
2	Compound 4	253-333	2.12 (253K)	This work
3	ZJU-88 \supset perylene	293-353	1.28 (293K)	1
4	Tb _{0.99} Eu _{0.01} (BDC) _{1.5} (H ₂ O) ₂	298-320	0.14 (314 K)	2
5	Tb _{0.7} Eu _{0.3} L MOF	40 - 300	0.17 (300 K)	3
6	(Eu _x Tb _{1-x}) ₂ (DMBDC) ₃ (H ₂ O) ₄ .DMF.H ₂ O	10-300	1.3 (284 K)	4
7	[(Tb _{0.914} Eu _{0.086}) ₂ (PDA) ₃ (H ₂ O)]·2H ₂ O	10-325	0.07 (325 K)	5
8	Nd _{0.577} Yb _{0.423} BDC-F ₄	293-313	1.201 (313 K)	6
9	Tb _{0.999} Eu _{0.001} BPDC	100-300	1.23	7
10	EuTb@ In(OH)(bpydc)	283-333	4.97	8
11	Tb _{0.9} Eu _{0.1} PIA	10-300	3.53	9

Metal- and Covalent Organic Frameworks for Advanced Applications: Heterogeneous Catalysis and Sensing

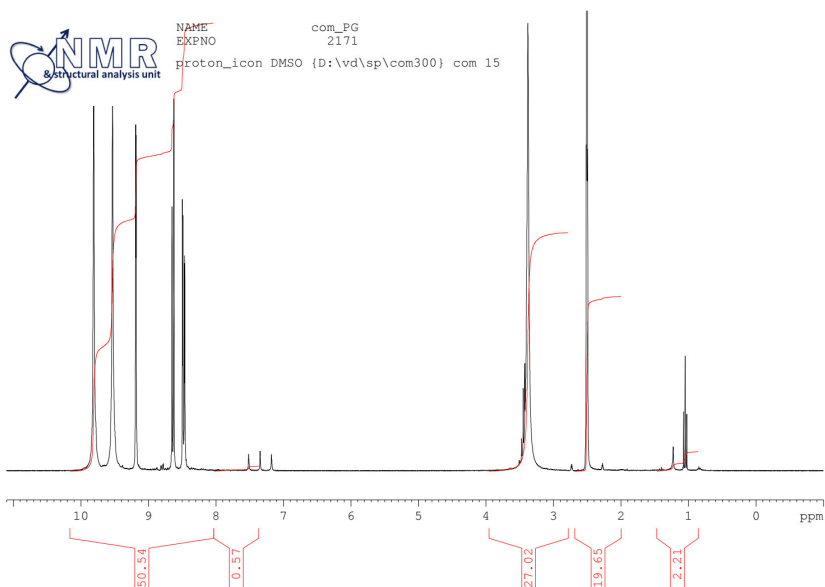
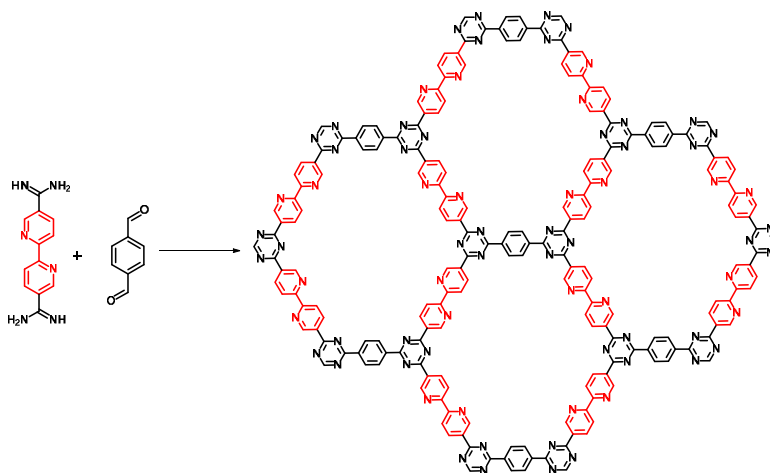


Figure S7.12. ¹H NMR of 2,2'-bipyridine-5,5'-diamidine tetrahydrochloride.

unit cell (a, b, c) parameters were allowed to vary freely during refinement. Peaks were fit using Pseudo-Voigt functions and background was modelled using a 20-order polynomial. Crystallite size or lattice strain broadening was not taken into account during refinement. To determine the correct structure of the Bipy-CTF, a theoretical PXRD pattern was modelled using Materials Studio 2017 software. Both eclipsed (AA) and staggered (AB) structures were generated (Figure S7.14) but based on the major differences between the experimental pattern and the AB modelled one, only the eclipsed structure was taken into consideration. Subsequently, the eclipsed structure was Pawley refined to the experimental data (both the raw and background corrected data were used, from 2 to 40° 2 θ), obtaining an optimized structure assigned to the Cmmm space group with optimized unit cell parameter of a = 30.91, b = 20.76 and c = 3.51 (for raw data) and a = 30.95, b = 20.79 and c = 3.50 when using background corrected data. With low R_{wp} and R_p values (6.69% and 5.24% respectively, for the raw data and 2.22% and 1.51% respectively for the background corrected data) and no visible deviations from the experimental pattern or significant peaks in the difference plot, this model proves to be a good fit. In Figure S7.15 the Pawley refinement of the raw experimental pattern without background correction is presented.



Scheme S7.1. The possible framework of condensation of [2,2'-bipyridine]-5,5' bis(carboximidamide) and terephthalaldehyde.

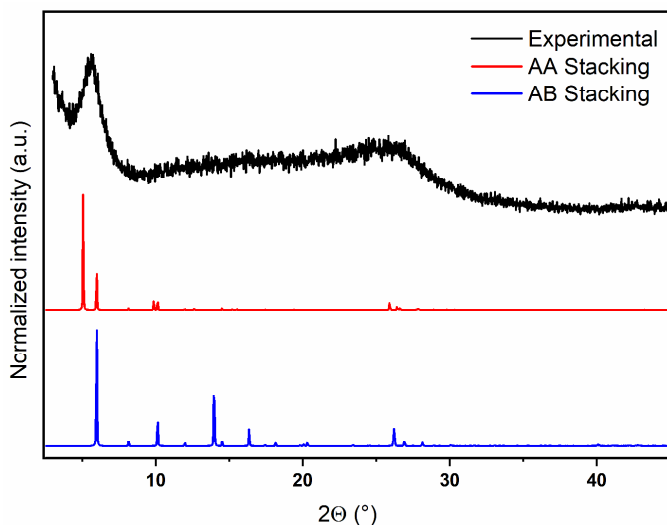


Figure S7.14. The normalized experimental PXRD pattern (black) compared to the normalized modelled stacking modes for Bipy-CTF (red for AA stacking, blue for AB stacking).

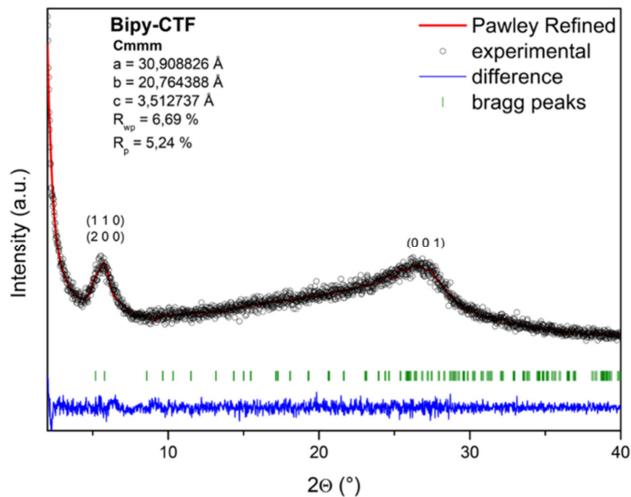


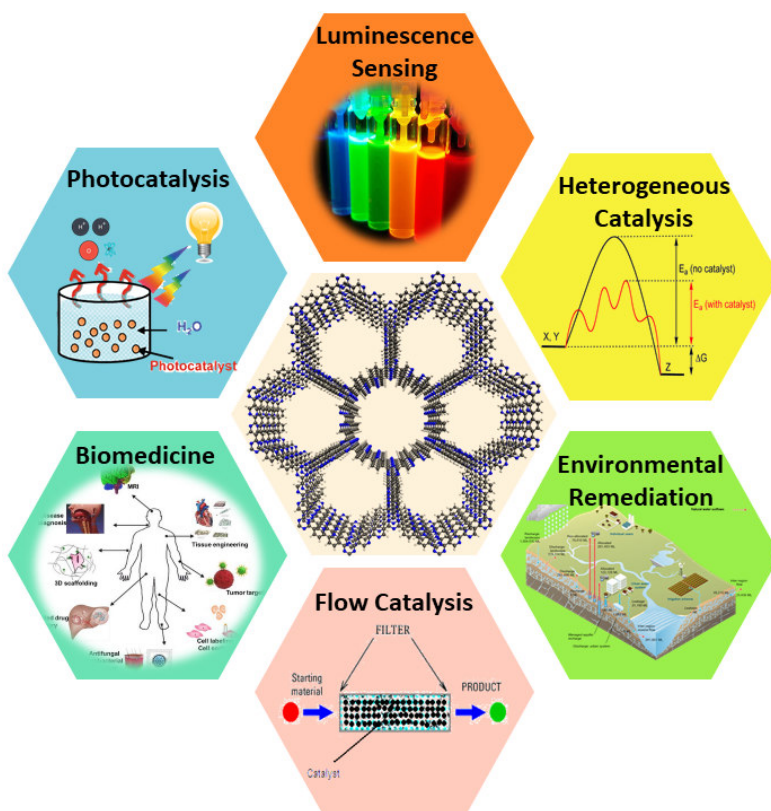
Figure S7.15. Experimental (black) and Pawley refined (red) PXRD patterns of modelled Bipy CTF, accompanied with the difference plot (blue) and Bragg peak positions (green) of the corresponding model.

References

1. Cui, Y. J.; Song, R. J.; Yu, J. C.; Liu, M.; Wang, Z. Q.; Wu, C. D.; Yang, Y.; Wang, Z. Y.; Chen, B. L.; Qian, G. D., Dual-Emitting MOF superset of Dye Composite for Ratiometric Temperature Sensing. *Adv Mater* **2015**, *27* (8), 1420-+.
2. Cadiau, A.; Brites, C. D. S.; Costa, P. M. F. J.; Ferreira, R. A. S.; Rocha, J.; Carlos, L. D., Ratiometric Nanothermometer Based on an Emissive Ln(3+)-Organic Framework. *Acs Nano* **2013**, *7* (8), 7213-7218.
3. Zhao, S. N.; Li, L. J.; Song, X. Z.; Zhu, M.; Hao, Z. M.; Meng, X.; Wu, L. L.; Feng, J.; Song, S. Y.; Wang, C.; Zhang, H. J., Lanthanide Ion Codoped Emitters for Tailoring Emission Trajectory and Temperature Sensing. *Adv Funct Mater* **2015**, *25* (9), 1463-1469.
4. Cui, Y. J.; Xu, H.; Yue, Y. F.; Guo, Z. Y.; Yu, J. C.; Chen, Z. X.; Gao, J. K.; Yang, Y.; Qian, G. D.; Chen, B. L., A Luminescent Mixed-Lanthanide Metal-Organic Framework Thermometer. *J Am Chem Soc* **2012**, *134* (9), 3979-3982.
5. Wang, Z. P.; Ananias, D.; Carne-Sanchez, A.; Brites, C. D. S.; Imaz, I.; MasPOCH, D.; Rocha, J.; Carlos, L. D., Lanthanide-Organic Framework Nanothermometers Prepared by Spray-Drying. *Adv Funct Mater* **2015**, *25* (19), 2824-2830.
6. Lian, X. S.; Zhao, D.; Cui, Y. J.; Yang, Y.; Qian, G. D., A near infrared luminescent metal-organic framework for temperature sensing in the physiological range. *Chem Commun* **2015**, *51* (100), 17676-17679.
7. Shen, X.; Lu, Y.; Yan, B., Lanthanide Complex Hybrid System for Fluorescent Sensing as Thermometer. *Eur J Inorg Chem* **2015**, (6), 916-919.
8. Zhou, Y.; Yan, B.; Lei, F., Postsynthetic lanthanide functionalization of nanosized metal-organic frameworks for highly sensitive ratiometric luminescent thermometry. *Chem Commun* **2014**, *50* (96), 15235-15238.
9. Rao, X. T.; Song, T.; Gao, J. K.; Cui, Y. J.; Yang, Y.; Wu, C. D.; Chen, B. L.; Qian, G. D., A Highly Sensitive Mixed Lanthanide Metal-Organic Framework Self-Calibrated Luminescent Thermometer. *J Am Chem Soc* **2013**, *135* (41), 15559-15564.
10. Feldblyum, J. I.; McCreery, C. H.; Andrews, S. C.; Kurosawa, T.; Santos, E. J. G.; Duong, V.; Fang, L.; Ayzner, A. L.; Bao, Z. N., Few-layer, large-area, 2D covalent organic framework semiconductor thin films. *Chem Commun* **2015**, *51* (73), 13894-13897.

CHAPTER 8

CONCLUSIONS AND OUTLOOK



Porous and ordered materials have a pivotal role in several applications, such as sorption, heterogeneous catalysis and sensing. The microporous zeolites have played a dominant role in the last decades and are still an active research field. Over the last 20 years, other porous materials have been developed, and Metal-Organic Frameworks (MOFs) and Covalent Organic Frameworks (COFs) have been studied in detail. Both MOFs and COFs have some specific advantages over zeolites or porous oxides: (a) their designable and diverse structures, providing a control over morphology, pore size, and functionalities in the walls (the so-called reticular chemistry); (b) the crystalline nature of their frameworks, allowing dispersion of catalytically active sites in large-range ordered structures; (c) the possibility to introduce compatible multi-active sites, tuning these materials towards a plethora of different applications.

8.1. Heterogeneous catalysis with MOFs

Most approaches for preparing organic fine chemicals are accompanied by catalytic transformations as essential synthetic steps. Worth mentioning in this regard is the exploitation of homogeneous catalysts, such as transition metal complexes, for chemical industries. One advantage of homogeneous catalysts is that the catalytically active sites are easily accessible for the substrates. This advantage outweighs the practical challenges of catalyst recovery from the reaction mixture. Rational design of heterogeneous catalysts could endow them with similar catalytic activity to their homogeneous analogues and facilitate their separation and recyclability. In order to efficiently design heterogeneous catalysts, several parameters need to be met, including possible application of versatile modification approaches, construction of well-defined active sites, creation of high diffusion dynamics, and prevention of the catalyst leaching.

To this end, the use of MOFs and Covalent Triazine Frameworks (CTFs) as catalysts and scaffolds for metal coordination has been explored in this thesis. Accordingly, we showed the importance of synthesis strategy in designing distinctive structures and the effect on the properties of the materials. Three new 1D, 2D, and 3D Ce(III)-based frameworks were obtained by small changes in the synthetic routes. Our findings prove that Ce(III) ions are

outstanding candidates for adopting distinct coordination environments due to their adjustable coordination modes, which is an important step toward the design of Ce(III)-based frameworks for more specialized applications. The 3D MOF demonstrated excellent activity and selectivity in acetalization reaction (up to 98% conversion and 99% selectivity). Along with Ce(III)-based frameworks, MOFs can also be designed using Ce(IV) metal centers to perform various photocatalytic reactions. Moreover, various lanthanides can be applied to design MOFs with particular topology and structure that can be used for specific advanced applications such as temperature sensing and luminescence.

Besides the direct synthesis of MOFs, modification of these materials with active metal centers is highly desirable. However, very few papers report on the importance of the different functionalization routes for the introduction of metal complexes into MOFs and the effect on the properties of the materials. One such study was successfully performed in this thesis through modification of a certain MOF (COMOC-4), with an Ir(III) complex attached to the bipyridine functionalities as the docking sites. Our results revealed that the pre-functionalization approach was a powerful way to obtain a high Ir loading and surface area and preserve the formation of the desired MOF topology. The $\text{Ir}^{\text{III}}\text{Cp}^*\text{Cl}@ \text{COMOC-4}$ ($\text{Cp}^*=1,2,3,4,5\text{-pentamethylcyclopentadienyl}$) material exhibits a good catalytic performance with 54% conversion and 99% selectivity in the oxidation of benzyl alcohol, using O_2 as a clean oxidant. Along with Iridium, numerous other metals can coordinate strongly onto bipyridine sites through both post- and pre-functionalization to adapt them to the optimal parameters (surface area, pore volume, metal loading, etc.) to promote a specific catalytic reaction. In this thesis, we have shown that both methodologies, either post- or pre-functionalization, can be applied to design bimetallic MOFs. However, a clearer picture of the conditions and limitations of both strategies is still missing in the area, as well as a clearer understanding of when the MM-MOF formation is controlled by thermodynamics and when by kinetics. The field also needs more examples addressing a detailed characterization of regio- and/or size-selective properties and performing more complex catalytic reactions with the aforementioned properties.

8.2. Heterogeneous catalysis with CTFs

A major challenge in the development of heterogeneous catalysts is their recyclability. One of the typical drawbacks of MOFs is their low stability in moisture and potential metal leaching in liquids. CTFs are a great platform for designing highly stable heterogeneous catalysts. As a result, we made use of a highly stable CTF containing bipyridine coordination sites. The bipyridine sites within the CTF provide excellent anchoring points for the $[\text{Ru}(\text{acac})_2(\text{CH}_3\text{CN})_2]\text{PF}_6$ complex. The obtained robust $\text{Ru}^{\text{III}}@$ bipy-CTF material was applied for the selective tandem aerobic oxidation–Knoevenagel condensation reaction which showed great activity and recyclability.

It is important to note that the properties of the catalyst support (surface area, diffusion of reactants, chemistry and nature of the support, etc.) have a direct impact on the catalytic activity, which is less explored. In this thesis, the bipy-CTF support for the Ru^{III} complex is compared to the well-known UiO-67 MOF. Both catalysts were synthesized under the same reaction conditions and showed similar structural properties (Ru loading and microporous nature). $\text{Ru}^{\text{III}}@$ bipy-CTF proved to be a very active and selective catalyst for the aerobic oxidation of benzyl alcohol (99% conversion and selectivity) under green conditions. $\text{Ru}^{\text{III}}@$ UiO-67, however, did not exhibit comparable activity (46% conversion). Aiming at highly attractive synergistic strategies in heterogeneous catalysis, we unveil the activity of the bipy-CTF support with the capability of activating O_2 . We observed an unusual synergistic effect between the bipy-CTF support and the anchored Ru complex. We attribute the excellent performance of the $\text{Ru}^{\text{III}}@$ bipy-CTF catalyst to the combined functions of the bipy-CTF (activation of oxygen and substrate) and the Ru centers (adsorption of the activated substrate). This study represents one of the rare reports on the promoted catalytic alcohol oxidation through the assistance of both metal centers and catalyst support.

CTFs prepared under ionothermal conditions represent a higher degree of structural defects than MOFs. In some catalytic reactions, they may show advantages over simple MOFs in regards to their properties and applications. Examples have been presented showing that introduction of a metal ion to the nitrogen functionalities can result in observation of new properties and activity, along with the occurrence of synergic effects

on the resulting CTF-based catalysts. Our results demonstrate that CTFs are particularly promising catalysts in tandem reactions. This is due to the ability of incorporated metal centers to act as active sites for one of the elementary steps in the tandem reaction, and due to the intrinsic basicity of nitrogen sites, which can promote several organic transformations. This shows the capability of CTF materials to be applied as green alternatives to industrially used homogenous catalysts. Moreover, it would be interesting to perform these reactions under flow conditions in future work. This would facilitate technology transfer from lab scale to industrial scales. Despite the remarkable catalytic performance of CTFs, an insufficient understanding of the exact active sites within the catalysts and the exact catalytic mechanism limit the control over their activity and selectivity. To overcome this barrier, further computational studies should be performed. Such theoretical calculations would assist in providing more insight into the exact active sites and catalytic mechanism.

8.3. Heterogeneous photocatalysis with CTFs

In this thesis, two new highly N,S-rich CTFs are synthesized via the condensation reaction of aldehydes and amidines in mild conditions. The introduction of S-containing linkers (based on thiophene functionalities) into the structure of donor-acceptor CTFs could effectively expand visible light harvesting and enhance the charge transfer by π -electron delocalization. The highly active CTFs were used as metal-free photocatalysts for the degradation of Rhodamine B from aqueous media under visible light irradiation and air atmosphere (98% removal after 50 minutes). Since the metal-free photocatalysts are prepared under mild conditions and the photocatalytic reactions are performed under environmentally friendly conditions, the overall catalytic system can be considered entirely green.

Wastewater treatment in industries is typically done applying cheap solid-state adsorbents. Most often, activated carbons or bio-adsorbents, possibly in combination with synthetic ion exchange resins, are able to adsorb the (organic) pollutants. Although these conventional materials are usually very effective for removing a significant amount of the

targeted pollutants, removal of contaminants at lower concentrations remains a major challenge. Several photocatalytic degradation systems exist, but most photocatalysts suffer from large bandgaps and inefficient use of the solar spectrum. Moreover, problems associated with the low adsorption capacity of contaminants and post-recovery of the leached metals from metal-based catalysts after water treatment prove the urgent need for the design and development of alternative materials. The intrinsic advantages of CTFs, particularly high porosity, structural diversity, great stability, and the possibility to introduce various heteroatoms are beneficial to boost the photocatalytic activity and exceed the mentioned limitations. Upscaling process and suitable shaping of materials are highly important from an industrial point of view. On the other hand, in many cases, synthesis conditions at small scale do not translate directly into large scale setups. Further attempts to make CTFs at large scales in various shapes would be highly desirable. In addition, development of porous CTF membranes could lead to breakthroughs in photocatalytic systems.

8.4. Physiological luminescent thermometry with CTFs

The accurate sensing of local temperatures is a very important diagnostic tool for biomedical applications, such as treatment of cancer and inflammatory diseases. For the first time, we report a unique application of highly crystalline CTFs as a biocompatible molecular thermometer in the physiological temperature range in water. A highly crystalline bipyridine-based CTF (Bipy-CTF) is synthesized in mild conditions. The controlled tethering of lanthanide ions ($\text{Ln} = \text{Eu}^{3+}$ and Tb^{3+}) onto Bipy-CTF, combined with a selective photoexcitation, results in a ratiometric luminescent thermometer (LnCTF). So far, various luminescent materials have been proposed for biological thermometry applications (e.g. organic dyes, lanthanide MOFs, lanthanide complexes, etc.) and have most likely been selected on the basis of ease of access and cost effectivity. Despite these advantages, they exhibit significant drawbacks such as low thermal sensitivity, low stability and poor reusability. The designed LnCTF thermometer in this thesis exhibits an excellent linear response in the solid state over a wide range of temperatures (200 to 340 K), and a very good reusability (up to 98.5% repeatability).

The great importance of temperature measurements in biological systems inspires the development of multifunctional luminescent temperature sensor nanoplatfoms for biomedical purposes. However, such multifunctional sensors should meet specific requirements. Such materials must be non-toxic, biocompatible, photo and chemically stable, show bright fluorescence, and be well-dispersible in the biological media. The continuous development of new materials brings new possibilities to the field of sensors. We believe that this thesis inspires the scientific community to design nanosized CTFs to be applied in biomedical applications.

8.5. General outlook

Without reservations, we can conclude throughout these chapters that both MOFs and CTFs have tremendous potential as smart materials. Huge developments are possible in the field of heterogeneous catalysis, environmental remediation and sensing. Although the number of reports on CTFs is still limited, it can be predicted that this area will soon grow very rapidly.

In the field of heterogeneous catalysis, the most important feature of MOFs is the possibility to increase the complexity of materials. Accordingly, their properties can be tuned to adapt them to the optimal parameters required to promote a specific catalytic reaction. A higher degree of complexity can be implemented in MOFs than in CTFs because their synthesis can be designed with a large predictive capacity. One obvious example of this increased complexity for enhanced catalytic performance is mixed-metal MOFs (MM-MOFs). We have shown in this thesis that either pre-synthetic or post-synthetic modifications can be applied for the preparation of MM-MOFs. It would be interesting to apply the complexity of MOFs to design advanced catalysts with the desired chemo-, stereo- and regioselectivity in future work. Inspiration could be found in biochemistry and biomimetic catalysis. However, some challenges need to be addressed. These include the limited thermal and chemical stability of MOFs. Very few systems have been established which are stable up to 500 °C. In addition, MOF-based catalysts are not applicable for highly acidic or basic conditions.

Bringing the catalytic processes to industrial application entails enhancing productivity and stability and, in turn, developing novel catalytic systems. CTFs are particularly promising catalysts due to their outstanding thermal and chemical stability. The opportunity to tune the catalytic activity of CTFs via introducing numerous heteroatoms makes them ideal candidates for use in metal-free catalysis. So far, various carbon materials (N-doped activated carbon¹, P-doped graphitic carbon², and N-doped graphene³) have shown the potential to be used as metal-free catalysts. However, these catalysts often exhibit fundamental drawbacks, such as low efficiency (conversion <20%) or high catalyst loadings (200 wt %), as well as problems with catalyst recovery. The field of CTFs as metal-free catalysts is still in its early development. Further studies to explore these materials in metal-free catalysis for organic transformations are highly desirable. The field should be expanded from thermal catalysis to photocatalysis, electrocatalysis, flow catalysis and even plasma catalysis. However, one of the challenges to make CTFs under ionothermal conditions is the restricted structural characterization. One solution for this would be making use of computational studies. Such theoretical modelling would assist in providing more understanding of the structure and features of the materials. Moreover, more synthetic methods should be developed to make crystalline and porous CTFs using mild methods which can be characterized via typical existing techniques. The crystallization problem to make ordered CTFs remains a scientific challenge needing urgent attention.

From my perspective, I would like to mention that no single class of porous material is ideal for all purposes. For instance, crystallinity and long-range order might improve selectivity for a molecular separation while also decreasing mechanical resistance and/or chemical stability. For industrial applications, porous materials must be scalable and must fulfil multiple criteria, such as long-term stability, selectivity, adsorption kinetics, and processability. Based on my personal experience, CTFs meet many of these criteria. They have shown long-term stability and are chemically resistant to acidic and basic conditions. In addition, they are highly reproducible, making them ideal for industrial applications. However, a gap still exists between the studies and practical industrial use. R&D on catalysis is critical to accelerating the transition from lab scale to industrial scales.

The luminescent applications of CTFs, particularly mixed lanthanides, are also highly interesting. Temperature-controlled luminescent materials have, in our opinion, a huge potential in biomedicine, e.g., as thermochromic thermometers capable of measuring local temperature. The results in this thesis bring the inspiration of developing multifunctional luminescent temperature sensor nanoplatfroms using CTFs for biomedical purposes. In such applications, CTFs must be non-toxic, biocompatible, photo and chemically stable, show bright fluorescence, and be well-dispersible in the biological media. The continuous development of multifunctional CTFs brings new possibilities to the field of sensors.

Finally, I would like to highlight an important field of research, belonging to multidisciplinary teams; biomedicine. Biomedicine is a growing area for the field of MOFs and CTFs, not only by themselves but also certainly in combination with science and technology already existing in the literature. To reach this, further *in vivo* studies are needed in this field and collaborations must be found in other domains of research, belonging to multidisciplinary teams and even getting the support of pharmaceutical companies.

8.6. References

1. Watanabe, H.; Asano, S.; Fujita, S.; Yoshida, H.; Arai, M., Nitrogen-Doped, Metal-Free Activated Carbon Catalysts for Aerobic Oxidation of Alcohols. *Acs Catal* **2015**, *5* (5), 2886-2894.
2. Patel, M. A.; Luo, F. X.; Khoshi, M. R.; Rabie, E.; Zhang, Q.; Flach, C. R.; Mendelsohn, R.; Garfunkel, E.; Szostak, M.; He, H. X., P-Doped Porous Carbon as Metal Free Catalysts for Selective Aerobic Oxidation with an Unexpected Mechanism. *Acs Nano* **2016**, *10* (2), 2305-2315.
3. Long, J. L.; Xie, X. Q.; Xu, J.; Gu, Q.; Chen, L. M.; Wang, X. X., Nitrogen-Doped Graphene Nanosheets as Metal-Free Catalysts for Aerobic Selective Oxidation of Benzylic Alcohols. *Acs Catal* **2012**, *2* (4), 622-631.

APPENDIX

Materials and instrumentation

All chemicals were purchased from Sigma-Aldrich or TCI Europe and used without further purification. Diffuse reflectance infrared Fourier transform spectroscopy (DRIFTS) measurements were obtained on a Thermo Nicolet 6700 FT-IR spectrometer equipped with a nitrogen cooled MCT-A (mercury– cadmium–tellurium) detector and a KBr beam splitter. Far-IR spectra were recorded in the region of 50 to 700 cm^{-1} using a BRUKER Vertex 80v Vacuum FT-IR spectrometer.

Powder X-ray diffraction (XRD) patterns were collected on a Thermo Scientific ARL X'Tra diffractometer, operated at 40 kV, 40 mA using $\text{Cu-K}\alpha$ radiation ($\lambda = 1.5406 \text{ \AA}$). Nitrogen sorption studies were performed at $-196 \text{ }^\circ\text{C}$ using a Belsorp-mini II gas analyzer. Before the adsorption experiments, the samples were outgassed under vacuum at $120 \text{ }^\circ\text{C}$ to remove adsorbed water. The specific surface area was calculated in the linear range determined through the consistency criteria (microporous materials ($0.010 < P/P_0 < 0.045$), mesoporous materials ($0.05 < P/P_0 < 0.3$)). Thermogravimetric analysis (TGA) was carried out to determine the stability of the materials using a NET-ZSCH STA 409 PC/PGTG instrument. The samples were heated from 30 to $1000 \text{ }^\circ\text{C}$ in air or N_2 at a constant rate of $10 \text{ }^\circ\text{C}/\text{min}$.

^1H NMR spectra are recorded in DMSO-d_6 on a Bruker 400 MHz AVANCE spectrometer with chemical shifts (δ) expressed in ppm relative to a tetramethylsilane standard. Elemental analyses were performed on a ICP-OES Optima 8000 (inductively coupled plasma optical emission spectroscopy) atomic emission spectrometer. The nitrogen content of the modified materials was determined with a Thermo Flash 200 elemental analyzer is used with V_2O_5 as catalyst. The ^{13}C MAS NMR spectra were collected at 125.69 MHz using a 4 mm MAS NMR probe with a spinning rate of 8 kHz and a pulse width of $2.5 \mu\text{s}$ for a $\pi/4$ pulse, and 1800-2700 scans were gathered with a 4 s recycle delay.

The morphology of the sample was observed using field–emission scanning electron microscope (FE-SEM) FEI Nova NanoSEM 450. High angle annular dark-field scanning transmission electron microscopy (HAADF STEM) images were collected using a JEOL JEM-2200FS transmission electron microscope with a post-sample Cs corrector and an

accelerating voltage of 200 kV. For the sample preparation, the materials were dispersed in isopropanol by using an ultrasonic bath for 15 minutes. A copper support TEM grid (200 mesh) was dipped in the dispersion and air-dried before measurement. Annular dark-field scanning transmission electron microscopy (ADF-STEM) imaging was performed using an FEI Titan electron microscope operated at an accelerating voltage of 300 kV and equipped with a spherical aberration corrector unit. The samples were prepared by dispersing in ethanol and dropping onto the carbon coated TEM copper grid. The diffuse reflectance spectra (DRS) were collected using a Perkin Elmer Lambda 1050 UV-Vis-NIR spectrophotometers. An ultra-fast GC equipped with a flame ionization detector (FID) and a 5% diphenyl/95% polydimethylsiloxane column, with 10 m length and 0.10 mm internal diameter was used to follow the conversion of the products during the catalytic tests. Helium was used as carrier gas and the flow rate was programmed as 0.8 mL/min. The reaction products were identified with a TRACE GC × GC (Thermo, Interscience), coupled to a TEMPUS TOF-MS detector (Thermo, Interscience). The first column consists of a dimethyl polysiloxane package and has a length of 50 m, with an internal diameter of 0.25 mm, whereas the second column has a length of 2 m with an internal diameter of 0.15 mm. The package of the latter is a 50% phenyl polysilphenylene-siloxane. Helium was used as carrier gas with a constant flow (1.8 mL/min).

X-ray Crystallography. For the structures of **1** and **2**, X-ray intensity data were collected at 100 K, on a Rigaku Oxford Diffraction Supernova Dual Source (Cu at zero) diffractometer equipped with an Atlas CCD detector using ω scans and $\text{CuK}\alpha$ ($\lambda = 1.54184 \text{ \AA}$) or $\text{MoK}\alpha$ ($\lambda = 0.71073 \text{ \AA}$) radiation, for **1** and **2**, respectively. For the structure of **3**, graphite monochromatic $\text{Mo-K}\alpha$ radiation ($\lambda = 0.71073 \text{ \AA}$) on a four-circle κ geometry KUMA KM-4 diffractometer, with a two-dimensional area CCD detector, was used. The images were interpreted and integrated with the program CrysAlisPro.⁴² Using Olex2,⁴⁸ the structures were solved by direct methods using the SHELXT program and refined by full-matrix least-squares on F^2 using the SHELXL program package.⁴⁹⁻⁵⁰ Non-hydrogen atoms were anisotropically refined and the hydrogen atoms in the riding mode and isotropic temperature factors fixed at 1.2 times $U(\text{eq})$ of the parent atoms. Hydroxyl H-atoms were located when possible through a Fourier difference electron density map (refined with isotropic temperature factors fixed at 1.5 times $U(\text{eq})$). In crystal **3** it was

possible to localize and refine some of the disordered solvent/water molecules. The rest of the solvent molecules (nicotinamide) are highly disordered. The correct modelling of the disordered molecules was not possible and we performed a “squeeze” treatment to remove the scattering contribution of these molecules, which could not to be satisfactory modelled. The final difference Fourier maps showed no peaks of chemical significance. CCDC 1897917-1897919 contain the supplementary crystallographic data for this paper and can be obtained free of charge via www.ccdc.cam.ac.uk/conts/retrieving.html (or from the Cambridge Crystallographic Data Centre, 12, Union Road, Cambridge CB2 1EZ, UK; fax: +44-1223-336033; or deposit@ccdc.cam.ac.uk).

Luminescence. The luminescence of solid samples was studied. Solid powdered samples were put between quartz plates (Starna cuvettes for powdered samples, type 20/C/Q/0.2). Colloidal suspensions were measured in quartz cuvettes with a path length of 10 mm. Luminescence measurements were performed on an Edinburgh Instruments FLSP920 UV-vis-NIR spectrometer setup. A 450W xenon lamp was used as the steady state excitation source. Luminescence decay times were recorded using a 60W pulsed Xe lamp, operating at a frequency of 100 Hz. A Hamamatsu R928P photomultiplier tube was used to detect the emission signals in the near UV to visible range. All of the luminescence measurements were recorded at room temperature unless indicated otherwise. The temperature-dependent luminescent measurements of the powder samples were measured using an ARS CS202-DMX-1SS closed cycle cryostat (4K – 800 K) controlled with a Lake Shore Model 336 temperature controller. The temperature-dependent luminescent measurements of the CTF material suspended in water were performed using a Julabo refrigerated and heating F-25 circulator in a temperature range of 283.15 K to 323.15 K with steps of 5 K, which was circulating through the cuvette holder supplied by the Edinburgh Instruments. All emission spectra in the manuscript have been corrected for detector response. The luminescence decay curves of the samples were measured when excited into the maximum of the broad ligand band and monitored at the appropriate wavelength (strongest peak of the given lanthanide). All of the decay curves could be well fitted using either a single exponential function or biexponential function.

$$I = A \exp\left(-\frac{t}{\tau}\right)$$

$$I = A_1 \exp\left(-\frac{t}{\tau_1}\right) + A_2 \exp\left(-\frac{t}{\tau_2}\right)$$

Where I represents the luminescence intensity of a transition and A , A_1 and A_2 are constants, t is time and τ , τ_1 and τ_2 are the luminescence lifetimes. The temperature-measurements were performed using an ARS closed cycle cryostat at a temperature range between 200 – 340 K. For the conversion of intensity into temperature the thermometric parameter Δ was employed. Here, $\alpha = W_0/W_R$ is the ratio between the nonradiative (W_0 at $T = 0$ K) and radiative (W_R) rates, ΔE is the activation energy for the nonradiative channel, and Δ_0 is the thermometric parameter at $T = 0$ K.

$$\Delta = \frac{I_1}{I_2} = \frac{\Delta_0}{1 + \alpha \exp\left(-\frac{\Delta E}{k_B T}\right)}$$

The relative temperature sensitivity S_r was calculated using the following equation:

$$S_r = 100\% \times \left| \frac{1}{\Delta} \frac{\partial \Delta}{\partial T} \right|$$

S_r indicates the relative change of the thermometric parameter per degree of temperature change (% K^{-1}). S_r is independent of the nature of the thermometer and allows direct and quantitative comparison of different materials. All calculations were carried out employing the TeSen software. To fully evaluate the performance of the thermometer additionally the uncertainty was calculated as well as the reproducibility after several cycles. The temperature uncertainty δT is one of the important parameters in assessment of the performance of the desired thermometer. Calculation of the δT can be determined with the following equation:

$$\delta T = \frac{1}{S_r} \frac{\delta \Delta}{\Delta}$$

The performance stability of thermometers is estimated by cycling the temperature in the given temperature interval ensuring that the thermometer reaches the thermal equilibrium for each measurement and it can be given with:

$$R = 1 - \frac{\max(|\Delta_c - \Delta_i|)}{\Delta_c}$$

Appendix

where the Δ_c is the mean thermometric parameter extracted from the calibration curve and Δ_i is value of each thermometric parameter measurement.

Cell cultivation. NHDF Fibroblastic cell of NHDF cells were cultured in DMEM (Cat. No. D5546) supplemented with 10% FBS, 2 mM glutamine, and 100 $\mu\text{g/ml}$ penicillin/streptomycin. The media were replaced every 3 days, and the cells were maintained in a humidified incubator at 37 °C with 5% CO_2 (Innova CO-170, New Brunswick Scientific).

Cell Viability. NHDF cells were seeded into 96-well cell culture plates at a cell density of 10×10^4 /well. After 24 h cultivation, particles from 0.001 mg/well till 1 mg/well were placed into the plate in the culture medium and incubated overnight at 37 °C under 5% CO_2 . Subsequently, cells were incubated (Innova CO-170, New Brunswick Scientific) at 37 °C for 4 h, together with 10 μL of fluorescence dye was added to each well (Alamar Blue, Sigma-Aldrich). In the last step fluorescent (540/610 nm) intensity was measured by a spectrophotometer (Synergy H1Multi-Mode Reader).

Fluorescence microscopy: To visualize viable cells a Nikon TI (Nikon, Japan) fluorescence microscope with the following objective 10X and appropriate filters was used. After 1 days of incubation with Bipy-CTF particles, cell layers were then stained with calcein AM. Cells were incubated with a medium containing 0.1 mM of the reagent for 10 min at RT.

BET surface area. The determination of surface areas from the BET theory is a straightforward application of equation:

$$\frac{1}{V_a \left[\left(\frac{P}{P_0} \right) - 1 \right]} = \frac{1}{V_m C} + \frac{C - 1}{V_m C} \frac{P}{P_0}$$

A plot of $1/[V_a [(P/P_0) - 1]]$ versus P/P_0 will yield a straight line, usually in the range $0.05 \leq (P/P_0) \leq 0.30$. Caution, however, as this is not automatically the case, and the operator should always inspect the BET plot and manually select the points that best produce a linear BET plot! The slopes and intercepts of the BET plot are:

$$s = \frac{C - 1}{V_m C}$$

$$i = \frac{1}{V_m C}$$

Solving the preceding equations yields:

$$V_m = \frac{1}{s + i}$$

$$C = \frac{s}{i} + 1$$

V_m is then used, similar as for the Langmuir model, to calculate the surface area, by means of equation:

$$S[m^2 g^{-1}] = m_m N_A A \cdot 10^{-18}$$

in which m_m is the number of moles adsorbate that is adsorbed per gram of adsorbent; it is obtained by dividing V_m by 22 400; and A is the “mean cross-sectional area” of the adsorbate. For the dinitrogen molecule, the mean cross-sectional area is 0.162 nm².

Catalytic stability studies.

Turnover number and Turnover frequency.

The turnover number (TON) refers to the number of moles of substrate that a mole of active sites in a catalyst can convert before becoming inactivated. As this is often too long for practical use, the TON is often reported after t after a prolonged but clearly defined period of time.

Turnover number (TON) = number of moles of reactant converted/ (mole of active sites in catalyst).

The **turnover frequency** (TOF) refers to the turnover number per unit time. As the rate of a reaction (especially in a batch reactor, not so much in a plug flow reactor) is not

Appendix

constant as a function of time, the turnover frequency should be reported at maximum speed of the catalyst, i.e. at the beginning of the reaction.

TON is just number without unit and TOF is per unit time for example h^{-1} or s^{-1} .

Recycling test. The recycling runs are performed immediately after the full conversion was achieved. While it is better to perform recyclability tests at intermediate conversion rates (e.g. 50%), the recyclability tests when the full conversion is only just reached are also meaningful. Deactivation will result in a lower conversion percentage in the next runs.

The recycling tests are just an indication and are not definitive proof of catalyst stability.